Target Induced Halo Formation and Collimation Following MAGIX at MESA

Dissertation submitted for the award of the title
“Doctor of Natural Sciences”

to the Faculty of Physics, Mathematics, and Computer Science
of the Johannes Gutenberg-University Mainz

Ben Ledroit
born in Mainz

Mainz, 16th December 2020

Date of doctoral viva: 19th April 2021

Abstract

The Mainz Energy-recovering Superconducting Accelerator (MESA) is a recirculating electron linear accelerator (Linac), that is currently under construction in the Institute for Nuclear Physics at the Johannes Gutenberg-University Mainz. MESA will be able to operate in energy recovery linac (ERL) mode, in which the energy of the accelerated beam is recovered through subsequent deceleration. This technique enables reaching high beam powers and therefore high luminosities available for experiments with considerably less installed amplifier power compared to conventional Linacs. The Mainz Gas Internal Target Experiment (MAGIX) takes advantage of the MESA beam currents of initially up to 1 mA at 105 MeV beam energy available in ERL mode to realize a variety of nuclear physics experiments. These experiments aim for a luminosity of minimum $10^{35}\,\mathrm{cm}^{-2}\,\mathrm{s}^{-1}$. The ERL mode requires recirculation of the accelerated beam through the accelerator after passing the target and degradation of the beam through the beam-target interaction must be limited to ensure proper beam transport for energy recovery. The beam degradation at MAGIX is governed by scattering of beam electrons on the target, which leads to beam halo formation after the target and induces beam losses in following accelerator sections. Collimators are needed in sections downstream of MAGIX to intercept the beam halo in order to control beam losses and the lost beam power leads to a reduction of ERL efficiency as well as radioactive activation of exposed equipment. The target induced beam degradation consequently limits the practically achievable luminosity at the experiment. The formation of the halo and the behavior of subsequently occurring beam losses for the envisaged MAGIX experiments at MESA are studied in simulations in this thesis. A suitable collimation system is presented in the following and the resulting activation of accelerator equipment is examined to estimate a luminosity limit for MAGIX operation in MESA ERL mode. The presented results show that the operation of hydrogen and helium targets at the aimed at luminosity is possible, whereas a restriction of luminosity is required for heavier target gases.

Zusammenfassung

Der Mainz Energy-recovering Superconducting Accelerator (MESA) ist ein rezirkulierender Elektronen-Linearbeschleuniger (Linac), der sich derzeit am Institut für Kernphysik der Johannes Gutenberg-Universität Mainz im Bau befindet. MESA wird in der Lage sein, im Energy Recovery Linac (ERL) Modus zu arbeiten, in dem die Energie des beschleunigten Strahls durch anschließende Entschleunigung zurückgewonnen wird. Diese Technik ermöglicht das Erreichen von hohen Strahlleistungen und damit verbundenen hohen Luminositäten, die für Experimente zur Verfügung stehen, bei bedeutend kleinerer installierter Verstärkerleistung im Vergleich zu konventionellen Linacs. Das Mainz Gas Internal Experiment (MAGIX) nutzt die MESA Strahlströme von anfangs 1 mA bei 105 MeV Strahlenergie im ERL Modus, um eine Vielzahl von kernphysikalischen Experimenten mit Gas-Jet Targets zu realisieren. Für diese Experimente wird eine Luminosität von mindestens $10^{35}\,\mathrm{cm}^{-2}\,\mathrm{s}^{-1}$ angestrebt. Der ERL Modus setzt eine Rezirkulation des beschleunigten Strahls durch den Beschleuniger nach Passieren des Targets voraus und die Degradierung des Strahls durch die Strahl-Target-Wechselwirkung muss begrenzt werden, um den ordungsgemäßen Strahltransport für die Energierückgewinnung zu gewährleisten. Die Strahldegradierung an MAGIX ist bestimmt durch die Streuung von Strahlelektronen am Target, was zu der Bildung eines Strahlhalos nach dem Target führt und Strahlverluste in nachfolgenden Beschleunigersektionen verursacht. Kollimatoren werden in den Sektionen nach MAGIX benötigt, um den Strahlhalo abzufangen damit Strahlverluste kontrolliert werden, und die verlorene Strahlleistung führt zu einer Reduzierung der Energierückgewinnungseffizienz sowie radioaktiver Aktivierung von bestrahltem Gerät. Die targetinduzierte Strahldegradierung limitiert folglich die praktisch erreichbare Luminosität am Experiment. Die Bildung des Halos und das Verhalten der nachfolgend auftretenden Strahlverluste für die angestrebten MAGIX-Experimente an MESA werden in Simulationen in dieser Arbeit studiert. Anschließend wird ein geeignetes Kollimationssystem präsentiert und die resultierende Aktivierung der Beschleunigerausstattung untersucht, um ein Luminositätslimit für den Betrieb von MAGIX im MESA ERL Modus abzuschätzen. Die vorgestellten Ergebnisse zeigen, dass der Betrieb von Wasserstoff- und Helium-Targets Targets bei der angestrebten Luminosität an MESA möglich ist, wohingegen eine Beschränkung der Luminosität für schwerere Targetgase benötigt wird.

Contents

1 Motivation

1.1 Physics Challenges

Particle accelerators are valuable instruments for physics experiments since their establishment in the last century. Their ability to reach energy scales not reasonably achievable otherwise has allowed physicists to discover a plentitude of particles and has been a crucial element in the construction and verification the standard model of particle physics. While the standard model proves exceptionally useful in many applications, its present form is not sufficient to describe e.g. the observation of dark matter or deviations from predicted particle abundances in astrophysical processes. As an example for the latter, an observed excess in photon production from e^+e^--annihilation in the milky way center is possibly explained by the introduction of an additional $U(1)$-symmetry in the standard model [Heinemeyer *et al.* 2007]. The additional symmetry is accompanied by a gauge boson, a dark photon, which is proposed to be found in the 1 MeV to 100 MeV scale. A second notable physics challenge is the so-called proton-radius puzzle, where results for the proton charge radius exhibit a significant discrepancy in measurements of electronic and muonic hydrogen [Karr & Marchand 2019]. To contribute to the resolution of the proton-radius puzzle, precision measurements of cross-sections and magnetic form factor of the proton with reduced background have been proposed by [Bernauer 2020]. Both of the aformentioned problems require experiments with high precision in the MeV scale rather than higher energy scales achievable with the current generation of energy frontier colliders, where the lower energy scale minimizes background from the production of extra particles. Accelerators for precision experiments therefore represent a complementary approach to high energy accelerators in understanding and extending the standard model of particle physics.

Precision physics experiments furthermore require large data sets to reduce statistical uncertainty and to be able to resolve the process of interest. A high interaction rate is therefore sought after, which is accordingly enhanced with the luminosity of an experiment. The luminosity itself can be maximized by increasing target thickness or beam current. It may be technically challenging or undesirable for a precision experiment to increase target thickness, so then the beam current must rather be increased. This can be achieved by accumulating beam charge in storage rings, where the beam deteriorates in every turn in the ring. A different approach is provided by energy recovery linacs, where the beam passes the interaction region only once, therefore conserving beam quality. The beam power can simultaneously be sustained with the recovery of beam energy after target passage without the need to install additional radio frequency power amplifiers.

The operation of an energy recovery linac requires that the beam power can be recovered after target passage. Scattering on the target however leads to beam halo formation and beam losses and consequently a fraction of the beam power cannot be recovered. The beam losses itself depend on the experiment scattering rate, so that the achievable luminosity cannot be increased arbitrarily. The target induced halo formation, countermeasures and luminosity limit for the Mainz Energy-recovering Superconducting Accelerator are presented in the following.

1.2 MESA

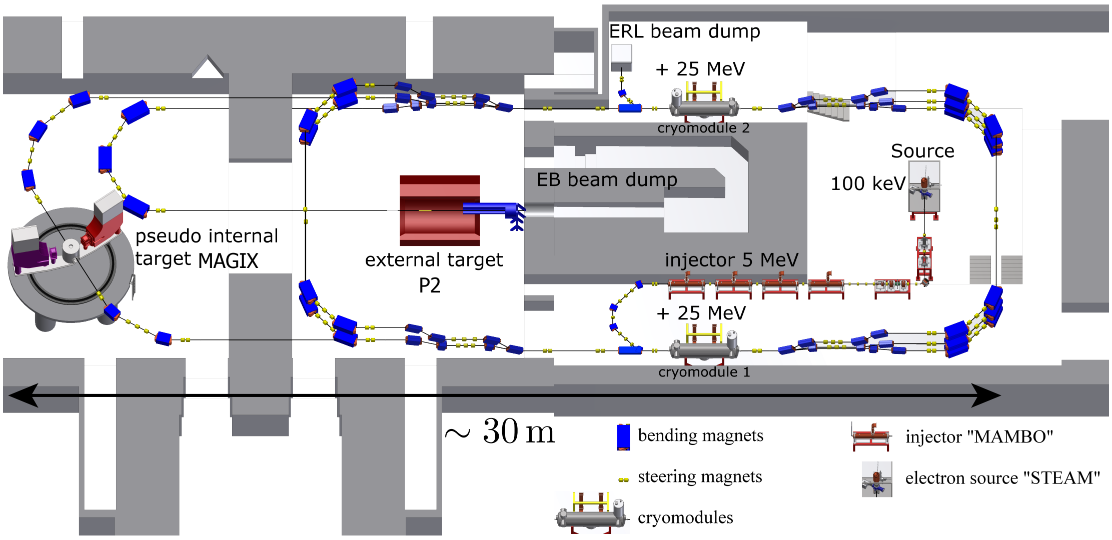

Figure 1.1: Schematic drawing of MESA with experiments MAGIX and P2 from 2018 [Simon & Stengler 2018]. The beam line is marked by a black path and steered with dipoles (blue) and quadrupoles (yellow). Electrons are generated in the source and pre-accelerated to 5 MeV in the injector MAMBO. The recirculation direction is counter clockwise.

The Mainz Energy-recovering Superconducting Accelerator (MESA) is a continuous wave (c.w.) recirculating electron linear accelerator (Linac) currently under construction. Electrons extracted from a photo-source are accelerated by radio frequency (RF) fields in superconducting cavities, which are housed in a thermally shielded tank, the cryomodules. Superconducting acceleration cavities are used to minimize ohmic power losses and give the opportunity for operation in energy recovery linac (ERL) mode. In ERL mode, the previously accelerated beam is decelerated, transferring its energy back to the RF field in the cavities. The idea to build an ERL is first mentioned in [Tigner 1965] and allows to bypass the RF amplifier power limit in c.w. operation to reach high beam currents, respectively beam powers. The flux of projectiles available for scattering experiments can therefore be substantially increased without major investments in installed RF power, which makes such a machine especially attractive for precision experiments that depend on high statistics. MESA is designed to operate at first up to 1 mA beam current (MESA stage 1) and after upgrade at up to 10 mA (MESA stage

2) at a nominal energy of 105 MeV in ERL mode. The MESA layout from 2018 discussed in this thesis is depicted in Figure 1.1. This layout has been changed to enable simultaneous civil construction work and commissioning of the injector as illustrated in Figure 1.2. In the course of this, the MAGIX target arc has been redesigned, which is not expected to change fundamental systematics discussed in later chapters, however these details need to be re-examined following on from this thesis.

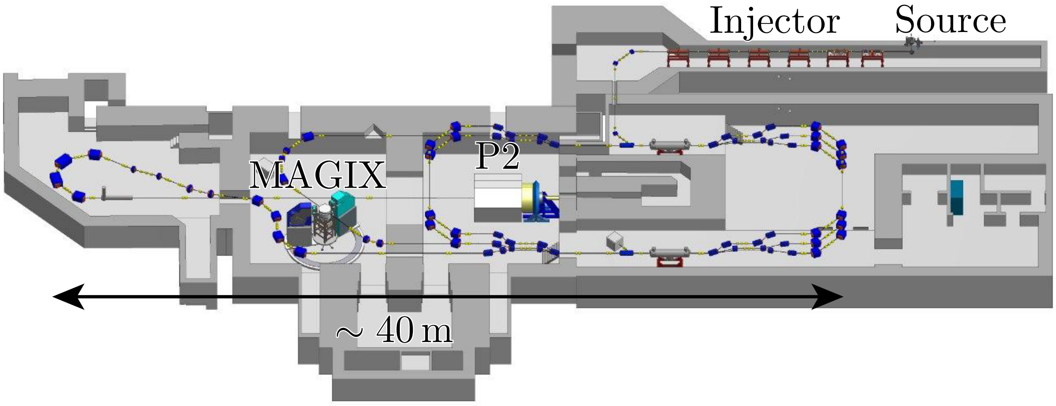

Figure 1.2: Schematic drawing of MESA from 2020 [Simon 2020]. The beam line is marked by a black path and steered with dipoles (blue) and quadrupoles (yellow). Source and injector are relocated in an already existing tunnel and the MAGIX and P2 arc are redesigned. The recirculation direction is clockwise.

1.3 MAGIX

The MESA Gas Internal Target Experiment (MAGIX) is a versatile windowless gas target experiment for the use in the MESA ERL beam line. It includes all the components required for the experiments such as the spectrometers and focal plane detectors for simple and incident particle detection as well as the gas target itself. The MAGIX target is designed without windows to reduce background signal originating from beam-window scattering (see Figure 1.3) and features operation with different target gases to perform a range of precision experiments at MESA energy ranges [Doria *et al.* 2018].

Measurement campaigns currently planned are:

- Proton radius measurement in a hydrogen target to tackle the proton radius puzzle [Bernauer 2020].
- Few body physics with a helium target [Schlimme 2020].
- Measurement of the astrophysical S-factor in the inverse solar fusion reaction $O(\gamma, \alpha)C$, important in astrophysics [Friščić *et al.* 2019].
- Search for dark photons in experiments with a heavy nuclear target (argon, xenon) [Doria *et al.* 2018], based on suggestions from [Heinemeyer *et al.* 2007].

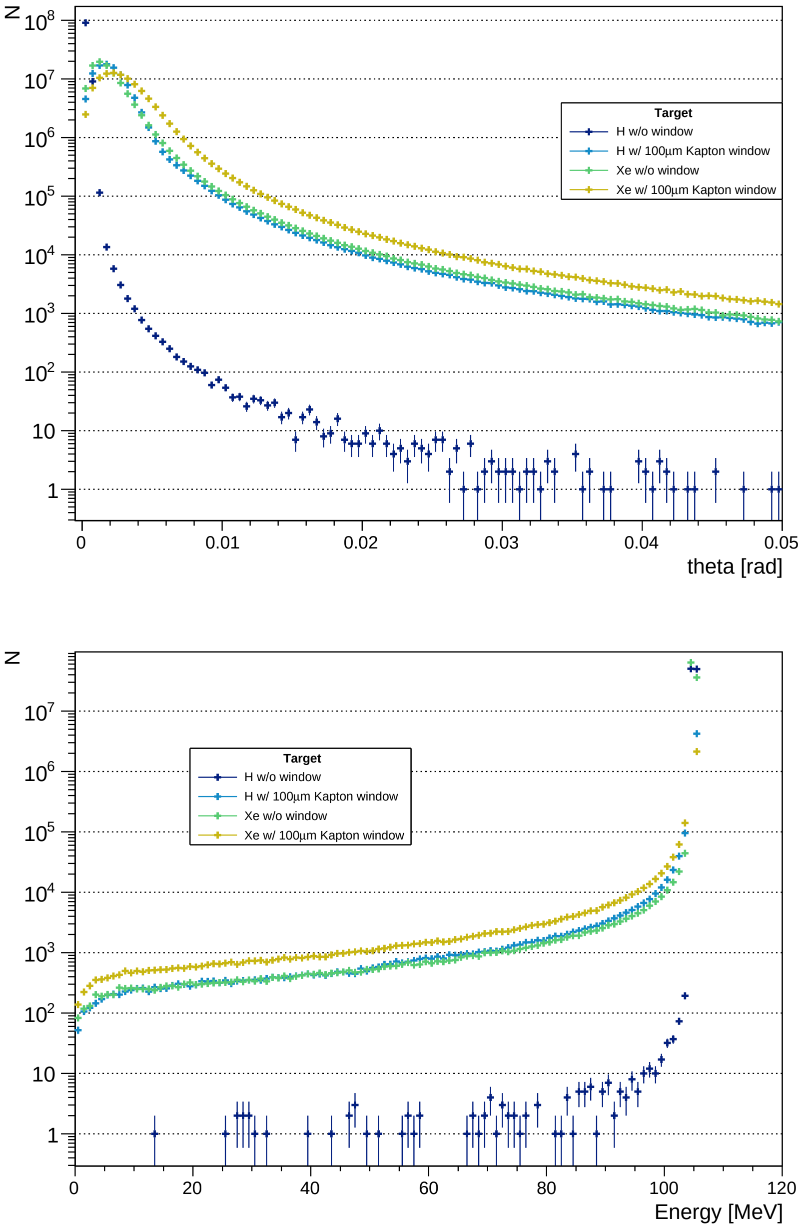

Figure 1.3: Comparison of angle (top) and energy distributions (bottom) with and without a 100 µm thick Kapton target window in a Geant4 simulation with 10^8 particles according to the setup described in Chapter 5. The targets comprise of hydrogen and xenon, the beam size is $\sigma_{x,y} = 25\,\mu\text{m}$ and the beam energy $E = 105\,\text{MeV}$. A drastic widening of angle distribution and enhanced energy loss from the target window is observed especially for hydrogen.

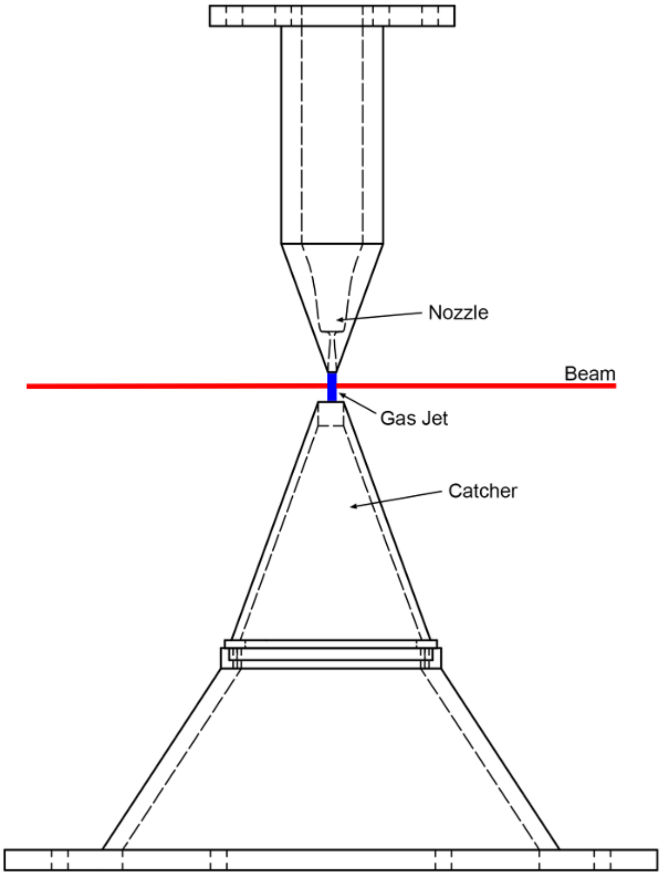

Figure 1.4: Side view of the MAGIX gas jet target [MAGIX group 2020]. The gas is contained in the blue area and accelerated downwards, the beam passes through the target horizontically.

To ensure the required vacuum conditions outside the interaction region and simultaneously maintain a high target density, the target is a gas jet produced by accelerating the gas from a pressurized reservoir through a Laval nozzle to supersonic speeds [Grieser *et al.* 2018] (see Figure 1.4). The majority of the gas jet is immediately collected in an opposing gas catcher before the gas can diffuse into the vacuum. The diffusion velocity is expected to further be decreased by establishing clustering, where gas atoms glue into larger and more massive compounds [Grieser *et al.* 2018, p.3]. All aforementioned experiments are prepared with unpolarized targets. Further experiments with polarized targets are also considered, which cannot be operated with a gas jet, since the polarization of the target gas decays during high pressure storage before injection into the vacuum. Tube targets are instead planned for polarized experiments. However, in this thesis only the gas jet target is discussed. Tube targets require dedicated treatment to account for the increased target length and gas diffusion outside the interaction region. A comparable experiment to the MAGIX hydrogen target experiment is DarkLight [Lee *et al.* 2019], which features the only internal target that has been operated in an ERL to date. DarkLight successfully delivered an electron beam to a hydrogen target with an areal particle density of $10^{18}\,\mathrm{cm}^{-2}$ and a length of 77 cm [Tennant 2018]. Energy recovery could however not be successfully applied, owing misalignments of baffles in the target region [Tennant 2018]. Continuing and expanding the idea of DarkLight, MAGIX therefore embodies important pioneering work in the field of ERL experiments and effects on the operation of MESA require investigation.

1.4 Target Induced Halo (TAIL)

The major expected effect of the internal ERL target is arising from the beam-target scattering, the target induced halo (TAIL). As in conventional linacs the beam is directly transported to the beam dump, relatively loose requirements on the beam quality after target passage can be accepted. Consequently thick targets can be deployed in a conventional linac. Storage rings, in contrast, feature thin targets (e.g. BLAST featured a $4.9 \times 10^{13}\,\mathrm{cm}^{-2}$ target [Crawford 2005, p.114], HERMES achieved around $1 \times 10^{14}\,\mathrm{cm}^{-2}$ areal target density [Baumgarten *et al.* 2003, p.1]) and it is well-known practice to tune the life time of the beam with variation of focus and therefore luminosity in the interaction region(s). Life time and luminosity are counteracting parts in such a machine. The MAGIX targets are however designed to operate in an intermediate region, between thin storage rings targets and thick linac targets, aiming to exploit the high luminosity and brilliance that an ERL can provide through high beam currents. This implies that ERL operation must be compatible with the target design and operation.

1.5 ERL Limitations

ERL beams intrinsically have no characteristic beam life time since the beam passes the machine only once and is continuously replenished. Storage ring operation, in contrast, faces continuous beam degradation from target scattering and hence the beam must be completely replenished as soon as the beam quality cannot be maintained for experimentation. The losses emerging from an internal target however still set a limit on the operation of an ERL, which is due to the loss of power that cannot be recovered (see Figure 1.5). As the available RF power at MESA is restricted to 150 kW and the greater part is needed to compensate ohmic losses in the injector, additional losses have to be well known in order to maintain beam powers in the MW regime in future upgrades. It can be necessary to put limits on luminosity in this context as well as in storage rings, while operating with considerably thicker targets at MESA.

Figure 1.5: Schematic illustration of power flow during ERL operation. 100 % refers to the total beam power without the injector power, which cannot be recovered. A fraction x is lost and must be compensated with wall-plug power from the RF amplifiers.

2 Theory

In this chapter the basic concepts of accelerator physics that are needed for the subsequent studies are provided in a compact form. The reader is advised to follow the references for additional and detailed information on the specific topics.

2.1 Linear Beam Dynamics

This section discusses the fundamental approach to linear beam dynamics for accelerator design and its quantities used throughout the thesis.

2.1.1 Curvilinear Coordinate System

The cartesian reference frame for the beam $\vec{x}$-$\vec{y}$-$\vec{z}$ is transformed into a curvilinear frame $\vec{x}$-$\vec{y}$-$\vec{s}$, so that $\vec{s}$ is always pointing into the direction of motion for a reference particle (i.e. reference energy and orbit) [Wille & McFall 2000, pp.44f]. In the convention used here, the $\vec{x}$-axis always denotes the horizontal and $\vec{y}$ the vertical direction (see Figure 2.1).

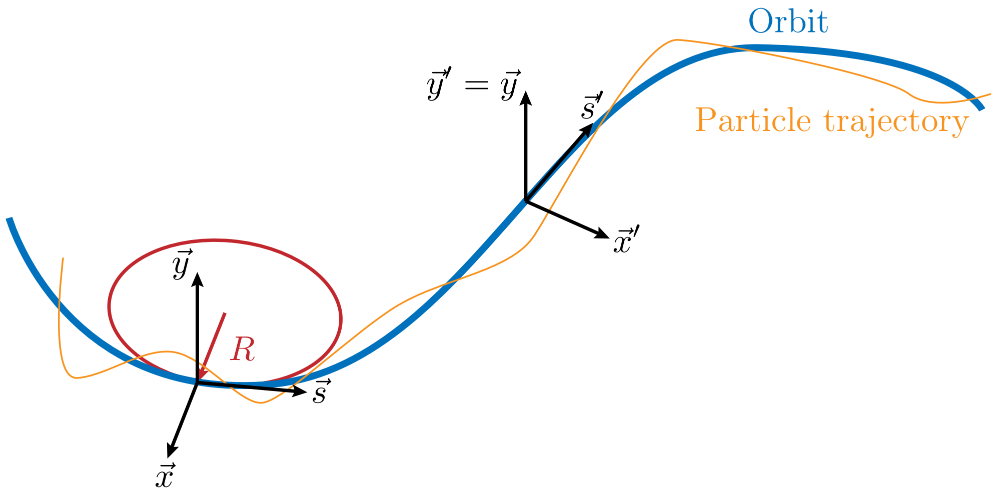

Figure 2.1: Illustration of a curvilinear coordinate frame $\vec{x}$-$\vec{y}$-$\vec{s}$ transforming into $\vec{x}'$-$\vec{y}'$-$\vec{s}'$ as it moves along the nominal orbit in the x-plane (blue) with a single particle trajectory (orange) and local curvature radius R (red).

2.1.2 Equations of Motion

The charged particle beam is controlled with magnetic fields of electron-optical elements. For the sequence of electron-optical elements, the term lattice is introduced. By only considering motion of particles with $\vec{p} = (0, 0, mv_s)$ in the x-plane through magnetic fields with transverse components $\vec{B}(x, y, s) = (B_x, B_y, 0)$, the Lorentz force [Wille & McFall 2000, p.44]:

$$\vec{F} = \dot{\vec{p}} = q(\vec{E} + \vec{v} \times \vec{B}),$$

generating the equation of motion becomes [Wille & McFall 2000, p.45]:

$$F_x = \frac{mv_s^2}{R(x, y, s)} = -qv_s B_y(x, y, s),$$

or [Wille & McFall 2000, p.45]:

$$\frac{1}{R(x, y, s)} = \frac{q}{p} B_y(x, y, s), \tag{2.1}$$

where $R(x, y, s)$ is the orbit curvature radius at a given point. Multipole expansion of the magnetic field around the reference orbit yields [Wille & McFall 2000, p.45]:

$$B_y(x) = \sum_{k=0}^{n} \frac{1}{k!} \frac{\mathrm{d}^k B_y}{\mathrm{d}x^k} x^k$$

and when terminated at the linear term, for Equation 2.1 follows [Wille & McFall 2000, p.45]:

$$\frac{q}{p} B_y(x) = \frac{q}{p} B_{y0} + \frac{q}{p} \frac{\mathrm{d}B_y}{\mathrm{d}x} x = \frac{1}{R} + kx$$

Here R is the orbit curvature radius in the dipole field and k the quadrupole strength. The quadrupole component provides a force linearly increasing with the offset of the particle from the reference orbit, which can be used for (de)focusing a particle collective distributed around the reference trajectory. Therefore considerations in accelerator design and beam steering with only these two multipoles present is called linear beam optics [Wille & McFall 2000, pp.45f]. For a layout with dipoles only in the x-plane and arbitrary quadrupole component $k(s)$, the equations of motion in both transverse dimensions is given as [Wille & McFall 2000, pp.56ff]:

$$\begin{gathered} \frac{\mathrm{d}^2 x(s)}{\mathrm{d}s^2} + \left(\frac{1}{R^2(s)} - k(s)\right) x(s) = \frac{1}{R(s)} \frac{\Delta p}{p} \\ \frac{\mathrm{d}^2 y(s)}{\mathrm{d}s^2} + k(s) y(s) = 0, \end{gathered} \tag{2.2}$$

where Δp denotes the momentum deviation from the nominal momentum p. It is noteworthy that the signs of k are opposite for x and y, so that a horizontally focusing quadrupole is vertically defocusing and vice versa.

2.1.3 Dispersion

Dispersion is introduced in Equation 2.2 by magnetic dipole fields ($k = 0$) and $\frac{\Delta p}{p} \neq 0$, meaning particles with a different than nominal energy experience different bending radii [Wille & McFall 2000, pp.74f]. This leads to a splitting according to energy of particles of a beam initially travelling through a dipole. The subsequent drift is then a dispersive section and the dispersion D of this section is a section property. Particles carrying a Δp difference to the design momentum p have an offset Δx to the design trajectory [Wille & McFall 2000, p.75]:

$$\Delta x = D \frac{\Delta p}{p}$$

This is applicable for y as well, however when considering a planar accelerator with dipoles in only the x-plane, the effect in y is non-existent.

2.1.4 Betatron Motion

When no dipoles are present ($\frac{1}{R} = 0$) and $\frac{\Delta p}{p} = 0$, Equation 2.2 becomes [Wille & McFall 2000, p.77]:

$$\frac{\mathrm{d}^2 x(s)}{\mathrm{d}s^2} - k(s)x(s) = 0,$$

which is Hill's equation and has the piecewise form of a harmonic oscillator, and can be solved by [Wille & McFall 2000, p.77]:

$$\begin{aligned} x(s) &= \sqrt{\varepsilon}\sqrt{\beta_\mathrm{T}(s)}\cos(\Psi(s) + \phi) \\ \Psi(s) &= \int_0^s \frac{\mathrm{d}\sigma}{\beta_\mathrm{T}(\sigma)} \end{aligned}$$

As consequence, particles in the beam will perform an oscillatory motion around the orbit. This process is called betatron oscillation. For the envelope of a particle collection E follows [Wille & McFall 2000, p.78]:

$$E(s) = \sqrt{\varepsilon \beta_\mathrm{T}(s)}, \tag{2.3}$$

where ε is the emittance and a constant of motion and $\beta_\mathrm{T}(s)$ the beta function. As can be seen from Equation 2.3, β_T is a measure for the beam size.

2.1.5 Phase Space Representation of Motion

It is useful to describe particle motion by means of collective quantities instead of single particle trajectories. This is achieved in the phase space ellipse equation [Wille & McFall 2000, p.80]:

$$\gamma_\mathrm{T}(s)x^2(s) + 2\alpha_\mathrm{T}(s)x(s)x'(s) + \beta_\mathrm{T}(s)x'^2(s) = \varepsilon_\mathrm{geo}, \tag{2.4}$$

which has the form of an ellipse with area $\pi\varepsilon_\mathrm{geo}$. The ellipse can be described by the Twiss parameters α_T, β_T and γ_T (see Figure 2.2). These are functions along the accelerator lattice and describe the beam at a given point for a periodical lattice. For a non-periodical lattice, the beam transformation is determined when the beam emittance at the entrance is known. The transverse momenta are translated into angles x' and y' w.r.t. p and for description of accelerator beam dynamics a small-angle approximation is made since mentioned angles are small (i.e. in the order of mrad):

$$p_x = p\sin(x') \approx p \cdot x',$$

and [Wille & McFall 2000, pp.79f]:

$$\alpha_\mathrm{T} = -\frac{1}{2}\frac{\mathrm{d}\beta_\mathrm{T}(s)}{\mathrm{d}s} \tag{2.5}$$

$$\gamma_\mathrm{T} = \frac{1+\alpha_\mathrm{T}^2(s)}{\beta_\mathrm{T}(s)}, \tag{2.6}$$

where α_T provides a measure for the divergence. The parameters α_T, β_T and γ_T are called Twiss parameters.

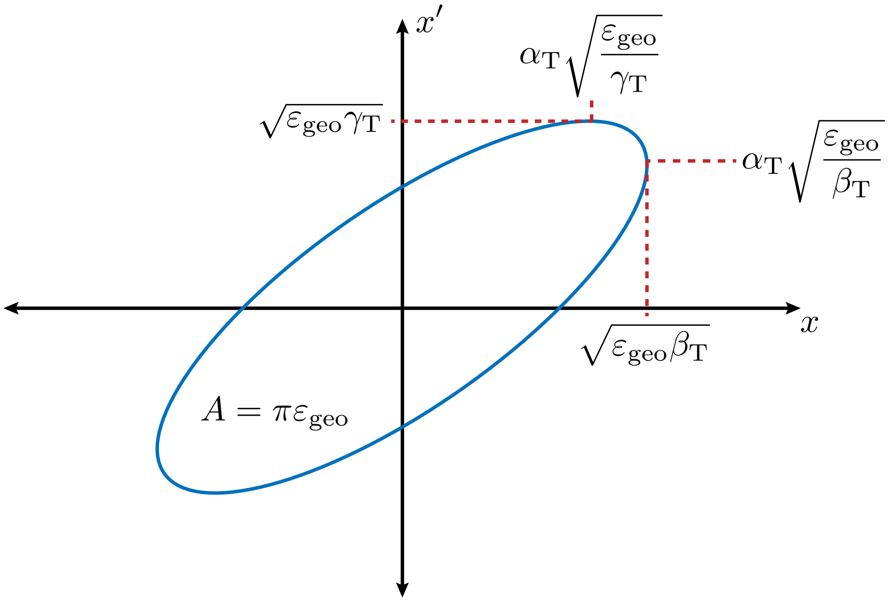

Figure 2.2: Illustration of a phase space ellipse in the x-x'-plane and relations to Twiss parameters.

The collective of particles that form (a bunch of) the beam occupies a volume in the 6-dimensional phase space x-p_x-y-p_y-s-p_s. The longitudinal components are translated

s-$p_s \rightarrow \varphi$-E w.r.t. the RF phase φ:

$$\begin{aligned} \varphi &= \frac{1}{T_{\mathrm{RF}}}\left(s - \frac{p_s}{m_0} t_{\mathrm{ref}}\right) \\ E &= p_s c \end{aligned}$$

As long as only non-coupling, linear fields (magnetic dipole and upright magnetic quadrupole, constant electric dipole) are present in the accelerator, the three 2-dimensional phase spaces x-p_x, y-p_y, φ-E decouple and can be treated independently [Chao *et al.* 2013, pp.67f].

2.1.6 Emittance

The emittance is defined as the phase space volume containing a certain amount of particles. The emittance is an invariant quantity under symplectic transformations, i.e. it is conserved in linear beam transport. In accelerator physics, the beam is considered to be generated in Gaussian shape and independently in each dimension. The beam distributions in the 2D subordinate phase spaces are therefore of 2-dimensional Gaussian shape. The RMS emittance can then be defined by taking into account the RMS contour lines of mentioned Gaussian charge density distribution [Wille & McFall 2000, p.81]:

$$\varrho(x, y) = \frac{Ne}{2\pi\sigma_x\sigma_y} \exp\left(-\frac{x^2}{2\sigma_x^2} - \frac{y^2}{2\sigma_y^2}\right),$$

where N is the number of particles and e the electric charge. The corresponding 1σ-contour line in the phase space diagram is elliptic and its area is:

$$A = \pi\varepsilon_{\mathrm{geo}},$$

with the geometrical emittance $\varepsilon_{\mathrm{geo}}$. The elliptical shape is conserved under symplectic transformations.

2.1.6.1 Adiabatic Damping and Normalized Emittance

The transverse emittances $\varepsilon_{\mathrm{geo}}$ defined in the trace space x-x' are due to their dependence on p_s shrinking during acceleration [Edwards & Syphers 1992, pp.83ff]. To compensate for this effect and obtain a quantity independent of beam energy that fulfils the Liouville theorem in the phase space x-p_x, the normalized emittance ε_{n} is defined so that [Edwards & Syphers 1992, pp.85]:

$$\varepsilon_{\mathrm{n}} = \beta\gamma\varepsilon_{\mathrm{geo}},$$

where β and γ denote the relativistic factors.

2.1.7 Limitations to Linear Beam Dynamics and Nonlinear Beam Dynamics

The previously discussed analytic approach to linear beam dynamics is a standard tool for accelerator design and serves to study the fundamental properties of an accelerator. It does however not account for non-linear effects found in higher order electric and magnetic fields, space charge repulsion or beam-target interaction. These effects require separate treatment and while analytic approaches exist for particular effects, they become cumbersome very quickly and provide limited insight. It is therefore common practice to engage numerical simulations for the investigation of non-linear effects. The beam-target interaction introduces energy losses of beam electrons as well as change in momentum direction and transverse offsets, for which treatment with the linear beam dynamics is not possible. This thesis therefore involves tracking simulations which are described in Section 2.5 and Chapter 3.

2.2 Luminosity Limit for Internal Targets in ERLs

This section provides an introduction to luminosity and luminosity limits from internal targets in ERLs.

2.2.1 Luminosity

The luminosity $\mathcal{L}$ is a measure for the scattering rate $\dot{N}$ at an experiment and defined as [Wille & McFall 2000, p.202]:

$$\dot{N} = \mathcal{L}\sigma,$$

where σ is the cross section for the scattering process. Higher luminosities enable to collect experimental data at higher rates and are therefore sought to be maximized. The dimension of $\mathcal{L}$ is [Wille & McFall 2000, p.202]:

$$[\mathcal{L}] = \mathrm{cm}^{-2}\,\mathrm{s}^{-1}$$

The luminosity for a fixed target is calculated as product of projectile flux Φ and the areal density of target scatter centers n_{target}:

$$\begin{aligned}\mathcal{L} &= \Phi n_{\mathrm{target}}\\ &= \frac{I}{q}\varrho_{\mathrm{p}} d,\end{aligned}$$

where I is the beam current, q the charge of the projectiles, ϱ_{p} the target particle density and d the target length. Here it is obvious that a high luminosity can be achieved by increasing the beam current or the target density or thickness.

2.2.2 Limitations

The maximum achievable luminosity for a fixed target experiment in an ERL depends on beam losses as the power lost must be compensated by RF amplifiers. The fundamental luminosity limit is then given by energy conservation:

$$P_{\text{loss}} = P_{\text{RF}} \tag{2.7}$$

The beam losses itself depend on the beam-target interaction since the amount of beam halo emerging from the target increases with increasing scattering rates. It is therefore crucial for an ERL experiment to ensure operation well below the luminosity limit stated in Equation 2.7. As ERLs today are subject to pioneering research, luminosity limits for ERL experiments are not well known to date. A simple estimation from Rutherford scattering theory and Gaussian approximation of multiple scattering is given in Table 2.1 and further explained in Section 2.4.

Table 2.1: Rudimentary loss limit estimation for different MAGIX targets from Section 2.4. The areal particle density of the target is $10^{19}\,\text{cm}^{-2}$ and a tolerable loss power of 100 W is assumed. Values for the atomic weight A are taken from [Lide 2004].

Parameter	**H**	**He**	**O**	**Ar**	**Xe**
Z	1	2	8	18	54
A	1.007 94	4.002 602	15.9994	39.948	131.293
Rutherford Scattering					
L_{max} [$\text{cm}^{-2}\,\text{s}^{-1}$]	2.477×10^{36}	6.192×10^{35}	3.870×10^{34}	7.644×10^{33}	8.494×10^{32}
Gaussian Approximation					
L_{max} [$\text{cm}^{-2}\,\text{s}^{-1}$]	N/A	N/A	N/A	N/A	9.249×10^{39}

It is visible that large discrepancies between the approaches exist and require more sophisticated treatment to be resolved. This is achieved with computational approaches in Chapter 6. It is furthermore shown in Chapter 8 that radioactive activation further lowers the practical luminosity limit in comparison to the energy conservation limit in Equation 2.7.

2.3 Electron Scattering on the MAGIX Target

The electron beam experiences elastic and inelastic scattering in the MAGIX gas target. The relevant processes needed for the treatment of beam-target interaction at MAGIX are introduced in the following.

2.3.1 Single Scattering

Single large-angle scattering events are specifically important for thin targets with a small number of scattering centers. Under the assumption that the nucleus is point-like, at rest, and that the projectile kinetic energy $E_{\text{kin}} \ll M_0c^2$ is much smaller than the nucleus rest energy M_0c^2, the nucleus recoil is negligible [Motz *et al.* 1964]. The scattering process is then described by the Rutherford differential cross section [Leo 1994, p.44]:

$$\frac{\mathrm{d}\sigma}{\mathrm{d}\Omega} = \left(\frac{Z_1 Z_2 \alpha \hbar c}{4E_{\text{kin}} \sin^2\left(\frac{\theta}{2}\right)} \right)^2 , \tag{2.8}$$

where Z_1 and Z_2 denote the charge of projectile and target in units of e and E_{kin} the kinetic energy of the projectile. The scattering angle θ is defined as the angle between momenta of incident and scattered projectile. α denotes the electromagnetic finestructure constant:

$$\alpha = \frac{e^2}{4\pi\varepsilon_0 \hbar c}$$

2.3.2 Plural Scattering

The region of > 1 and < 20 scatters is called plural scattering [Leo 1994, p.44]. Plural scattering events require advanced treatment in analytical approaches since they cannot be described by the single scattering Rutherford formula, neither is the number of scatters sufficiently high for statistical convergence. The behavior is captured in the Molière distribution in the following paragraph.

2.3.2.1 Molière Distribution

The Molière distribution unites the aforementioned processes in a small-angle approximation that is valid for a scattering angle $\theta < 30°$ and a relativistic electron velocity $\beta > 0.05$ [Leo 1994, pp.45f]. An additional exception is the scattering of electrons in heavy elements. The scattering probability under a certain angle is formulated as expanded series [Molière 1948, p.79],[Leo 1994, p.45]:

$$P(\theta)\ \theta\ \mathrm{d}\theta = \eta\ \mathrm{d}\eta \left(2\exp\left(-\eta^2\right) + \sum_i^n \frac{F_i(\eta)}{B^i} \right) , \tag{2.9}$$

with [Leo 1994, pp.45]:

$$\eta = \frac{\theta}{\theta_1 \sqrt{B}}$$

$$\theta_1 = 0.3965 \frac{zQ}{p\beta} \sqrt{\frac{\varrho \delta x}{A}}$$

Here, z is the projectile charge in units of e, δx and ϱ the material thickness in cm and density in $\mathrm{g\,cm^{-3}}$, A its atomic weight and:

$$Q = \begin{cases} \sqrt{Z(Z+1)} & \text{for } e^- \text{ and } e^+ \\ Z & \text{for other particles} \end{cases},$$

with the material atomic number Z. The parameter B is found by solving the equation [Leo 1994, p.45]:

$$\begin{aligned} g(B) &= \ln B - B + \ln\gamma - 0.154 = 0 \\ \gamma &= 8.831{\times}10^3 \frac{qz^2\varrho\delta x}{\beta^2 A\Delta} \\ \Delta &= 1.13 + 3.76\left(\frac{zZ}{137\beta}\right)^2 \\ q &= \begin{cases} (Z+1)Z^{1/3} & \text{for } e^- \text{ and } e^+ \\ Z^{4/3} & \text{for other particles} \end{cases} \end{aligned}$$

The $F_i(\eta)$ are obtained from [Molière 1948, p.88]:

$$F_i(\eta) = \frac{1}{i!}\int J_0(\eta y)\exp\left(\frac{-y^2}{4}\right)\left(\frac{y^2}{4}\ln\left(\frac{y^2}{4}\right)\right)^i y\;\mathrm{d}y,$$

with the Bessel function J_0. It is usually not necessary to go beyond $n = 2$ [Leo 1994, p.46]. The computation of the Molière distribution is expensive especially for the F_i as numerical integration methods must be involved. Since the figure of merit is the integral of Equation 2.9 over Ω, the effort of computing sufficient F_i is high. The Molière distribution is therefore not computed in this thesis, however it is referenced in the Gaussian approximation discussed in the following. A rudimentary estimation of beam losses is later found in the two cases of Rutherford scattering and the Gaussian approximation in the following section.

2.3.3 Multiple Scattering

When particles are scattered > 20 times, the distribution is described by multiple scattering. The mean number of scattering events is sufficiently high to approximate the total angular distribution with a Gaussian curve [Leo 1994, pp.46ff].

2.3.3.1 Gaussian Approximation

The following section is retraced from [Lynch & Dahl 1991]. The angular distribution of multiply scattered particles is approximated by a Gaussian shape, since the projectile has the highest probability to scatter at a small angle in a single scattering event and subsequent scattering let the form converge to a Gaussian shape in the center according to the central limit theorem. The probability density $p(\theta)$ for particles being scattered at the angle $\theta \approx 0$ is therefore [Leo 1994, p. 46]:

$$p(\theta) \approx \frac{2\theta}{\langle\theta^2\rangle} \exp\left(\frac{-\theta^2}{\langle\theta^2\rangle}\right) \mathrm{d}\theta,$$

with the mean scattering angle $\langle\theta\rangle = \sqrt{\langle\theta^2\rangle}$, which is defined as [Leo 1994, p. 47]:

$$\begin{aligned}\langle\theta^2\rangle &= 2\frac{\chi_c^2}{1+F^2}\left(\frac{1+\nu}{\nu}\ln(1+\nu)-1\right)\mathrm{rad}^2\\ \nu &= 0.5\frac{\Omega}{1-F}\end{aligned}$$

F is the fraction of the Molière-distribution taken into account and Ω the mean number of scatters:

$$\begin{aligned}\Omega &= \frac{\chi_c^2}{\chi_a^2}\\ \chi_c^2 &= 0.157z\left(\frac{Z(Z+1)}{A}\right)\frac{\varrho d}{p^2\beta^2}\\ \chi_a^2 &= 2.007{\times}10^{-5}Z^{2/3}\left(1+3.34\left(\frac{Zz\alpha}{\beta}\right)^2\right)\frac{1}{p^2},\end{aligned}$$

where z and p denote the projectile charge in units of e and the momentum in MeV/c, respectively, and β its velocity in units of c. Z and A denote the target nuclear charge and atomic weight, ϱ the mass density and d the thickness of the target and $\alpha = \frac{e^2}{\hbar c} = \frac{1}{137}$ the electromagnetic fine structure constant. The approximation deviates $< 2\,\%$ from the actual distribution for $90\,\% < F < 99.5\,\%$ and $10 < \Omega < 10^8$ [Lynch & Dahl 1991, p.9].

2.4 Rudimentary Estimation of Beam Losses

It is possible to roughly estimate beam losses in the drift region downstream from the target with the following considerations. The target thickness $d \ll l$ and the transverse beam size $\sigma_{x,y} \ll \frac{a}{2}$ are assumed to be sufficiently small to be treated as point-like. The first magnet – in this case a quadrupole – is $l = 2\,\mathrm{m}$ away from the target (see Figure 2.3). The aperture (beam pipe diameter) limiting the transverse size of the beam is $a = 40\,\mathrm{mm}$, meaning that electrons with:

$$\theta > \frac{a}{2l} = 10\,\mathrm{mrad}, \tag{2.10}$$

will hit the beam pipe before the quadrupole can correct their orbits. It is noted here, that beam focusing can also be achieved with a solenoid instead of a quadrupole, which enables simultaneous focusing in both transverse planes. A solenoid however requires considerably more space to achieve the magnetic field strengths necessary for focusing at 105 MeV and is therefore not considered here. The losses in the drift section can then

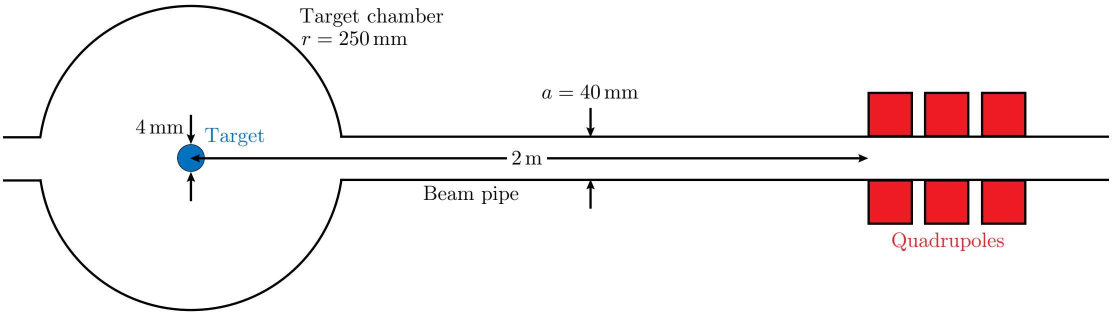

Figure 2.3: Illustration of the MAGIX area following the jet target (top view). A space of 2 m following the target is reserved for spectrometer movement under forward angles and therefore not occupied by any beam-optical elements.

be quantified with different models from Section 2.3.

2.4.1 Single Scattering

Using Equation 2.8, the cross section for electrons scattered into the solid angle Ω_r is:

$$\sigma = \int\limits_{\Omega_r} \frac{\mathrm{d}\sigma}{\mathrm{d}\Omega} \mathrm{d}\Omega$$

The solid angle Ω can be expressed by polar angle φ and azimuth θ:

$$\mathrm{d}\Omega = \sin\theta \; \mathrm{d}\theta \; \mathrm{d}\varphi$$

The rate $\dot{N}$ of particles scattered into a certain region is further obtained by multiplying the corresponding cross section with the luminosity $\mathcal{L}$ [Wille & McFall 2000, p.202]:

$$\dot{N} = \mathcal{L}\sigma, \tag{2.11}$$

where $\mathcal{L}$ is for a fixed target defined as the product of incident projectiles per time $\dot{N}_e$ and the areal density of scatter centers:

$$\begin{aligned} \mathcal{L} &= \dot{N}_e \cdot \varrho_\mathrm{p} d \\ &= \frac{I}{e} \cdot \varrho_\mathrm{p} d, \end{aligned}$$

where d is the thickness, I the beam current and ϱ_p the particle density of the target, which can be expressed by the mass density ϱ, Avogadro's constant N_A and the molar mass M by:

$$\varrho_\mathrm{p} = \frac{N_A}{M} \varrho,$$

Equation 2.11 then becomes:

$$\begin{aligned}
\dot{N} &= \mathcal{L} \int\limits_{\Omega_r} \frac{\mathrm{d}\sigma}{\mathrm{d}\Omega}\, \mathrm{d}\Omega \\
&= \mathcal{L} \int\limits_{0}^{2\pi} \mathrm{d}\varphi \int\limits_{\theta_0}^{\pi} \frac{\mathrm{d}\sigma}{\mathrm{d}\Omega} \sin\theta\, \mathrm{d}\theta \\
&= \mathcal{L}\ 2\pi \left(\frac{Z_1 Z_2 \alpha \hbar c}{4E_{\mathrm{kin}}}\right)^2 \int\limits_{\theta_0}^{\pi} \frac{\sin\theta}{\sin^4\left(\frac{\theta}{2}\right)}\, \mathrm{d}\theta
\end{aligned}$$

Using the sine double-angle identity [Spiegel *et al.* 2009, p.48]:

$$\sin(\theta) = 2\sin\left(\frac{\theta}{2}\right)\cos\left(\frac{\theta}{2}\right),$$

and substituting:

$$\begin{aligned}
u &= \frac{1}{\sin^4\left(\frac{\theta}{2}\right)} \\
\frac{\mathrm{d}u}{\mathrm{d}\theta} &= -2\frac{\cos\left(\frac{\theta}{2}\right)}{\sin^5\left(\frac{\theta}{2}\right)} \\
&= -2\frac{\cos\left(\frac{\theta}{2}\right)}{\sin^3\left(\frac{\theta}{2}\right)} \cdot \sqrt{u},
\end{aligned}$$

it follows that:

$$\begin{aligned}
\int\limits_{\theta_0}^{\pi} \frac{\sin\theta}{\sin^4\left(\frac{\theta}{2}\right)}\, \mathrm{d}\theta &= \int\limits_{\theta_0}^{\pi} \frac{2\cos\left(\frac{\theta}{2}\right)}{\sin^3\left(\frac{\theta}{2}\right)}\, \mathrm{d}\theta \\
&= -\int\limits_{u(\theta_0)}^{u(\pi)} \frac{1}{\sqrt{u}}\, \mathrm{d}u \\
&= -2\Big[\sqrt{u}\Big]_{u(\theta_0)}^{u(\pi)} \\
&= -2\left(1 - \frac{1}{\sin^2\left(\frac{\theta_0}{2}\right)}\right)
\end{aligned}$$

Since θ_0 is very small in this case, the expression simplifies to:

$$\int_{\theta_0}^{\pi} \frac{\sin\theta}{\sin^4\left(\frac{\theta}{2}\right)} \, \mathrm{d}\theta \approx -2 + \frac{8}{\theta_0^2}$$

The first term can further be neglected as the second term becomes very large for $\theta_0 \approx 0$. The final form of Equation 2.11 is then:

$$\begin{aligned} \dot{N} &= \mathcal{L} \; 2\pi \left(\frac{Z_1 Z_2 \alpha \hbar c}{4 E_{\mathrm{kin}}} \right)^2 \frac{8}{\theta_0^2} \\ &= \frac{I}{e} \varrho_{\mathrm{p}} d \cdot \pi \left(\frac{Z_1 Z_2 \alpha \hbar c}{E_{\mathrm{kin}} \theta_0} \right)^2 \end{aligned}$$

The projectile is charged $Z_1 = 1$ for an electron accelerator. The loss power P_{loss} associated with particles scattered into this region can be obtained by multiplying the equation above with the kinetic energy E_{kin} of the projectile. It is further handy to relabel $Z_2 = Z$, collect all constants in a single factor and use the mass density ϱ instead of the particle density ϱ_{p}, which yields:

$$P_{\mathrm{loss}} = E_{\mathrm{kin}} \dot{N}_{\mathrm{loss}} \approx 39.75\,\mathrm{W} \cdot Z^2 \cdot \frac{\varrho d}{\mathrm{g\,cm^{-2}}} \frac{\mathrm{g\,mol^{-1}}}{M} \frac{I}{\mathrm{mA}} \frac{\mathrm{MeV}}{E_{\mathrm{kin}}} \frac{\mathrm{rad}^2}{\theta_0^2} \tag{2.12}$$

By taking into account the condition in Equation 2.10 for θ_0, the equation becomes:

$$P_{\mathrm{loss}} \approx 1.59\,\mathrm{W} \cdot Z^2 \cdot \frac{\varrho d}{\mathrm{\mu g\,cm^{-2}}} \frac{\mathrm{g\,mol^{-1}}}{M} \frac{I}{\mathrm{mA}} \frac{100\,\mathrm{MeV}}{E_{\mathrm{kin}}} \frac{l^2}{\mathrm{m}^2} \frac{\mathrm{mm}^2}{a^2} \tag{2.13}$$

The expression yields a direct insight into the dependencies of the loss power on several target, beam and machine parameters. It is in particular noted, that the losses in Equation 2.13 depend quadratically on the atomic number Z.

2.4.2 Multiple Scattering and Gaussian Approximation

The loss power resulting from the Gaussian approximation model can be estimated in a similar manner like that in Equation 2.13 by multiplying the total beam power P_{beam} with the probability density and integrating over angles $> \theta_0$:

$$\begin{aligned} P_{\mathrm{loss}} &= P_{\mathrm{beam}} \int_{\Omega_r} p(\theta) \; \mathrm{d}\Omega \\ &= P_{\mathrm{beam}} \int_{\theta_0}^{\pi} p(\theta) \; \mathrm{d}\theta \end{aligned}$$

Although this expression does not yield direct dependencies of the loss power on beam and target parameters like in Equation 2.13, its beauty lies in the conserved applicability of linear beam dynamics due to the conservation of the Gaussian shape of the beam. An inspection of $\langle\theta\rangle$ and comparison against Equation 2.10 however allows to estimate whether multiple scattering dominantly contributes to losses, which is discussed in the following section.

2.4.3 Results

Table 2.2: Rudimentary loss limit estimation for different MAGIX targets with an areal particle density of $10^{19}\,\mathrm{cm}^{-2}$ and a tolerable loss power of 100 W in the region $\theta > 10\,\mathrm{mrad}$. The loss values are denoted for $\mathcal{L} = 6.241{\times}10^{34}\,\mathrm{cm}^{-2}\,\mathrm{s}^{-1}$. Values for A are taken from [Lide 2004].

Parameter	**H**	**He**	**O**	**Ar**	**Xe**
Z	1	2	8	18	54
A	1.007 94	4.002 602	15.9994	39.948	131.293
ϱd [mg cm^{-2}]	$1.674{\times}10^{-2}$	$6.647{\times}10^{-2}$	$2.657{\times}10^{-1}$	$6.634{\times}10^{-1}$	2.180
Rutherford Scattering					
$P_{[10\sigma,10\,\mathrm{mrad}]}$ [W]	2.520	$1.008{\times}10^{1}$	$1.613{\times}10^{2}$	$8.165{\times}10^{2}$	$7.348{\times}10^{3}$
$P_{>10\,\mathrm{mrad}}$ [W]	$6.286{\times}10^{-2}$	$2.514{\times}10^{-1}$	4.023	$2.037{\times}10^{1}$	$1.833{\times}10^{2}$
$\mathcal{L}_{\mathrm{max}}$ [cm^{-2} s^{-1}]	$2.477{\times}10^{36}$	$6.192{\times}10^{35}$	$3.870{\times}10^{34}$	$7.644{\times}10^{33}$	$8.494{\times}10^{32}$
Gaussian Approximation					
Ω	0.260	0.779	9.35	44.4	386
$\langle\theta\rangle$ [mrad]	$3.389{\times}10^{-2}$	$6.979{\times}10^{-2}$	$3.160{\times}10^{-1}$	$7.746{\times}10^{-1}$	2.595
$P_{[10\sigma,10\,\mathrm{mrad}]}$ [W]	0.0	0.0	$2.724{\times}10^{-6}$	$1.819{\times}10^{3}$	$7.314{\times}10^{5}$
$P_{>10\,\mathrm{mrad}}$ [W]	0.0	0.0	0.0	0.0	$6.748{\times}10^{-4}$
$\mathcal{L}_{\mathrm{max}}$ [cm^{-2} s^{-1}]	N/A	N/A	N/A	N/A	$9.249{\times}10^{39}$

The resulting values from the aforementioned estimations in Rutherford scattering and Gaussian approximation are given in Table 2.2. It is observed that the largest contribution for losses in the region $\theta > 10\,\mathrm{mrad}$ in all cases stems from Rutherford scattering. The requirement that $10 < \Omega < 10^{8}$ for the Gaussian approximation is only fulfilled for Ar and Xe, where $\langle\theta\rangle$ for Xe is still well below the 10 mrad from Equation 2.10. The Gaussian approximation therefore predicts only small amounts of losses for the region above and consequently largely overestimates the loss limit for MESA, while Rutherford scattering leads to limits below the nominal luminosity of $10^{35}\,\mathrm{cm}^{-2}\,\mathrm{s}^{-1}$ for all cases except H and He. Both approaches yield large discrepancies between them, which are addressed in the following.

2.4.4 Validity of the Estimation

Although it was shown, that a loss power and a resulting luminosity limit can be derived in a fairly simple manner, it is important to not ignore the assumptions made beforehand:

- The beam is point-like with respect to the aperture: $\sigma_r \ll a$
- The beam is monoenergetic: $\sigma_E = 0$
- The beam size stays constant during the scattering process, i.e. the target is point-like or at least sufficiently short to maintain little change in β function: $l_{\text{target}} \approx 0$
- The same has to be fulfilled since only beam angular widening is taken into account and in a long target also spatial widening may occur through several scattering events
- The beam carries no angular distribution, i.e. it is focused: $\alpha \approx 0$
- The remaining intrinsic beam divergence is negligible: $\sigma_{p_r} \ll \theta_0$
- The scattering model on which the process depends is correctly describing the reality, i.e. no other processes occur
- Only losses in a drift section following the target are taken into account
- Particles lose no energy in the scattering process
- Electrons experience no delay through flight path elongation in the target

The following is therefore not resolved:

- Losses throughout the whole accelerator
- Behavior of finite spatial and angular beam distribution
- Long target effects
- Strong focus and high divergence in the interaction region
- Intermediate regions between single and multiple scattering
- Inelastic scattering and bremsstrahlung
- Longitudinal halo effects, i.e. change in energy and phase of the beam
- Variation in target density

Some of the above-mentioned assumptions can be maintained reasonable enough to estimate at least the order of magnitude of lost beam power in the vicinity of the target and an upper limit for the luminosity. However the lack of crucial information on disturbances of beam properties for accelerator operation and behavior of further losses for radiation protection requires a more sophisticated approach, which shall be discussed in the following.

2.4.5 Beyond a Basic Estimation

The estimation of more precise predictions for power losses involves the use of different methods, that mostly rely on numerical computation power. The few used in this thesis are shortly introduced.

Acceptance

The magnets in the accelerator are able to properly transport only a finite volume of the 6D phase space through the lattice, which is called the acceptance. Acceptances can be calculated for the whole accelerator or for specific parts of it. Consequently, scattered electrons that can be transported through the drift after the target may still lie outside the acceptance of downstream sections so that losses will most likely also appear for electrons in the region $10\sigma_r < \theta < \theta_0$ and therefore further downstream the target drift region. A better value for overall power losses can therefore be obtained by integrating over angles outside the acceptance.

Target Interaction

The target properties such as geometry and density can be more realistically approximated and its effects studied in particle tracking codes that additionally involve physical interaction modelling.

2.5 Monte-Carlo Methods and Tracking

Whilst a single interaction process between two particles can be well described with a model in a given kinematic regime, modelling of realistic geometries with many participating processes is often intractable to calculate analytically. Therefore, a numerical approach - the Monte Carlo method - is used to randomly sample particle kinematics and its propagation through a 3D model with a random sampling of all relevant processes. The simulation framework Geant4 uses the MC integration technique based on the accept-reject algorithm [Geant4 Collaboration 2019, p.5]. The chaining of probabilistic scattering processes for a multiple particles can be interpreted as multidimensional integration problem.

2.5.1 MC Integration and Accept-Reject Algorithm

Only the fundamental technique for MC integration is introduced here. For a more detailed discussion on MC techniques see [Robert & Casella 2005]. The goal of MC integration is to approximate the integral of a probability density function (PDF) of arbitrary shape by drawing a number of samples that is proportional to the integral in a given interval. Mentioned sampling can be achieved with the accept-reject algorithm [Robert & Casella 2005, p.47ff]. The PDF $f(x)$ can be treated as an integral over a uniformly distributed variable u [Robert & Casella 2005, p.47]:

$$f(x) = \int_{0}^{f(x)} \mathrm{d}u$$

Given that a random number generator is available, that generates independent and uniform distributions on the intervals $x \in [a, b]$ and $f(x), u \in [0, M]$, number pairs (x, u) are generated and accepted if:

$$u \in [0, f(x)],$$

and rejected otherwise. The fraction of accepted number pairs (samples) is then proportional to $\int_a^b f(x)\,\mathrm{d}x$.

2.5.2 Tracking

Tracking describes the calculation of how particles are propagated. This section discusses the fundamental tracking algorithm that Geant4 applies following [Geant4 Collaboration 2019, pp.7ff]. Geant4 models are divided into non-overlapping volumes, each of which is made of a defined material. The tracking routine calculates the mean free path $\lambda(E)$ of the propagated particle from the total cross section as a sum over the elements in the material composition [Geant4 Collaboration 2019, p.8]:

$$\lambda(E) = \left(\sum_i n_i \cdot \sigma(Z_i, E) \right)^{-1}$$

Here, n_i denotes the atom density of a composition element, E the projectile energy and $\sigma(Z_i, E)$ the corresponding partial cross section. The actual multiples n_λ of λ, that the particles travel before they interact is sampled from [Geant4 Collaboration 2019, p.8]:

$$n_\lambda = -\log(\eta),$$

with a random number $\eta \in [0, 1]$. The actual step length that is tracked can be further limited by other processes such as volume boundary crossing or continuous energy loss in order to ensure accurate representation of cross sections due to the energy dependence. The specific process is triggered at the step with the least distance to the sampled n_λ. For propagation within outer fields, the equation of motion [Geant4 Collaboration 2019, p.9]:

$$\frac{\mathrm{d}\vec{p}}{\mathrm{d}s} = \frac{q}{v}(\vec{E} + \vec{v} \times \vec{B}),$$

is solved using Runge-Kutta methods.

2.6 Electron Energy Loss Mechanisms in Matter

Electrons lose energy in matter through inelastic collisions and bremsstrahlung [Leo 1994, p.37]. The total energy loss per path length from both collision losses $\left(\frac{\mathrm{d}E}{\mathrm{d}x}\right)_{\mathrm{coll}}$ and radiation losses $\left(\frac{\mathrm{d}E}{\mathrm{d}x}\right)_{\mathrm{rad}}$ can be expressed as:

$$\left(\frac{\mathrm{d}E}{\mathrm{d}x}\right)_{\mathrm{total}} = \left(\frac{\mathrm{d}E}{\mathrm{d}x}\right)_{\mathrm{coll}} + \left(\frac{\mathrm{d}E}{\mathrm{d}x}\right)_{\mathrm{rad}}, \tag{2.14}$$

where $\frac{\mathrm{d}E}{\mathrm{d}x}$ is also referred to as the stopping power and sometimes found as the mass stopping power [Leo 1994, p.29]:

$$\frac{1}{\varrho}\frac{\mathrm{d}E}{\mathrm{d}x}$$

2.6.1 Collision Losses

When charged particles pass through a medium, collisions lead to an excitation of the shell electrons or an ionization of the medium [Leo 1994, p.21]. The energy is then transferred from the impacting particle to the medium and and the impacting particle is deflected. The collision energy loss of an electron impacting a medium is described by the Bethe-Bloch-formula [Leo 1994, pp.37f]:

$$\begin{aligned} -\left(\frac{\mathrm{d}E}{\mathrm{d}x}\right)_{\mathrm{coll}} &= 2\pi N_A r_e^2 m_e c^2 \varrho \frac{Z}{A}\frac{1}{\beta^2}\left(\ln\frac{\tau^2(\tau+2)}{2(I/m_e c^2)^2} + F(\tau) - \delta - 2\frac{C}{Z}\right) \\ F(\tau) &= 1 - \beta^2 + \frac{\frac{\tau^2}{8} - (2r+1)\ln 2}{(\tau+1)^2}, \end{aligned}$$

where $N_A = 6.022\times10^{23}\,\mathrm{mol}^{-1}$ denotes Avogadro's constant [Leo 1994, p.357], r_e the classical electron radius and $m_e c^2$ the electron rest mass. The medium properties are the density ϱ, nuclear charge Z and atomic weight A. δ and C are density and shell corrections, respectively, and $\beta = \frac{v}{c}$ the relativistic velocity. τ denotes the kinetic energy of the electron in units of $m_e c^2$. The collision losses in the target contribute to the total beam losses and linearly with Z. Collision losses at MAGIX are the dominating mechanism for energy losses in the target for H and He, since the critical energies lie above the 105 MeV beam energy (see Table 2.3).

2.6.2 Bremsstrahlung

The electron experiences large deflections when scattering on the coulomb field of the medium due to its small mass and emits bremsstrahlung in this process [Leo 1994, p.38]. The electron energy loss from radiation is of the form [Leo 1994, p.39]:

$$-\left(\frac{\mathrm{d}E}{\mathrm{d}x}\right)_{\mathrm{rad}} = NE\Phi_{\mathrm{rad}}, \tag{2.15}$$

with:

$$\Phi_{\text{rad}} = \frac{1}{E_0} \int_0^{E_0/h} h\nu \frac{\mathrm{d}\sigma}{\mathrm{d}\nu}(E_0, \nu)\ \mathrm{d}\nu,$$

where $N = \varrho N_A A^{-1}$ is the scatter center density, E_0 the total energy of the incoming electron and $h\nu$ and ν the emitted photon's energy and frequency, respectively. Φ_{rad} involves the cross-section $\mathrm{d}\sigma$ and is nearly independent of ν and therefore a material property [Leo 1994, p.39]. Equation 2.15 can be understood as DE with the solution [Leo 1994, p.41]:

$$E = E_0 \exp\left(-\frac{x}{L_{\text{rad}}}\right),$$

where L_{rad} denotes the radiation length and is a material property. The radiation length can be approximated with [Leo 1994, p.42]:

$$L_{\text{rad}} = \frac{716.4\,\mathrm{g\,cm^{-2}}A}{Z(Z+1)\ \ln\left(\frac{287}{\sqrt{Z}}\right)}, \tag{2.16}$$

and is accurate to 2.5 % except for Helium [Leo 1994, p.42]. The electron energy where radiative and collision losses are equal is identified as the critical energy [Leo 1994, p.41]:

$$E_c \simeq \frac{800\,\mathrm{MeV}}{Z + 1.2},$$

with radiative losses dominating when $E_0 > E_c$, which at MAGIX applies for heavier gases than He (see Table 2.3). It is noteworthy that bremsstrahlung cannot be influenced by electron-optical elements, so that the emitted photons will be stopped in forward direction of the target.

Table 2.3: Critical energies for the MAGIX target gases.

Target	**Atomic Number** Z	**Critical Energy** E_c [MeV]
H	1	364
He	2	250
O	8	87.0
Ar	18	41.7
Xe	54	14.4

2.6.3 Continuous Slowing Down Approximation

It is not possible to determine a priori how far an electron travels through a medium since the stopping process is involving discrete interactions also inducing deflections that shorten the path length projected onto the impact axis [Leo 1994, p.42]. An average range (neglecting deflections) can however be determined in the continuous slowing down approximation (CSDA) by integration of $\frac{\mathrm{d}E}{\mathrm{d}x}$ until the kinetic energy is zero [Leo 1994; Berger & Seltzer 1982, p.31, p.27] and is useful for collective considerations.

2.7 Photon Energy Loss Mechanisms

From bremsstrahlung emitted in the electron stopping process arises the necessity to also account for photon stopping for a collimation system. Photon stopping involves the photoelectric effect, Compton scattering, pair production and if the energy is sufficiently high also photo-nuclear desintegration [Leo 1994, p.53]. All processes produce secondary particles and especially electrons, which is a special challenge in collimating electron beams. The processes are not further discussed in detail, however it is important for collimation to note the exponential nature of photon intensity I passing through matter [Leo 1994, p.53]:

$$I(x) = I_0 \exp(-\mu x),$$

where I_0 denotes the incident photon intensity, μ the absorption coefficient of the absorber and x the absorber thickness. The produced bremsstrahlung is the dominant source of remanent radioactivity through the process discussed in the following section and therefore of great importance for the studies conducted in Chapter 8.

2.8 Radioactivity

The term radioactivity includes the transformation of nuclei with initial atomic weight A and nuclear charge Z into different species under the emission or absorption of additional charged or uncharged particles. The process emitting radiation may occur when nuclei are exposed to radiation or due to the instability of the initial nucleus. The radiation itself can induce processes in surrounding stable nuclei and activate stable nuclei by transforming them into unstable ones. A radioactive sample consisting of N nuclei with a decay constant per unit time [Leo 1994, p.10]:

$$\lambda = \sum_i \lambda_i,$$

where λ_i are decay constants of the involved decay modes, decays exponentially over time [Leo 1994, pp.10f]:

$$N(t) = N(0)\exp(-\lambda t) = N(0)\left(\frac{1}{2}\right)^{\frac{t}{\tau_{1/2}}},$$

with the number of original nuclei $N(t)$ at time t and $N(0)$ at time 0. The alternative representation to λ is the half life [Leo 1994, p.11]:

$$\tau_{1/2} = \frac{\ln 2}{\lambda}$$

2.8.1 Photonuclear Processes

The photonuclear processes, also known as nuclear photoeffect, are an important mechanism in the production of remanent radioactivity [Krieger 2017, p.195]. An incoming photon is able to transform nuclei into unstable isotopes through the reactions (γ, n), $(\gamma, 2n)$ and (γ, p) or induce nuclear fission in heavy nuclei. The reactions appear as consequence of the giant resonance, for which the cross section is at maximum at 20 MeV to 25 MeV for light and 10 MeV to 15 MeV for heavy nuclei [Krieger 2017, p.196] and are therefore also occuring at MESA energies. The reaction itself releases neutrons and protons, which can trigger subsequent nuclear reactions, while an unstable product nucleus undergoes subsequent β^+, β^-, electron capture (EC) or γ decay [Krieger 2017, p.196]. If material is irradiated intense and long enough to accumulate unstable isotopes, the remanent radiation possesses characteristic cool down times depending on the decay reactions in the material.

2.8.2 Units

This section provides a brief overview of dosimetric units.

2.8.2.1 Activity

The activity A of a source is defined as the number of decays per unit time [Leo 1994, pp.9f]:

$$A = -\frac{\mathrm{d}N}{\mathrm{d}t} = \lambda N,$$

with the unit Becquerel defined as [Leo 1994, p.10]:

$$1\,\mathrm{Bq} \ = 1 \text{ decay per second}$$

2.8.2.2 Absorbed Dose

The absorbed dose D is a measure for the received energy per unit mass from radiation [Leo 1994, p.70]:

$$D = \frac{E_{\mathrm{dep}}}{m},$$

and the corresponding unit is Gray [Leo 1994, p.70]:

$$1\,\mathrm{Gy} = 1\,\mathrm{J\,kg^{-1}}$$

2.8.2.3 Equivalent Dose

The absorbed dose is a strictly physical quantity and does not take the actual biological effect into account, which additionally depends on the type and energy of the radiation. A quantity which yields a measure to compare the biological impact is the equivalent dose [Leo 1994, p.72]:

$$H = \sum_R w_R D_R,$$

where D_R and w_R are the absorbed doses received from a specific type of radiation R in a certain energy range and their corresponding weight, respectively. The unit of H is Sievert (Sv) and has the same dimension of D. The weight w_R is the relative biological effectiveness (RBE) [Leo 1994, p.71] (compare Table 2.4).

Table 2.4: Relative biological effectiveness w_R for different types of radiation [Leo 1994, p.71].

Radiation type	**Energy**	w_R
γ	all	1
e^-, e^+	all	1
n	$< 10\,\mathrm{keV}$	5
n	$10\,\mathrm{keV} - 100\,\mathrm{keV}$	10
n	$0.1\,\mathrm{MeV} - 2\,\mathrm{MeV}$	20
n	$2\,\mathrm{MeV} - 20\,\mathrm{MeV}$	10
n	$> 20\,\mathrm{MeV}$	5
p	$> 2\,\mathrm{MeV}$	5
α	all	20

Another useful quantity is the equivalent dose rate:

$$\frac{\mathrm{d}H}{\mathrm{d}t},$$

which denotes the received equivalent dose per unit time to compare the time evolution of radioactive doses in Chapter 8.

2.9 Machine Protection

Operation of particle accelerators usually involves high energies and powers in the beam itself or other machine parts like power supplies or stored pressures. It is hence of special importance to account for both personnel and machine protection aspects. A machine protection strategy follows the P^3-rule [Schmidt 2014, pp.15f]:

- Protect the machine: Avoid damage of accelerator equipment.
- Protect the beam: Ensure maximum beam time by avoiding shutdowns caused by false failures.
- Provide evidence: Monitor machine operation and log failure events with sufficient information to understand the event to be able to mitigate it in the future.

As MESA is aiming for high intensity beams at medium energies, hazards and machine protection aspects specifically emerging from these intensities in combination with MAGIX are discussed.

2.9.1 Hazards

The beam poses several hazards for MESA through its intensity and energy. It follows a short discussion of the hazards specially important for MAGIX operation and countermeasures.

2.9.1.1 Power Densities

The MESA beam carries currents of 1 mA and upgrade plans foresee operation of up to 10 mA, corresponding to 105 kW and 1.05 MW beam power at peak energy, respectively. The beam power is confined to a small space, so that high power densities are present. In order to melt 1 kg of steel, 800 kJ of heat is needed [Schmidt 2014, p.3]. A direct impact of the 105 kW beam is able to provide enough heat in several seconds to damage beam pipes or cavities irreversibly and even break the vacuum. Even impact of percent level fractions of the beam for longer time periods will lead to heating and may apply high stresses on the affected components. The MESA cryomodules require cooling at 2 K to maintain superconductivity [Stengler 2020, p.79]. If heat load is applied to the cryomodules, it may lead to quenches interrupting operation even if the total energy deposited is not deforming the material.

2.9.1.2 Prompt Radiation

When the electron beam impacts on matter, it produces temporary X-ray radiation through bremsstrahlung and secondary particles. When occurring over longer time periods, the bremsstrahlung can trip sensitive electronics or damage them irreversibly [Schmidt 2014, pp.96ff]. It is therefore important to identify locations which are expected to reveal high loss rates in order to equip these with proper shielding.

2.9.1.3 Radioactive Activation

When equipment is exposed to the beam, it is activated in inelastic scattering events with radioactive products [Schmidt 2014, p.89]. The isotopes accumulate over the irradiation time and further decay with emission of radiation after the beam is shut down. Further radionuclides can be produced during the decay of the primary isotopes. Radiation protection regulations limit the dose level of accessed areas for personnel protection, so that significant cooldown times can be necessary before access when the initial level at machine shutdown exceeds the tolerated amount. The materials exposed to high activation doses can suffer from ageing and radiation damage, decreasing life time and structural integrity.

2.9.2 Countermeasures

It is necessary to develop strategies to minimize negative consequences from the mentioned hazards, such as long or frequent shutdowns or replacement of damaged equipment. A protection system pursuing this task can be divided into active and passive mechanisms [Schmidt 2014, pp.16f], where an active mechanism is able to detect failures and actively counteract possible damage, while a passive mechanism is automatically interfering with a misfired beam.

2.9.2.1 Collimators

Collimators represent an intentionally narrow aperture that is designed to absorb (parts of) the beam and therefore confine it to a desired extent for further transport. This mechanism can be used to collimate beam halo whilst leaving the beam core intact [Schmidt 2014, p.405]. A collimation system can be designed as a single-stage system, where only one collimator is intercepting a particle to be stopped, or as multi-stage system with a longer secondary collimator that is absorbing particles which are scattered out of the primary one [Schmidt 2014, pp.411ff]. A multi-stage system requires subsequent collimators to have equal or larger aperture/beam size-ratios than the preceding ones. Since it is always present it is a passive mechanism and has to be designed to absorb the beam without damage in a possible failure [Schmidt 2014, p.17].

2.9.2.2 Shielding

As the MESA electron beam is generating bremsstrahlung photons in the collimation process, it is important to minimize dose through bremsstrahlung in the surrounding to mitigate trips in electronics and radioactive activation in sensitive equipment. Since the photon-absorbing photoelectric effect is enhanced in high-Z materials [Schmidt 2014, p.99], it is convenient to install lead shields around the collimators.

3 Simulation Tools

This chapter provides a short overview over the simulation tools used in this thesis.

3.1 MAD-X

MAD-X (Methodical Accelerator Design) is a tool for the design of accelerators, originally developed for the design of the LHC (Large Hadron Collider) [Deniau *et al.* 2019]. It features matrix descriptions of an accelerator layout with electron-optical elements and accelerator-specific quantities and allows to examine beam properties over the accelerator. A MAD-X model for MESA is described in [Simon 2014] and a modified version from November 2018 used in this thesis. MAD-X provides the ability to calculate and iteratively optimize Twiss parameters at given locations in the lattice via the Twiss-module [Deniau *et al.* 2019, pp.127ff], which is utilized in the following chapters to adapt the MAD-X model to meet values relevant for MAGIX.

3.2 Geant4

Geant4 (Geometry And Tracking) is a C++ simulation toolkit for passage of particles through matter based on Monte Carlo techniques [Agostinelli *et al.* 2003; Allison *et al.* 2016]. It is a widely used software in detector development, high energy physics, radiation protection and other fields. The toolkit delivers data for various physics processes, random number generators and the simulation construct that the application developer can use to develop a physics simulation. The toolkit is continuously validated against experimental data and has therefore become a reliable standard tool in particle physics. Geant4 is used explicitly in Chapter 5 to simulate the beam-target interaction at MAGIX and the formation of target induced halo. All simulations in this thesis are conducted with Geant4 10.04.p03.

3.3 BDSIM

BDSIM (Beam Delivery Simulation) is a simulation program for the passage of particles through matter in accelerators based on the Geant4 toolkit [Nevay *et al.* 2020]. BDSIM is designed to utilize Geant4 for simulations in the accelerator context and therefore provides standardized construction classes for typical accelerator elements such as magnets, beam pipes and collimators from GMAD input, which is a MAD-X-like script language. Furthermore, it provides routines to calculate beam properties from accumulated single events and a standard ROOT output format and analysis tool. It also delivers a Python tool to convert MAD-X models into BDSIM ones, matching magnet strengths and other parameters previously set. BDSIM is used in Chapter 6 and Chapter 7 to track target induced halo particles generated in Chapter 5 to analyze losses and simulate collimation concepts. All simulations in this thesis are conducted with BDSIM 1.3. development version (git scoring branch, HEAD 87291ae4695260ed81ed116badd086d2d3f3499a, checked out on 22.10.2019) built against Geant4 10.04.p03. The parallelization of several simulations is achieved with GNU Parallel [Tange 2018].

4 Adaption of Beam Optics in the MAGIX Arc

The lattice used for simulation is based on [Simon 2018]. Some aspects are altered to fit to the different scenarios investigated in this thesis, which are shortly discussed.

4.1 Beta Matching on Target

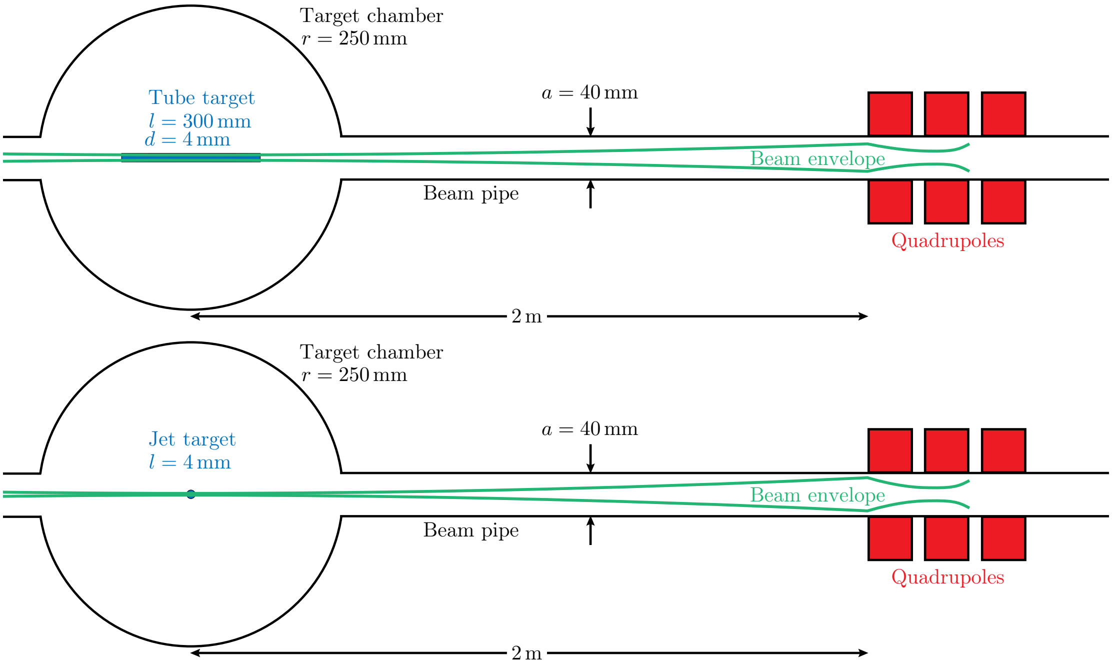

Figure 4.1: Comparison of constraints on the beam optics for a tube target discussed in [Aulenbacher 2014] (top) and a jet target (bottom). The beam can be focused sharper for a jet target, while the beam size at the ends of the tube target has to be restricted with a weaker focus.

The optics from [Simon 2018] are designed symmetrically up- and downstream of the target until the nearest quadrupole with a 4 m drift between them as it can be seen in Figure 4.2. The focus ($\alpha_\text{T} = 0$ according to Equation 2.5) must lie in the middle, where the target is located. This is ensured by the symmetry in quadrupole adjustments. The beam profile should further be symmetric in x and y. The intrinsic angle distribution at the focus is defined through Equation 2.6:

$$\gamma_* = \frac{1}{\beta_*},$$

or:

$$\pi\sigma_x\sigma_{x'} = \pi\varepsilon_{\text{geo}},$$

and therefore fixed as soon as β_* and correspondingly σ_x is defined. The only degree of freedom is then the emittance, which consequently must be sufficiently small to ensure requirements on σ_x and $\sigma_{x'}$. In [Simon 2018] the optics are optimized for a tube target of 30 cm length as described in [Aulenbacher 2014], which demands a sufficiently small beam size ($\beta_\text{T} < 15$ cm) 15 cm upstream and downstream of the interaction point to ensure that the beam entirely fits in the tube as illustrated in Figure 4.1. These constraints are relaxed for a jet target, owing the lack of a physical tube, and providing additional degrees of freedom in quadrupole adjustments. The demand on the beam at the interaction point is $\sigma_{x,y} < 300\,\mu$m [Merkel 2018]. Assuming that the beam at the injector meets $\varepsilon_n = 1$ mm mrad and deteriorates due to rest gas scattering and other effects down to 1.5 mm mrad ($\varepsilon_{\text{geo}} = 7.3\,\mu$m mrad at 105 MeV) [Matejcek *et al.* 2019], this constraint corresponds to $\beta_* < 12.33$ m. The optics in the target arc are set to different target beta values at the interaction point β_* in the range 30 cm $\leq \beta_* \leq$ 100 cm for loss dependence studies discussed in Section 6.5, since this region requires the least alteration of the magnet strengths and provides sufficient headroom for MAGIX.

4.2 Introduction of Halo Collimators in the Lattice

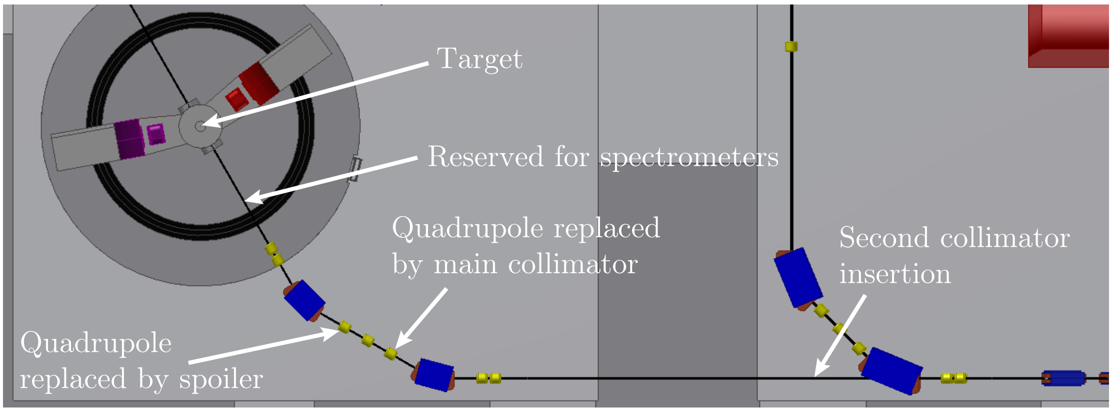

Figure 4.2: Collimator insertions for halo collimation in the MAGIX arc. Dipoles are shown in blue, quadrupoles in yellow. The area in the circular platform around the MAGIX target is reserved for spectrometer movement.

Halo collimators are not foreseen in the fundamental lattice and therefore need to be introduced for the studies in Chapter 7 as shown in Figure 4.2. It is preferable to place the collimators shortly after the MAGIX target to intercept the halo early. The space between target and the first downstream quadrupole triplet is however reserved for the movable MAGIX spectrometers, so that no elements of large transverse extent are allowed in that area. As the first and last quadrupoles of the triplet in the dispersive section between the following dipoles are not active in the present layout ($k = 0$), they are replaced with halo spoiler and collimator pairs, respectively. A placement in the dispersive section also yields the advantage of collimating electrons with energy deviations from the nominal energy, which is not be possible if the collimators are placed in the preceding non-dispersive section. A third collimator pair is introduced before the merger section to cover a location with approximately 90° betatron phase shift w.r.t the main collimator. As the space between the building wall and the merger section is restricted, this is the only available location for a collimator placement in the MAGIX arc. Placement in the shared section carrying beams from multiple turns is not possible since the lower-energy beams have a larger beam size due to adiabatic damping.

4.3 Beta Matching on Collimator

It is preferable to maximize the beam size at the collimators to allow for additional precision in the separation of halo from the beam core. This optimization however involves quadrupoles also ensuring the target focus and the achievable effect is therefore limited.

5 TAIL Formation

The target is first simulated in Geant4 without any accelerator parts to get a better model of TAIL distributions. The target is modelled as a cylinder filled with a given gas of homogenous density. The gases used in this thesis are taken from the Geant4 database, which incorporates the National Institute of Standards and Technology (NIST) database. The electron beam has a 2-dimensional Gaussian shape in the transverse dimensions and Gaussian energy distribution. The longitudinal shape is a delta peak at $t = 0$ as Geant4 does on this point not natively support generation of temporal distributions in its GeneralParticleSource class. An overview over the target and beam parameters is given in Table 5.1.

Table 5.1: Target and beam parameters for the Geant4 simulations.

Parameter	**Description**	**Value**
$\varepsilon_{\mathrm{n,rms}}$	Normalized Emittance	1.5 mm mrad
E	Beam Energy	105 MeV
σ_E	Energy Spread	10.5 keV
$\sigma*$	Transv. Size	46.8 µm
$\sigma_{p,*}$	Transv. Angle Spread	156 µrad
β_*	Target β (Twiss)	30 cm
α_*	Target α (Twiss)	0
d	Target Length	4 mm
ϱ_{p}	Target Particle Density	$10^{19}\,\mathrm{cm}^{-2}$
Z	Target Gas Atomic Number	1 (H), 2 (He), 8 (O), 18 (Ar), 54 (Xe)

5.1 Idealized Target

At the current date the MAGIX gas jet target is still under active development and has already shown first results in a proton radius measurement at the Mainz Microtron (MAMI) [Gagneur 2018]. The assumption of an idealized target has to be made until the target and accelerator design are finalized. The design value of the normalized emittance at the injector entrance is 1 mm mrad and expected to deteriorate to around 1.5 mm mrad at the target during the transport due to scattering from residual vacuum gas, intra-beam scattering, coulomb space charge repulsion and higher order magnetic multipoles [Matejcek *et al.* 2019]. The target shape is assumed to be cylindrical with 4 mm height and diameter between the Laval nozzle and catcher (see Figure 5.1), the density to be homogenous. The model uses the nominal areal particle density of $10^{19}\,\mathrm{cm}^{-2}$. The

Table 5.2: Target material properties at standard temperature and pressure from the Geant4 database [Geant4 Collaboration 2017, p.392f] and target densities at particle densities of $10^{19}\,\mathrm{cm}^{-2}$.

Target	$\varrho_{\mathbf{STP}}$ [mg cm^{-3}]	$\varrho_{\mathbf{target}}$ [mg cm^{-3}]
H	8.3748×10^{-2}	5.328×10^{-2}
He	$1.663\,22\times10^{-1}$	2.116×10^{-1}
O	1.331 51	8.457×10^{-1}
Ar	1.662 01	2.111
Xe	5.485 36	6.94

generated beam distribution is radial symmetric in transverse directions according to a round beam focus at the target. The experiments require $\sigma_r \leq 300\,\mu\mathrm{m}$, the target beta function is therefore being agreed on to be $\beta_* = 30\,\mathrm{cm}$, corresponding to $\sigma_r = 46.8\,\mu\mathrm{m}$ [Merkel 2018].

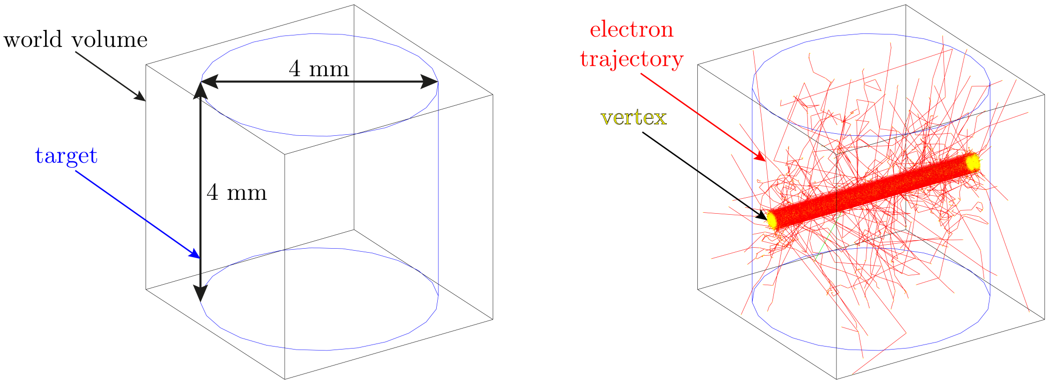

Figure 5.1: Geant4 model of the target (left) and a simulation of 10^5 electrons hitting a Xe target with a particle density of $10^{19}\,\mathrm{cm}^{-2}$ (right).

5.1.1 Angle Distribution

Single beam electrons are generated according to the assumed beam parameters and tracked through the target. The predefined FTFP_BERT physics process list is used for tracking. Particle parameters are stored when exiting the world volume (i.e. the target) and evaluated. The angular distributions for the different target gases are shown in Figure 5.2.

The obtained values for power contained in certain angle regions for a 1 mA beam are summarized in Table 5.3. A comparison with Table 2.2 reveals that the simulated losses in the region between 10σ and 10 mrad fluctuate from 39 % to 62 % of the predicted values from Rutherford scattering, which are overestimated. These deviations presumably arise from the assumptions made for the application of Rutherford scattering, e.g. point-like beam and target. The prediction however yields agreement in the order of

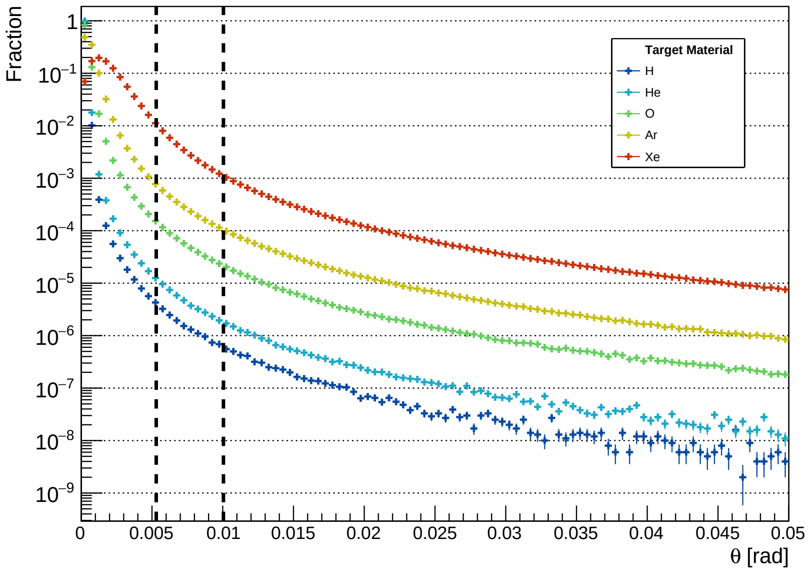

Figure 5.2: Angular distributions of the beam exiting the target for different MAGIX target gases. The vertical lines mark 10σ of the incoming beam (left) and 10 mrad (right). Error bars are according to the statistical error.

magnitude for the mentioned region. It is further observed that the region > 10 mrad is underestimated by Rutherford scattering with simulation values exceeding the predicted values about a factor of 5 to 10. Comparison of both cases shows a confined deviation interval although not agreeing. The numbers estimated through Gaussian approximation however deviate largely from the simulated values. It is therefore concluded that single scattering dominates the halo formation process with multiple scattering playing a minor role.

Losses expected at > 10 mrad on the first two meters behind the target lie in the region of watts for H and He. The powers substantially increase to few tens of watts for O. Losses in the region of 100 W for Ar and several kW for Xe (corresponding to 4.3 % of total beam power) are considered to be unreasonable for ERL operation. The luminosity for such targets must then be reduced to ensure a sustainable amount of losses. Dedicated attention is required for the powers between 10σ of the beam transverse size (which is expected to be properly transported through the accelerator) and 10 mrad as these values exceed the first losses considerably. It is therefore not sufficient to only take the angular distribution of the exiting beam into account.

Table 5.3: Power densities emerging from the different MAGIX targets between 10σ of the beam and 10 mrad and above 10 mrad in the Geant4 simulation. The values from Table 2.2 are included for comparison.

	Geant4	
Target	$P_{10\sigma-10\,\mathrm{mrad}}$ [W]	$P_{>10\,\mathrm{mrad}}$ [W]
H	1.97	0.61
He	5.85	1.86
O	71.18	21.98
Ar	354.38	105.90
Xe	4556.04	1033.80
	Rutherford Scattering	
H	2.52	0.06
He	10.08	0.25
O	161.3	4.023
Ar	816.5	20.37
Xe	7348	183.3
	Gaussian Approximation	
H	0	0
He	0	0
O	0	2.724×10^{-6}
Ar	0	1819
Xe	0	73 140

5.1.2 Energy Distribution

Beam electrons lose kinetic energy in inelastic scattering processes and produce a continuous low energy tail in the energy distribution as observed in Figure 5.3. The values are collected in Table 5.4.

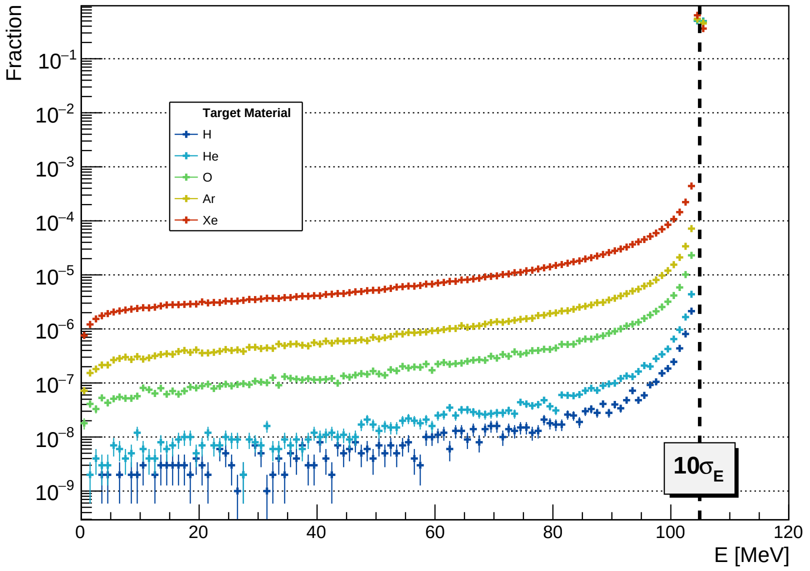

Figure 5.3: Energy distributions of the beam exiting the target for different MAGIX target gases.

Table 5.4: Power in the low energy tail of the exiting beam lying $> 10\sigma_E = 105\,\mathrm{keV}$ away from the center energy and shifts in peak energy $\Delta\bar{E}$. Resolution for $\Delta\bar{E}$ is limited by the bin width of 1 keV.

Target	$P_{>10\sigma_E}$ [W]	$\Delta\bar{E}$ [keV]
H	3.60	0
He	7.39	0
O	34.39	0
Ar	94.35	1
Xe	534.72	3

The powers in the low energy tail lie approximately in the region of the values for the transverse halo > 10 mrad from the Geant4 values in Table 5.3, however exceeding them except for the Ar and Xe targets. It is to note that the real energy acceptance is expected to be larger than 10σ around the nominal energy, which will relax the loss power estimation in Table 5.4. An additional shift in peak energy $\Delta\bar{E}$ is visible in Figure 5.4 for Ar and Xe. The shifts of 1 keV and 3 keV however lie well below $1\sigma_E$

and are therefore expected to be negligible. The low energy tail is expected to be lost gradually after passage of dipole magnets where the requirements to the energy spread cannot be fulfilled, leading to a large deflection into the beam pipes. The largest fraction of total losses is expected to appear after the first dipole magnet.

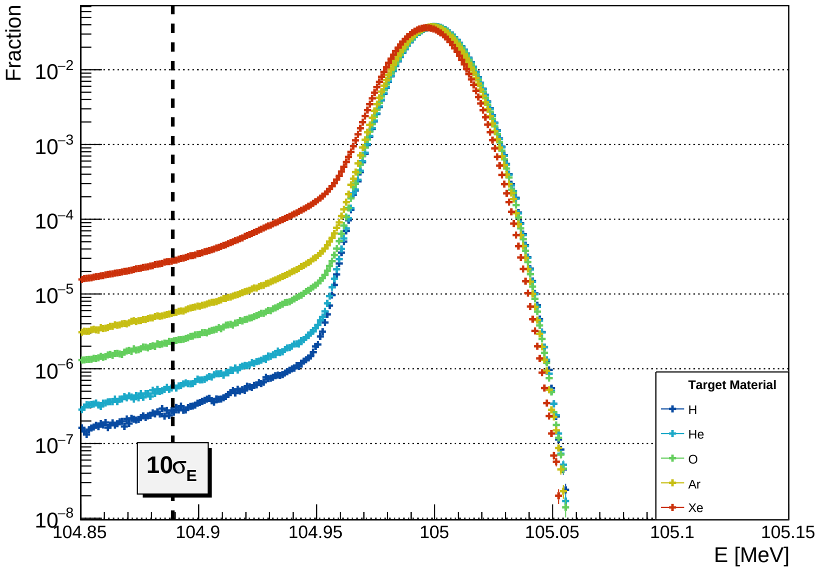

Figure 5.4: Energy distributions for different target gases in the region around the peak energy. A small shift of peak energy can be observed for Ar and Xe.

5.1.3 Delayed Electrons

The primary particle distribution generator Geant4 distribution does not allow the generation of a beam with a temporal distribution, i.e. the simulated beam is point-like in z. It is however possible to look at the time of flight in the simulation and compare it against the time needed for an electron to travel at c through the model. Delays may arise from elongation of flight paths through multiple scattering and loss of kinetic energy and thus deviation of velocity from c. The temporal delay distributions are shown in Figure 5.5, values are summarized in Table 5.5.

The fraction of delayed electrons is small for all targets compared to the period of 769.2 ps for the 1.3 GHz MESA RF. The effects of delayed electrons are therefore negligible.

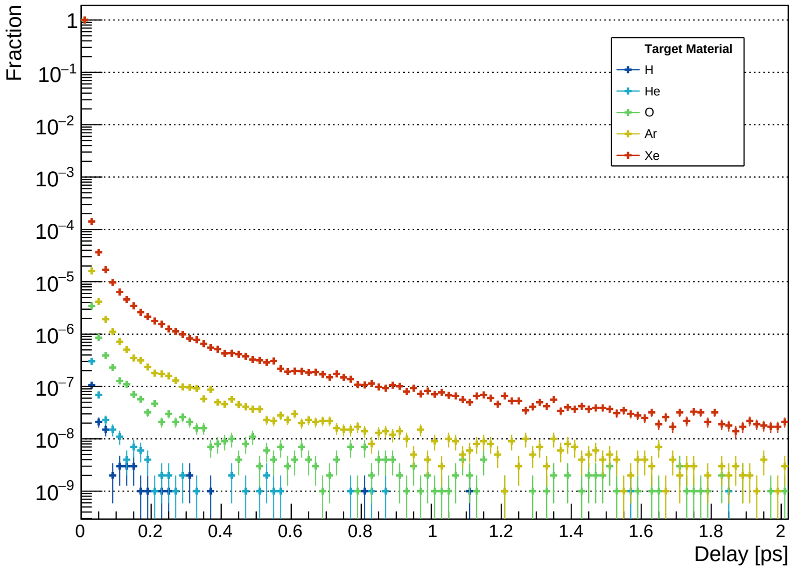

Figure 5.5: Delay distributions of beam electrons after the target.

Table 5.5: Fractions of electrons delayed $> 100\,\mathrm{fs}$.

Target	$N_{>100\,\mathrm{fs}}$ $[10^{-6}]$
H	0.02
He	0.05
O	0.71
Ar	3.80
Xe	34.02

5.1.4 Phase Space

The electrons are plotted in the phase space x-x' in Figure 5.6, Figure 5.7 and Figure 5.8, the corresponding emittances are calculated in Table 5.6 from the N single particle coordinates momenta [Barletta *et al.* 2012]:

$$\begin{aligned}
\varepsilon_{\text{geom}} &= \sqrt{\langle x^2\rangle\langle x'^2\rangle - \langle xx'\rangle^2} \\
\langle x^2\rangle &= \frac{1}{N}\sum_{i=1}^{N}(x_i - \langle x\rangle)^2 \\
\langle x'^2\rangle &= \frac{1}{N}\sum_{i=1}^{N}(x'_i - \langle x'\rangle)^2 \\
\langle xx'\rangle &= \frac{1}{N}\sum_{i=1}^{N}(x_i - \langle x\rangle)(x'_i - \langle x'\rangle)
\end{aligned}$$

The phase spaces exhibit a strong correlation between large angles and offsets in $+x$-$+x'$, respectively $-x$-$-x'$. Said correlation is explained by the travel distance of particles through the target, where large deflections in a certain direction result in a spatial offset in the same direction after the target. The smearing of the distribution is due to the length of the target, where scattering at the beginning results in larger spatial offset, whereas scattering at the target end only shows large angles and – lacking travel distance – no spatial offset.

Table 5.6: Geometrical and normalized emittance values calculated from the distribution of particles in the x phase space.

Target	$\varepsilon_{\mathbf{geom}}$ [nm rad]	$\varepsilon_{\mathbf{n}}$ [mm mrad]	$\sqrt{\langle x^2\rangle}$ [µm]	$\sqrt{\langle x'^2\rangle}$ [µrad]
No target	7.300	1.5	46.80	156
H	8.193	1.680	46.82	175
He	9.479	1.943	46.82	202
O	21.584	4.425	46.83	461
Ar	44.501	9.123	46.88	950
Xe	126.537	25.940	47.26	2695

A considerable degradation of the emittance through the target is observed, while the RMS value in x does not change accordingly. The elliptical shape is largely distorted by large angle electrons with fractions increasing with higher nuclear charges of the target gas as already shown in Figure 5.2. This is also reflected in the rapid increase of x' RMS values. Although the amount outside the former elliptical area in phase space after passage of a H or He target are rather small, the number of halo particles quickly increases to non-negligible amounts with heavier target gases. Owing to this distortion of the elliptical shape, a further treatment cannot be reasonably done with only taking emittance growth with shape conservation into account.

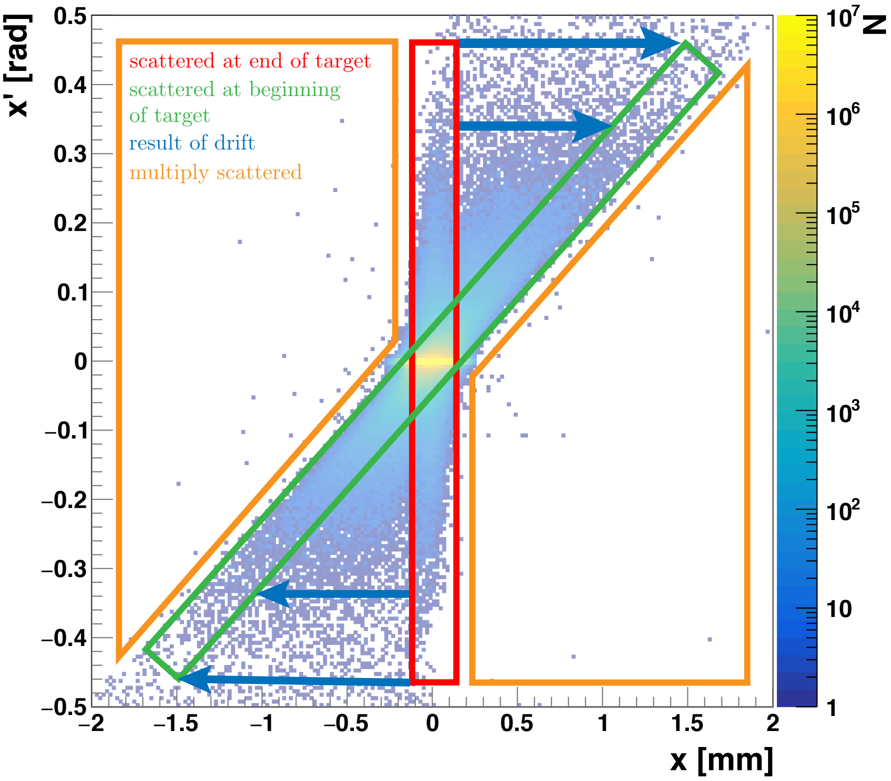

Figure 5.6: x phase space of the beam exiting the Xe target with description of different scattering regions. It is to note that multiply scattered electrons possibly lie in every region of the phase space, however potentionally being shadowed by different, more visible scattering effects.

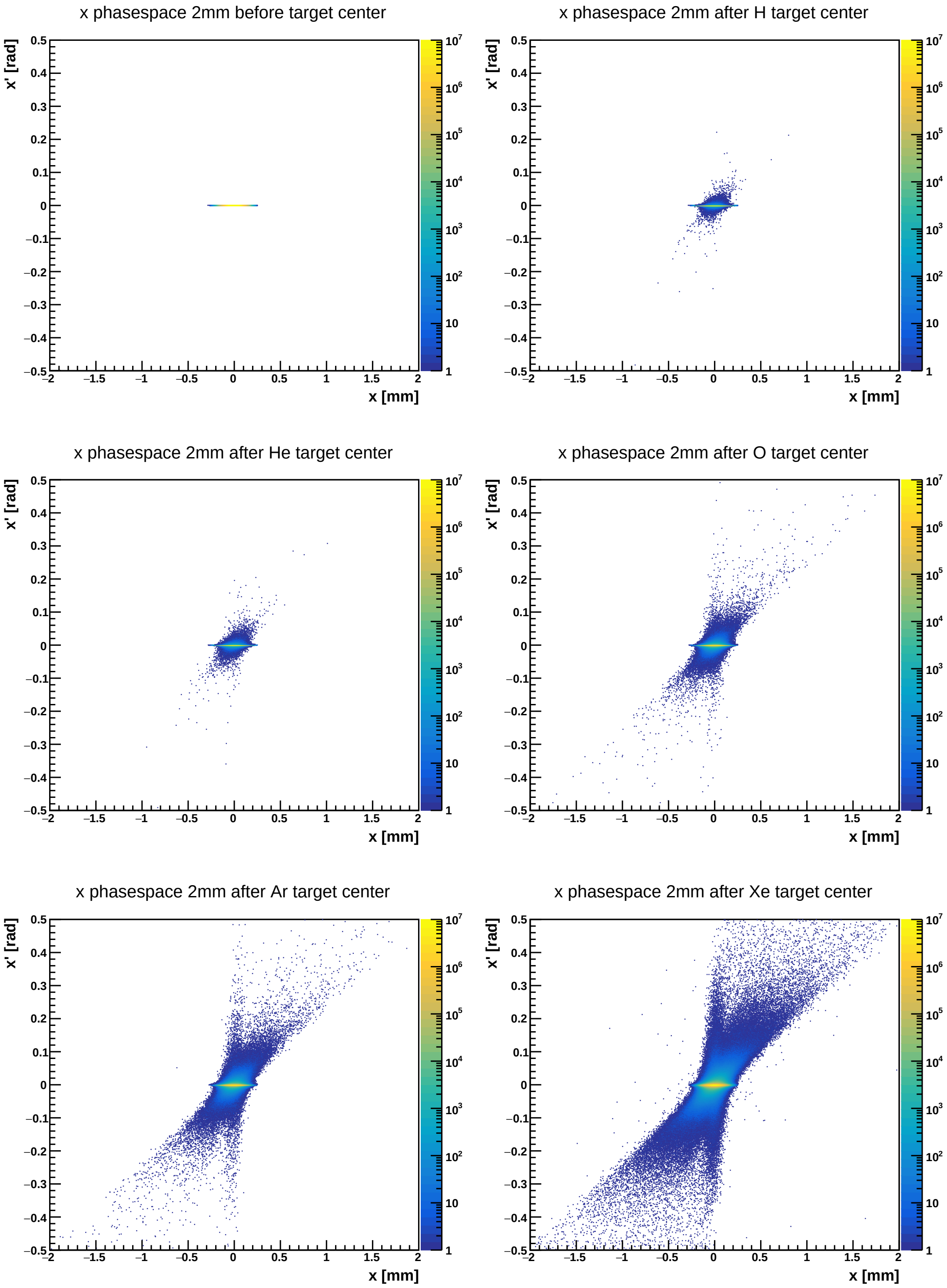

Figure 5.7: x phase spaces of the beam exiting different MAGIX target gases with plotted up to 500 mrad. Each simulation contains 10^9 particles. The color scale denotes the particle density in units of $2.5\,\mathrm{nm}^{-1}\,\mathrm{rad}^{-1}$.

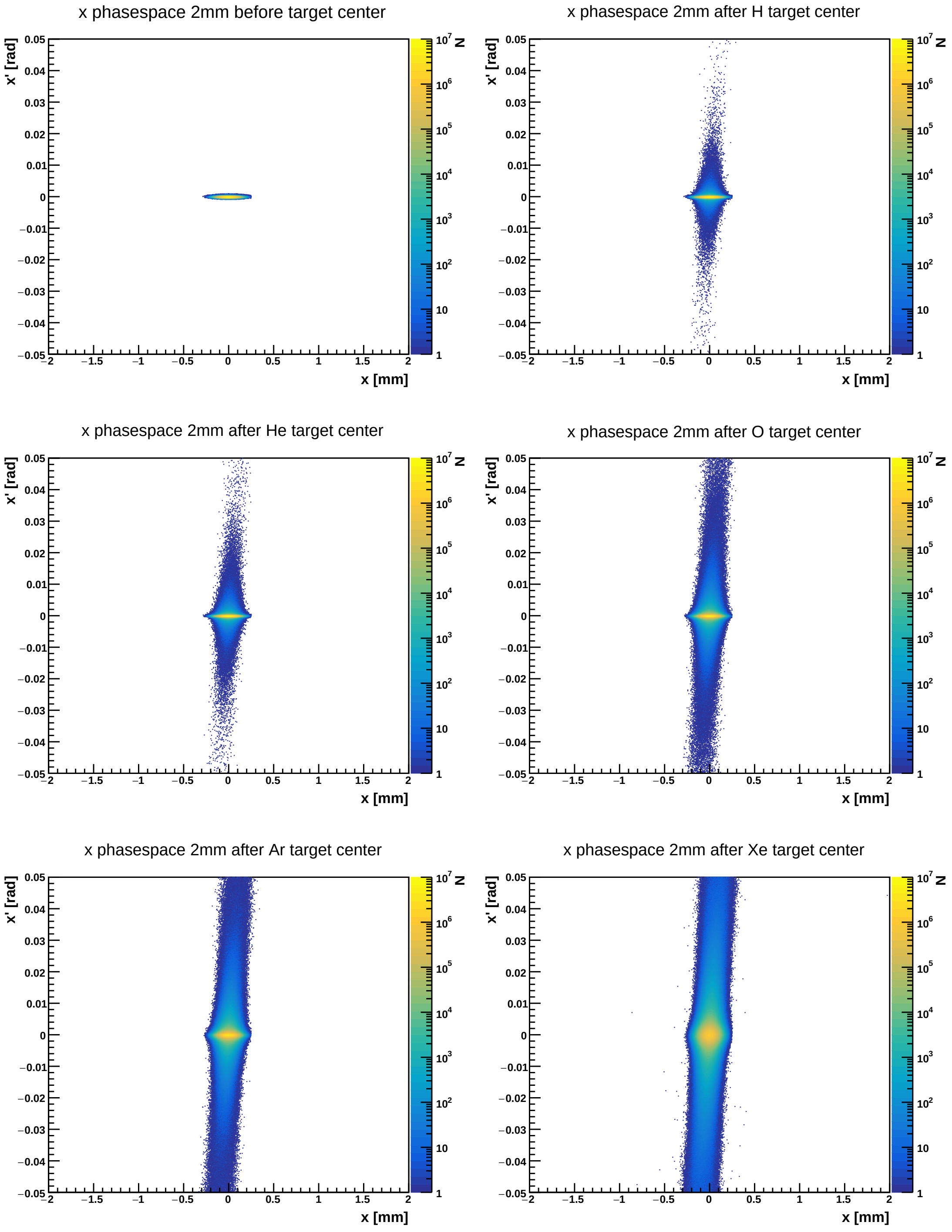

x phasespace 2mm before target center

x phasespace 2mm after H target center

x phasespace 2mm after He target center

x phasespace 2mm after O target center

x phasespace 2mm after Ar target center

x phasespace 2mm after Xe target center

Figure 5.8: x phase spaces of the beam exiting different MAGIX target gases with plotted up to 50 mrad. Each simulation contains 10^9 particles. The color scale denotes the particle density in units of $2.5\,\mathrm{nm}^{-1}\,\mathrm{rad}^{-1}$.

5.2 Summary of Geant4 Simulations

The simulations conducted in this chapter exhibit partly severe impacts of the target on the beam quality. Transverse angular distributions and energy distributions show the largest effects and lead to a degenerated emittance with non-elliptical shape. The sum of all these effects requires dedicated treatment to locate and counteract losses. The resulting beam parameter distributions are further tracked through the accelerator sections downstream MAGIX.

5.3 Realistic Target

All simulations in this chapter are based on idealized target parameters, while first jet profile measurements at MAMI show a Gaussian density distribution [Gagneur 2018]. A realistic target is expected to diffuse gas into larger volumes inside the target vacuum chamber. The target is neither being expected to be homogeneous nor of purely cylindrical shape. The effective length of the real target on the beam axis increases due to gas diffusion, while the highest density of scattering centers is expected to be mostly confined around the center. Halo effects may however arise along a larger path and a changing beam size traversing the target like visible in Figure 5.6 must be taken into account. Due to the lack of sufficient characterization of the target properties up to the current date, only the idealized target is considered for this thesis. This treatment however allows to obtain fundamental insights into beam-target interaction at MAGIX.

6 Halo Tracking and Beam Loss

This chapter is dedicated to the beam losses which occur downstream of MAGIX due to TAIL. Data generated by Geant4 in the previous chapter is now used as input for tracking simulations in BDSIM to determine location and amount of lost power in the accelerator. A view of the MESA model in BDSIM is shown in Figure 6.1. The arcs Tn (Turn n) with $n = 1 - 4$ are labeled according to the order of passage during acceleration. Different machine parameters are varied and the occuring losses are extracted to investigate their dependencies and to compare with the luminosity limit estimation. It is to be noted that the recirculation direction in Figure 6.1 is reversed with respect to the layout in Figure 1.1. This a consequence of the conversion routine and does not change the beam dynamics behavior. The same holds true for the intentionally flipped dipole pairs, which are introduced to avoid volume collision in the simulation model. The tracking lattice is split into parts corresponding to their optical purposes and the division is illustrated in Figure 6.1 and Figure 6.2 and explained in Table 6.1.

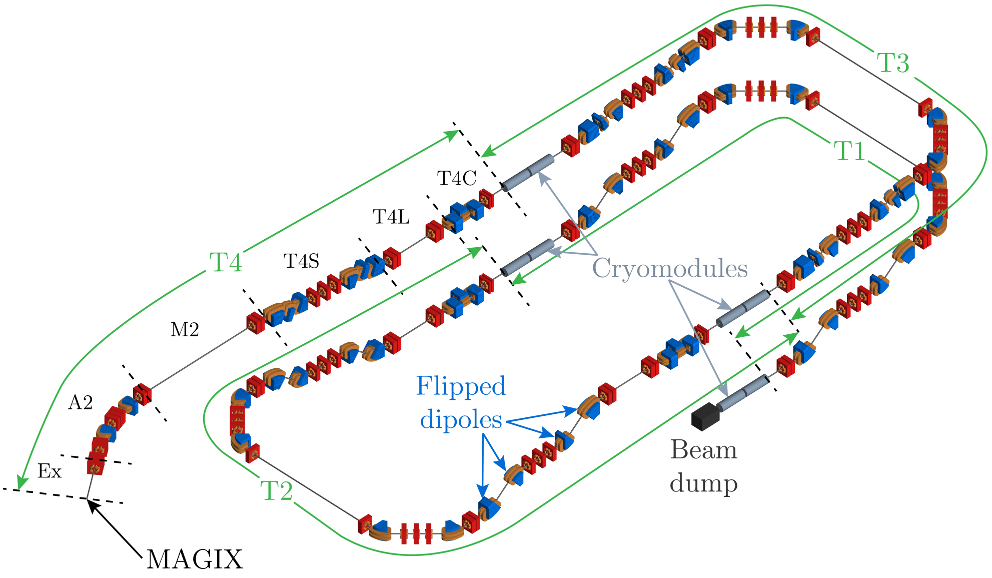

Figure 6.1: BDSIM MESA model. Since BDSIM currently cannot handle splitting and merging of overlapping geometries, two vertical dipole pairs are turned upside down and the accelerator is modelled sequentially to avoid volume collisions in the simulation.

An overview of the parameters used in all following tracking simulations – unless

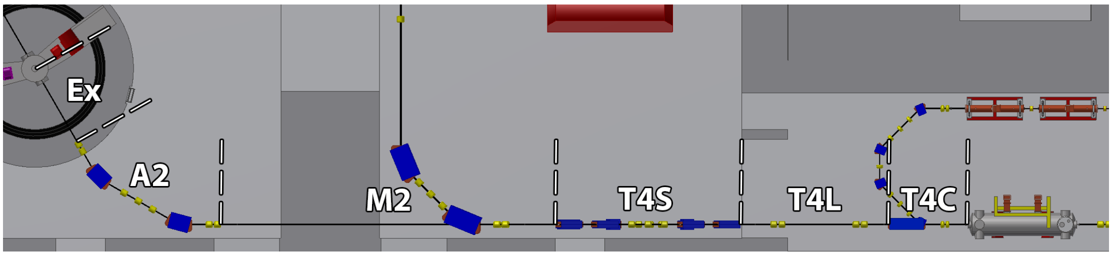

Figure 6.2: Close view of the MAGIX arc from MAGIX to the first cryomodule with section labels.

Table 6.1: Description of lattice sections used in the BDSIM simulations.

Abbreviation	Description
Ex	Experiment Section
A2	Double Bend Achromat 2
M2	Matching Section 2
T4S	Turn 4 Spreader Section
T4L	Turn 4 Linac Section
T4C	Turn 4 Chicane

otherwise noted – is given in Table 6.2. The Xenon TAIL is used since it shows the largest halo intensity and is therefore favorable in the sense of computational efficiency. The normalized emittance is assumed to be enlarged by 50 % in comparison to the design injector emittance of 1 mm mrad [Alexander 2018] to account for emittance growth due to space charge and other nonlinear effects such as multipole components in magnets or misalignment.

6.1 Variance Reduction

Variance reduction techniques reduce the errors on estimates for the same computational effort [Robert & Casella 2005, pp.90ff]. Commonly used techniques for Monte Carlo-simulations in nuclear physics are importance and geometrical sampling and are aimed to give more focus to events in a region of interest, while discarding events in other regions. Since the largest fraction of the scattered beam is still contained in the core, respectively inside the machine acceptance, it is favorable to discard these core electrons for tracking simulations to save computation time without affecting the calculated loss power emerging from beam halo. The procedure is divided into different parts.

6.1.1 Beam Core Tracking

The beam core in the nominal 10σ volume of the 5D phase space x, p_x, y, p_y, E is generated uniformly and uncorrelated (i.e. not Gaussian like the expected real beam) and tracked through the accelerator lattice. The particle hits and losses are checked to be

Table 6.2: Default simulation parameters in BDSIM simulations unless otherwise noted.

Parameter	**Description**	**Value**
$\varepsilon_{\mathrm{n,rms}}$	Normalized Emittance	1.5 mm mrad
E	Beam Energy	105 MeV
σ_E	Energy Spread	10.5 keV
$\sigma*$	Transv. Size	46.8 µm
$\sigma_{p,*}$	Transv. Angle Spread	156 µrad
I	Beam Current	1 mA
P	Beam Power	105 kW
β_*	Target β (Twiss)	30 cm
α_*	Target α (Twiss)	0
a	Aperture	40 mm
d	Target Length	4 mm
ϱ_{p}	Target Particle Density	$10^{19}\,\mathrm{cm}^{-2}$
Z	Target Gas Atomic Number	54 (Xe)
$\mathcal{L}$	Luminosity	$6.242\times10^{34}\,\mathrm{cm}^{-2}\,\mathrm{s}^{-1}$

zero, so no particles are lost in the 10σ parameter space. This set of parameters is therefore assumed to pass the accelerator model without collisions and is excluded from further simulations.

6.1.2 Discard Criterion

For the two-dimensional acceptances in x, y an ellipse is identified which contains the aforementioned 10σ environment around the beam center and nominal energy. The region is completely enclosed by the acceptance and follows the form of an upright ellipse at the focus point at the target ($\alpha_{\mathrm{T}} = 0$):

$$\left(\frac{r_i}{r_{i,\max}}\right)^2 + \left(\frac{p_i}{p_{i,\max}}\right)^2 = 1 \tag{6.1}$$

For the z respectively E acceptance the ellipse expression simplifies to a 1-dimensional interval:

$$\left(\frac{E - E_{\mathrm{center}}}{E_{\max}}\right)^2 = 1 \tag{6.2}$$

The volumes inside the ellipses are denoted by A_i and are chosen so that primaries j with parameters:

$$(x_j, p_{x,j}) \in A_x \wedge (y_j, p_{y,j}) \in A_y \wedge E_j \in A_z, \tag{6.3}$$

are fully inside the machine acceptance and can therefore be discarded without impact on loss power estimation.

6.1.3 Primary Distribution Generation

The BDSIM primary distribution is generated in Geant4 according to the respective beam optics at the target (i.e. the beam size, divergence, energy etc. are identical to the values simulated in BDSIM). The target tracking is carried out as described in Chapter 5. After every event, the primary track is either rejected according to Equation 6.3 or its exit coordinates are stored in a CSV (Comma Separated Value) file to be used as input in BDSIM. To be able to accurately obtain power losses, the number of stored halo electrons and the total number of simulated events are recorded. The halo intensity with respect to the total beam power is obtained from the fraction of both numbers.

6.2 Simulation Procedure

The distributions generated as described in the previous section are used as custom input distributions for the BDSIM tracking simulation. BDSIM stores integrated energy deposition for every event both per element as in the lattice definition and per specified length along the accelerator, which includes any energy deposited in material by primaries or non-primaries. This data is averaged using the rebdsim analysis tool to give a per-event average in units of GeV ($\mathrm{GeV\,m^{-1}}$ respectively). Escaping particles are not recorded as energy deposition. The specified processes contribute to the production of secondaries and power losses, in this case the FTFP_BERT physics list, which includes bremsstrahlung, secondary production processes, inelastic scattering, ionization etc. A detailed overview of the processes included is given in [Geant4 Collaboration 2019].

6.3 Postprocessing Procedure

Since the previously discarded beam core is not simulated in this step, the energy loss per event generated in BDSIM needs to be scaled by the intensity fraction obtained before. The data then yields the average energy loss per beam electron. The values are further scaled to match the beam power as a meaningful figure of merit. The loss power per element can be expressed as product of the number of primary electrons, i.e. I/e, and energy deposited in this specific element per primary electron:

$$\begin{aligned} P &= \frac{N_e}{t} \cdot E_{\mathrm{dep}} \\ &= \frac{I}{e} \cdot \mathrm{GeV} \cdot \frac{E_{\mathrm{dep}}}{\mathrm{GeV}} \\ &= I \cdot \mathrm{GV} \cdot \frac{E_{\mathrm{dep}}}{\mathrm{GeV}} \\ &= 1\,\mathrm{mA}\,\mathrm{GV} \cdot \frac{I}{\mathrm{mA}} \cdot \frac{E_{\mathrm{dep}}}{\mathrm{GeV}} \\ &= 10^6\,\mathrm{W} \cdot \frac{I}{\mathrm{mA}} \cdot \frac{E_{\mathrm{dep}}}{\mathrm{GeV}} \end{aligned}$$

Aiming for an operation with $I = 1\,\mathrm{mA}$, the stored losses $E_{\mathrm{dep}}\mathrm{GeV}^{-1}$ translate to:

$$P = 10^6\,\mathrm{W} \cdot \frac{E_{\mathrm{dep}}}{\mathrm{GeV}} \tag{6.4}$$

Losses in several succeeding elements are further summarized to obtain losses in the sections illustrated in Figure 6.2 and downstream sections of the machine as well as total losses.

6.4 Analysis Procedure

The losses per section and total losses are plotted against the varied quantity to examine and discuss their behavior. Only the total losses are fitted with suitable functions to derive simplified dependencies of losses on the respective quantity as loss behavior in subsections can vary in different ways. The fit function is chosen to suit the data in an empirical rather than a theoretical manner. Owing this circumstance, χ and error on the fit values are not discussed as a measure of fit quality. The maximum relative deviation Δ_{max} of the actual data from the fit value is instead considered as error of the simplified model.

6.5 Beta on Target Study

The lattice optics in the turn 4 arc succeeding the MAGIX target are varied to generate different β_* in order to find a region where losses are minimal and to study the behavior of losses on variation of optics. β_* is is varied from 30 cm to 100 cm in steps of 10 cm and the optics matched to the next section in MAD-X. The optimized optics are then converted into GMAD magnet strengths that are read by BDSIM. The range of β_* is chosen according to an agreed on value of $\beta_* = 30\,\mathrm{cm}$ and its direct surrounding.

The variation in this range is possible in MAD-X with the variation of a minimal set of complementary magnet strengths which are shown in Figure 6.5. Outside this range, the MAD-X optimization routine requires additional free parameters to properly match the beam to the next lattice section.

Every simulation uses a dedicated primary starting distribution. The results are shown in Figure 6.6. The results show only a slight variation of total losses over the simulated β_* range. However, a shift of losses from away from section Ex to further downstream sections (most notably M2) is observed for increasing β_* values, providing the opportunity to counteract losses in the direct vicinity of the gas target as long as the experimental criteria on the beam are not violated.

The fit function is chosen to be a polynomial of first order:

$$f(\beta_*) = a + b\beta_* \tag{6.5}$$

The obtained parameters are summarized in Table 6.3.

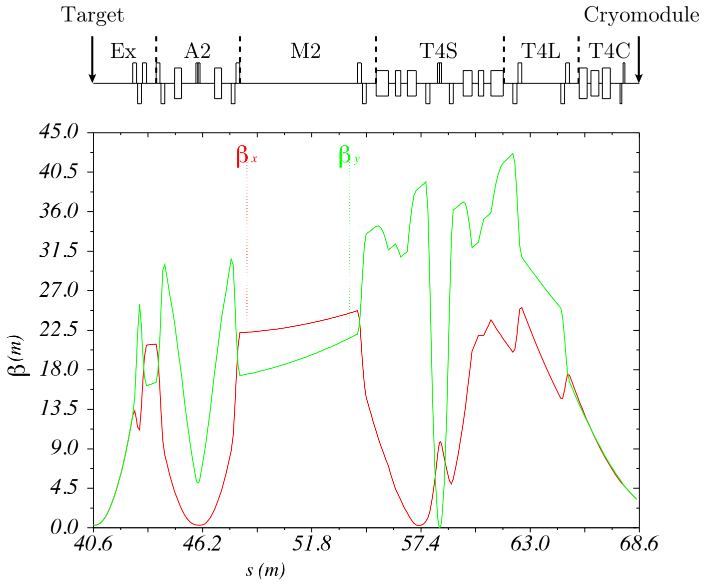

Figure 6.3: β-functions of the experimental beam line for $\beta_* = 30\,\mathrm{cm}$ as optimized by MAD-X.

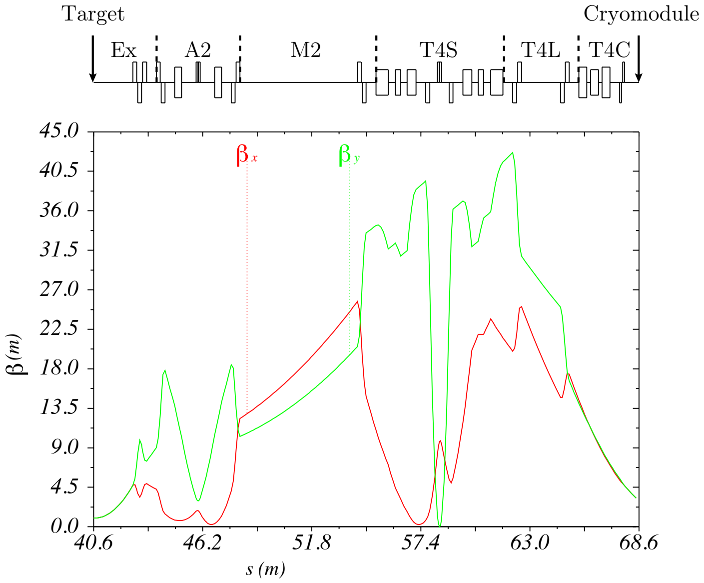

Figure 6.4: β-functions of the experimental beam line for $\beta_* = 100\,\mathrm{cm}$ as optimized by MAD-X.

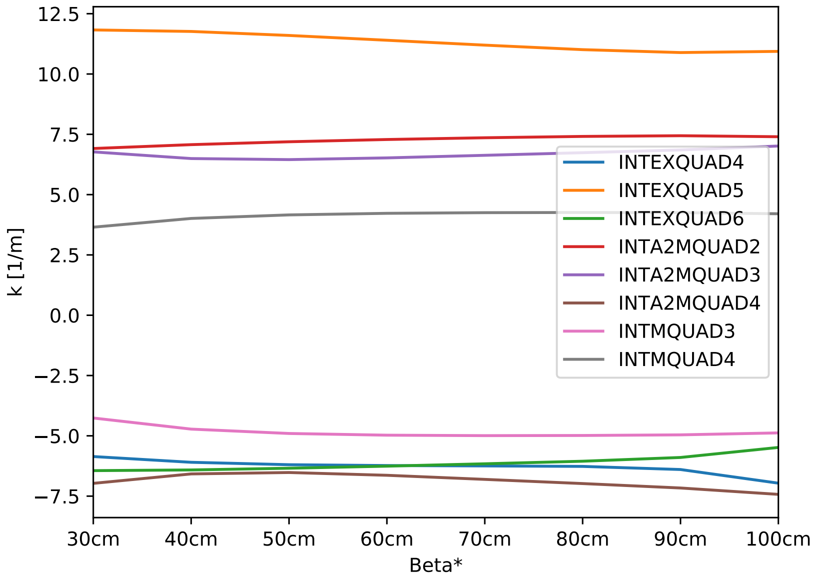

Figure 6.5: Magnet strengths for different values of β_* as optimized by MAD-X.

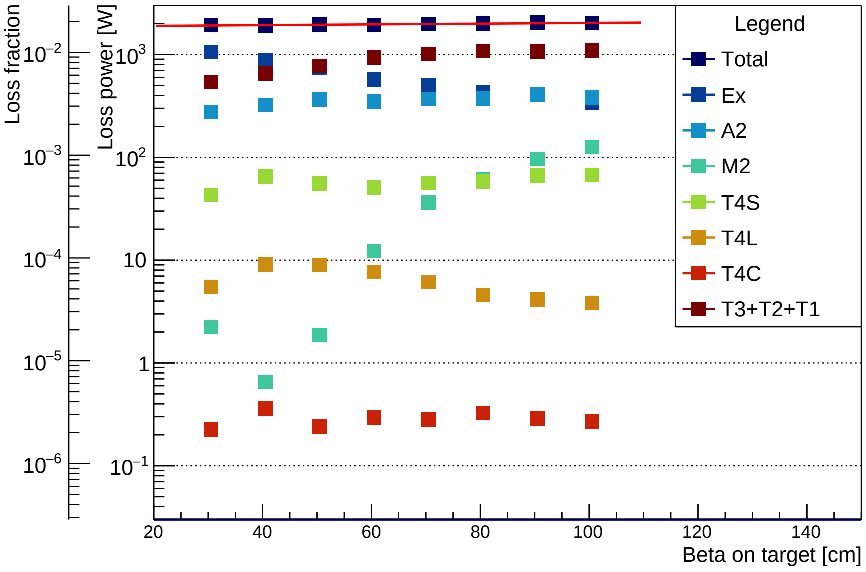

Figure 6.6: Loss distributions and fit of total losses (red line) for different values of β_*.

Table 6.3: Fit parameters obtained from Equation 6.5.

Parameter	**Value**
a_{β_*}	$1866.75\,\mathrm{W}$
b_{β_*}	$1.622\,01\,\mathrm{W\,cm^{-1}}$
$\Delta_{\mathrm{max},\beta_*}$	$1.93\,\%$

6.6 Target Gas Study

Since MAGIX is designed to operate with target gases up to xenon, it is important to take the loss behavior for different nuclear charges Z of the target gas into account.

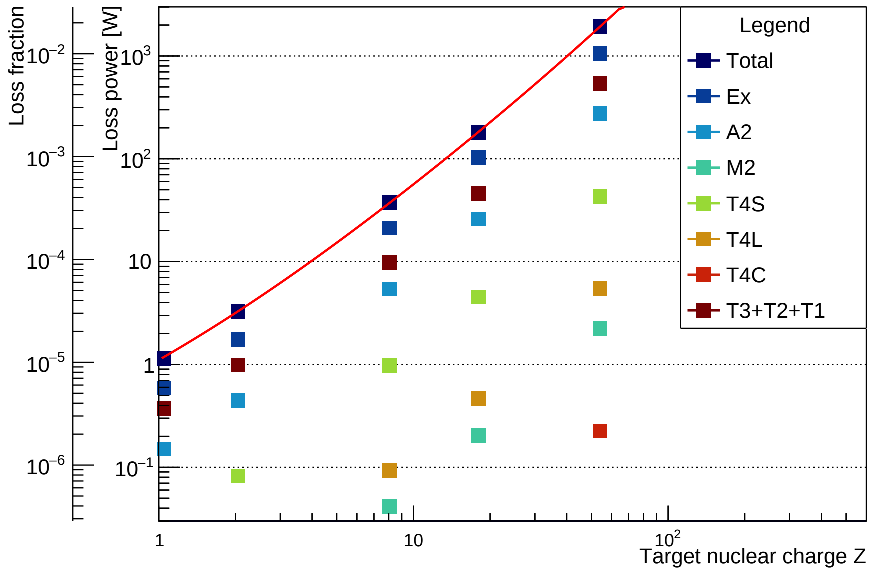

Figure 6.7: Loss distributions and fit of total losses (red line) for H, He, O, Ar and Xe.

Figure 6.7 shows the loss distributions for the considered target gases, corresponding total loss powers are denoted in Table 6.4. It is noteworthy that the ratio of P_{loss} and $P_{>10\,\text{mrad}}$ ranges from 1.69 to 1.88 and appears to vary only slightly. It can therefore be used to roughly estimate actual losses along the accelerator lattice from the halo intensity. While a mostly quadratic dependence of P_{loss} from Z is expected, a polynomial of third order without a constant term (since $Z = 0$ should lead to no losses) is determined as fit function to reduce deviation:

Table 6.4: Total loss powers from the BDSIM gas sweep. The Geant4 values from Table 5.3 are included for comparison.

	Geant4		**BDSIM**	
Target	$P_{10\sigma-10\,\text{mrad}}$ [W]	$P_{>10\,\text{mrad}}$ [W]	$P_{\textbf{loss}}$ [W]	$P_{\textbf{loss}}/P_{>10\,\text{mrad}}$
H	1.97	0.61	1.144	1.88
He	5.85	1.86	3.264	1.75
O	71.18	21.98	37.497	1.71
Ar	354.38	105.90	179.495	1.69
Xe	4556.04	1033.80	1928.660	1.86

$$f(Z) = a_Z Z + b_Z Z^2 + c_Z Z^3$$

The fit results are shown in Table 6.5. It is observed, that the linear and quadratic dependence is in the same order of magnitude with the quadratic one being the dominant, while the third power is suppressed by two orders of magnitude. The largest deviation is present at $Z = 1$.

Table 6.5: Fit parameters obtained from Table 6.6.

Parameter	**Value**
a_Z	0.467 34 W
b_Z	0.633 35 W
c_Z	0.003 36 W
$\Delta_{\mathrm{max},E}$	3.64 %

6.7 Target Density Study

A second target property impacting loss behavior is the target density ϱ or ϱ_p respectively. This study measures the particle density ϱ_p because it is a quantity independent from the nuclear charge Z, which is discussed in the previous section, and directly relates to the density of scattering centers in the way of the electron beam. A linear dependence is expected as the number of scatterings is proportional to the density of scattering centers. The resulting losses for a xenon target are plotted in Figure 6.8.

Deviation from the linear behavior of losses is visible above $\varrho_\mathrm{p} = 10^{19}\,\mathrm{cm}^{-2}$. Taking into account the mean scattering angle in the Gaussian approximation, which takes values of 9.14 mrad for $\varrho_\mathrm{p} = 10^{20}\,\mathrm{cm}^{-2}$ and 31.58 mrad for $\varrho_\mathrm{p} = 10^{21}\,\mathrm{cm}^{-2}$, it is concluded that this behavior stems from the transition into the multiple scattering regime, while the region below is governed by single scattering. The largest deviation is observed for $\varrho_\mathrm{p} = 10^{21}\,\mathrm{cm}^{-2}$, corresponding to a density of $\varrho = 218\,\mathrm{mg\,cm}^{-2}$ that is considered to be of no interest for a thin target. The point is therefore excluded from the fit. The fit function is chosen to be a quadratic polynomial with constraint $P_\mathrm{loss}(\varrho_\mathrm{p} = 0) = 0$:

$$f(\varrho_\mathrm{p} d) = a_\varrho \varrho_\mathrm{p} d + b_\varrho (\varrho_\mathrm{p} d)^2 \tag{6.6}$$

The parameters obtained from the fit are shown in Table 6.6. The fit reveals a dominant linear behavior for the range $\varrho_\mathrm{p} = 10^{16} \ldots 10^{19}\,\mathrm{cm}^{-2}$ and giving rise to the quadratic term above that range due to multiple scattering. A reduction of ϱ_p can counteract the increase in losses at high target nuclear charges discussed in the previous section at the expense of decreasing luminosity.

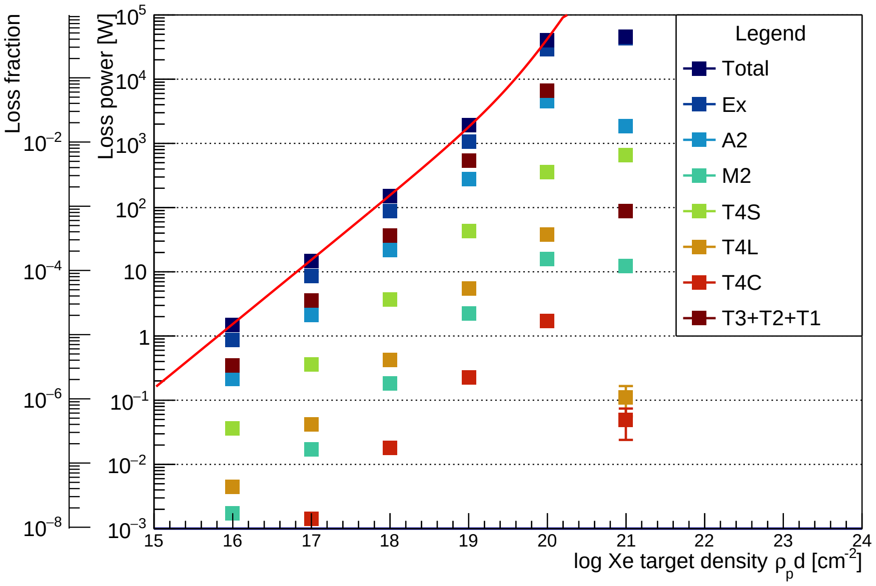

Figure 6.8: Loss distributions and fit of total losses (red line) for Xe target particle densities of different orders of magnitude. $\varrho_\text{p} = 10^{21}\,\text{cm}^{-2}$ is excluded from the fit.

Table 6.6: Fit parameters obtained from Equation 6.6.

Parameter	**Value**
a_ϱ	$1.240\,22\times10^{-16}\,\text{W}\,\text{cm}^2$
b_ϱ	$2.715\,29\times10^{-36}\,\text{W}\,\text{cm}^4$
$\Delta_{\text{max},\varrho}$	$6.79\,\%$

6.8 Beam Energy Study

The beam energy impacts losses in several different ways: the Rutherford scattering process is enhanced for large angles at lower energies (see Equation 2.13) and due to the stiffness of the beam the absolute energy acceptance is larger for higher energies. In addition to these two effects, the length of the accelerator that is to be traversed by the beam exiting the target depends on whether the accelerator is operated in single pass or double pass mode. Taking the design energy gain per cryomodule of 25 MeV into account, energies up to 55 MeV can be achieved in single pass mode, while energies above require double pass mode operation. On the other hand, energies possible in single pass operation can also be maintained in double pass mode as long as the separator magnets are capable of separating the energies at the given ratio. For this reason and given the current design of the injector separator magnet, energies below 30 MeV are considered to be not achievable. It is generally preferable to minimize the required lattice length on deceleration, so energies below 55 MeV are simulated in single pass mode only. Figure 6.9 shows the losses simulated for different beam energies at the xenon target.

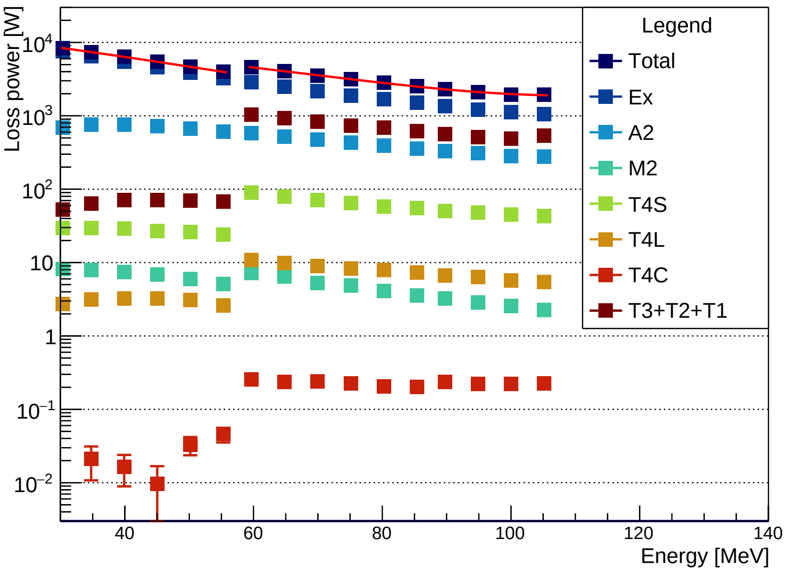

Figure 6.9: Power loss distributions for different beam energies and piecewise fits (red lines) for single pass mode and double pass mode.

It is observed that total losses appear to be larger for a longer lattice. This is expected since the acceptance for longer sections can only be reduced and thus a larger fraction of the beam is hitting the aperture. This can explicitly be read from the amount of losses in the recirculation arcs T3 to T1, which are enlarged by roughly an order of magnitude for double pass operation. The corresponding increase of losses in M2 through T4C is interpreted as consequence of the radiation produced in the T2 arc, which is not in use for the single pass mode. Losses in the direct vicinity of the target in sections Ex and A2 are reduced for stiffer beams. The fit function is chosen to be a polynomial of second order:

$$f(E) = a_E + b_E E + c_E E^2 \tag{6.7}$$

The power loss distributions are fitted separately for single and double pass mode operation. The extracted parameters are shown in Table 6.7. When simplifying the energy dependence and extrapolating the double pass mode fit to the single pass mode region, the maximum deviation is enlarged to $\Delta_{\max} = 22.39\,\%$ at 55 MeV.

6.9 Aperture Study

The aperture denotes the beam pipe diameter of an accelerator section. When the aperture is increased, the acceptance of the specific accelerator section also increases

Table 6.7: Fit parameters from Equation 6.7 with values for single-pass for energies $\leq 55\,\mathrm{MeV}$ and double-pass for energies $> 55\,\mathrm{MeV}$.

Parameter	**Value Single-Pass**	**Value Double-Pass**
a_E	$17\,455.1\,\mathrm{W}$	$15\,113.6\,\mathrm{W}$
b_E	$-366.300\,\mathrm{W\,MeV^{-1}}$	$-243.168\,\mathrm{W\,MeV^{-1}}$
c_E	$2.215\,16\,\mathrm{W\,MeV^{-2}}$	$1.118\,68\,\mathrm{W\,MeV^{-2}}$
$\Delta_{\max,E}$	$1.09\,\%$	$1.92\,\%$

and a larger fraction of the beam halo fits into it. The simulations for different apertures are presented in Figure 6.10.

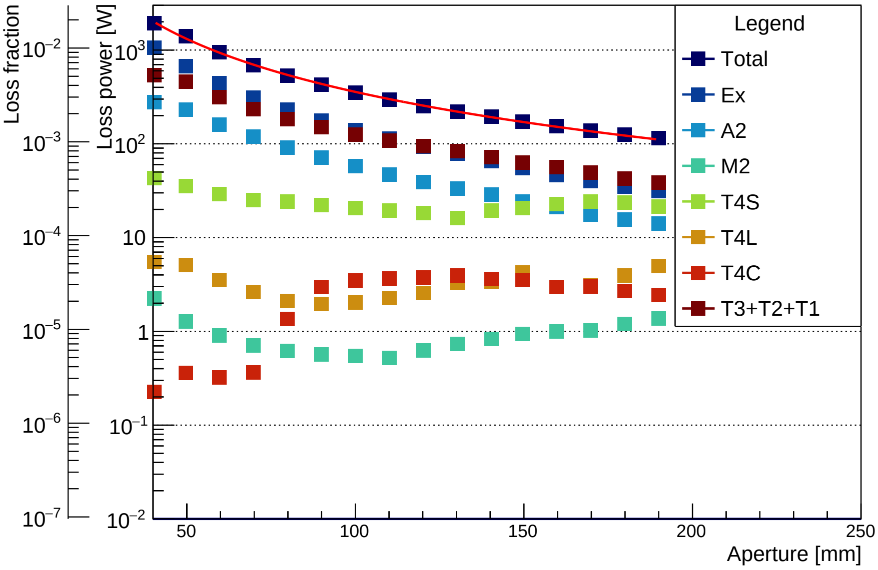

Figure 6.10: Power loss distributions and fit (red line) for different beam pipe diameters.

The large aperture sizes are unrealistic, since it appears not to be justifiable to construct magnets or maintain vacuum conditions for a 100 mm diameter beam pipe or above throughout the whole accelerator. However, the loss behavior can comfortably be studied. The power loss drops as expected when increasing the aperture as more halo can be captured in the acceptance. Most sections show a decrease in power deposition, while T4C shows an increase around 70 mm. This increase in losses is owed to the circumstance that halo can be transported easily through upstream sections and after passage of several dipoles varies greatly from the design orbit. The fit function is determined to be:

$$f(a) = a_a \cdot \left(\frac{a}{\mathrm{mm}} - c_a\right)^{-b_a} \tag{6.8}$$

Table 6.8: Fit parameters for losses on aperture variation according to Equation 6.8.

Parameter	**Value**
a_a	1190.840 kW
b_a	1.775
c_a	3.669
$\Delta_{\mathrm{max},a}$	6.890 %

The aperture dependence can be utilized to counteract beam losses. However, the aperture is limited in specific parts of the accelerator, e.g. the cryomodules. Furthermore, magnet design and vacuum pumping must adapt to larger beam pipes and their extensions may quickly grow into regions that are technically and economically unreasonable. The possibilities to enhance the aperture are therefore limited, however it may be favorable to shift losses from parts with larger aperture around the MAGIX target to downstream sections, where the aperture is again decreased.

6.10 Summary

The dependencies previously discussed in this chapter can be put together in a multivariate formula that roughly describes loss behavior on variation of the parameters:

$$P_{\mathrm{loss}} = c_P \cdot \frac{I}{\mathrm{mA}} \cdot f(Z) \cdot f(\varrho_{\mathrm{p}} d) \cdot f(a) \cdot f(E) \cdot f(\beta_*), \tag{6.9}$$

with the f_i obtained in the previous sections. The normalization factor c_P is determined by the required condition:

$$P_{\mathrm{loss}}(I_0, Z_0, (\varrho_{\mathrm{p}} d)_0, a_0, E_0, \beta_{*0}) = 1928.66\,\mathrm{W},$$

so that the equation yields the simulated loss value for the default parameters in Table 6.2. The condition yields:

$$c_P = 2.066{\times}10^{-19}\,\mathrm{W}^{-4}$$

When applying $f(E)$ from the double pass mode universally, the maximum error of P_loss is:

$$\begin{aligned}\frac{\Delta P_\text{loss}}{P_\text{loss}} &= \frac{1}{P_\text{loss}}\sqrt{\sum_i \left(\frac{\partial P_\text{loss}}{\partial f_i}\cdot \Delta f_i\right)^2} \\ &< \frac{1}{P_\text{loss}}\sqrt{\sum_i \left(\frac{\partial P_\text{loss}}{\partial f_i}\cdot f_i \cdot \Delta_{\text{max},i}\right)^2} \\ &= \sqrt{\sum_i \left(\Delta_{\text{max},i}\right)^2} \\ &= 24.74\,\%\end{aligned}$$

It is additionally convenient to rearrange Equation 6.9 for practical purposes. Coefficients of linear terms are factored out, so that:

$$P_\text{loss} = \frac{I}{\text{mA}}\frac{1}{C}\cdot f'(Z)\cdot f'(\varrho_\text{p} d)\cdot f'(a)\cdot f'(E)\cdot f'(\beta_*), \tag{6.10}$$

with:

$$\begin{aligned}C &= \frac{1}{c_P\cdot a_Z\cdot a_\varrho\cdot a_a\cdot(-b_E)\cdot b_{\beta_*}} = 5.127{\times}10^{20}\,\text{MeV}\,\text{W}^{-1}\,\text{cm}^{-1} \\ f'(Z) &= Z + \frac{b_Z}{a_Z}Z^2 + \frac{c_Z}{a_Z}Z^3 \\ f'(\varrho_\text{p} d) &= \varrho_\text{p} d\left(1 + \frac{b_\varrho}{a_\varrho}\text{cm}^{-2}\cdot\frac{\varrho_\text{p} d}{\text{cm}^{-2}}\right) \\ f'(a) &= \left(\frac{a}{\text{mm}} - c_a\right)^{-b_a} \\ f'(E) &= \text{MeV}\left(\frac{a_E}{-b_E}\frac{1}{\text{MeV}} - \frac{E}{\text{MeV}} + \frac{c_E}{-b_E}\text{MeV}\cdot\left(\frac{E}{\text{MeV}}\right)^2\right) \\ f'(\beta_*) &= \text{cm}\left(\frac{a_{\beta_*}}{b_{\beta_*}}\frac{1}{\text{cm}} + \frac{\beta_*}{\text{cm}}\right)\end{aligned}$$

Equation 6.10 can be translated into a luminosity limit when taking into account the maximum tolerable losses $P_\text{loss,max}$ and the simulation luminosity $\mathcal{L}_\text{sim}$:

$$\mathcal{L}_\text{max} = \mathcal{L}_\text{sim}\frac{P_\text{loss,max}}{P_\text{loss}}$$

Combining all constants, renaming f_i coefficients and substituting the mass density $\varrho \frac{M}{N_A}$ for ϱ_p yields:

$$
\begin{aligned}
P_\mathrm{loss} = 3.387{\times}10^{-8}\,\mathrm{W} \cdot \frac{I}{\mathrm{mA}} (Z + s_{Z1} Z^2 + s_{Z2} Z^3) \left(s_{E1} - \frac{E}{\mathrm{MeV}} + s_{E2} \left(\frac{E}{\mathrm{MeV}} \right)^2 \right) \\
\cdot \left(\frac{a}{\mathrm{mm}} - s_{a1} \right)^{-s_{a2}} \left(\frac{\varrho d}{\mathrm{\mu g\,cm^{-2}}} \frac{\mathrm{g\,mol^{-1}}}{M} + s_\varrho \left(\frac{\varrho d}{\mathrm{\mu g\,cm^{-2}}} \frac{\mathrm{g\,mol^{-1}}}{M} \right)^2 \right) \left(s_{\beta_*} + \frac{\beta_*}{\mathrm{cm}} \right),
\end{aligned}
$$

$$
\mathcal{L}_\mathrm{max} = \frac{3.200{\times}10^{36}\,\mathrm{cm^{-2}\,s^{-1}} \cdot P_\mathrm{loss,max}}{(Z + s_{Z1} Z^2 + s_{Z2} Z^3) \left(1 + s_\varrho \frac{\varrho d}{\mathrm{\mu g\,cm^{-2}}} \frac{\mathrm{g\,mol^{-1}}}{M} \right) \left(\frac{a}{\mathrm{mm}} - s_{a1} \right)^{-s_{a2}} \left(s_{E1} - \frac{E}{\mathrm{MeV}} + s_{E2} \left(\frac{E}{\mathrm{MeV}} \right)^2 \right) \left(s_{\beta_*} + \frac{\beta_*}{\mathrm{cm}} \right)} \tag{6.11}
$$

with the parameters in Table 6.9.

Table 6.9: Coefficients for Equation 6.11. s_{Ei} are calculated from the double pass mode values in Section 6.8

Coefficient	**Value**
s_{Z1}	1.355
s_{Z2}	0.007
s_ϱ	0.132
s_{a1}	3.669
s_{a2}	1.775
s_{E1}	62.15
s_{E2}	$4.600{\times}10^{-3}$
s_{β_*}	1151

The results in Chapter 8 suggest that the affordable loss power should be limited to $P_\mathrm{loss,max} = 100\,\mathrm{W}$. Figure 6.11 shows the luminosity limit for this case in dependence of Z. The corresponding values are given in Table 6.10. The luminosity limit is well above the nominal luminosity for the H and He targets with headroom of more than an order of magnitude. As the limit for the O target case only lies just above the nominal luminosity and considering that collimation will further contribute to losses, real operation is expected to require a reduction in target luminosity. This applies even more to Ar and Xe targets, where the limit is already exceeded by the nominal luminosity without additional collimator losses.

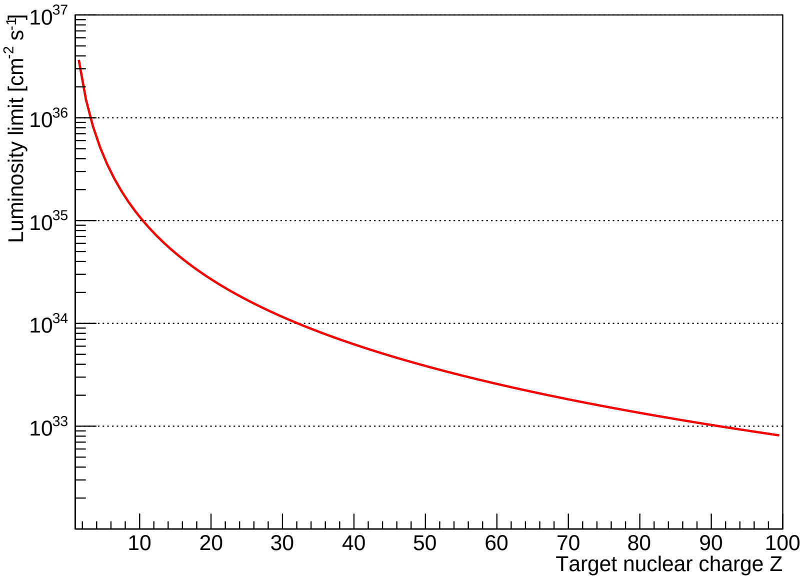

Figure 6.11: Luminosity limit in dependence of Z for $P_{\mathrm{loss,max}} = 100\,\mathrm{W}$. The areal particle density is $\varrho_{\mathrm{p}} = 10^{19}\,\mathrm{cm}^{-2}$.

Table 6.10: Luminosity limit values for Figure 6.11.

Target	$\mathcal{L}_{\mathbf{max}}$ [cm^{-2} s^{-1}]
H	7.039×10^{36}
He	2.224×10^{36}
O	1.690×10^{35}
Ar	3.332×10^{34}
Xe	3.236×10^{33}

6.11 Validity of the Obtained Behavior

It is a priori assumed that the amount of losses scales on variation of different parameters independently, i.e. when varying one parameter it doesn't affect how dependencies on other parameters behave. This is however not necessarily ensured. Especially the dependence on beam energy will affect which scattering processes will be dominant and how the halo is formed. The effect of target length is not explicitly investigated in this context, however impacts on the emittance degradation and halo formation are visible in Chapter 5 and when increasing the particle density of the target, i.e. the number of scatterers in the beam path. Some properties are assumed to be universally valid also for other ERL machines, like the aperture or target nuclear charge and density dependence. The interaction point beta dependence is however highly machine layout dependent and cannot be assumed to behave similar in other machines or even for different MESA lattice configurations. The same applies for the distribution of loss fractions along the machine lattice.

7 Halo Collimation

Halo transport and resulting beam losses were studied in Chapter 6. However, widely spread losses over the accelerator are undesirable during regular machine operation since they lead to high radiation levels and damages in the environment. The goal is to keep high loss rates in confined areas that also allow for simple shielding of radiation. The aforementioned confinement is ensured by insertion of collimators. Collimators are devices that intentionally limit the aperture at certain points and absorb particles with large offsets to ensure that the passing beam fits within the acceptance of following accelerator sections. Special requirements for electron beam collimators emerge from the low mass of the electron (i.e. large scattering angles) and the large amount of produced bremsstrahlung during the absorption process. The collimators must therefore exhibit a high stopping power for both electrons and photons to also absorb the bremsstrahlung emerging from electron stopping. This unavoidably leads to higher total losses as collimators intentionally intercept parts of the beam which otherwise may travel through the accelerator untouched. A reasonable compromise in the enhancement of total losses to the reduction in specific sections of the lattice is therefore sought for.

Suitable locations for collimator insertion are studied in this chapter, as well as impact of different collimator materials on loss distribution.

7.1 Collimation Requirements

The collimation set up should consist of a minimum set of collimators to be spatially and costly economical. Three stages are taken into account:

- Halo spoiler: to widen the halo distribution before collimation; allows for better separation from core and reduces power densities at the main collimator.
- Main collimator: absorbs the largest fraction of the halo.
- Second collimator: restricts the acceptance further and absorbs halo able to pass the main collimator, therefore enhancing machine protection.

Every stage consists of two subsequent jaw pairs with square aperture limiting the aperture on both sides for horizontal and vertical transverse directions. All three parts furthermore have different requirements to fulfil their function.

7.1.1 Halo Spoiler

The halo spoiler is the first collimation device in the setup. Both collimators are placed downstream from the spoiler. The spoiler should have low stopping power for electrons, since its function is only to scatter halo electrons and not absorb them. The spoiler should therefore be thin and should consist of a material with small nuclear charge Z and density ϱ. The length of the spoiler jaws is chosen to be 1 cm and the jaw material is beryllium ($Z = 4$).

7.1.2 Main Collimator

The main collimator is expected to be impacted by the largest fraction of the halo and consequently absorbs high power. The initially large angles of the scattered beam may translate into spatial offsets due to betatron oscillation and vice versa, so that a betatron phase shift φ_β of 90° (or $(2n+1)\cdot 90°$ respectively) relative to the target would be optimal to intercept particles at their largest excursion. It should be able to stop electrons and the emerging bremsstrahlung entirely and its location should be as close as possible to the MAGIX target to achieve as good as possible protection for parts in the vicinity of the target. It must therefore be long enough to do so and have a high stopping power. Since the proximity to the target also increases the amount of bremsstrahlung produced in the collimator that impacts MAGIX, suitable shielding must be ensured. The main collimator should be equipped with cooling to ensure sufficient heat transport and be shielded to minimize radiation in the environment. The length is chosen to be 10 cm. The behavior and suitability of different main collimator materials is studied and discussed in the following sections.

7.1.3 Second Collimator

The purpose of the second collimator is to intercept halo that passes the main collimator. It is therefore preferable to find a location with 90° betatron phase shift with respect to the main collimator in order to absorb the largest fraction of beam halo. Dimension and material requirements are shared with the main collimator.

7.2 Suitable Collimator Locations

After the basic requirements are identified, suitable locations for the different stages need to be found. The x- and y-jaws are placed so that a spacing of 10 cm is maintained in between.

7.2.1 Halo Spoiler and Main Collimator

Both parts should be placed as close as possible to the target. The straight section following the target is reserved for the experimental set up and considered unsuitable as spoilers and collimators may have large transverse dimensions that prohibit spectrometer movement. The next possible section is A2 after the bending magnet (see Figure 4.2 and Figure 6.1). The quadrupole triplet in the dispersive section between the bending magnets currently only utilizes the middle quadrupole. The outer quadrupoles can therefore be replaced by the halo spoiler and the main collimator. Collimator placement following the dipole is furthermore preferable since low energy electrons are deflected under larger angles and can be separated with better precision. Beam parameters at the chosen locations are summarized in Table 7.1. The position offers a nearly 90° y and a 270° x phase advance for the main collimator and is therefore considered to be a preferable position to place the first collimator. It is to be noted, that the achievable x beam sizes are fairly small so that an aperture of $10\sigma_x$ is equal to 0.72 mm at the spoiler and 0.66 mm at the collimator. An adjustment precision in the region of µm for the collimator jaws is desirable. It is however considered reasonable to achieve said precision regarding the micrometer resolution of commercially available step motors and the possibility to install levers to drive the jaws [Ledroit 2016, pp.68f].

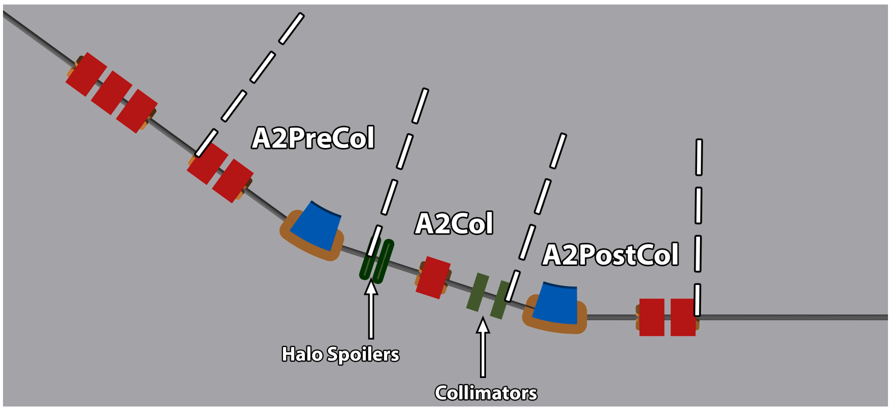

Figure 7.1: Halo spoiler and main collimator setup in A2. Outer quadrupoles of the triplet are replaced.

7.2.2 Second Collimator

The main requirement for the location of the second collimator is a betatron phase shift of 90° with respect to the main collimator. It is preferable to place this collimator also as close as possible to the main collimator to ensure that the largest part of the machine is protected. It is furthermore necessary to put the collimator in sections exclusively traversed by the peak energy beam, since it is not possible to separate beams in different recirculations in shared beam paths. As the separation magnets offer little space to place additional devices, the collimator is placed 2 m before the first separation magnet in the accelerator building (see Figure 4.2). Such a placement yields notably less than 90° phase advance w.r.t. the main collimator (see Table 7.1).

7.3 Collimator Aperture Setting

Once the collimators are placed, a suitable setting for the apertures has to be found. Too wide apertures can lead to poor collimation performance and machine protection while too narrow apertures on the other hand may damage the mostly intact core beam and lead to higher than necessary beam losses in and through additional scattering even outside the collimators. For this simulation series a tungsten main collimator is used

Table 7.1: Beam and collimator parameters at halo spoiler, main and second collimator locations for a nominal normalized emittance of 1.5 mm mrad. Due to variation, $\beta_{x,y}$ and $\sigma_{x,y}$ denote the largest value of the parameter over the length of the corresponding collimator jaws. $\varphi_{\beta,x,y}$ denote values w.r.t. the target. Collimator apertures are obtained from $10\sigma_{x,y}$.

Parameter	Description	Halo Spoiler	Main Collimator	Second Collimator
$\varphi_{\beta,x}$	x betatron phase shift	119.9°	248.9°	294.4°
$\varphi_{\beta,y}$	y betatron phase shift	89.6°	98.3°	115.2°
β_x	x beta (Twiss)	0.71 m	0.60 m	23.50 m
β_y	y beta (Twiss)	11.69 m	13.38 m	20.15 m
σ_x	x beam size	71.8 µm	66.2 µm	414.2 µm
σ_y	y beam size	292.1 µm	312.5 µm	383.6 µm
D_x	x dispersion	0.192 m	0.189 m	2.152×10^{-8} m
l	collimator jaw length	1 cm	10 cm	10 cm

and the apertures are varied in multiples n of two times the beam σ ($n\sigma$ single-sided around the beam center) at the collimator location for the different targets used at MAGIX. Dispersion is taken into account for aperture widths so that:

$$a_{\mathrm{col},x} = n \cdot 2(\sigma_x + D\sigma_E)$$
$$a_{\mathrm{col},y} = n \cdot 2\sigma_y$$

Results for H and Xe target induced halos are shown in Figure 7.2 and Figure 7.3. Figures for other targets are placed in Section A.2.

Losses are consistently governed by the collimator absorption and scattering effects except for the Xe target induced halo. This is concluded from the proportional behavior of the losses appearing in A2PostCol, M2 and T4S, which follow directly after the collimator section A2Col. The Xe target induced halo shows a different behavior as the losses in A2PostCol and M2 reach a maximum around $n = 8$ and do not vary as much as for other halos regarding relative loss fractions. For further studies the collimator width is chosen where the losses in the recirculation arcs T3 through T1 are attenuated by 90 % of the uncollimated value as summarized in Table 7.2. This criterion is a compromise between loss enhancement in T4 and loss reduction in other arcs. Inspection of loss behaviors for different target gases shows that collimator widths $a_{\mathrm{crit}} = n_{\mathrm{crit}} \cdot \sigma$ corresponding to this criterion increase with target Z. Here, the emittance cannot be calculated due to the removed beam core as described in Section 6.1. The emittance is however expected to be reduced notably by the collimator.

7.4 Collimator Material Study

After the collimator setup is defined, it is of interest which material is suitable for collimation. An overview over the materials used is given in Table 7.3.

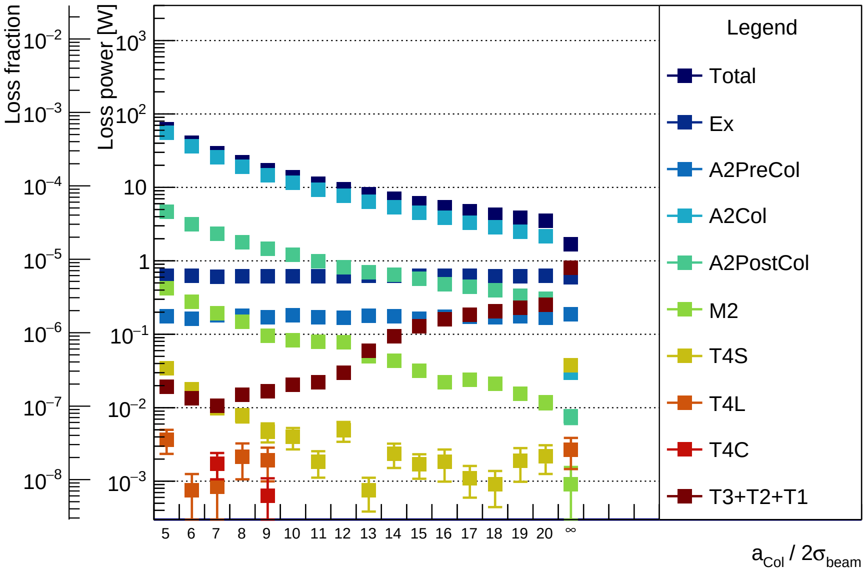

Figure 7.2: Collimator aperture sweep for a H target induced halo.

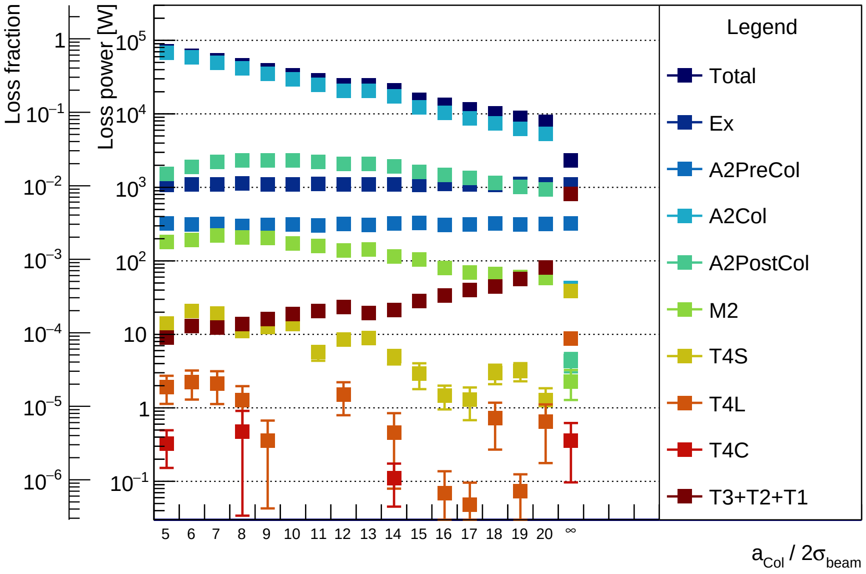

Figure 7.3: Collimator aperture sweep for a Xe target induced halo.

Figure 7.4 shows results for a Xe target induced halo and reveals a significant increase in total losses as the overall acceptance is restricted by the collimator compared to the uncollimated setup. Losses in sections A2PostCol, M2 and T4S directly downstream of

Table 7.2: Collimator widths that lead to a loss reduction of 90 % in T3 through T1 and emerging total loss values for different target induced halos.

Target	$n_{\textbf{crit,col}}$	$P_{\textbf{loss,total}}$ [W]	$P_{\textbf{loss,total}}/P_{\textbf{beam}}$
H	13	8.029±0.084	$(7.547\pm0.080)\times10^{-5}$
He	13	24.236±0.267	$(2.308\pm0.025)\times10^{-4}$
O	14	251.330±2.943	$(2.393\pm0.028)\times10^{-3}$
Ar	18	758.298±11.046	$(7.222\pm0.105)\times10^{-3}$
Xe	20	7824.320±76.726	$(7.452\pm0.073)\times10^{-2}$

Table 7.3: Properties of selected collimator materials. Nuclear charges and densities are according to the Geant4 material database. Stopping powers and CSDA ranges are taken from [Berger *et al.* 2020]. L_{rad} is calculated according to Equation 2.16 with molar masses taken from [Lide 2004, pp.1-12ff].

Parameter	**Description**	**Unit**	**Be**	**Graphite**	**Cu**	**W**
Z	Nuclear Charge	1	4	6	29	74
M	Molar Mass	$\mathrm{g\,mol^{-1}}$	9.012	12.011	63.546	183.840
ϱ	Mass Density	$\mathrm{g\,cm^{-3}}$	1.848	2.210	8.960	19.300
$S(105\,\mathrm{MeV})$	Stopping Power	$\mathrm{MeV\,cm^2\,g^{-1}}$	3.136	4.110	9.119	15.680
$L_{\mathrm{CSDA}}(100\,\mathrm{MeV})$	CSDA Range	$\mathrm{g\,cm^{-2}}$	4.524	37.350	25.910	19.600
$L_{\mathrm{CSDA}}\cdot\varrho^{-1}$		cm	2.448	16.900	2.892	1.016
L_{rad}	Radiation Length	$\mathrm{g\,cm^{-2}}$	65.001	43.007	13.161	6.766
$L_{\mathrm{rad}}\cdot\varrho^{-1}$		cm	35.174	19.460	1.468	0.351

the collimator are reduced with increasing collimator material nuclear charge. This is however not observed for the losses in T3 through T1, where the collimator material does not yield a difference in the amount of losses. This behavior is consistent among all studied TAILs, corresponding plots can be found in Section A.3. It is therefore preferable to use tungsten main collimators for the most efficient loss reduction outside the collimators.

7.5 Halo Spoiler Aperture Setting

Further simulations are conducted including the halo spoiler to investigate on how the spoiler can improve the collimation process. The collimator setups from Table 7.2 are used again for this purpose. The spoiler aperture is varied in the same manner as in the previous section in multiples n_{spoiler} of $\sigma_{\mathrm{spoiler}}$.

Figure 7.5 and Figure 7.6 show the aperture sweeps for a H and Xe target induced halo. Figures for other target induced halos are found in Section A.4. Total losses do not vary notably for $n_{\mathrm{spoiler}} \geq n_{\mathrm{crit,col}}$, while losses appearing in A2PostCol directly after the main collimator exhibit a significant reduction for $n_{\mathrm{spoiler}} = n_{\mathrm{crit,col}}$ with a fairly small increase in total losses $\Delta P_{\mathrm{loss,total}} = P_{\mathrm{loss,col+spoiler}} - P_{\mathrm{loss,col}}$ emerging from the additional spoiler losses. The Xe TAIL is an exception where the mentioned reduction takes place at $n_{\mathrm{spoiler}} = n_{\mathrm{crit,col}} - 2$, owing the largely distorted beam shape. When going

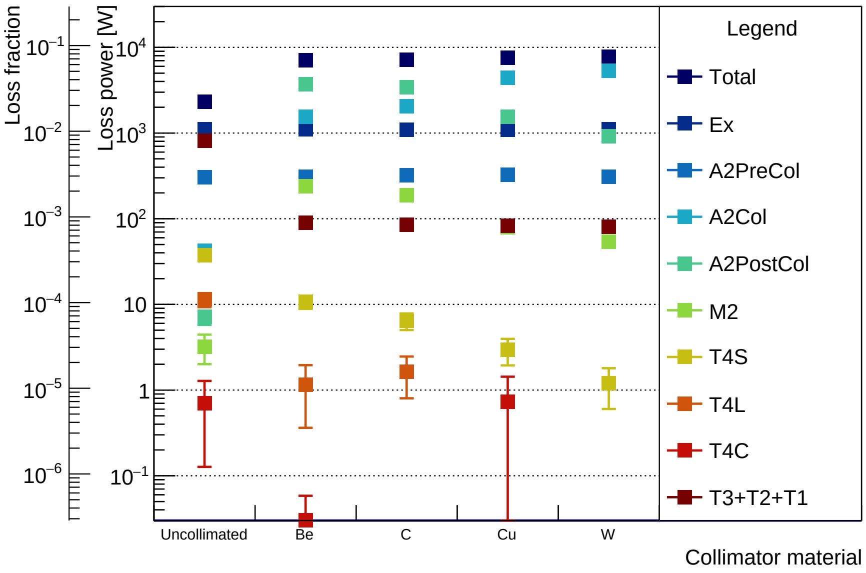

Figure 7.4: Power losses with only the main collimator intercepting beam halo after a Xe target for different main collimator materials.

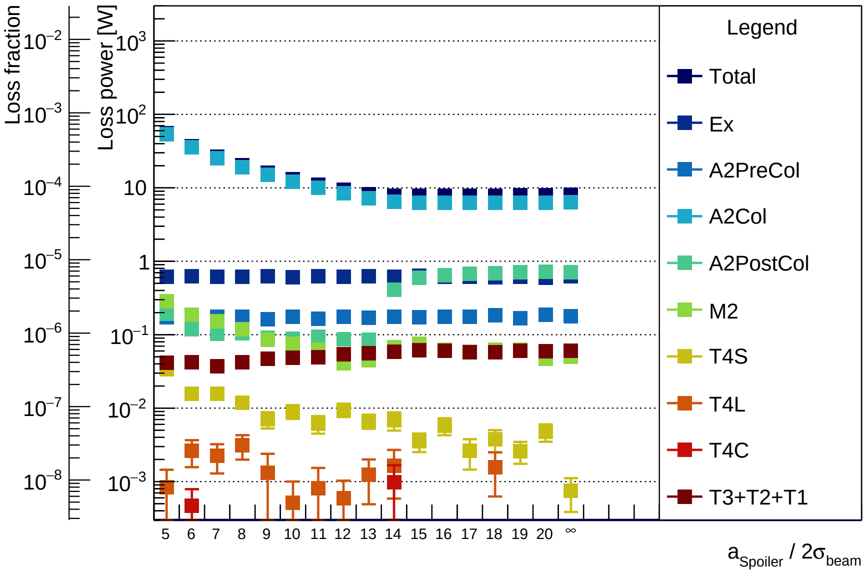

Figure 7.5: Spoiler aperture sweep for a H target induced halo.

to narrow spoiler apertures, the total losses increase as the spoiler limits the aperture in this case and results in an enhancement of losses in M2, whereas the reduction of losses

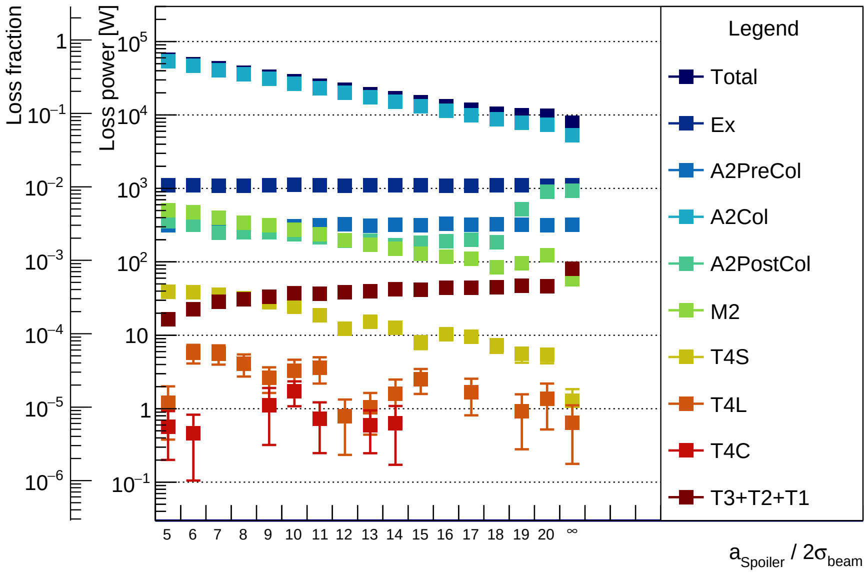

Figure 7.6: Spoiler aperture sweep for a Xe target induced halo.

in T3 through T1 is marginal. The working point of the spoiler aperture is therefore determined to be $n_{\text{spoiler}} = n_{\text{crit,col}}$ for TAILs except Xe, where it is $n_{\text{spoiler}} = n_{\text{crit,col}} - 2$. The values are summarized in Table 7.4.

Table 7.4: Maximum halo spoiler widths and total loss values for different target induced halos that lead to significant loss reduction in A2PostCol.

Target	$n_{\text{crit,spoiler}}$	$P_{\text{loss,total}}$ [W]	$P_{\text{loss,total}}/P_{\text{beam}}$	$\Delta P_{\text{loss,total}}/P_{\text{loss,col}}$ [%]
H	13	8.217±0.080	$(7.825\pm0.076)\times10^{-5}$	2.3
He	13	24.914±0.254	$(2.373\pm0.024)\times10^{-4}$	2.8
O	14	259.225±2.814	$(2.469\pm0.027)\times10^{-3}$	3.1
Ar	18	788.405±10.725	$(7.509\pm0.102)\times10^{-3}$	4.0
Xe	18	10 472.500±88.428	$(9.974\pm0.084)\times10^{-2}$	33.8

A summary of achievable luminosities for a 100 W power loss budget and a collimation setup with halo spoiler and main collimator is given in Table 7.5. Here it is especially visible that headroom of about an order of magnitude in losses for collimation is needed with respect to the luminosity limit in Equation 6.11. The 100 W loss limit is exceeded by the oxygen TAIL although the luminosity limit from Table 6.10 lies closely above the simulated luminosity. To ensure losses within the limit for Ar and Xe, the luminosity must effectively be reduced by factors 10^2 and $> 10^3$.

Table 7.5: Maximum achievable luminosities for a 100 W power loss budget and discussed halo spoiler and main collimator widths.

Target	$n_{\mathbf{spoiler}}$	$n_{\mathbf{col}}$	$\mathcal{L}_{\mathbf{max}}$ [$\mathrm{cm}^{-2}\,\mathrm{s}^{-1}$]
H	13	13	7.595×10^{35}
He	13	13	2.505×10^{35}
O	14	14	2.408×10^{34}
Ar	18	18	7.916×10^{33}
Xe	18	20	5.959×10^{32}

7.6 Second Collimator Aperture Setting

An additional improvement in machine protection can potentially be achieved with the second collimator. To look for effects, the previous setups are now expanded with the subsequent second collimator. The simulations are conducted for two scenarios:

- The main collimator enabled without halo spoiler; settings from Table 7.2 apply.
- The main collimator and halo spoiler enabled; settings from Table 7.4 apply.

The apertures are again varied through n_{2ndCol}. All figures for the simulations can be found in Section A.5. Figure 7.7 and Figure 7.8 show losses for different apertures and a H TAIL with and without halo spreader, respectively. Figure 7.9 and Figure 7.10 depict the same study for a Xe TAIL.

Overall losses are consistently dominated by the second collimator, greatly enhancing losses in M2. A significant reduction of losses in downstream sections can however not be observed, except for the arcs T3 through T1. Regarding the large additional losses in M2, the insertion of the second collimator is however not reasonably compensating these with reduction in other sections. The comparison of the scenarios with and without halo spoiler exhibits no mentionable difference in the efficiency of the second collimator. The most visible effect is the increase of losses in the upstream section A2PostCol and a reduction in A2Col when the halo spoiler is removed. Based on these observations a second collimator does not appear to be a suitable replacement for a halo spoiler, however it can be an additional protection measure during operation.

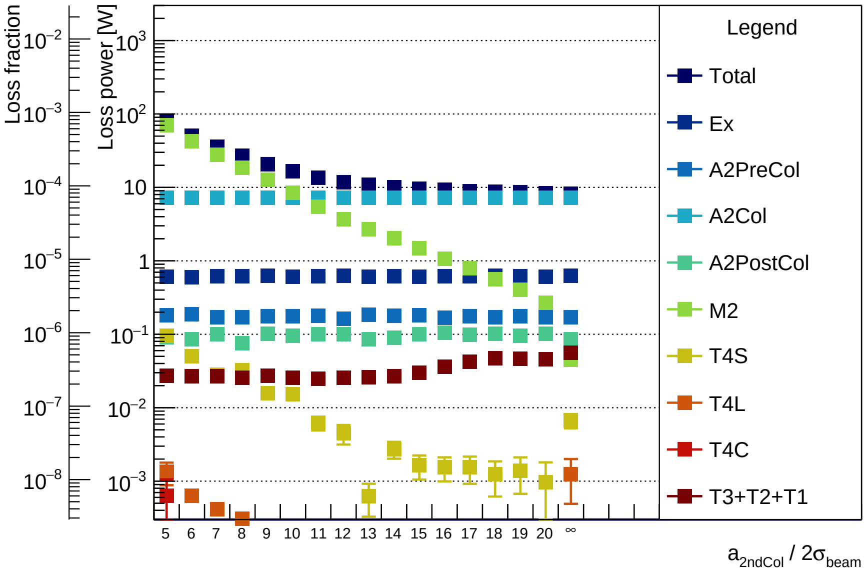

Figure 7.7: Aperture sweep of the second collimator with halo spoiler for a H target induced halo.

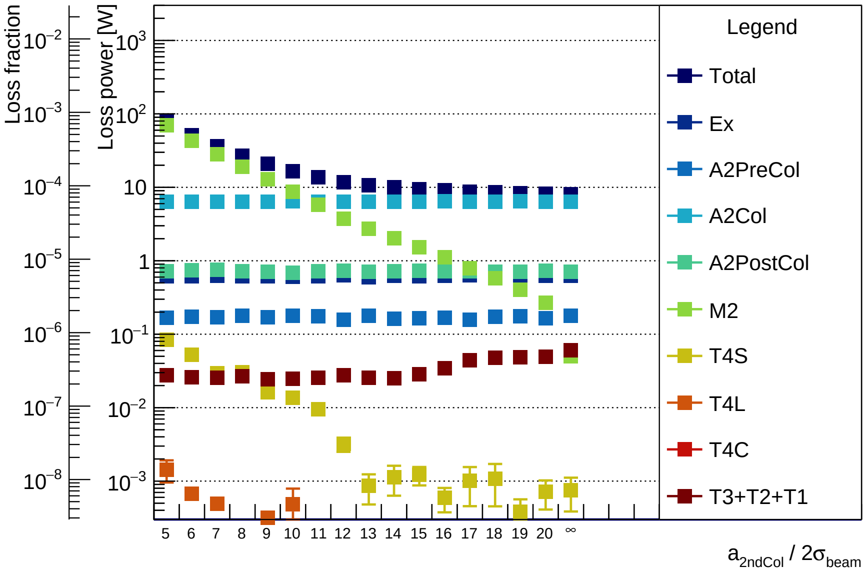

Figure 7.8: Aperture sweep of the second collimator without halo spoiler for a H target induced halo.

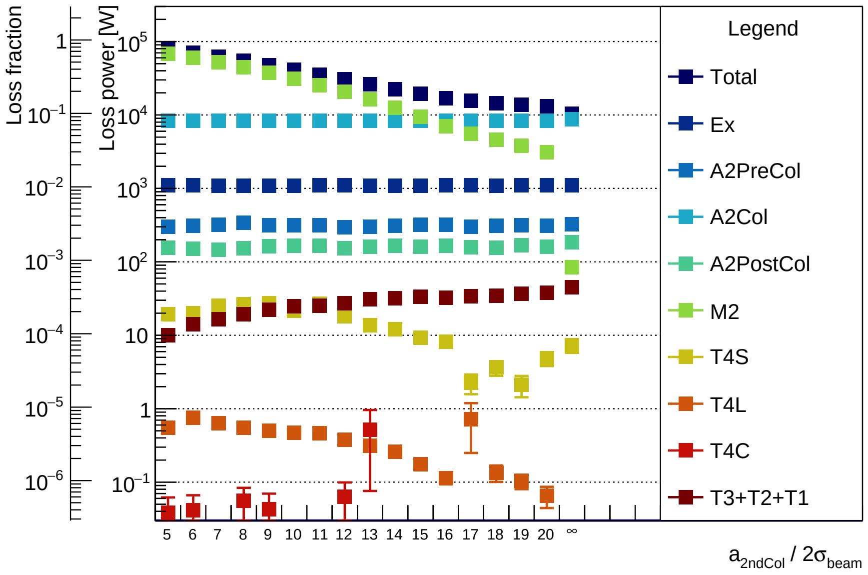

Figure 7.9: Aperture sweep of the second collimator with halo spoiler for a Xe target induced halo.

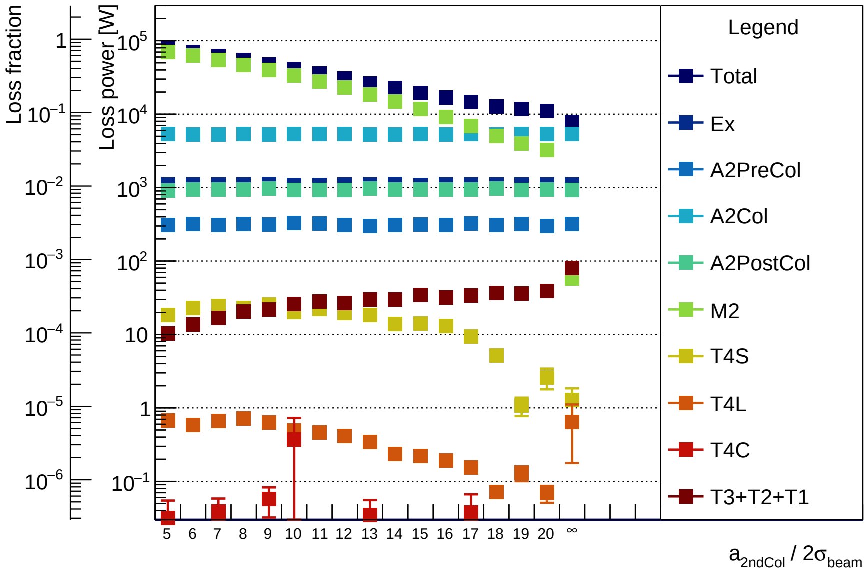

Figure 7.10: Aperture sweep of the second collimator without halo spoiler for a Xe target induced halo.

8 Radioactive Activation from Beam Losses

For the operation of MESA it is essential to estimate the accruing radiation dose during beam time through activation. The radioactive isotopes accumulate as long as beam losses are present and decay after machine shutdown. The isotope flavors and decay times are crucial for radiation safety regulations and dictate the cool down time until the area can be accessed. Simulations with FLUKA [Ferrari *et al.* 2005; Böhlen *et al.* 2014] are therefore conducted in [Diefenbach 2020b] and evaluated in this thesis. The simulation is split into two parts, one simulating the losses in the beam pipe directly after the target and one simulating the losses impacting the collimators directly. The collimator losses are taken from Chapter 7. The target is modelled as a 3 mm diameter cylinder filled with hydrogen and xenon, respectively, with the density matched to the prior simulated luminosity of $\mathcal{L} = 6.241 \times 10^{34}\,\mathrm{cm}^{-2}\,\mathrm{s}^{-1}$ to account for the two most extreme cases.

8.1 Assessment Criteria

The regulations foresee two categories of exposed personnel (§71, §137 StrlSchV, [Bundesamt für Strahlenschutz 2018]):

- Category A: Potentially exposed to $> 6\,\mathrm{mSv\,a^{-1}}$ and $< 20\,\mathrm{mSv\,a^{-1}}$
- Category B: Potentially exposed to $> 1\,\mathrm{mSv\,a^{-1}}$ and $< 6\,\mathrm{mSv\,a^{-1}}$

It has to be guaranteed, that the dose received by personnel with a respective classification does not exceed the maximum value for their category. To ensure this, the following assumptions are made [Diefenbach 2020a]:

- An experimental beam time has a duration of 2 weeks
- 6 hours of maintenance work have to be carried out in the experimental area between beam times
- Half of the year is available for MAGIX beam times with 2 weeks between beam times

These assumptions allow for 13 beam times and maintenance periods over a year. In order for a category B person to work without additional safety guidelines, it is then necessary to ensure that no dose greater than 0.46 mSv is received during a maintenance session. The isotopes with the highest abundance and their influence on the cool down time are in addition considered [Diefenbach 2020a].

8.2 Hydrogen Target

The experimental beam line model includes a model of the target as well as beam pipes and yokes before the following dipole. The beam is modelled as stated in Chapter 5. The H target is simulated in combination with aluminium and stainless steel beam pipes with materials taken from the library of FLUKA. Magnet yokes consist of pure iron. For the H target the simulated luminosity is well below the limit examined in the previous chapters.

8.2.1 Stainless Steel Beam Pipe

Figure 8.1 shows the evolution of the equivalent dose rates around the target beam line from the point of beam shutdown until 28 d after the shutdown. The dose rate decays to a value $< 10\,\mu\mathrm{Sv\,h^{-1}}$ in a 50 cm distance from the beam pipes in 1 h and partially takes $> 28\,\mathrm{d}$ to decay further to $< 1\,\mu\mathrm{Sv\,h^{-1}}$. The highest dose rate concentration accumulates directly before the dipole. It is visible, that the activity is accumulated in the stainless steel pipes, since less dose rate appears in the magnet yokes made of pure iron. Figure 8.2 reveals that the alloy elements of stainless steel are responsible for the accumulated dose rate. The isotope $^{51}_{24}\mathrm{Cr}$ (EC) remains with $> 5\times10^{7}$ Bq, while $^{48}_{23}\mathrm{V}$ (β^+), $^{54}_{25}\mathrm{Mn}$ (β^+), $^{55}_{26}\mathrm{Fe}$ (EC) and $^{57}_{27}\mathrm{Mn}$ (EC) expose between 1×10^{6} Bq and 1×10^{7} Bq for the whole time span. Not shown in Figure 8.2 is $^{3}_{1}\mathrm{H}$ (β^-) with $\sim 1\times10^{5}$ Bq from 0 s to 28 d after shutdown. These isotopes will accumulate further and consequently expose increasing dose rates over subsequent experimental periods. Decay modes are taken from [Lide 2004, pp.11-51ff]. Taking the aforementioned assumptions into account, working near the target beam line in the month after shutdown is advised to be conducted with special activity measurements and distance.

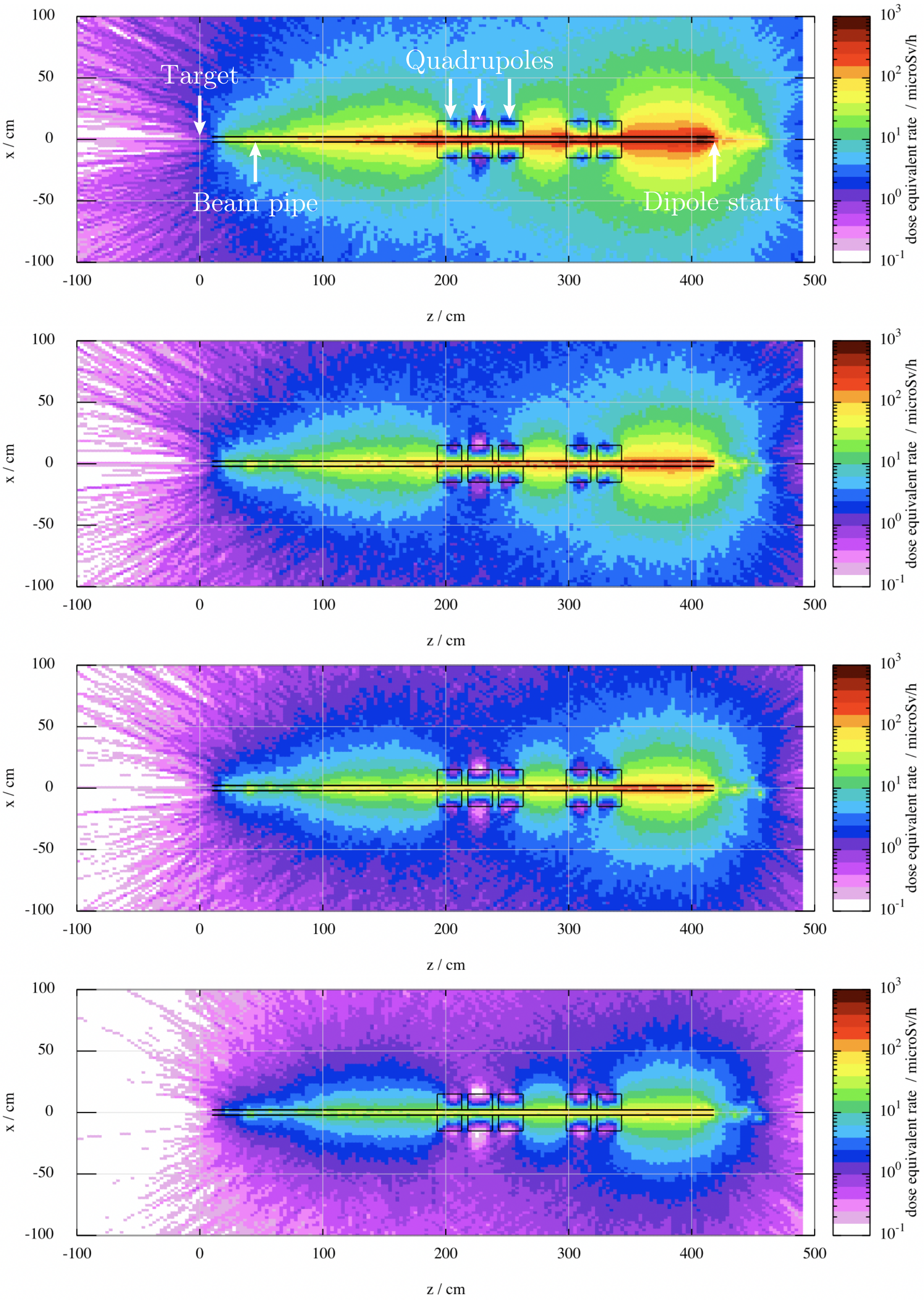

Figure 8.1: Top views of mean dose rates after the hydrogen target projected between $y = \pm 10\,\mathrm{cm}$ from the beam axis height. The beam pipe consists of stainless steel. From top to bottom: 0 s, 1 h, 1 d, 28 d after shutdown.

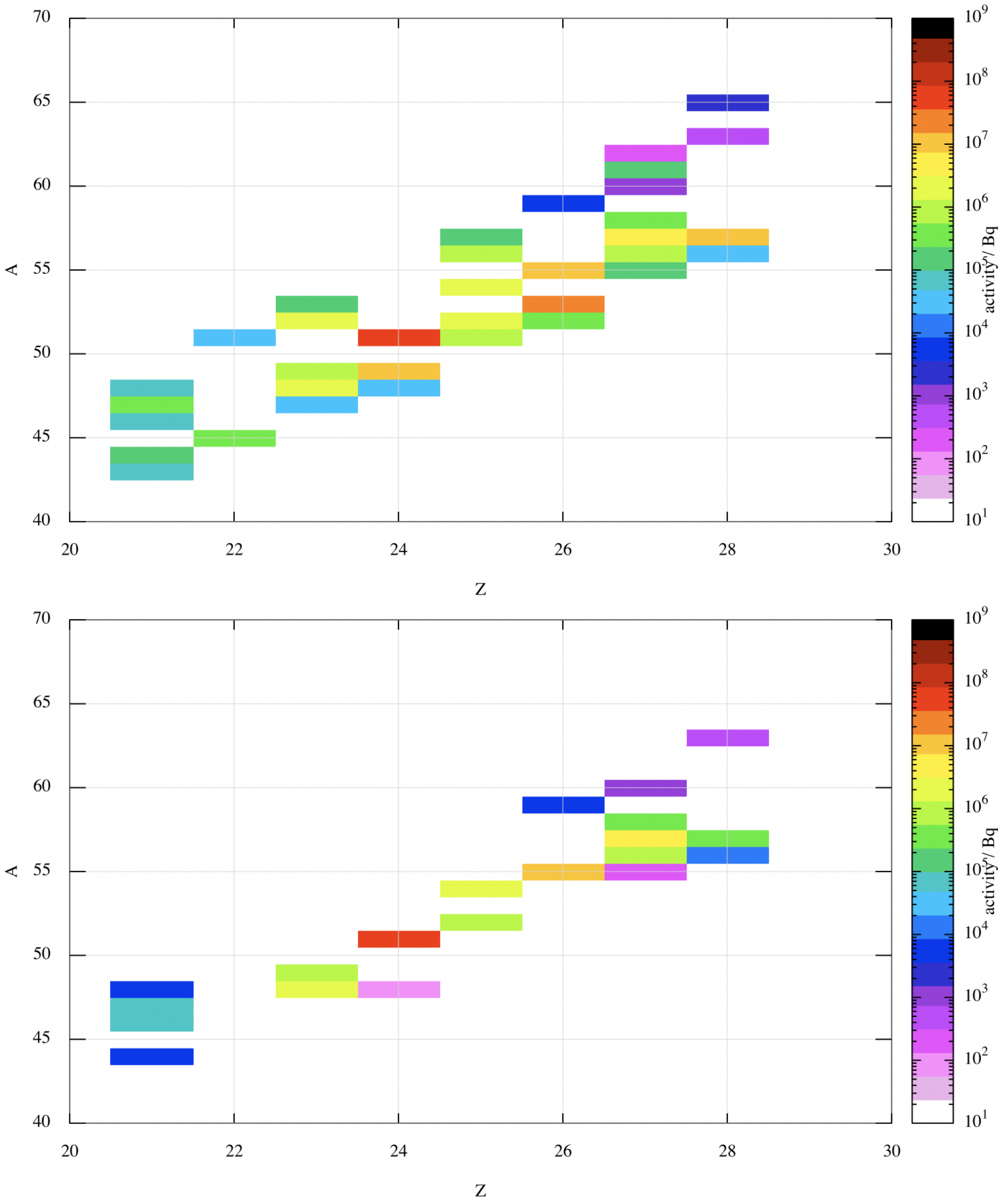

Figure 8.2: Isotopes produced in the stainless steel beam pipes after the MAGIX hydrogen target during beam time with atomic mass A and nuclear charge Z. From top to bottom: 0 s and 28 d after shutdown.

8.2.2 Aluminium Beam Pipe

The cooldown process of same scenario with aluminium beam pipes is depicted in Figure 8.3, where the dose rate decays orders of magnitudes faster compared to stainless steel beam pipes, so that a dose rate $< 10\,\mu\mathrm{Sv\,h^{-1}}$ 50 cm away from the beam pipe is reached in 1 h. Figure 8.6 shows that in total less isotopes are produced which expose high activities after 28 d. The highest activity after one month originates from $^{22}_{11}\mathrm{Na}$ (β^{+}) with $< 1{\times}10^{5}$ Bq. It is therefore preferable in terms of personnel radiation safety protection to install aluminium beam pipes at the target beam line.

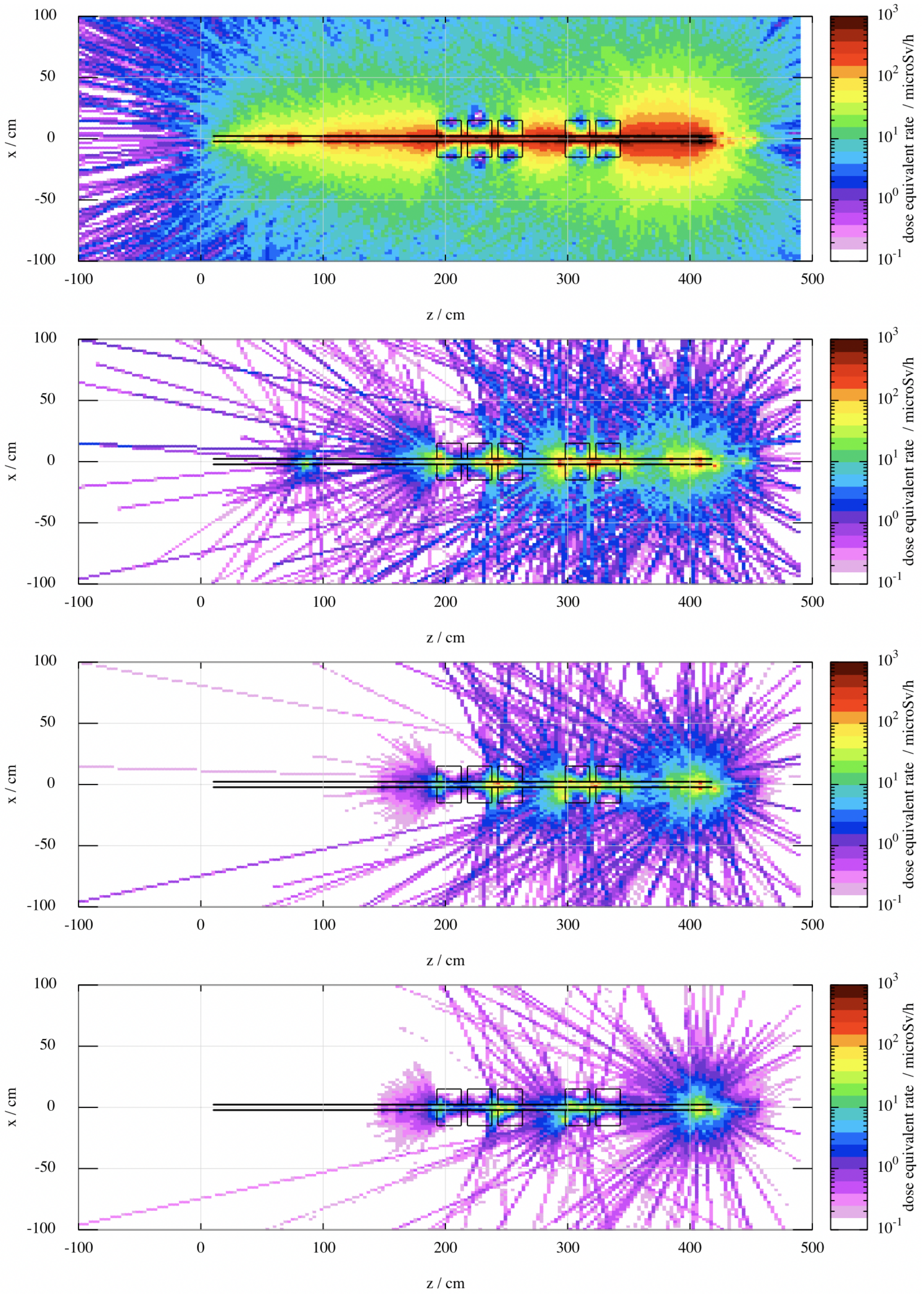

Figure 8.3: Top views of mean dose rates after the hydrogen target projected between $y = \pm 10\,\mathrm{cm}$ from the beam axis height. The beam pipe consists of aluminium. From top to bottom: 0 s, 1 h, 1 d, 28 d after shutdown.

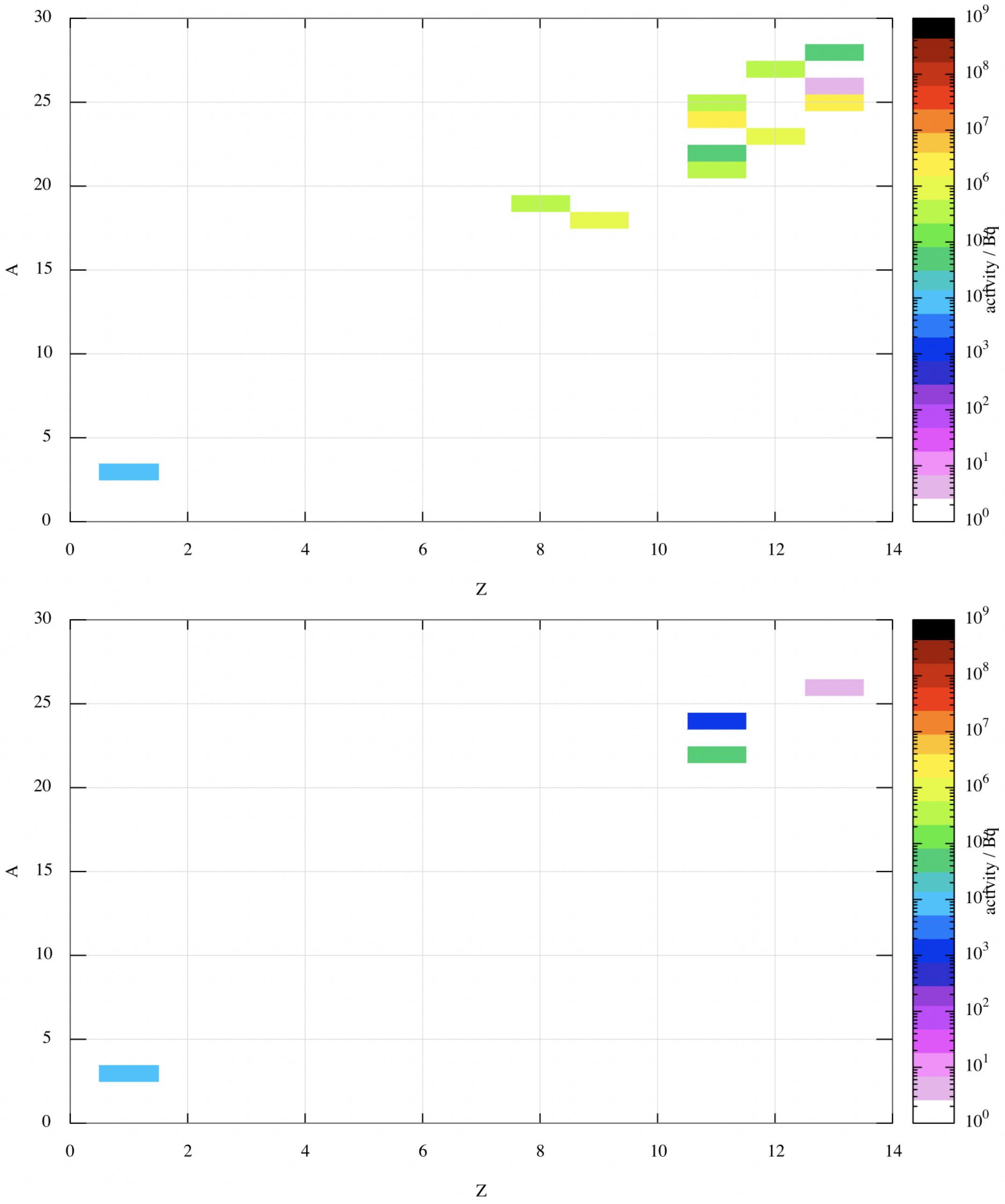

Figure 8.4: Isotopes produced in the aluminium beam pipes after the MAGIX hydrogen target during beam time with atomic mass A and nuclear charge Z. From top to bottom: 0 s and 28 d after shutdown.

8.2.3 Collimators

The FLUKA simulation of the collimator section is only conducted with stainless steel beam pipes. The model consists of halo spoilers and main collimators for horizontal and vertical directions with beam pipes between the dipoles. The coordinates of beam particles impinging the spoilers or collimators in Chapter 7 are exported to a CSV file, which is imported for input in this simulation. The beam pipe apertures are chosen large enough to enclose all collimators, which is a simplified resemblance of the future real enclosure through vacuum chambers. Figure 8.5 shows the cooldown process after 14 d beam time. The highest dose rates appear in the main collimators and decay by approximately one order of magnitude over a month. Considering the dose rates of $< 100\,\mu\mathrm{Sv\,h^{-1}}$ within 24 h directly at the beam pipe, this area must be accessed with special protection or in short time spans. The simulation input however considers only the electrons directly impacting the collimators, so that the beam pipe effectively displays a shielding in the simulation. The real dose rates are higher through direct activation of the beam pipes. Additional lead shielding can be installed to achieve smaller dose rates for personnel in the area. Furthermore it can be reasonably assumed that the collimators will not need frequent maintenance. The predominant activity in the x collimator emerges from the tungsten isotopes $^{185}_{74}\mathrm{W}$ (β^-, $\tau_{1/2} = 74.8\,\mathrm{d}$) and $^{185}_{74}\mathrm{W}$ (EC, $\tau_{1/2} = 121.2\,\mathrm{d}$) with $> 10^{11}\,\mathrm{Bq}$ and $^{177}_{74}\mathrm{W}$ (EC, $\tau_{1/2} = 2.21\,\mathrm{h}$) with $> 10^{10}\,\mathrm{Bq}$. The first two isotopes will accumulate over several beam times due to their half lives.

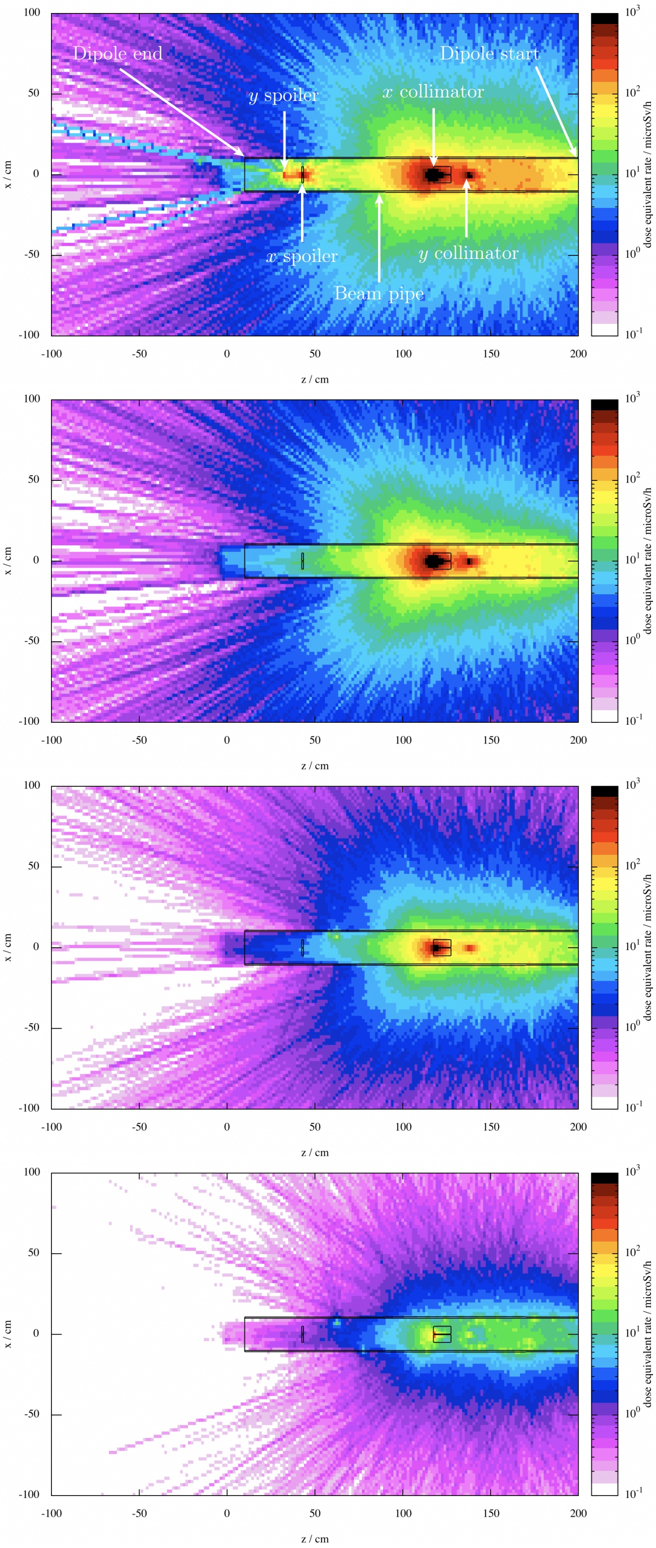

Figure 8.5: Top views of mean dose rates in the collimator section after the hydrogen target projected between $y = \pm 10\,\mathrm{cm}$ from the beam axis height. The beam pipe consists of stainless steel, the vertical spoiler and collimator are not drawn owing the chosen projection range. From top to bottom: 0 s, 1 h, 1 d, 28 d after shutdown.

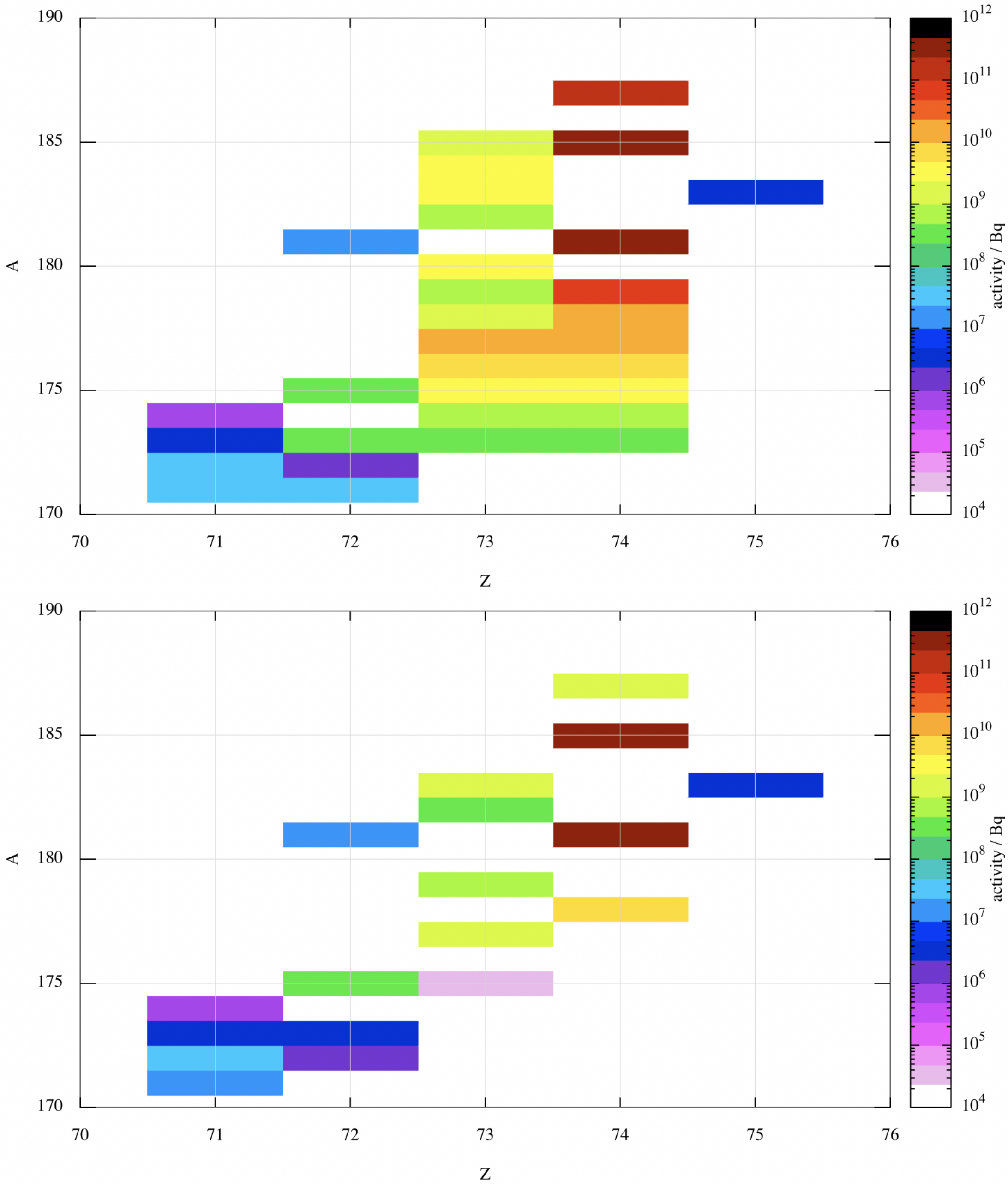

Figure 8.6: Isotopes produced in the x collimator after the MAGIX hydrogen target during beam time with atomic mass A and nuclear charge Z. From top to bottom: 0 s and 28 d after shutdown.

8.3 Xenon Target

The xenon target is simulated with the nominal particle density of $10^{19}\,\mathrm{cm}^{-2}$ and stainless steel beam pipes. The dose equivalent rates in the target beam line in Figure 8.7 and in the collimator section in Figure 8.8 exceed the tolerable range for any access by personnel even after 28 d. The dose equivalent rates in both sections must be reduced by two to three orders of magnitude to achieve a feasible operation scenario at MESA and show that a 100 W total loss limit as mentioned in the previous chapters, which for Xe is a reduction by a factor of $> 10^3$, is reasonable. As already mentioned in previous chapters, a suitable reduction of target density or beam current reduces losses and consequently radioactive activation for targets with high nuclear charges like xenon. Furthermore replacing the stainless steel beam pipes is preferable to lower the activity levels as seen in the previous section.

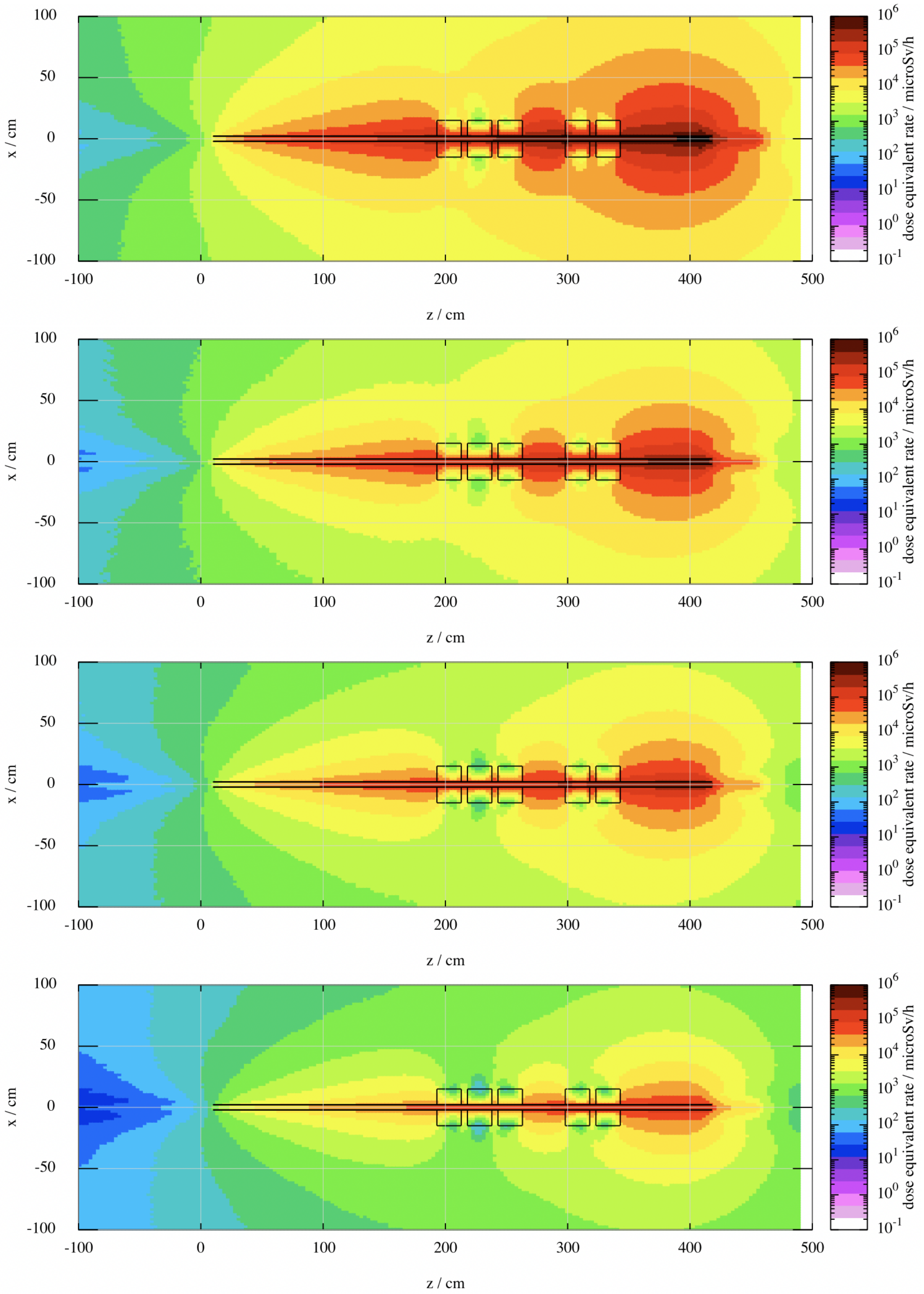

Figure 8.7: Top views of mean dose rates after the xenon target projected between $y = \pm 10$ cm from the beam axis height. The beam pipe consists of stainless steel. From top to bottom: 0 s, 1 h, 1 d, 28 d after shutdown.

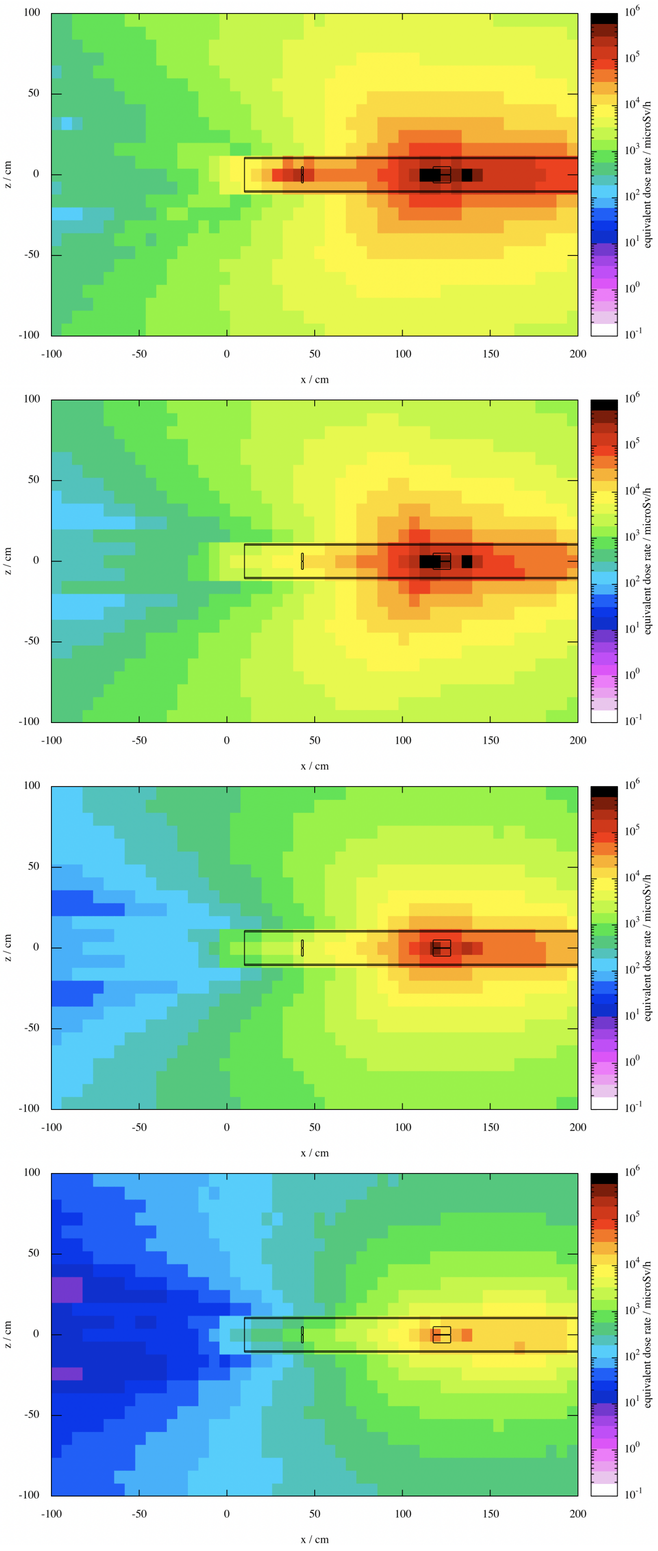

Figure 8.8: Top views of mean dose rates in the collimator section after the xenon target projected between $y = \pm 10\,\text{cm}$ from the beam axis height. The beam pipe consists of stainless steel, the vertical spoiler and collimator are not drawn owing the chosen projection range. From top to bottom: 0 s, 1 h, 1 d, 28 d after shutdown.

8.4 Discussion of Results

The two most extreme envisaged operation cases of using a hydrogen and xenon target are simulated in a simplistic model by [Diefenbach 2020b] and analyzed in this chapter. The results show that even though the operation of a hydrogen target with nominal conditions at MAGIX is possible, the radioactive activation of accelerator equipment through target induced halo must be examined and mitigated with special care. This is especially illustrated in the xenon target case, where nominal target conditions are not suitable for operation over relevant time periods. Considering that the simulated luminosity must be reduced by at least a factor of 10^3 in operation, the activity levels are expected to approach an order of magnitude comparable to the H target case. Furthermore, it is preferable to avoid alloys with large activation potential, such as stainless steel, for beam pipes. Aluminium beam pipes exhibit considerably less radioactive isotopes after beam times and their use is advised until the halo can be collimated in a controlled way in the collimator section. The intermediate cases with He, O and Ar targets and scenarios with modified target conditions still have to be investigated.

9 Summary

The simulations conducted in this thesis are aimed at a better understanding of the halo formation process through the use of internal gas targets in the MESA ERL mode as well as consequences for the maximum achievable luminosity and revealed the fundamental mechanisms important to the operation of MESA. The impacts of target induced halo on emittance degradation and resulting beam losses differ greatly in shape and intensity from the ones in storage rings and have to be carefully studied when establishing experiments like MAGIX. It must be noted that a physical internal target inherently puts limits on the maximum luminosity reasonably achievable with ERLs which cannot be avoided. The first crucial step in the design of an ERL target is therefore to choose suitable operation parameters like density, length, energy and a tailored interaction section of the accelerator. With the investigated set of said parameters, the systematics could be studied and it was shown that the halo formation is governed by single scattering events for light targets and that the multiple scattering regime must be avoided. While some of the systematics are expected to be reproducible at different accelerator facilities, especially the loss dependence on the Twiss functions requires dedicated investigations in a different layout. The investigation enabled provision of a luminosity limit estimation for the studied MESA layout. Furthermore, a reasonable tolerable loss power of 100 W was found and the results revealed that it is possible to operate MAGIX at MESA at the nominal luminosity $\mathcal{L} = 10^{35}\,\mathrm{cm}^{-2}\,\mathrm{s}^{-1}$ with sufficient loss headroom for the light target gases H and He. The results furthermore suggest that operation at slightly higher beam currents and luminosities than the envisaged is possible. For O, a maximum luminosity $\mathcal{L} = 10^{34}\,\mathrm{cm}^{-2}\,\mathrm{s}^{-1}$ is achievable, while for Ar and Xe target operation the luminosity must be further reduced to $\mathcal{L} = 10^{33}\,\mathrm{cm}^{-2}\,\mathrm{s}^{-1}$, respectively $\mathcal{L} = 10^{32}\,\mathrm{cm}^{-2}\,\mathrm{s}^{-1}$. Considering that either Ar or Xe will be operated for the search of dark matter, it is preferable from a beam dynamics point of view to choose Ar over Xe. This can however be relativized by the bremsstrahlung yield from the target for the experiment. Of note is that all scenarios assume an idealized target and a possible further reduction in achievable luminosity for a real target needs to be investigated. For protection of the accelerator equipment, a suitable collimation system was proposed that is capable of protecting downstream accelerator sections from beam losses without sacrificing critical fractions of beam power and hence ERL efficiency. In particular, it is favorable to use a combination of one main collimator and a preceding halo spoiler as close as possible to the target to protect large machine parts from TAIL losses and that advantages of this setup cannot be approximated through the establishment of several collimators along downstream sections in MESA.

10 Outlook

As mentioned in the beginning of this document, the layout of MESA has changed while the presented studies were conducted. Once the design of MAGIX and the corresponding MESA interaction region approaches a final design, the machine protection aspects discussed in this thesis need to be adapted to match the new requirements and peculiarities. In the course of this, deviations from the luminosity limit estimation through a change in TAIL systematics in the changed layout can be identified, which can be further utilized to improve and refine the limit estimation and to adapt it to a real target. Further manpower needs to be put into the development of the physical collimator system and proper shielding from the fundamental aspects discussed. Simultaneously, solid beam loss detection devices and radiation monitoring are necessary to experimentally verify the results obtained through simulation and to ensure machine and personnel radiation protection. As soon as MESA is commissioned and in operation, the models developed in this thesis can be verified.

11 Acknowledgements

We thankfully acknowledge funding for this thesis from the Deutsche Forschungsgesellschaft (DFG) through the Research Training Group 2128 “AccelencE” and the Helmholtz Institute Mainz. We further acknowledge the exchange on collimator design with the accelerator group of the Institute for Nuclear Physics at the Technical University Darmstadt and strong support on BDSIM related topics from the accelerator group of the John Adams Institute at the Royal Holloway University London.

A Appendix

A.1 Parameter Sweeps from Chapter 6

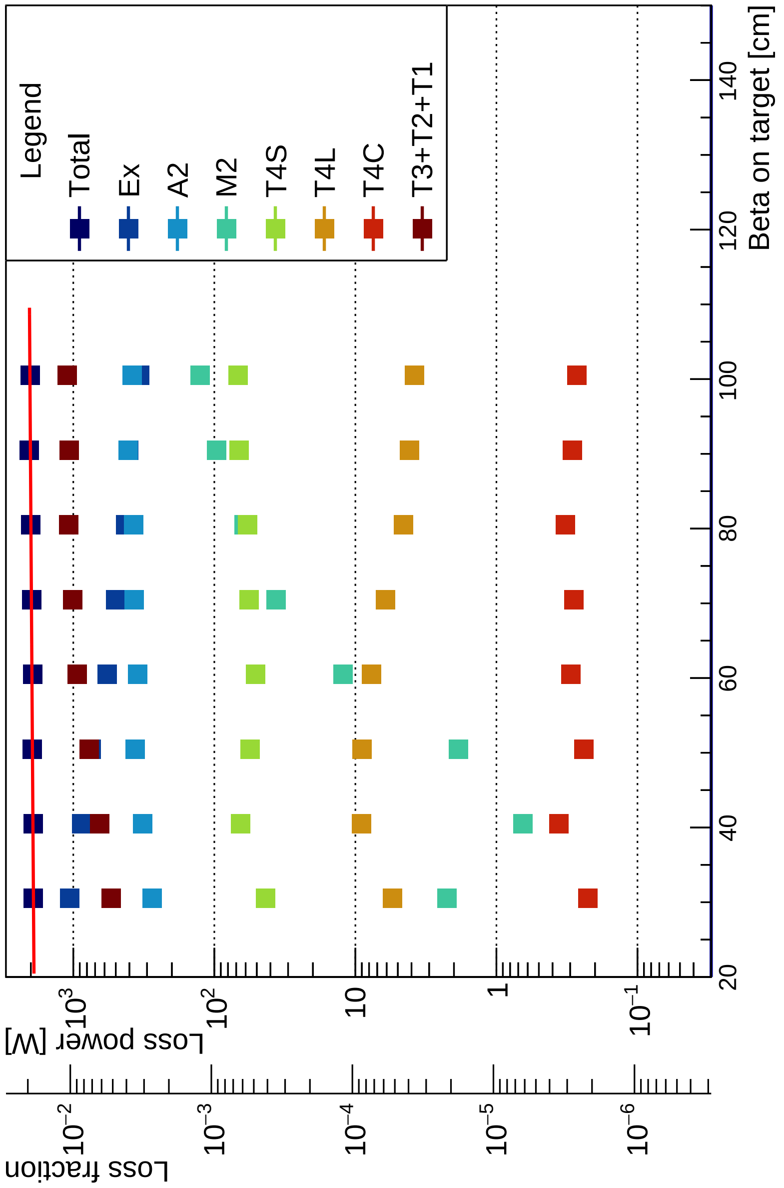

Figure A.1: Loss distributions and fit of total losses (red line) for different values of β_*.

Table A.1: Loss power numbers from the β_* sweep in Figure A.1.

β_* [cm]	**30**		**40**		**50**		**60**	
Section	P_{loss}[W]	ΔP_{loss}[W]	P_{loss}[W]	ΔP_{loss}[W]	P_{loss}[W]	ΔP_{loss}[W]	P_{loss}[W]	ΔP_{loss}[W]
Total	1.929×10^{3}	1.880	1.920×10^{3}	2.694	1.950×10^{3}	2.526	1.935×10^{3}	2.535
Ex	1.062×10^{3}	1.259	8.704×10^{2}	1.599	7.476×10^{2}	1.350	5.741×10^{2}	1.167
A2	2.769×10^{2}	5.478×10^{-1}	3.222×10^{2}	8.576×10^{-1}	3.633×10^{2}	8.471×10^{-1}	3.508×10^{2}	8.440×10^{-1}
M2	2.248	4.558×10^{-2}	6.515×10^{-1}	2.950×10^{-2}	1.864	5.407×10^{-2}	1.221×10^{1}	1.496×10^{-1}
T4S	4.321×10^{1}	1.858×10^{-1}	6.510×10^{1}	3.301×10^{-1}	5.566×10^{1}	2.801×10^{-1}	5.102×10^{1}	2.717×10^{-1}
T4L	5.477	7.225×10^{-2}	9.045	1.335×10^{-1}	8.980	1.235×10^{-1}	7.666	1.155×10^{-1}
T4C	2.249×10^{-1}	1.364×10^{-2}	3.610×10^{-1}	2.458×10^{-2}	2.401×10^{-1}	1.839×10^{-2}	2.960×10^{-1}	2.101×10^{-2}
T3+T2+T1	5.388×10^{2}	6.460×10^{-1}	6.519×10^{2}	1.083	7.719×10^{2}	1.154	9.387×10^{2}	1.366

β_* [cm]	**70**		**80**		**90**		**100**	
Section	P_{loss}[W]	ΔP_{loss}[W]	P_{loss}[W]	ΔP_{loss}[W]	P_{loss}[W]	ΔP_{loss}[W]	P_{loss}[W]	ΔP_{loss}[W]
Total	1.977×10^{3}	2.957	1.998×10^{3}	2.740	2.052×10^{3}	2.742	2.018×10^{3}	2.470
Ex	5.011×10^{2}	1.236	4.253×10^{2}	1.034	4.059×10^{2}	9.846×10^{-1}	3.383×10^{2}	8.111×10^{-1}
A2	3.687×10^{2}	1.001	3.720×10^{2}	9.291×10^{-1}	4.091×10^{2}	9.600×10^{-1}	3.812×10^{2}	8.445×10^{-1}
M2	3.655×10^{1}	3.079×10^{-1}	6.170×10^{1}	3.775×10^{-1}	9.667×10^{1}	4.696×10^{-1}	1.265×10^{2}	4.954×10^{-1}
T4S	5.649×10^{1}	3.259×10^{-1}	5.813×10^{1}	3.036×10^{-1}	6.672×10^{1}	3.167×10^{-1}	6.765×10^{1}	2.872×10^{-1}
T4L	6.110	1.177×10^{-1}	4.560	9.401×10^{-2}	4.145	8.772×10^{-2}	3.819	7.758×10^{-2}
T4C	2.827×10^{-1}	2.174×10^{-2}	3.254×10^{-1}	2.058×10^{-2}	2.896×10^{-1}	1.747×10^{-2}	2.684×10^{-1}	1.282×10^{-2}
T3+T2+T1	1.008×10^{3}	1.657	1.076×10^{3}	1.603	1.069×10^{3}	1.562	1.100×10^{3}	1.460

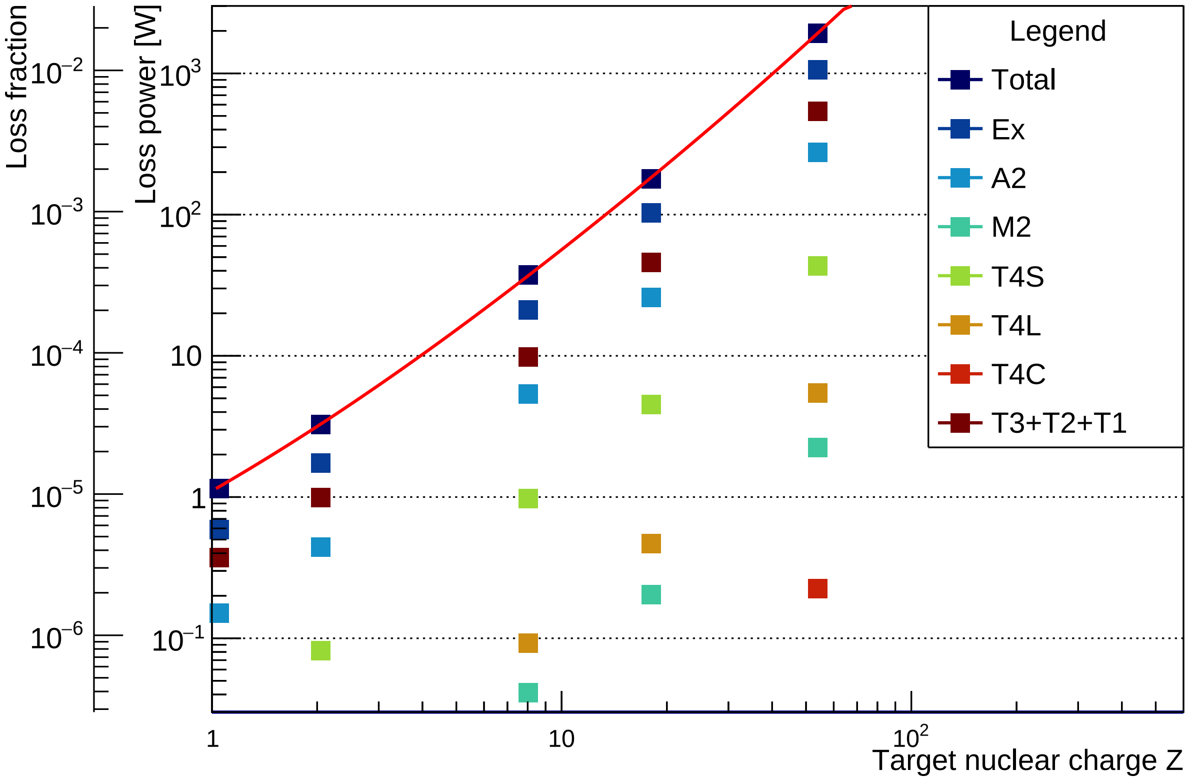

Figure A.2: Loss distributions and fit of total losses (red line) for H, He, O, Ar and Xe.

Table A.2: Loss power numbers from the target gas sweep in Figure A.2.

Target Gas	**H**		**He**		**O**		**Ar**		**Xe**	
Section	P_{loss}[W]	ΔP_{loss}[W]	P_{loss}[W]	ΔP_{loss}[W]	P_{loss}[W]	ΔP_{loss}[W]	P_{loss}[W]	ΔP_{loss}[W]	P_{loss}[W]	ΔP_{loss}[W]
Total	1.144	7.166×10^{-3}	3.264	1.214×10^{-2}	3.750×10^{1}	4.135×10^{-2}	1.795×10^{2}	2.339×10^{-1}	1.929×10^{3}	1.880
Ex	5.906×10^{-1}	4.605×10^{-3}	1.739	7.949×10^{-3}	2.116×10^{1}	2.805×10^{-2}	1.026×10^{2}	1.600×10^{-1}	1.062×10^{3}	1.259
A2	1.508×10^{-1}	1.978×10^{-3}	4.435×10^{-1}	3.403×10^{-3}	5.385	1.195×10^{-2}	2.586×10^{1}	6.787×10^{-2}	2.769×10^{2}	5.478×10^{-1}
M2	7.964×10^{-4}	1.319×10^{-4}	2.986×10^{-3}	2.576×10^{-4}	4.132×10^{-2}	9.567×10^{-4}	2.038×10^{-1}	5.541×10^{-3}	2.248	4.558×10^{-2}
T4S	2.858×10^{-2}	7.532×10^{-4}	8.188×10^{-2}	1.278×10^{-3}	9.776×10^{-1}	4.435×10^{-3}	4.533	2.462×10^{-2}	4.321×10^{1}	1.858×10^{-1}
T4L	1.263×10^{-3}	1.732×10^{-4}	6.168×10^{-3}	3.880×10^{-4}	9.262×10^{-2}	1.487×10^{-3}	4.667×10^{-1}	8.595×10^{-3}	5.477	7.225×10^{-2}
T4C	9.608×10^{-5}	3.384×10^{-5}	2.658×10^{-4}	7.443×10^{-5}	4.263×10^{-3}	2.994×10^{-4}	2.055×10^{-2}	1.620×10^{-3}	2.249×10^{-1}	1.364×10^{-2}
T3+T2+T1	3.721×10^{-1}	2.828×10^{-3}	9.901×10^{-1}	4.540×10^{-3}	9.841	1.380×10^{-2}	4.577×10^{1}	7.612×10^{-2}	5.388×10^{2}	6.460×10^{-1}

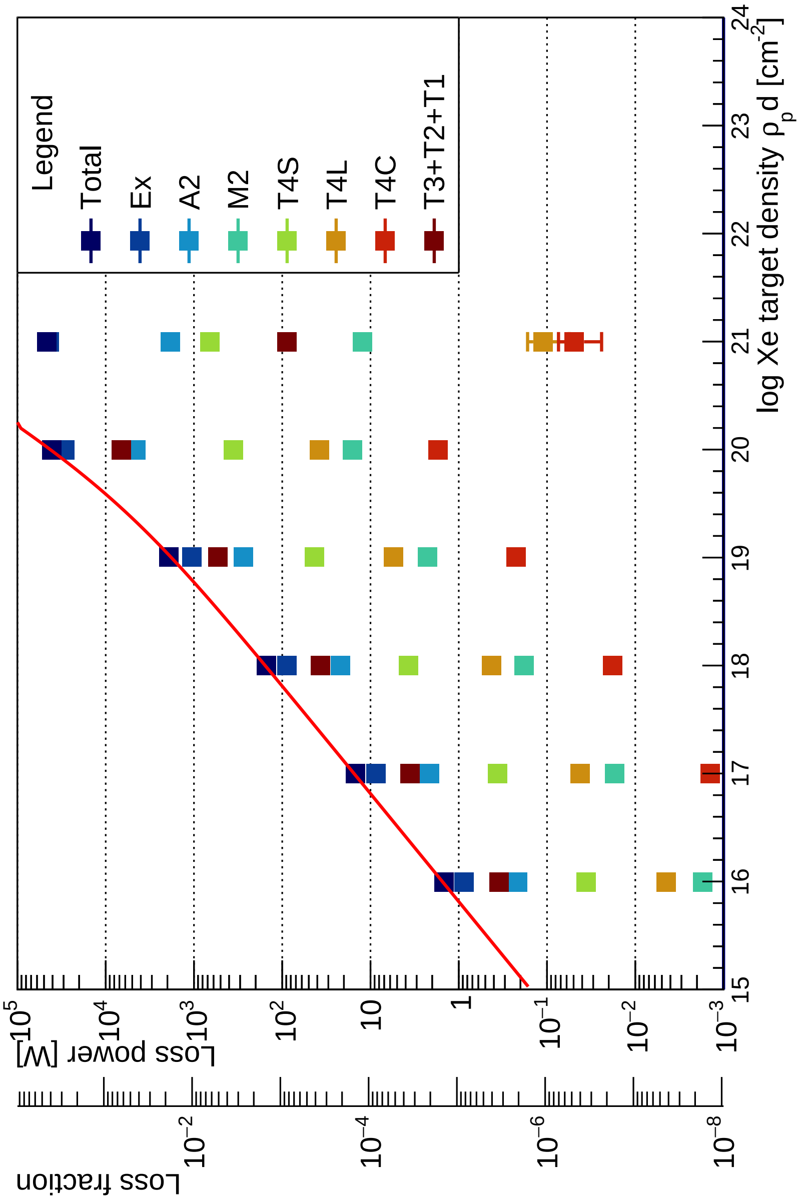

Figure A.3: Loss distributions and fit of total losses (red line) for Xe target particle densities of different orders of magnitude. $\varrho_\mathrm{p} = 10^{21}$ cm^{-2} is excluded from the fit.

Table A.3: Loss power numbers from the target density sweep in Figure A.3.

ϱ_p [cm^{-2}]	10^{16}		10^{17}		10^{18}		10^{19}		10^{20}		10^{21}	
Section	P_loss[W]	ΔP_loss[W]	P_loss[W]	ΔP_loss[W]	P_loss[W]	ΔP_loss[W]	P_loss[W]	ΔP_loss[W]	P_loss[W]	ΔP_loss[W]	P_loss[W]	ΔP_loss[W]
Total	1.473	8.223×10^{-3}	1.478×10^{1}	2.602×10^{-2}	1.513×10^{2}	1.862×10^{-1}	1.926×10^{3}	1.878	4.068×10^{4}	6.106×10^{1}	4.624×10^{4}	7.047×10^{1}
Ex	8.670×10^{-1}	5.719×10^{-3}	8.666	1.807×10^{-2}	8.820×10^{1}	1.289×10^{-1}	1.059×10^{3}	1.257	2.909×10^{4}	4.653×10^{1}	4.364×10^{4}	6.631×10^{1}
A2	2.142×10^{-1}	2.399×10^{-3}	2.134	7.539×10^{-3}	2.190×10^{1}	5.413×10^{-2}	2.782×10^{2}	5.490×10^{-1}	4.538×10^{3}	1.303×10^{1}	1.842×10^{3}	8.929
M2	1.725×10^{-3}	2.047×10^{-4}	1.723×10^{-2}	6.320×10^{-4}	1.811×10^{-1}	4.563×10^{-3}	2.235	4.538×10^{-2}	1.594×10^{1}	6.475×10^{-1}	1.235×10^{1}	4.207×10^{-1}
T4S	3.618×10^{-2}	8.487×10^{-4}	3.626×10^{-1}	2.694×10^{-3}	3.699	1.924×10^{-2}	4.268×10^{1}	1.848×10^{-1}	3.552×10^{2}	3.080	6.602×10^{2}	5.040
T4L	4.475×10^{-3}	3.335×10^{-4}	4.201×10^{-2}	9.990×10^{-4}	4.224×10^{-1}	7.100×10^{-3}	5.555	7.305×10^{-2}	3.784×10^{1}	1.105	1.111×10^{-1}	5.499×10^{-2}
T4C	5.056×10^{-5}	4.182×10^{-5}	1.420×10^{-3}	1.676×10^{-4}	1.806×10^{-2}	1.287×10^{-3}	2.477×10^{-1}	1.413×10^{-2}	1.723	2.188×10^{-1}	4.910×10^{-2}	2.501×10^{-2}
T3+T2+T1	3.493×10^{-1}	2.534×10^{-3}	3.558	8.110×10^{-3}	3.685×10^{1}	5.846×10^{-2}	5.384×10^{2}	6.454×10^{-1}	6.639×10^{3}	1.372×10^{1}	8.834×10^{1}	1.744

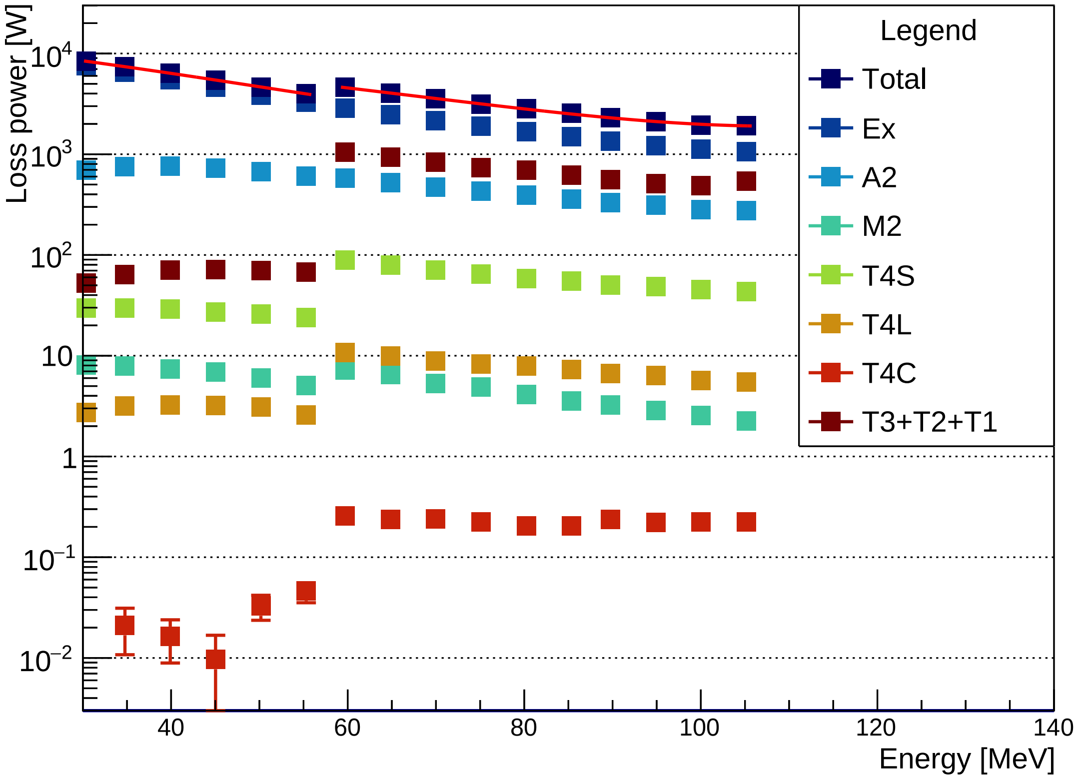

Figure A.4: Power loss distributions for different beam energies and piecewise fits (red lines) for single pass mode and double pass mode.

Table A.4: Loss power numbers from the beam energy sweep in Figure A.4.

E [MeV] **(Single Pass)**	**30**		**35**		**40**		**45**		**50**		**55**	
Section	P_{loss}[W]	ΔP_{loss}[W]	P_{loss}[W]	ΔP_{loss}[W]	P_{loss}[W]	ΔP_{loss}[W]	P_{loss}[W]	ΔP_{loss}[W]	P_{loss}[W]	ΔP_{loss}[W]	P_{loss}[W]	ΔP_{loss}[W]
Total	8.368×10^{3}	1.100×10^{1}	7.398×10^{3}	1.085×10^{1}	6.378×10^{3}	8.122	5.450×10^{3}	7.782	4.648×10^{3}	5.251	3.976×10^{3}	5.013
Ex	7.582×10^{3}	1.008×10^{1}	6.538×10^{3}	9.759	5.506×10^{3}	7.179	4.617×10^{3}	6.783	3.873×10^{3}	4.523	3.272×10^{3}	4.280
A2	6.930×10^{2}	2.241	7.552×10^{2}	2.494	7.608×10^{2}	2.049	7.248×10^{2}	2.098	6.697×10^{2}	1.486	6.054×10^{2}	1.465
M2	8.127	2.148×10^{-1}	7.886	2.233×10^{-1}	7.384	1.773×10^{-1}	6.872	1.786×10^{-1}	6.010	1.231×10^{-1}	5.083	1.178×10^{-1}
T4S	2.961×10^{1}	4.001×10^{-1}	2.973×10^{1}	4.238×10^{-1}	2.918×10^{1}	3.392×10^{-1}	2.706×10^{1}	3.413×10^{-1}	2.593×10^{1}	2.446×10^{-1}	2.402×10^{1}	2.433×10^{-1}
T4L	2.727	1.260×10^{-1}	3.162	1.418×10^{-1}	3.260	1.191×10^{-1}	3.220	1.241×10^{-1}	3.096	8.952×10^{-2}	2.585	8.463×10^{-2}
T4C	1.225×10^{-3}	5.673×10^{-4}	2.098×10^{-2}	1.021×10^{-2}	1.641×10^{-2}	7.501×10^{-3}	9.652×10^{-3}	7.147×10^{-3}	3.278×10^{-2}	9.120×10^{-3}	4.623×10^{-2}	1.090×10^{-2}
T3+T2+T1	5.263×10^{1}	4.167×10^{-1}	6.389×10^{1}	4.863×10^{-1}	7.114×10^{1}	4.168×10^{-1}	7.144×10^{1}	4.344×10^{-1}	7.009×10^{1}	3.167×10^{-1}	6.736×10^{1}	3.216×10^{-1}

E [MeV] **(Double Pass)**	**60**		**65**		**70**		**75**		**80**	
Section	P_{loss}[W]	ΔP_{loss}[W]	P_{loss}[W]	ΔP_{loss}[W]	P_{loss}[W]	ΔP_{loss}[W]	P_{loss}[W]	ΔP_{loss}[W]	P_{loss}[W]	ΔP_{loss}[W]
Total	4.610×10^{3}	5.423	4.032×10^{3}	5.204	3.545×10^{3}	4.085	3.141×10^{3}	3.942	2.830×10^{3}	3.314
Ex	2.877×10^{3}	3.878	2.480×10^{3}	3.693	2.157×10^{3}	2.881	1.895×10^{3}	2.767	1.676×10^{3}	2.301
A2	5.799×10^{2}	1.461	5.221×10^{2}	1.426	4.710×10^{2}	1.137	4.293×10^{2}	1.114	3.925×10^{2}	9.433×10^{-1}
M2	7.206	1.476×10^{-1}	6.474	1.442×10^{-1}	5.281	1.090×10^{-1}	4.876	1.084×10^{-1}	4.103	8.865×10^{-2}
T4S	8.944×10^{1}	4.951×10^{-1}	7.897×10^{1}	4.780×10^{-1}	7.071×10^{1}	3.784×10^{-1}	6.431×10^{1}	3.693×10^{-1}	5.829×10^{1}	3.100×10^{-1}
T4L	1.076×10^{1}	1.804×10^{-1}	9.895	1.777×10^{-1}	8.909	1.423×10^{-1}	8.311	1.410×10^{-1}	7.901	1.223×10^{-1}
T4C	2.571×10^{-1}	2.583×10^{-2}	2.359×10^{-1}	2.588×10^{-2}	2.405×10^{-1}	2.232×10^{-2}	2.242×10^{-1}	2.092×10^{-2}	2.055×10^{-1}	1.915×10^{-2}
T3+T2+T1	1.045×10^{3}	1.608	9.336×10^{2}	1.564	8.327×10^{2}	1.238	7.393×10^{2}	1.196	6.917×10^{2}	1.035

E [MeV] **(Double Pass)**	**85**		**90**		**95**		**100**		**105**	
Section	P_{loss}[W]	ΔP_{loss}[W]	P_{loss}[W]	ΔP_{loss}[W]	P_{loss}[W]	ΔP_{loss}[W]	P_{loss}[W]	ΔP_{loss}[W]	P_{loss}[W]	ΔP_{loss}[W]
Total	2.548×10^{3}	3.218	2.302×10^{3}	2.796	2.099×10^{3}	2.729	1.946×10^{3}	2.427	1.824×10^{3}	2.404
Ex	1.500×10^{3}	2.226	1.348×10^{3}	1.927	1.220×10^{3}	1.871	1.123×10^{3}	1.664	1.061×10^{3}	1.652
A2	3.593×10^{2}	9.219×10^{-1}	3.325×10^{2}	8.100×10^{-1}	3.118×10^{2}	8.020×10^{-1}	2.836×10^{2}	7.070×10^{-1}	2.782×10^{2}	7.136×10^{-1}
M2	3.536	8.368×10^{-2}	3.229	7.320×10^{-2}	2.853	7.013×10^{-2}	2.543	6.145×10^{-2}	2.153	5.708×10^{-2}
T4S	5.494×10^{1}	3.076×10^{-1}	5.054×10^{1}	2.694×10^{-1}	4.832×10^{1}	2.684×10^{-1}	4.514×10^{1}	2.413×10^{-1}	4.326×10^{1}	2.400×10^{-1}
T4L	7.320	1.208×10^{-1}	6.655	1.052×10^{-1}	6.354	1.057×10^{-1}	5.684	9.350×10^{-2}	5.792	9.627×10^{-2}
T4C	2.036×10^{-1}	1.901×10^{-2}	2.361×10^{-1}	1.877×10^{-2}	2.224×10^{-1}	1.807×10^{-2}	2.231×10^{-1}	1.699×10^{-2}	2.249×10^{-1}	1.757×10^{-2}
T3+T2+T1	6.223×10^{2}	1.004	5.611×10^{2}	8.709×10^{-1}	5.102×10^{2}	8.474×10^{-1}	4.853×10^{2}	7.654×10^{-1}	4.340×10^{2}	7.338×10^{-1}

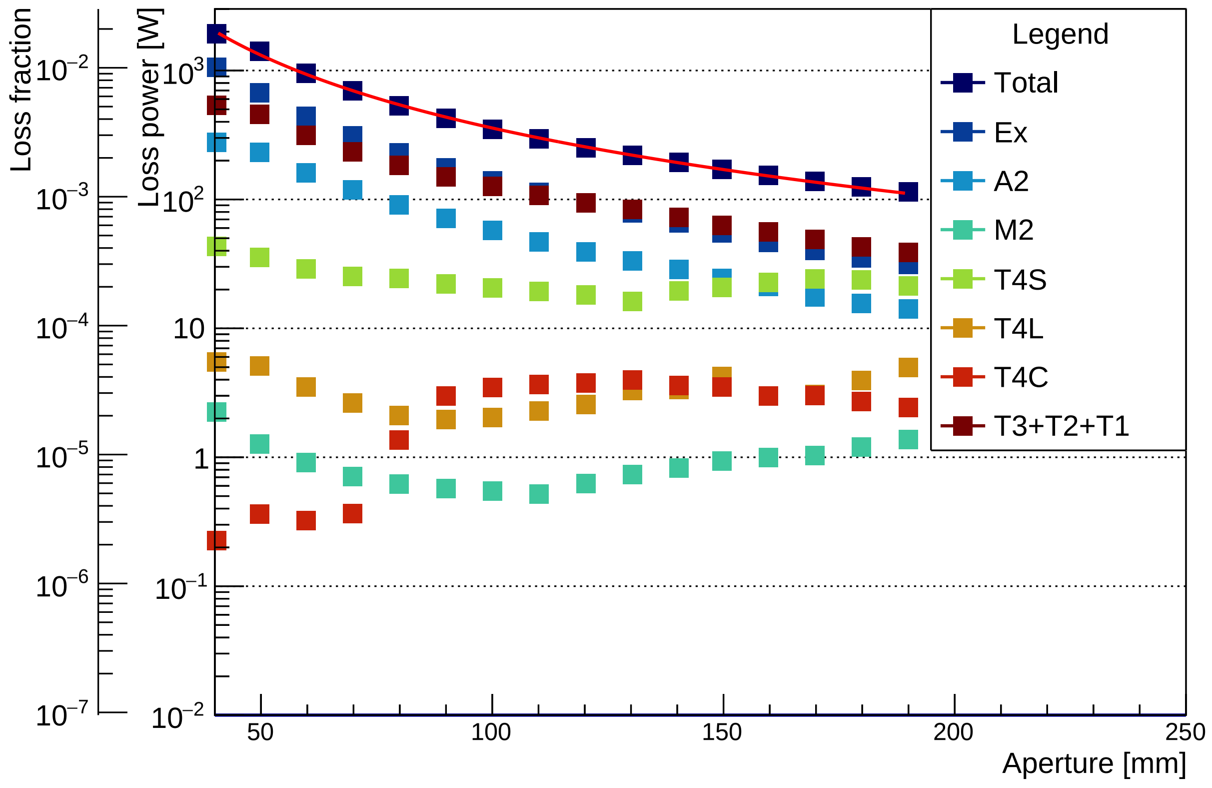

Figure A.5: Power loss distributions and fit (red line) for different beam pipe diameters.

Table A.5: Loss power numbers from beam pipe aperture sweep in Figure A.5.

a [mm]	**40**		**50**		**60**		**70**		**80**		**90**	
Section	P_{loss}[W]	ΔP_{loss}[W]	P_{loss}[W]	ΔP_{loss}[W]	P_{loss}[W]	ΔP_{loss}[W]	P_{loss}[W]	ΔP_{loss}[W]	P_{loss}[W]	ΔP_{loss}[W]	P_{loss}[W]	ΔP_{loss}[W]
Total	1.929×10^{3}	1.880	1.404×10^{3}	1.471	9.524×10^{2}	1.109	6.934×10^{2}	8.883×10^{-1}	5.333×10^{2}	7.439×10^{-1}	4.255×10^{2}	6.408×10^{-1}
Ex	1.062×10^{3}	1.259	6.711×10^{2}	9.392×10^{-1}	4.427×10^{2}	7.278×10^{-1}	3.113×10^{2}	5.911×10^{-1}	2.303×10^{2}	4.971×10^{-1}	1.763×10^{2}	4.281×10^{-1}
A2	2.769×10^{2}	5.478×10^{-1}	2.327×10^{2}	4.876×10^{-1}	1.611×10^{2}	3.918×10^{-1}	1.189×10^{2}	3.272×10^{-1}	9.082×10^{1}	2.792×10^{-1}	7.159×10^{1}	2.423×10^{-1}
M2	2.248	4.558×10^{-2}	1.269	3.459×10^{-2}	9.075×10^{-1}	2.905×10^{-2}	7.070×10^{-1}	2.550×10^{-2}	6.183×10^{-1}	2.363×10^{-2}	5.697×10^{-1}	2.233×10^{-2}
T4S	4.321×10^{1}	1.858×10^{-1}	3.549×10^{1}	1.685×10^{-1}	2.894×10^{1}	1.509×10^{-1}	2.525×10^{1}	1.391×10^{-1}	2.431×10^{1}	1.360×10^{-1}	2.212×10^{1}	1.289×10^{-1}
T4L	5.477	7.225×10^{-2}	5.112	7.026×10^{-2}	3.510	5.772×10^{-2}	2.629	4.954×10^{-2}	2.107	4.386×10^{-2}	1.960	4.258×10^{-2}
T4C	2.249×10^{-1}	1.364×10^{-2}	3.610×10^{-1}	1.662×10^{-2}	3.229×10^{-1}	1.581×10^{-2}	3.652×10^{-1}	1.645×10^{-2}	1.361	3.397×10^{-2}	2.990	4.984×10^{-2}
T3+T2+T1	5.388×10^{2}	6.460×10^{-1}	4.578×10^{2}	5.808×10^{-1}	3.150×10^{2}	4.547×10^{-1}	2.342×10^{2}	3.764×10^{-1}	1.837×10^{2}	3.243×10^{-1}	1.499×10^{2}	2.864×10^{-1}

a [mm]	**100**		**110**		**120**		**130**		**140**		**150**	
Section	P_{loss}[W]	ΔP_{loss}[W]	P_{loss}[W]	ΔP_{loss}[W]	P_{loss}[W]	ΔP_{loss}[W]	P_{loss}[W]	ΔP_{loss}[W]	P_{loss}[W]	ΔP_{loss}[W]	P_{loss}[W]	ΔP_{loss}[W]
Total	3.501×10^{2}	5.645×10^{-1}	2.940×10^{2}	5.047×10^{-1}	2.523×10^{2}	4.583×10^{-1}	2.197×10^{2}	4.216×10^{-1}	1.941×10^{2}	3.925×10^{-1}	1.716×10^{2}	3.635×10^{-1}
Ex	1.399×10^{2}	3.766×10^{-1}	1.133×10^{2}	3.352×10^{-1}	9.367×10^{1}	3.017×10^{-1}	7.849×10^{1}	2.743×10^{-1}	6.577×10^{1}	2.492×10^{-1}	5.506×10^{1}	2.247×10^{-1}
A2	5.775×10^{1}	2.139×10^{-1}	4.691×10^{1}	1.894×10^{-1}	3.908×10^{1}	1.702×10^{-1}	3.331×10^{1}	1.548×10^{-1}	2.866×10^{1}	1.420×10^{-1}	2.432×10^{1}	1.281×10^{-1}
M2	5.472×10^{-1}	2.157×10^{-2}	5.207×10^{-1}	2.090×10^{-2}	6.266×10^{-1}	2.291×10^{-2}	7.346×10^{-1}	2.411×10^{-2}	8.267×10^{-1}	2.472×10^{-2}	9.354×10^{-1}	2.631×10^{-2}
T4S	2.055×10^{1}	1.224×10^{-1}	1.934×10^{1}	1.190×10^{-1}	1.820×10^{1}	1.155×10^{-1}	1.612×10^{1}	1.111×10^{-1}	1.944×10^{1}	1.282×10^{-1}	2.071×10^{1}	1.322×10^{-1}
T4L	2.035	4.295×10^{-2}	2.279	4.502×10^{-2}	2.566	4.752×10^{-2}	3.285	5.347×10^{-2}	3.356	5.317×10^{-2}	4.221	5.897×10^{-2}
T4C	3.483	5.310×10^{-2}	3.659	5.436×10^{-2}	3.766	5.438×10^{-2}	3.962	5.553×10^{-2}	3.609	5.256×10^{-2}	3.509	5.162×10^{-2}
T3+T2+T1	1.258×10^{2}	2.577×10^{-1}	1.080×10^{2}	2.349×10^{-1}	9.443×10^{1}	2.175×10^{-1}	8.384×10^{1}	2.040×10^{-1}	7.244×10^{1}	1.866×10^{-1}	6.285×10^{1}	1.717×10^{-1}

a [mm]	**160**		**170**		**180**		**190**	
Section	P_{loss}[W]	ΔP_{loss}[W]	P_{loss}[W]	ΔP_{loss}[W]	P_{loss}[W]	ΔP_{loss}[W]	P_{loss}[W]	ΔP_{loss}[W]
Total	1.535×10^{2}	3.383×10^{-1}	1.381×10^{2}	3.153×10^{-1}	1.248×10^{2}	2.943×10^{-1}	1.144×10^{2}	2.754×10^{-1}
Ex	4.660×10^{1}	2.047×10^{-1}	4.021×10^{1}	1.874×10^{-1}	3.504×10^{1}	1.713×10^{-1}	3.136×10^{1}	1.588×10^{-1}
A2	2.106×10^{1}	1.158×10^{-1}	1.754×10^{1}	1.026×10^{-1}	1.555×10^{1}	9.518×10^{-2}	1.416×10^{1}	8.863×10^{-2}
M2	9.988×10^{-1}	2.740×10^{-2}	1.028	2.746×10^{-2}	1.197	2.908×10^{-2}	1.375	3.114×10^{-2}
T4S	2.266×10^{1}	1.363×10^{-1}	2.414×10^{1}	1.376×10^{-1}	2.366×10^{1}	1.324×10^{-1}	2.137×10^{1}	1.189×10^{-1}
T4L	2.978	4.856×10^{-2}	3.072	4.807×10^{-2}	3.944	5.543×10^{-2}	4.991	6.217×10^{-2}
T4C	2.991	4.748×10^{-2}	3.005	4.596×10^{-2}	2.701	4.271×10^{-2}	2.436	3.874×10^{-2}
T3+T2+T1	5.620×10^{1}	1.612×10^{-1}	4.913×10^{1}	1.487×10^{-1}	4.272×10^{1}	1.368×10^{-1}	3.868×10^{1}	1.304×10^{-1}

A.2 Main Collimator Aperture Sweeps

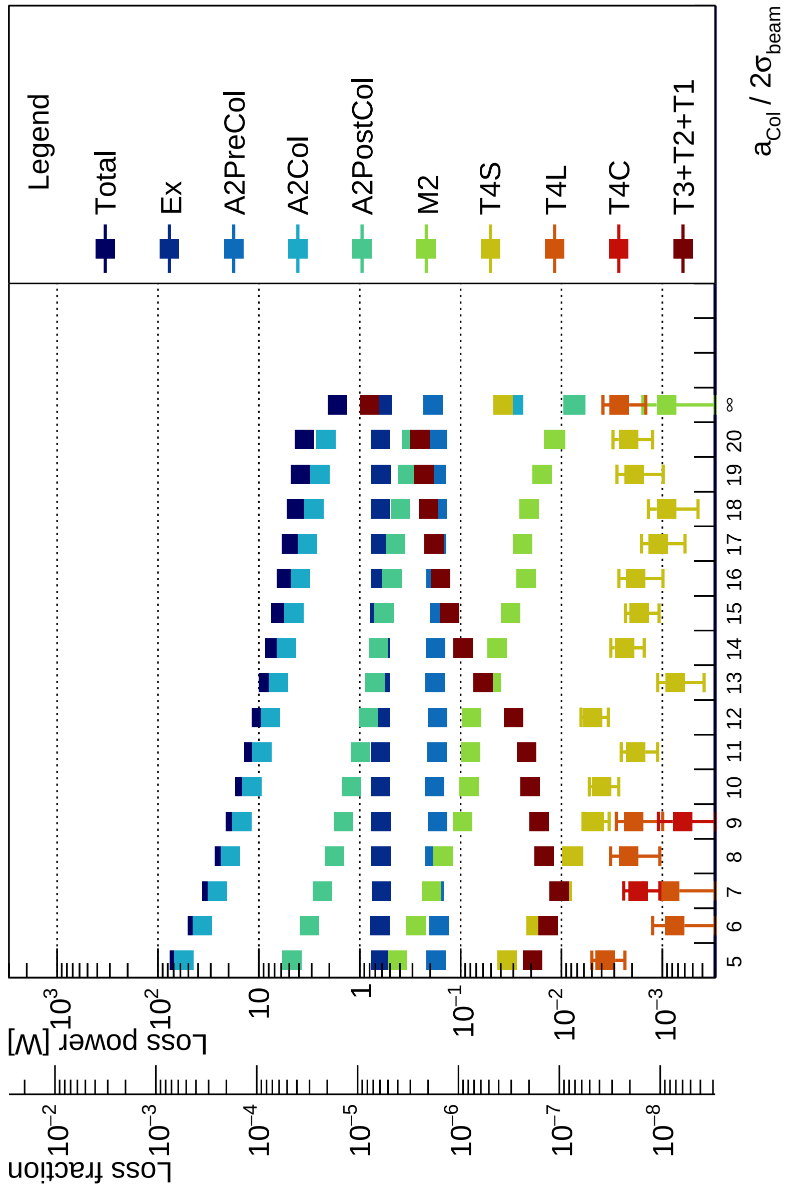

Figure A.6: Main collimator aperture sweep for a H target induced halo.

Table A.6: Loss power numbers from H TAIL main collimator aperture sweep in Figure A.6.

$\frac{a_{\text{Col}}}{2\sigma_{\text{beam}}}$	**5**		**6**		**7**		**8**		**9**		**10**	
Section	P_{loss}[W]	ΔP_{loss}[W]	P_{loss}[W]	ΔP_{loss}[W]	P_{loss}[W]	ΔP_{loss}[W]	P_{loss}[W]	ΔP_{loss}[W]	P_{loss}[W]	ΔP_{loss}[W]	P_{loss}[W]	ΔP_{loss}[W]
Total	6.151×10^{1}	2.725×10^{-1}	4.074×10^{1}	2.122×10^{-1}	2.916×10^{1}	1.744×10^{-1}	2.187×10^{1}	1.480×10^{-1}	1.710×10^{1}	1.287×10^{-1}	1.377×10^{1}	1.141×10^{-1}
Ex	6.225×10^{-1}	1.817×10^{-2}	6.275×10^{-1}	1.823×10^{-2}	6.105×10^{-1}	1.795×10^{-2}	6.143×10^{-1}	1.817×10^{-2}	6.165×10^{-1}	1.811×10^{-2}	6.216×10^{-1}	1.806×10^{-2}
A2PreCol	1.748×10^{-1}	9.146×10^{-3}	1.630×10^{-1}	8.426×10^{-3}	1.830×10^{-1}	9.407×10^{-3}	1.795×10^{-1}	9.406×10^{-3}	1.693×10^{-1}	8.745×10^{-3}	1.822×10^{-1}	9.595×10^{-3}
A2Col	5.555×10^{1}	2.554×10^{-1}	3.650×10^{1}	2.006×10^{-1}	2.580×10^{1}	1.654×10^{-1}	1.912×10^{1}	1.404×10^{-1}	1.473×10^{1}	1.221×10^{-1}	1.166×10^{1}	1.079×10^{-1}
A2PostCol	4.679	4.186×10^{-2}	3.136	3.330×10^{-2}	2.350	2.834×10^{-2}	1.778	2.443×10^{-2}	1.458	2.205×10^{-2}	1.206	1.999×10^{-2}
M2	4.208×10^{-1}	1.479×10^{-2}	2.778×10^{-1}	1.216×10^{-2}	1.938×10^{-1}	1.014×10^{-2}	1.488×10^{-1}	8.880×10^{-3}	9.526×10^{-2}	6.979×10^{-3}	8.298×10^{-2}	6.644×10^{-3}
T4S	3.472×10^{-2}	3.352×10^{-3}	1.788×10^{-2}	2.243×10^{-3}	9.901×10^{-3}	1.648×10^{-3}	7.905×10^{-3}	1.604×10^{-3}	4.740×10^{-3}	1.373×10^{-3}	4.001×10^{-3}	1.295×10^{-3}
T4L	3.675×10^{-3}	1.324×10^{-3}	7.521×10^{-4}	4.979×10^{-4}	8.440×10^{-4}	7.085×10^{-4}	2.162×10^{-3}	1.102×10^{-3}	1.926×10^{-3}	9.326×10^{-4}	0	0
T4C	9.778×10^{-6}	4.497×10^{-6}	2.003×10^{-6}	1.356×10^{-6}	1.738×10^{-3}	6.791×10^{-4}	1.372×10^{-6}	1.009×10^{-6}	6.310×10^{-4}	4.630×10^{-4}	2.743×10^{-7}	2.154×10^{-7}
T3+T2+T1	1.926×10^{-2}	2.271×10^{-3}	1.353×10^{-2}	1.905×10^{-3}	1.061×10^{-2}	1.317×10^{-3}	1.492×10^{-2}	1.583×10^{-3}	1.670×10^{-2}	1.726×10^{-3}	2.041×10^{-2}	2.068×10^{-3}

$\frac{a_{\text{Col}}}{2\sigma_{\text{beam}}}$	**11**		**12**		**13**		**14**		**15**		**16**	
Section	P_{loss}[W]	ΔP_{loss}[W]	P_{loss}[W]	ΔP_{loss}[W]	P_{loss}[W]	ΔP_{loss}[W]	P_{loss}[W]	ΔP_{loss}[W]	P_{loss}[W]	ΔP_{loss}[W]	P_{loss}[W]	ΔP_{loss}[W]
Total	1.124×10^{1}	1.020×10^{-1}	9.401	9.230×10^{-2}	8.029	8.440×10^{-2}	6.954	7.767×10^{-2}	6.039	7.143×10^{-2}	5.347	6.673×10^{-2}
Ex	6.201×10^{-1}	1.837×10^{-2}	6.203×10^{-1}	1.828×10^{-2}	6.288×10^{-1}	1.836×10^{-2}	6.275×10^{-1}	1.836×10^{-2}	6.274×10^{-1}	1.815×10^{-2}	6.243×10^{-1}	1.805×10^{-2}
A2PreCol	1.712×10^{-1}	8.836×10^{-3}	1.687×10^{-1}	9.026×10^{-3}	1.797×10^{-1}	9.202×10^{-3}	1.767×10^{-1}	9.206×10^{-3}	1.622×10^{-1}	8.675×10^{-3}	1.746×10^{-1}	9.290×10^{-3}
A2Col	9.361	9.618×10^{-2}	7.682	8.673×10^{-2}	6.406	7.883×10^{-2}	5.359	7.193×10^{-2}	4.513	6.573×10^{-2}	3.884	6.091×10^{-2}
A2PostCol	9.823×10^{-1}	1.800×10^{-2}	8.175×10^{-1}	1.598×10^{-2}	7.036×10^{-1}	1.511×10^{-2}	6.506×10^{-1}	1.445×10^{-2}	5.737×10^{-1}	1.361×10^{-2}	4.807×10^{-1}	1.272×10^{-2}
M2	7.932×10^{-2}	6.542×10^{-3}	7.767×10^{-2}	6.443×10^{-3}	5.014×10^{-2}	5.149×10^{-3}	4.337×10^{-2}	4.946×10^{-3}	3.205×10^{-2}	3.997×10^{-3}	2.234×10^{-2}	3.309×10^{-3}
T4S	1.836×10^{-3}	7.200×10^{-4}	4.915×10^{-3}	1.481×10^{-3}	7.491×10^{-4}	3.635×10^{-4}	2.377×10^{-3}	8.645×10^{-4}	1.700×10^{-3}	6.227×10^{-4}	1.841×10^{-3}	8.551×10^{-4}
T4L	0	0	0	0	0	0	0	0	0	0	0	0
T4C	0	0	4.343×10^{-7}	4.234×10^{-7}	0	0	9.097×10^{-6}	9.097×10^{-6}	2.814×10^{-6}	2.771×10^{-6}	3.611×10^{-8}	3.611×10^{-8}
T3+T2+T1	2.208×10^{-2}	2.103×10^{-3}	2.991×10^{-2}	2.378×10^{-3}	6.006×10^{-2}	3.329×10^{-3}	9.449×10^{-2}	4.318×10^{-3}	1.290×10^{-1}	4.996×10^{-3}	1.591×10^{-1}	5.602×10^{-3}

$\frac{a_{\text{Col}}}{2\sigma_{\text{beam}}}$	**17**		**18**		**19**		**20**		∞	
Section	P_{loss}[W]	ΔP_{loss}[W]	P_{loss}[W]	ΔP_{loss}[W]	P_{loss}[W]	ΔP_{loss}[W]	P_{loss}[W]	ΔP_{loss}[W]	P_{loss}[W]	ΔP_{loss}[W]
Total	4.766	6.222×10^{-2}	4.267	5.811×10^{-2}	3.864	5.485×10^{-2}	3.528	5.161×10^{-2}	1.670	2.567×10^{-2}
Ex	6.249×10^{-1}	1.829×10^{-2}	6.218×10^{-1}	1.812×10^{-2}	6.149×10^{-1}	1.801×10^{-2}	6.227×10^{-1}	1.820×10^{-2}	6.025×10^{-1}	1.771×10^{-2}
A2PreCol	1.742×10^{-1}	9.035×10^{-3}	1.716×10^{-1}	9.045×10^{-3}	1.759×10^{-1}	9.100×10^{-3}	1.686×10^{-1}	8.798×10^{-3}	1.884×10^{-1}	9.309×10^{-3}
A2Col	3.313	5.610×10^{-2}	2.848	5.186×10^{-2}	2.489	4.854×10^{-2}	2.166	4.505×10^{-2}	2.978×10^{-2}	3.256×10^{-3}
A2PostCol	4.438×10^{-1}	1.222×10^{-2}	3.960×10^{-1}	1.144×10^{-2}	3.354×10^{-1}	1.047×10^{-2}	3.052×10^{-1}	9.893×10^{-3}	7.711×10^{-3}	1.714×10^{-3}
M2	2.419×10^{-2}	3.565×10^{-3}	2.106×10^{-2}	3.336×10^{-3}	1.558×10^{-2}	2.763×10^{-3}	1.195×10^{-2}	2.436×10^{-3}	9.117×10^{-4}	6.484×10^{-4}
T4S	1.103×10^{-3}	5.072×10^{-4}	9.093×10^{-4}	4.662×10^{-4}	1.899×10^{-3}	9.192×10^{-4}	2.168×10^{-3}	9.149×10^{-4}	3.806×10^{-2}	4.012×10^{-3}
T4L	0	0	0	0	9.315×10^{-5}	9.315×10^{-5}	0	0	2.669×10^{-3}	1.210×10^{-3}
T4C	0	0	0	0	0	0	0	0	1.518×10^{-6}	1.054×10^{-6}
T3+T2+T1	1.842×10^{-1}	6.044×10^{-3}	2.070×10^{-1}	6.503×10^{-3}	2.309×10^{-1}	6.862×10^{-3}	2.523×10^{-1}	7.129×10^{-3}	8.001×10^{-1}	1.449×10^{-2}

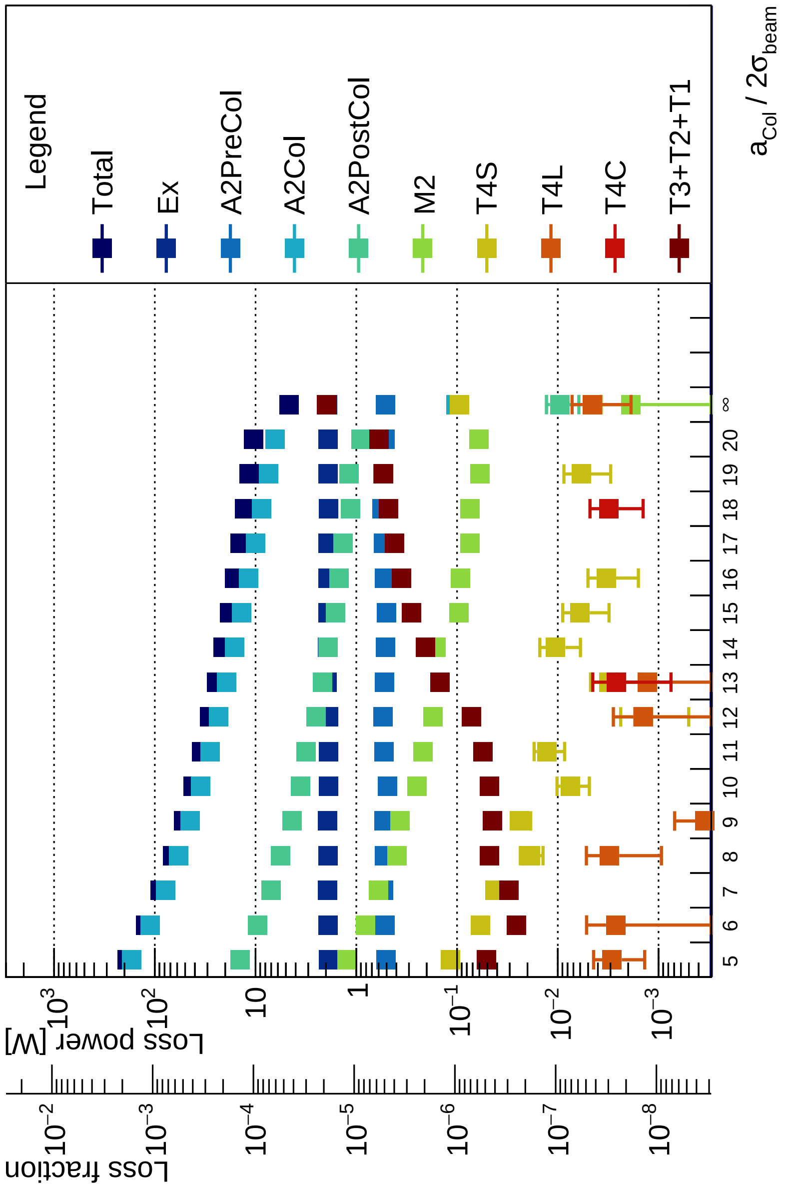

Figure A.7: Main collimator aperture sweep for a He target induced halo.

Table A.7: Loss power numbers from He TAIL main collimator aperture sweep in Figure A.7.

$\frac{a_{\mathrm{Col}}}{2\sigma_{\mathrm{beam}}}$	**5**		**6**		**7**		**8**		**9**		**10**	
Section	P_{loss}[W]	ΔP_{loss}[W]	P_{loss}[W]	ΔP_{loss}[W]	P_{loss}[W]	ΔP_{loss}[W]	P_{loss}[W]	ΔP_{loss}[W]	P_{loss}[W]	ΔP_{loss}[W]	P_{loss}[W]	ΔP_{loss}[W]
Total	1.874×10^{2}	8.686×10^{-1}	1.238×10^{2}	6.755×10^{-1}	8.850×10^{1}	5.548×10^{-1}	6.659×10^{1}	4.703×10^{-1}	5.194×10^{1}	4.093×10^{-1}	4.153×10^{1}	3.611×10^{-1}
Ex	1.885	5.654×10^{-2}	1.897	5.777×10^{-2}	1.921	5.869×10^{-2}	1.911	5.823×10^{-2}	1.936	5.861×10^{-2}	1.881	5.699×10^{-2}
A2PreCol	5.092×10^{-1}	2.819×10^{-2}	5.211×10^{-1}	2.786×10^{-2}	5.351×10^{-1}	2.926×10^{-2}	5.249×10^{-1}	2.844×10^{-2}	5.279×10^{-1}	2.930×10^{-2}	4.900×10^{-1}	2.779×10^{-2}
A2Col	1.694×10^{2}	8.140×10^{-1}	1.110×10^{2}	6.387×10^{-1}	7.836×10^{1}	5.258×10^{-1}	5.807×10^{1}	4.458×10^{-1}	4.472×10^{1}	3.878×10^{-1}	3.529×10^{1}	3.419×10^{-1}
A2PostCol	1.427×10^{1}	1.337×10^{-1}	9.497	1.062×10^{-1}	7.010	9.007×10^{-2}	5.618	7.981×10^{-2}	4.320	6.930×10^{-2}	3.564	6.317×10^{-2}
M2	1.242	4.633×10^{-2}	8.078×10^{-1}	3.770×10^{-2}	5.988×10^{-1}	3.203×10^{-2}	3.967×10^{-1}	2.557×10^{-2}	3.672×10^{-1}	2.585×10^{-2}	2.500×10^{-1}	2.106×10^{-2}
T4S	1.165×10^{-1}	1.212×10^{-2}	5.879×10^{-2}	8.247×10^{-3}	4.210×10^{-2}	6.990×10^{-3}	1.876×10^{-2}	4.748×10^{-3}	2.410×10^{-2}	5.505×10^{-3}	7.521×10^{-3}	2.658×10^{-3}
T4L	2.893×10^{-3}	1.521×10^{-3}	2.658×10^{-3}	2.524×10^{-3}	1.161×10^{-4}	8.725×10^{-5}	3.069×10^{-3}	2.133×10^{-3}	3.461×10^{-4}	3.461×10^{-4}	0	0
T4C	6.275×10^{-6}	4.131×10^{-6}	5.574×10^{-6}	4.661×10^{-6}	9.495×10^{-6}	5.614×10^{-6}	1.533×10^{-4}	1.431×10^{-4}	3.504×10^{-6}	3.462×10^{-6}	2.805×10^{-8}	2.805×10^{-8}
T3+T2+T1	5.122×10^{-2}	7.029×10^{-3}	2.574×10^{-2}	3.906×10^{-3}	3.066×10^{-2}	5.200×10^{-3}	4.761×10^{-2}	5.852×10^{-3}	4.442×10^{-2}	5.395×10^{-3}	4.768×10^{-2}	5.544×10^{-3}

$\frac{a_{\mathrm{Col}}}{2\sigma_{\mathrm{beam}}}$	**11**		**12**		**13**		**14**		**15**		**16**	
Section	P_{loss}[W]	ΔP_{loss}[W]	P_{loss}[W]	ΔP_{loss}[W]	P_{loss}[W]	ΔP_{loss}[W]	P_{loss}[W]	ΔP_{loss}[W]	P_{loss}[W]	ΔP_{loss}[W]	P_{loss}[W]	ΔP_{loss}[W]
Total	3.416×10^{1}	3.236×10^{-1}	2.844×10^{1}	2.928×10^{-1}	2.424×10^{1}	2.670×10^{-1}	2.088×10^{1}	2.453×10^{-1}	1.812×10^{1}	2.266×10^{-1}	1.607×10^{1}	2.108×10^{-1}
Ex	1.886	5.755×10^{-2}	1.891	5.815×10^{-2}	1.953	5.920×10^{-2}	1.921	5.818×10^{-2}	1.915	5.816×10^{-2}	1.915	5.781×10^{-2}
A2PreCol	5.318×10^{-1}	2.838×10^{-2}	5.404×10^{-1}	2.982×10^{-2}	5.251×10^{-1}	2.883×10^{-2}	5.137×10^{-1}	2.873×10^{-2}	5.012×10^{-1}	2.863×10^{-2}	5.239×10^{-1}	2.791×10^{-2}
A2Col	2.832×10^{1}	3.047×10^{-1}	2.325×10^{1}	2.750×10^{-1}	1.929×10^{1}	2.490×10^{-1}	1.615×10^{1}	2.273×10^{-1}	1.372×10^{1}	2.090×10^{-1}	1.171×10^{1}	1.926×10^{-1}
A2PostCol	3.138	5.896×10^{-2}	2.511	5.189×10^{-2}	2.162	4.819×10^{-2}	1.916	4.534×10^{-2}	1.606	4.070×10^{-2}	1.478	3.957×10^{-2}
M2	2.166×10^{-1}	1.998×10^{-2}	1.726×10^{-1}	1.684×10^{-2}	1.477×10^{-1}	1.638×10^{-2}	1.614×10^{-1}	1.685×10^{-2}	9.585×10^{-2}	1.297×10^{-2}	9.253×10^{-2}	1.280×10^{-2}
T4S	1.287×10^{-2}	4.307×10^{-3}	1.439×10^{-3}	9.372×10^{-4}	3.118×10^{-3}	1.608×10^{-3}	1.052×10^{-2}	4.557×10^{-3}	6.017×10^{-3}	2.917×10^{-3}	3.300×10^{-3}	1.715×10^{-3}
T4L	0	0	1.421×10^{-3}	1.387×10^{-3}	1.286×10^{-3}	1.286×10^{-3}	7.543×10^{-7}	7.543×10^{-7}	0	0	0	0
T4C	0	0	0	0	2.625×10^{-3}	1.873×10^{-3}	0	0	0	0	0	0
T3+T2+T1	5.512×10^{-2}	6.218×10^{-3}	7.201×10^{-2}	7.041×10^{-3}	1.476×10^{-1}	9.894×10^{-3}	2.055×10^{-1}	1.165×10^{-2}	2.834×10^{-1}	1.360×10^{-2}	3.544×10^{-1}	1.522×10^{-2}

$\frac{a_{\mathrm{Col}}}{2\sigma_{\mathrm{beam}}}$	**17**		**18**		**19**		**20**		∞	
Section	P_{loss}[W]	ΔP_{loss}[W]	P_{loss}[W]	ΔP_{loss}[W]	P_{loss}[W]	ΔP_{loss}[W]	P_{loss}[W]	ΔP_{loss}[W]	P_{loss}[W]	ΔP_{loss}[W]
Total	1.430×10^{1}	1.966×10^{-1}	1.288×10^{1}	1.852×10^{-1}	1.163×10^{1}	1.725×10^{-1}	1.042×10^{1}	1.618×10^{-1}	4.624	7.944×10^{-2}
Ex	1.897	5.739×10^{-2}	1.888	5.833×10^{-2}	1.901	5.722×10^{-2}	1.918	5.862×10^{-2}	1.929	5.830×10^{-2}
A2PreCol	5.363×10^{-1}	2.939×10^{-2}	5.556×10^{-1}	3.016×10^{-2}	5.430×10^{-1}	2.934×10^{-2}	5.168×10^{-1}	2.854×10^{-2}	5.119×10^{-1}	2.785×10^{-2}
A2Col	1.002×10^{1}	1.776×10^{-1}	8.741	1.654×10^{-1}	7.400	1.518×10^{-1}	6.431	1.409×10^{-1}	1.028×10^{-1}	1.071×10^{-2}
A2PostCol	1.351	3.835×10^{-2}	1.141	3.494×10^{-2}	1.184	3.602×10^{-2}	8.960×10^{-1}	2.999×10^{-2}	9.569×10^{-3}	3.388×10^{-3}
M2	7.437×10^{-2}	1.146×10^{-2}	7.446×10^{-2}	1.179×10^{-2}	5.908×10^{-2}	9.883×10^{-3}	6.029×10^{-2}	1.025×10^{-2}	1.883×10^{-3}	1.814×10^{-3}
T4S	0	0	0	0	5.840×10^{-3}	2.853×10^{-3}	2.236×10^{-5}	2.183×10^{-5}	9.518×10^{-2}	1.220×10^{-2}
T4L	0	0	4.111×10^{-5}	3.464×10^{-5}	0	0	0	0	4.543×10^{-3}	2.668×10^{-3}
T4C	0	0	3.107×10^{-3}	1.685×10^{-3}	1.799×10^{-7}	1.799×10^{-7}	0	0	0	0
T3+T2+T1	4.177×10^{-1}	1.664×10^{-2}	4.770×10^{-1}	1.853×10^{-2}	5.341×10^{-1}	1.911×10^{-2}	5.972×10^{-1}	2.010×10^{-2}	1.969	4.128×10^{-2}

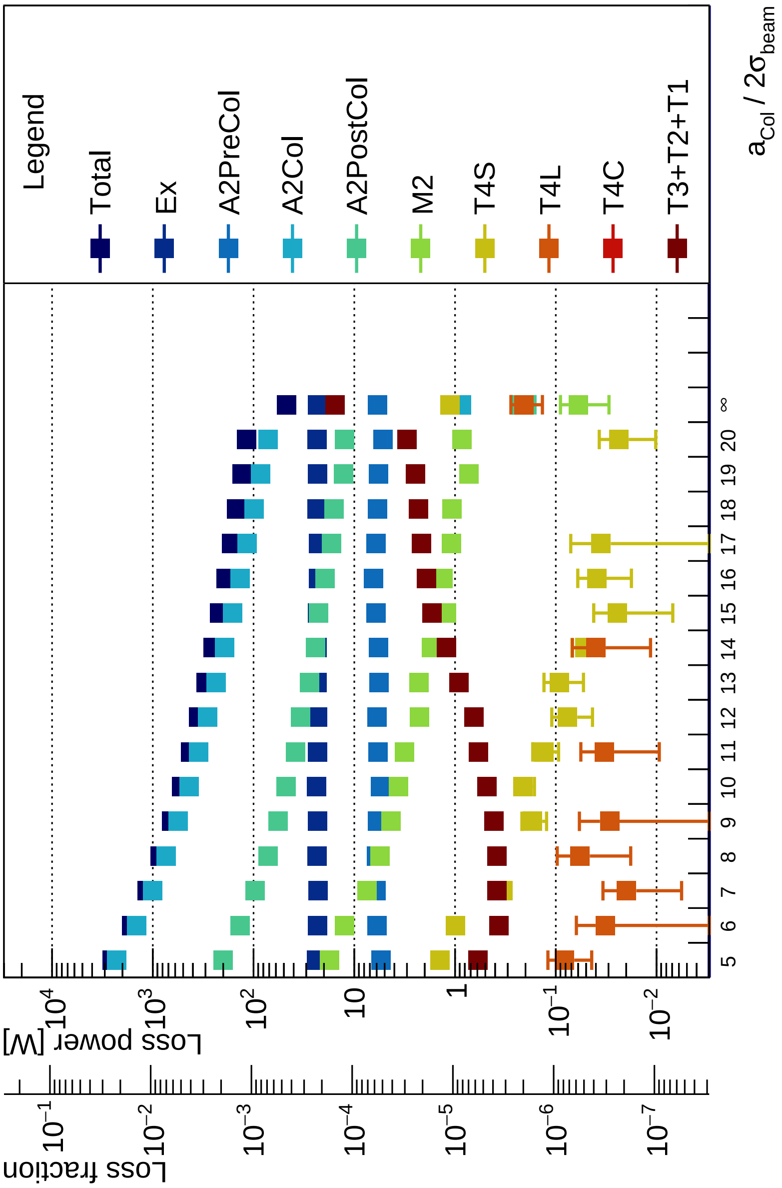

Figure A.8: Main collimator aperture sweep for a O target induced halo.

Table A.8: Loss power numbers from O TAIL main collimator aperture sweep in Figure A.8.

$\frac{a_{\mathrm{Col}}}{2\sigma_{\mathrm{beam}}}$	**5**		**6**		**7**		**8**		**9**		**10**	
Section	P_{loss}[W]	ΔP_{loss}[W]	P_{loss}[W]	ΔP_{loss}[W]	P_{loss}[W]	ΔP_{loss}[W]	P_{loss}[W]	ΔP_{loss}[W]	P_{loss}[W]	ΔP_{loss}[W]	P_{loss}[W]	ΔP_{loss}[W]
Total	2.537×10^{3}	1.111×10^{1}	1.631×10^{3}	8.488	1.139×10^{3}	6.876	8.421×10^{2}	5.788	6.495×10^{2}	5.004	5.174×10^{2}	4.401
Ex	2.362×10^{1}	7.002×10^{-1}	2.324×10^{1}	6.949×10^{-1}	2.282×10^{1}	6.927×10^{-1}	2.341×10^{1}	7.002×10^{-1}	2.316×10^{1}	7.021×10^{-1}	2.382×10^{1}	7.131×10^{-1}
A2PreCol	5.433	3.201×10^{-1}	5.923	3.372×10^{-1}	6.087	3.420×10^{-1}	6.013	3.433×10^{-1}	5.880	3.407×10^{-1}	5.473	3.167×10^{-1}
A2Col	2.289×10^{3}	1.040×10^{1}	1.451×10^{3}	8.000	1.005×10^{3}	6.519	7.344×10^{2}	5.496	5.581×10^{2}	4.747	4.362×10^{2}	4.164
A2PostCol	1.995×10^{2}	1.724	1.365×10^{2}	1.400	9.649×10^{1}	1.152	7.193×10^{1}	9.819×10^{-1}	5.743×10^{1}	8.744×10^{-1}	4.760×10^{1}	7.831×10^{-1}
M2	1.753×10^{1}	6.042×10^{-1}	1.247×10^{1}	5.171×10^{-1}	7.444	3.979×10^{-1}	5.550	3.379×10^{-1}	4.318	2.968×10^{-1}	3.626	2.745×10^{-1}
T4S	1.418	1.471×10^{-1}	9.886×10^{-1}	1.173×10^{-1}	3.338×10^{-1}	6.564×10^{-2}	3.828×10^{-1}	7.457×10^{-2}	1.702×10^{-1}	4.668×10^{-2}	2.109×10^{-1}	4.797×10^{-2}
T4L	8.187×10^{-2}	3.786×10^{-2}	3.226×10^{-2}	3.024×10^{-2}	1.983×10^{-2}	1.419×10^{-2}	5.743×10^{-2}	3.938×10^{-2}	2.916×10^{-2}	2.916×10^{-2}	0	0
T4C	1.457×10^{-4}	9.559×10^{-5}	1.585×10^{-3}	1.483×10^{-3}	0	0	4.768×10^{-5}	3.983×10^{-5}	1.121×10^{-5}	1.121×10^{-5}	5.440×10^{-5}	5.440×10^{-5}
T3+T2+T1	5.911×10^{-1}	7.829×10^{-2}	3.666×10^{-1}	5.385×10^{-2}	3.858×10^{-1}	6.081×10^{-2}	3.860×10^{-1}	5.368×10^{-2}	4.097×10^{-1}	5.483×10^{-2}	4.809×10^{-1}	6.754×10^{-2}

$\frac{a_{\mathrm{Col}}}{2\sigma_{\mathrm{beam}}}$	**11**		**12**		**13**		**14**		**15**		**16**	
Section	P_{loss}[W]	ΔP_{loss}[W]	P_{loss}[W]	ΔP_{loss}[W]	P_{loss}[W]	ΔP_{loss}[W]	P_{loss}[W]	ΔP_{loss}[W]	P_{loss}[W]	ΔP_{loss}[W]	P_{loss}[W]	ΔP_{loss}[W]
Total	4.212×10^{2}	3.927	3.514×10^{2}	3.549	2.941×10^{2}	3.217	2.513×10^{2}	2.943	2.163×10^{2}	2.693	1.873×10^{2}	2.487
Ex	2.311×10^{1}	6.909×10^{-1}	2.325×10^{1}	6.985×10^{-1}	2.331×10^{1}	7.058×10^{-1}	2.352×10^{1}	7.110×10^{-1}	2.306×10^{1}	6.962×10^{-1}	2.269×10^{1}	6.866×10^{-1}
A2PreCol	5.813	3.286×10^{-1}	5.945	3.397×10^{-1}	5.718	3.413×10^{-1}	5.754	3.369×10^{-1}	6.090	3.445×10^{-1}	6.420	3.661×10^{-1}
A2Col	3.500×10^{2}	3.707	2.851×10^{2}	3.330	2.341×10^{2}	3.005	1.948×10^{2}	2.730	1.615×10^{2}	2.475	1.354×10^{2}	2.262
A2PostCol	3.835×10^{1}	7.075×10^{-1}	3.416×10^{1}	6.734×10^{-1}	2.769×10^{1}	5.959×10^{-1}	2.427×10^{1}	5.549×10^{-1}	2.275×10^{1}	5.426×10^{-1}	1.957×10^{1}	5.136×10^{-1}
M2	3.182	2.646×10^{-1}	2.256	2.195×10^{-1}	2.292	2.182×10^{-1}	1.705	1.908×10^{-1}	1.217	1.503×10^{-1}	1.318	1.698×10^{-1}
T4S	1.315×10^{-1}	3.768×10^{-2}	7.640×10^{-2}	3.316×10^{-2}	9.206×10^{-2}	3.894×10^{-2}	5.135×10^{-2}	1.765×10^{-2}	2.446×10^{-2}	1.756×10^{-2}	3.912×10^{-2}	2.136×10^{-2}
T4L	3.291×10^{-2}	2.351×10^{-2}	0	0	0	0	3.995×10^{-2}	2.848×10^{-2}	0	0	8.703×10^{-7}	8.703×10^{-7}
T4C	0	0	6.283×10^{-5}	6.283×10^{-5}	2.481×10^{-5}	2.481×10^{-5}	0	0	0	0	2.804×10^{-5}	2.537×10^{-5}
T3+T2+T1	5.844×10^{-1}	6.980×10^{-2}	6.464×10^{-1}	6.942×10^{-2}	9.165×10^{-1}	8.457×10^{-2}	1.211	9.571×10^{-2}	1.686	1.148×10^{-1}	1.921	1.245×10^{-1}

$\frac{a_{\mathrm{Col}}}{2\sigma_{\mathrm{beam}}}$	**17**		**18**		**19**		**20**		∞	
Section	P_{loss}[W]	ΔP_{loss}[W]	P_{loss}[W]	ΔP_{loss}[W]	P_{loss}[W]	ΔP_{loss}[W]	P_{loss}[W]	ΔP_{loss}[W]	P_{loss}[W]	ΔP_{loss}[W]
Total	1.647×10^{2}	2.307	1.474×10^{2}	2.158	1.304×10^{2}	2.016	1.170×10^{2}	1.881	4.714×10^{1}	9.073×10^{-1}
Ex	2.267×10^{1}	6.861×10^{-1}	2.345×10^{1}	7.093×10^{-1}	2.315×10^{1}	7.037×10^{-1}	2.354×10^{1}	7.098×10^{-1}	2.323×10^{1}	6.993×10^{-1}
A2PreCol	6.076	3.412×10^{-1}	5.857	3.393×10^{-1}	5.772	3.341×10^{-1}	5.162	3.111×10^{-1}	5.895	3.490×10^{-1}
A2Col	1.159×10^{2}	2.087	9.879×10^{1}	1.919	8.551×10^{1}	1.782	7.183×10^{1}	1.631	8.632×10^{-1}	1.103×10^{-1}
A2PostCol	1.684×10^{1}	4.656×10^{-1}	1.592×10^{1}	4.541×10^{-1}	1.276×10^{1}	4.008×10^{-1}	1.256×10^{1}	4.023×10^{-1}	2.169×10^{-1}	5.597×10^{-2}
M2	1.088	1.475×10^{-1}	1.075	1.512×10^{-1}	7.308×10^{-1}	1.284×10^{-1}	8.528×10^{-1}	1.361×10^{-1}	5.976×10^{-2}	3.010×10^{-2}
T4S	3.551×10^{-2}	3.551×10^{-2}	4.236×10^{-4}	4.169×10^{-4}	6.638×10^{-4}	6.098×10^{-4}	2.360×10^{-2}	1.342×10^{-2}	1.118	1.317×10^{-1}
T4L	0	0	0	0	0	0	0	0	2.074×10^{-1}	7.160×10^{-2}
T4C	0	0	2.832×10^{-6}	2.832×10^{-6}	2.454×10^{-6}	2.454×10^{-6}	1.420×10^{-6}	1.420×10^{-6}	0	0
T3+T2+T1	2.149	1.304×10^{-1}	2.301	1.376×10^{-1}	2.462	1.402×10^{-1}	2.996	1.554×10^{-1}	1.554×10^{1}	4.000×10^{-1}

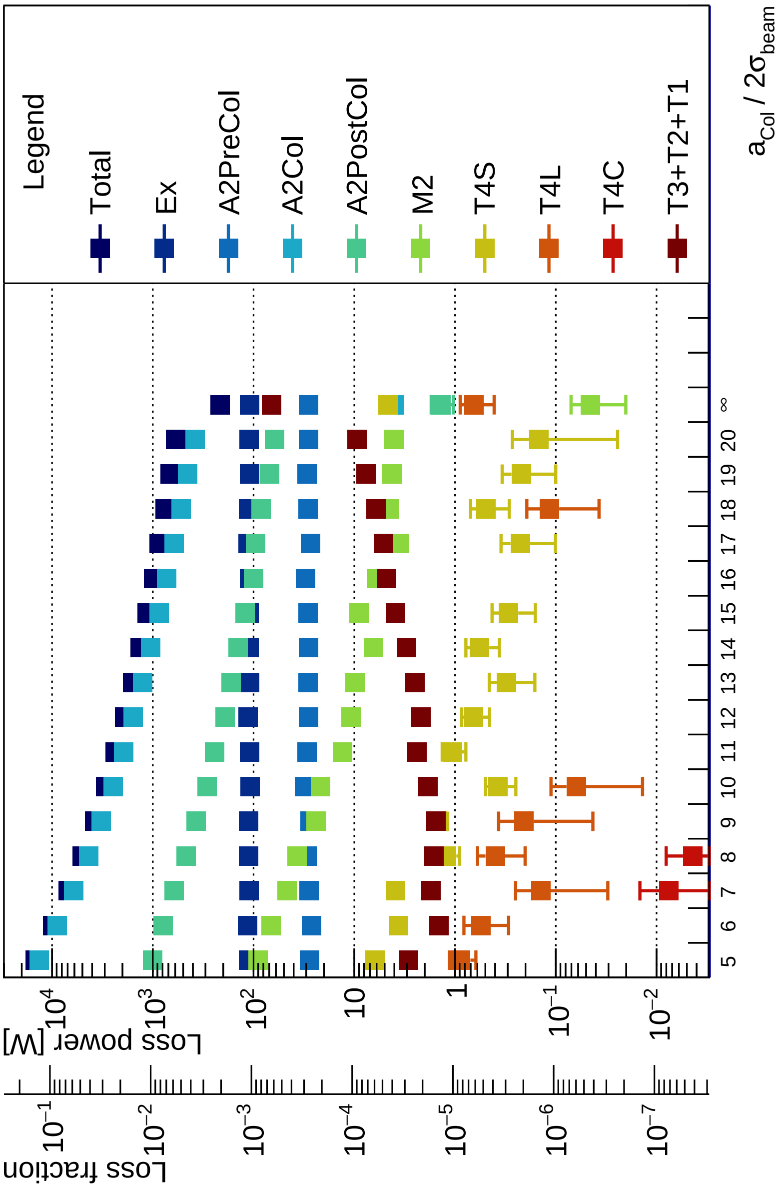

Figure A.9: Main collimator aperture sweep for a Ar target induced halo.

Table A.9: Loss power numbers from Ar TAIL main collimator aperture sweep in Figure A.9.

$\frac{a_{\mathrm{Col}}}{2\sigma_{\mathrm{beam}}}$	**5**		**6**		**7**		**8**		**9**		**10**	
Section	P_{loss}[W]	ΔP_{loss}[W]	P_{loss}[W]	ΔP_{loss}[W]	P_{loss}[W]	ΔP_{loss}[W]	P_{loss}[W]	ΔP_{loss}[W]	P_{loss}[W]	ΔP_{loss}[W]	P_{loss}[W]	ΔP_{loss}[W]
Total	1.463×10^{4}	6.287×10^{1}	9.846×10^{3}	4.857×10^{1}	6.885×10^{3}	3.892×10^{1}	5.000×10^{3}	3.221×10^{1}	3.774×10^{3}	2.736×10^{1}	2.938×10^{3}	2.373×10^{1}
Ex	1.119×10^{2}	3.439	1.148×10^{2}	3.507	1.112×10^{2}	3.427	1.124×10^{2}	3.476	1.119×10^{2}	3.472	1.087×10^{2}	3.411
A2PreCol	2.787×10^{1}	1.616	2.651×10^{1}	1.600	2.818×10^{1}	1.612	2.936×10^{1}	1.690	2.759×10^{1}	1.600	3.112×10^{1}	1.710
A2Col	1.338×10^{4}	5.910×10^{1}	8.841×10^{3}	4.570×10^{1}	6.076×10^{3}	3.667×10^{1}	4.349×10^{3}	3.040×10^{1}	3.238×10^{3}	2.584×10^{1}	2.484×10^{3}	2.240×10^{1}
A2PostCol	1.009×10^{3}	8.684	7.910×10^{2}	7.559	6.171×10^{2}	6.597	4.690×10^{2}	5.679	3.697×10^{2}	5.035	2.905×10^{2}	4.387
M2	9.039×10^{1}	3.118	6.690×10^{1}	2.667	4.672×10^{1}	2.241	3.686×10^{1}	1.949	2.387×10^{1}	1.571	2.152×10^{1}	1.530
T4S	6.209	6.845×10^{-1}	3.658	4.880×10^{-1}	3.919	5.240×10^{-1}	1.212	3.123×10^{-1}	1.519	3.363×10^{-1}	3.738×10^{-1}	1.247×10^{-1}
T4L	8.792×10^{-1}	2.583×10^{-1}	5.552×10^{-1}	2.611×10^{-1}	1.405×10^{-1}	1.101×10^{-1}	3.995×10^{-1}	1.979×10^{-1}	2.061×10^{-1}	1.632×10^{-1}	6.268×10^{-2}	4.891×10^{-2}
T4C	6.717×10^{-5}	5.488×10^{-5}	2.214×10^{-4}	1.571×10^{-4}	7.559×10^{-3}	7.067×10^{-3}	4.371×10^{-3}	3.656×10^{-3}	2.159×10^{-3}	1.855×10^{-3}	1.212×10^{-4}	1.212×10^{-4}
T3+T2+T1	2.905	3.564×10^{-1}	1.439	2.378×10^{-1}	1.735	2.953×10^{-1}	1.615	2.500×10^{-1}	1.550	2.309×10^{-1}	1.854	2.609×10^{-1}

$\frac{a_{\mathrm{Col}}}{2\sigma_{\mathrm{beam}}}$	**11**		**12**		**13**		**14**		**15**		**16**	
Section	P_{loss}[W]	ΔP_{loss}[W]	P_{loss}[W]	ΔP_{loss}[W]	P_{loss}[W]	ΔP_{loss}[W]	P_{loss}[W]	ΔP_{loss}[W]	P_{loss}[W]	ΔP_{loss}[W]	P_{loss}[W]	ΔP_{loss}[W]
Total	2.351×10^{3}	2.094×10^{1}	1.909×10^{3}	1.865×10^{1}	1.585×10^{3}	1.678×10^{1}	1.338×10^{3}	1.529×10^{1}	1.136×10^{3}	1.396×10^{1}	9.823×10^{2}	1.287×10^{1}
Ex	1.096×10^{2}	3.433	1.129×10^{2}	3.473	1.093×10^{2}	3.389	1.112×10^{2}	3.455	1.107×10^{2}	3.419	1.096×10^{2}	3.394
A2PreCol	2.934×10^{1}	1.677	2.834×10^{1}	1.589	2.863×10^{1}	1.633	2.833×10^{1}	1.616	2.868×10^{1}	1.665	3.062×10^{1}	1.763
A2Col	1.951×10^{3}	1.972×10^{1}	1.562×10^{3}	1.753×10^{1}	1.267×10^{3}	1.569×10^{1}	1.045×10^{3}	1.421×10^{1}	8.632×10^{2}	1.288×10^{1}	7.318×10^{2}	1.181×10^{1}
A2PostCol	2.441×10^{2}	4.042	1.915×10^{2}	3.527	1.669×10^{2}	3.326	1.427×10^{2}	3.080	1.207×10^{2}	2.830	9.953×10^{1}	2.531
M2	1.302×10^{1}	1.180	1.079×10^{1}	1.050	9.805	1.004	6.447	8.149×10^{-1}	8.960	9.485×10^{-1}	6.034	7.928×10^{-1}
T4S	1.061	2.801×10^{-1}	6.571×10^{-1}	2.023×10^{-1}	3.094×10^{-1}	1.479×10^{-1}	5.715×10^{-1}	2.091×10^{-1}	2.945×10^{-1}	1.347×10^{-1}	4.762×10^{-5}	4.762×10^{-5}
T4L	1.103×10^{-3}	7.804×10^{-4}	3.909×10^{-4}	3.909×10^{-4}	0	0	0	0	0	0	0	0
T4C	5.349×10^{-4}	5.349×10^{-4}	1.509×10^{-4}	1.509×10^{-4}	1.484×10^{-4}	1.484×10^{-4}	0	0	0	0	1.414×10^{-5}	1.414×10^{-5}
T3+T2+T1	2.384	3.240×10^{-1}	2.186	3.070×10^{-1}	2.490	3.183×10^{-1}	3.030	3.478×10^{-1}	3.919	4.183×10^{-1}	4.796	4.551×10^{-1}

$\frac{a_{\mathrm{Col}}}{2\sigma_{\mathrm{beam}}}$	**17**		**18**		**19**		**20**		∞	
Section	P_{loss}[W]	ΔP_{loss}[W]	P_{loss}[W]	ΔP_{loss}[W]	P_{loss}[W]	ΔP_{loss}[W]	P_{loss}[W]	ΔP_{loss}[W]	P_{loss}[W]	ΔP_{loss}[W]
Total	8.616×10^{2}	1.191×10^{1}	7.583×10^{2}	1.105×10^{1}	6.708×10^{2}	1.028×10^{1}	5.968×10^{2}	9.604	2.152×10^{2}	4.326
Ex	1.130×10^{2}	3.459	1.123×10^{2}	3.493	1.093×10^{2}	3.366	1.113×10^{2}	3.458	1.098×10^{2}	3.421
A2PreCol	2.726×10^{1}	1.609	2.867×10^{1}	1.644	2.934×10^{1}	1.736	2.850×10^{1}	1.607	2.846×10^{1}	1.614
A2Col	6.174×10^{2}	1.081×10^{1}	5.216×10^{2}	9.890	4.504×10^{2}	9.146	3.814×10^{2}	8.419	4.028	5.243×10^{-1}
A2PostCol	9.497×10^{1}	2.478	8.467×10^{1}	2.358	6.965×10^{1}	2.109	6.201×10^{1}	2.012	1.380	3.448×10^{-1}
M2	3.566	6.004×10^{-1}	4.456	6.669×10^{-1}	4.205	6.695×10^{-1}	4.032	6.245×10^{-1}	4.539×10^{-2}	2.521×10^{-2}
T4S	2.252×10^{-1}	1.244×10^{-1}	4.956×10^{-1}	2.059×10^{-1}	2.204×10^{-1}	1.203×10^{-1}	1.473×10^{-1}	1.229×10^{-1}	4.609	5.520×10^{-1}
T4L	0	0	1.156×10^{-1}	7.833×10^{-2}	0	0	1.597×10^{-3}	1.597×10^{-3}	6.489×10^{-1}	2.398×10^{-1}
T4C	0	0	2.141×10^{-4}	2.141×10^{-4}	0	0	0	0	0	0
T3+T2+T1	5.122	4.652×10^{-1}	6.056	5.151×10^{-1}	7.678	5.588×10^{-1}	9.414	5.766×10^{-1}	6.617×10^{1}	1.828

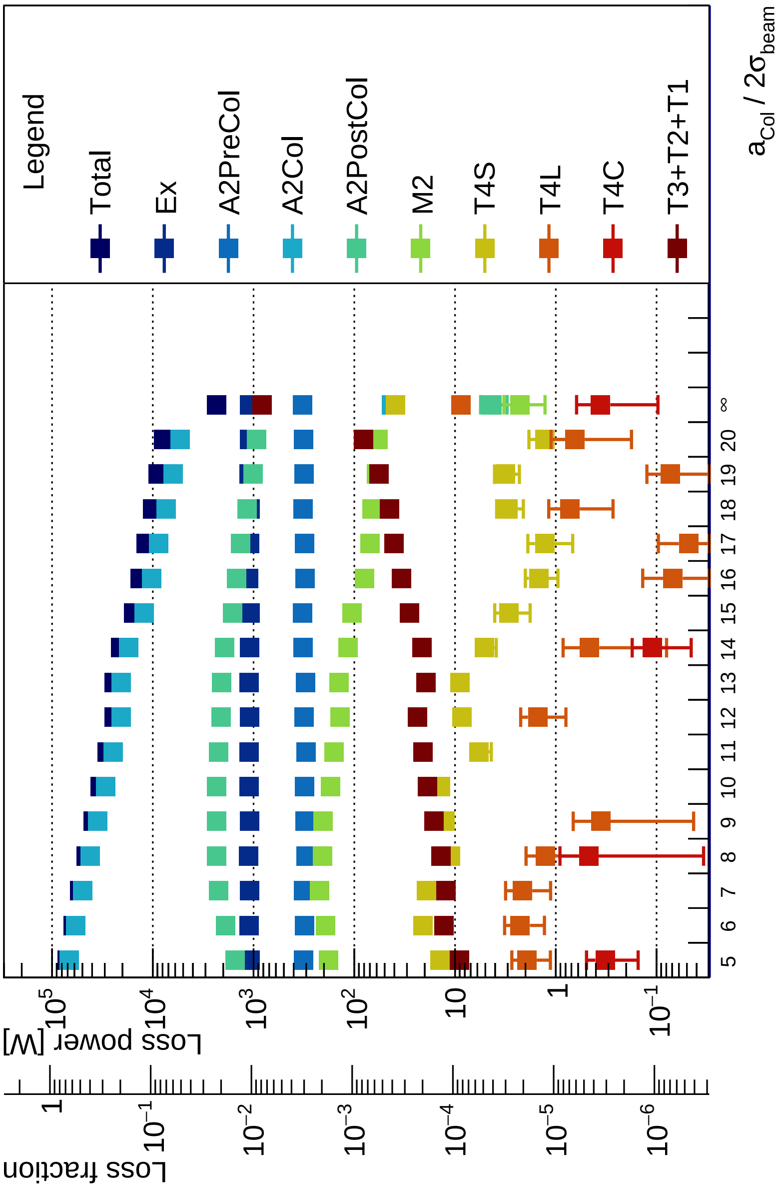

Figure A.10: Main collimator aperture sweep for a Xe target induced halo.

Table A.10: Loss power numbers from Xe TAIL main collimator aperture sweep in Figure A.10.

$\frac{a_{\mathrm{Col}}}{2\sigma_{\mathrm{beam}}}$	**5**		**6**		**7**		**8**		**9**		**10**	
Section	P_{loss}[W]	ΔP_{loss}[W]	P_{loss}[W]	ΔP_{loss}[W]	P_{loss}[W]	ΔP_{loss}[W]	P_{loss}[W]	ΔP_{loss}[W]	P_{loss}[W]	ΔP_{loss}[W]	P_{loss}[W]	ΔP_{loss}[W]
Total	7.102×10^{4}	3.554×10^{2}	6.190×10^{4}	3.183×10^{2}	5.344×10^{4}	2.834×10^{2}	4.586×10^{4}	2.519×10^{2}	3.918×10^{4}	2.239×10^{2}	3.339×10^{4}	1.993×10^{2}
Ex	1.077×10^{3}	2.214×10^{1}	1.101×10^{3}	2.231×10^{1}	1.097×10^{3}	2.240×10^{1}	1.123×10^{3}	2.285×10^{1}	1.092×10^{3}	2.235×10^{1}	1.101×10^{3}	2.256×10^{1}
A2PreCol	3.207×10^{2}	1.151×10^{1}	3.113×10^{2}	1.129×10^{1}	3.183×10^{2}	1.147×10^{1}	3.004×10^{2}	1.104×10^{1}	3.092×10^{2}	1.118×10^{1}	3.125×10^{2}	1.136×10^{1}
A2Col	6.789×10^{4}	3.424×10^{2}	5.836×10^{4}	3.037×10^{2}	4.955×10^{4}	2.676×10^{2}	4.189×10^{4}	2.360×10^{2}	3.521×10^{4}	2.083×10^{2}	2.945×10^{4}	1.840×10^{2}
A2PostCol	1.527×10^{3}	2.110×10^{1}	1.897×10^{3}	2.377×10^{1}	2.218×10^{3}	2.589×10^{1}	2.314×10^{3}	2.648×10^{1}	2.329×10^{3}	2.647×10^{1}	2.315×10^{3}	2.647×10^{1}
M2	1.797×10^{2}	8.959	1.926×10^{2}	9.225	2.204×10^{2}	9.781	2.065×10^{2}	9.590	2.038×10^{2}	9.324	1.713×10^{2}	8.649
T4S	1.414×10^{1}	2.014	2.074×10^{1}	2.489	1.921×10^{1}	2.444	1.107×10^{1}	1.908	1.260×10^{1}	2.092	1.389×10^{1}	1.901
T4L	1.931	7.993×10^{-1}	2.259	9.620×10^{-1}	2.138	1.012	1.268	7.053×10^{-1}	3.571×10^{-1}	3.143×10^{-1}	0	0
T4C	3.239×10^{-1}	1.716×10^{-1}	1.800×10^{-3}	1.144×10^{-3}	1.097×10^{-3}	1.096×10^{-3}	4.715×10^{-1}	4.373×10^{-1}	1.514×10^{-2}	1.434×10^{-2}	8.234×10^{-4}	7.668×10^{-4}
T3+T2+T1	9.019	1.472	1.294×10^{1}	1.638	1.236×10^{1}	1.686	1.379×10^{1}	1.703	1.615×10^{1}	1.793	1.880×10^{1}	1.723

$\frac{a_{\mathrm{Col}}}{2\sigma_{\mathrm{beam}}}$	**11**		**12**		**13**		**14**		**15**		**16**	
Section	P_{loss}[W]	ΔP_{loss}[W]	P_{loss}[W]	ΔP_{loss}[W]	P_{loss}[W]	ΔP_{loss}[W]	P_{loss}[W]	ΔP_{loss}[W]	P_{loss}[W]	ΔP_{loss}[W]	P_{loss}[W]	ΔP_{loss}[W]
Total	2.847×10^{4}	1.780×10^{2}	2.430×10^{4}	1.597×10^{2}	2.428×10^{4}	1.595×10^{2}	2.091×10^{4}	1.442×10^{2}	1.542×10^{4}	1.181×10^{2}	1.333×10^{4}	1.074×10^{2}
Ex	1.106×10^{3}	2.244×10^{1}	1.092×10^{3}	2.233×10^{1}	1.105×10^{3}	2.232×10^{1}	1.099×10^{3}	2.231×10^{1}	1.088×10^{3}	2.219×10^{1}	1.115×10^{3}	2.243×10^{1}
A2PreCol	3.023×10^{2}	1.100×10^{1}	3.154×10^{2}	1.146×10^{1}	3.059×10^{2}	1.117×10^{1}	3.217×10^{2}	1.141×10^{1}	3.260×10^{2}	1.148×10^{1}	3.077×10^{2}	1.107×10^{1}
A2Col	2.467×10^{4}	1.634×10^{2}	2.063×10^{4}	1.457×10^{2}	2.062×10^{4}	1.456×10^{2}	1.742×10^{4}	1.310×10^{2}	1.225×10^{4}	1.060×10^{2}	1.033×10^{4}	9.590×10^{1}
A2PostCol	2.213×10^{3}	2.566×10^{1}	2.092×10^{3}	2.493×10^{1}	2.078×10^{3}	2.482×10^{1}	1.929×10^{3}	2.392×10^{1}	1.612×10^{3}	2.177×10^{1}	1.469×10^{3}	2.056×10^{1}
M2	1.587×10^{2}	8.359	1.381×10^{2}	7.773	1.422×10^{2}	7.924	1.151×10^{2}	7.156	1.051×10^{2}	6.773	7.960×10^{1}	5.752
T4S	5.782	1.413	8.551	1.581	8.928	1.599	5.101	1.203	2.918	1.121	1.479	5.268×10^{-1}
T4L	0	0	1.512	7.183×10^{-1}	4.245×10^{-3}	4.245×10^{-3}	4.629×10^{-1}	3.834×10^{-1}	0	0	6.860×10^{-2}	6.860×10^{-2}
T4C	9.762×10^{-3}	8.891×10^{-3}	0	0	0	0	1.099×10^{-1}	6.456×10^{-2}	9.879×10^{-5}	9.205×10^{-5}	2.275×10^{-3}	1.613×10^{-3}
T3+T2+T1	2.084×10^{1}	1.914	2.356×10^{1}	2.047	1.952×10^{1}	1.777	2.133×10^{1}	2.004	2.847×10^{1}	2.322	3.383×10^{1}	2.490

$\frac{a_{\mathrm{Col}}}{2\sigma_{\mathrm{beam}}}$	**17**		**18**		**19**		**20**		∞	
Section	P_{loss}[W]	ΔP_{loss}[W]	P_{loss}[W]	ΔP_{loss}[W]	P_{loss}[W]	ΔP_{loss}[W]	P_{loss}[W]	ΔP_{loss}[W]	P_{loss}[W]	ΔP_{loss}[W]
Total	1.159×10^{4}	9.822×10^{1}	1.008×10^{4}	9.016×10^{1}	8.848×10^{3}	8.304×10^{1}	7.824×10^{3}	7.673×10^{1}	2.338×10^{3}	3.037×10^{1}
Ex	1.100×10^{3}	2.233×10^{1}	1.081×10^{3}	2.215×10^{1}	1.106×10^{3}	2.262×10^{1}	1.097×10^{3}	2.232×10^{1}	1.097×10^{3}	2.248×10^{1}
A2PreCol	3.135×10^{2}	1.147×10^{1}	3.239×10^{2}	1.163×10^{1}	3.143×10^{2}	1.156×10^{1}	3.199×10^{2}	1.135×10^{1}	3.248×10^{2}	1.158×10^{1}
A2Col	8.720×10^{3}	8.701×10^{1}	7.408×10^{3}	7.949×10^{1}	6.297×10^{3}	7.255×10^{1}	5.333×10^{3}	6.628×10^{1}	4.267×10^{1}	3.469
A2PostCol	1.347×10^{3}	1.969×10^{1}	1.157×10^{3}	1.809×10^{1}	1.011×10^{3}	1.669×10^{1}	9.335×10^{2}	1.619×10^{1}	4.308	1.264
M2	6.978×10^{1}	5.463	6.659×10^{1}	5.405	6.011×10^{1}	5.125	5.824×10^{1}	5.083	2.276	9.967×10^{-1}
T4S	1.287	6.074×10^{-1}	2.981	8.821×10^{-1}	3.176	8.791×10^{-1}	1.277	5.708×10^{-1}	3.889×10^{1}	3.520
T4L	4.801×10^{-2}	4.801×10^{-2}	7.225×10^{-1}	4.521×10^{-1}	7.300×10^{-2}	5.167×10^{-2}	6.452×10^{-1}	4.678×10^{-1}	8.779	1.744
T4C	0	0	4.875×10^{-3}	4.817×10^{-3}	0	0	0	0	3.593×10^{-1}	2.625×10^{-1}
T3+T2+T1	4.039×10^{1}	2.799	4.482×10^{1}	2.915	5.693×10^{1}	3.118	8.076×10^{1}	3.452	8.194×10^{2}	1.372×10^{1}

A.3 Main Collimator Material Simulations

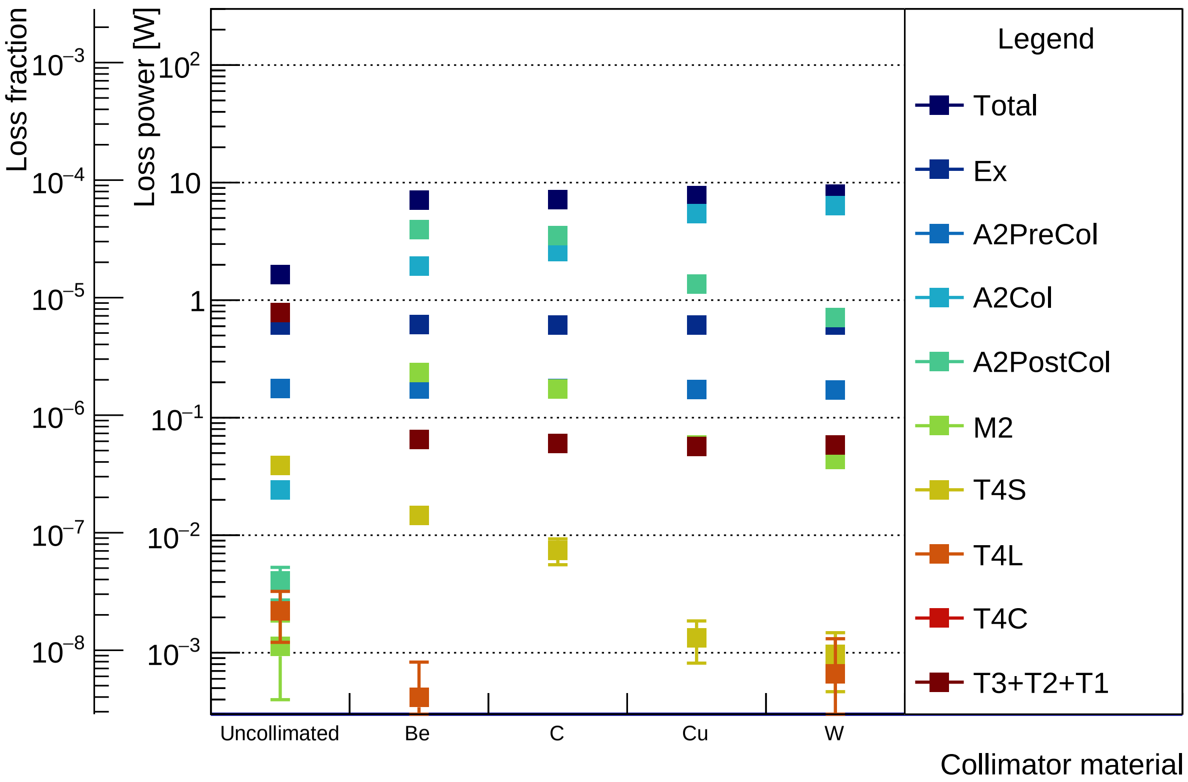

Figure A.11: Power losses for different main collimator materials and a H TAIL.

Table A.11: Loss power numbers from H TAIL main collimator material sweep in Figure A.11.

Collimator Material	**Uncollimated**		**Be**		**C**		**Cu**		**W**	
Section	P_{loss}[W]	ΔP_{loss}[W]	P_{loss}[W]	ΔP_{loss}[W]	P_{loss}[W]	ΔP_{loss}[W]	P_{loss}[W]	ΔP_{loss}[W]	P_{loss}[W]	ΔP_{loss}[W]
Total	1.650	2.574×10^{-2}	7.074	5.388×10^{-2}	7.169	5.598×10^{-2}	7.724	7.612×10^{-2}	8.005	8.420×10^{-2}
Ex	6.150×10^{-1}	1.789×10^{-2}	6.212×10^{-1}	1.814×10^{-2}	6.137×10^{-1}	1.798×10^{-2}	6.145×10^{-1}	1.813×10^{-2}	6.132×10^{-1}	1.795×10^{-2}
A2PreCol	1.772×10^{-1}	9.450×10^{-3}	1.759×10^{-1}	9.170×10^{-3}	1.768×10^{-1}	9.215×10^{-3}	1.733×10^{-1}	9.047×10^{-3}	1.727×10^{-1}	8.875×10^{-3}
A2Col	2.425×10^{-2}	3.075×10^{-3}	1.956	2.405×10^{-2}	2.579	3.209×10^{-2}	5.456	6.834×10^{-2}	6.401	7.880×10^{-2}
A2PostCol	4.069×10^{-3}	1.258×10^{-3}	3.998	3.838×10^{-2}	3.556	3.573×10^{-2}	1.364	2.002×10^{-2}	7.134×10^{-1}	1.505×10^{-2}
M2	1.130×10^{-3}	7.315×10^{-4}	2.416×10^{-1}	1.132×10^{-2}	1.762×10^{-1}	9.660×10^{-3}	5.861×10^{-2}	5.483×10^{-3}	4.430×10^{-2}	4.835×10^{-3}
T4S	3.931×10^{-2}	3.992×10^{-3}	1.478×10^{-2}	2.467×10^{-3}	7.456×10^{-3}	1.849×10^{-3}	1.341×10^{-3}	5.248×10^{-4}	9.737×10^{-4}	5.073×10^{-4}
T4L	2.277×10^{-3}	1.050×10^{-3}	4.163×10^{-4}	4.162×10^{-4}	1.092×10^{-5}	1.092×10^{-5}	0	0	6.621×10^{-4}	6.541×10^{-4}
T4C	0	0	7.729×10^{-7}	4.524×10^{-7}	3.149×10^{-7}	2.377×10^{-7}	0	0	1.504×10^{-6}	1.068×10^{-6}
T3+T2+T1	7.869×10^{-1}	1.441×10^{-2}	6.542×10^{-2}	3.605×10^{-3}	6.022×10^{-2}	3.393×10^{-3}	5.703×10^{-2}	3.153×10^{-3}	5.884×10^{-2}	3.279×10^{-3}

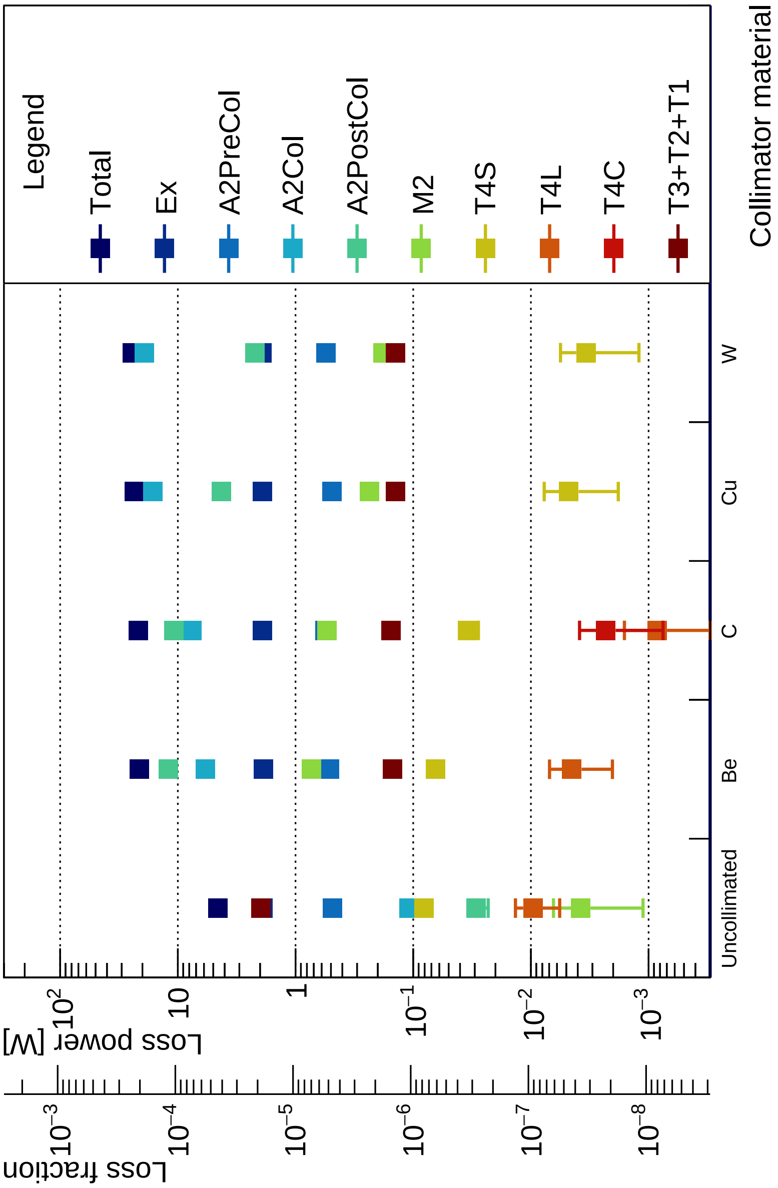

Figure A.12: Power losses for different main collimator materials and a He TAIL.

Table A.12: Loss power numbers from He TAIL main collimator material sweep in Figure A.12.

Collimator Material	**Uncollimated**		**Be**		**C**		**Cu**		**W**	
Section	P_{loss}[W]	ΔP_{loss}[W]	P_{loss}[W]	ΔP_{loss}[W]	P_{loss}[W]	ΔP_{loss}[W]	P_{loss}[W]	ΔP_{loss}[W]	P_{loss}[W]	ΔP_{loss}[W]
Total	4.581	7.880×10^{-2}	2.123×10^{1}	1.709×10^{-1}	2.164×10^{1}	1.776×10^{-1}	2.337×10^{1}	2.407×10^{-1}	2.425×10^{1}	2.674×10^{-1}
Ex	1.892	5.776×10^{-2}	1.870	5.759×10^{-2}	1.908	5.840×10^{-2}	1.916	5.766×10^{-2}	1.939	5.872×10^{-2}
A2PreCol	4.871×10^{-1}	2.754×10^{-2}	5.156×10^{-1}	2.855×10^{-2}	5.649×10^{-1}	3.004×10^{-2}	4.910×10^{-1}	2.789×10^{-2}	5.499×10^{-1}	2.961×10^{-2}
A2Col	1.085×10^{-1}	1.123×10^{-2}	5.834	7.570×10^{-2}	7.604	1.002×10^{-1}	1.633×10^{1}	2.152×10^{-1}	1.921×10^{1}	2.492×10^{-1}
A2PostCol	2.920×10^{-2}	6.126×10^{-3}	1.206×10^{1}	1.224×10^{-1}	1.084×10^{1}	1.137×10^{-1}	4.251	6.498×10^{-2}	2.221	4.929×10^{-2}
M2	3.773×10^{-3}	2.658×10^{-3}	7.326×10^{-1}	3.576×10^{-2}	5.397×10^{-1}	3.088×10^{-2}	2.356×10^{-1}	2.017×10^{-2}	1.808×10^{-1}	1.767×10^{-2}
T4S	8.110×10^{-2}	9.975×10^{-3}	6.486×10^{-2}	8.900×10^{-3}	3.459×10^{-2}	6.661×10^{-3}	4.759×10^{-3}	2.950×10^{-3}	3.406×10^{-3}	2.198×10^{-3}
T4L	9.610×10^{-3}	3.916×10^{-3}	4.488×10^{-3}	2.459×10^{-3}	8.438×10^{-4}	7.607×10^{-4}	0	0	0	0
T4C	0	0	1.002×10^{-4}	6.571×10^{-5}	2.307×10^{-3}	1.553×10^{-3}	0	0	8.855×10^{-7}	8.855×10^{-7}
T3+T2+T1	1.969	4.107×10^{-2}	1.503×10^{-1}	9.831×10^{-3}	1.538×10^{-1}	1.017×10^{-2}	1.412×10^{-1}	9.913×10^{-3}	1.412×10^{-1}	9.372×10^{-3}

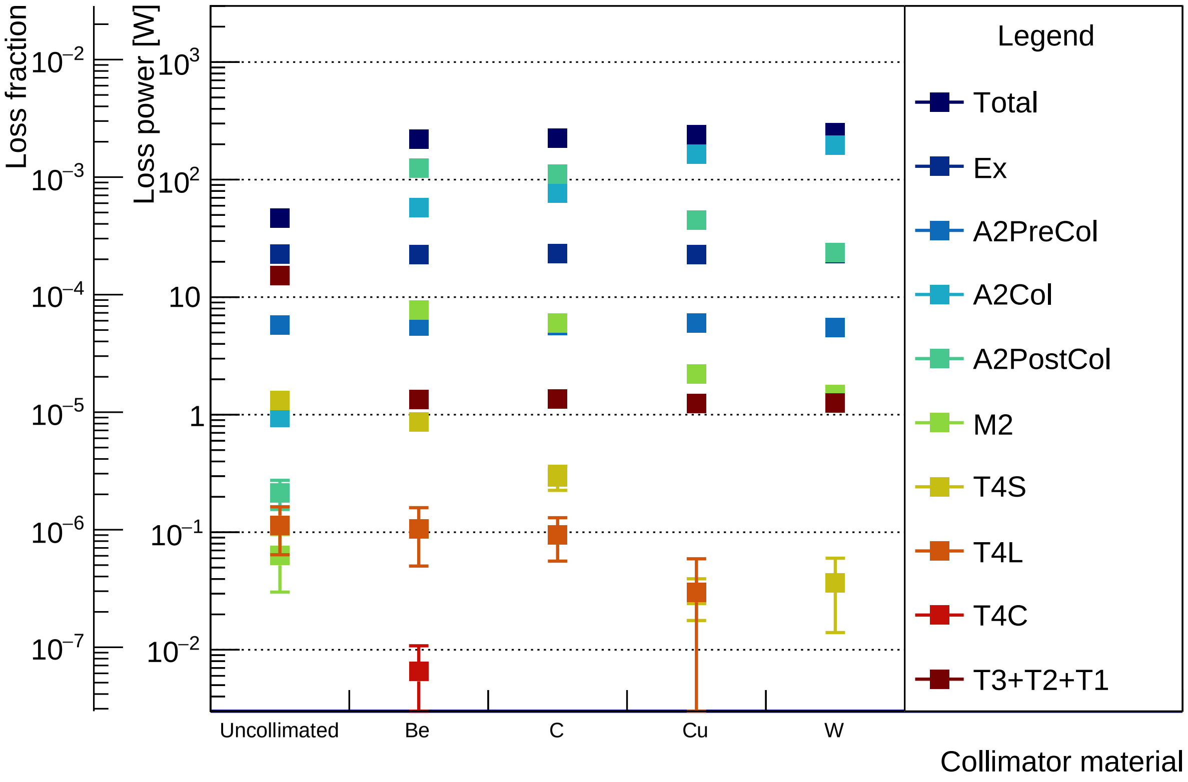

Figure A.13: Power losses for different main collimator materials and a O TAIL.

Table A.13: Loss power numbers from O TAIL main collimator material sweep in Figure A.13.

Collimator Material	**Uncollimated**		**Be**		**C**		**Cu**		**W**	
Section	P_{loss}[W]	ΔP_{loss}[W]	P_{loss}[W]	ΔP_{loss}[W]	P_{loss}[W]	ΔP_{loss}[W]	P_{loss}[W]	ΔP_{loss}[W]	P_{loss}[W]	ΔP_{loss}[W]
Total	4.699×10^{1}	9.100×10^{-1}	2.213×10^{2}	1.893	2.254×10^{2}	1.966	2.421×10^{2}	2.654	2.512×10^{2}	2.946
Ex	2.322×10^{1}	7.057×10^{-1}	2.304×10^{1}	6.989×10^{-1}	2.357×10^{1}	7.121×10^{-1}	2.294×10^{1}	6.994×10^{-1}	2.340×10^{1}	7.073×10^{-1}
A2PreCol	5.764	3.325×10^{-1}	5.651	3.302×10^{-1}	5.736	3.434×10^{-1}	6.000	3.360×10^{-1}	5.487	3.214×10^{-1}
A2Col	9.501×10^{-1}	1.191×10^{-1}	5.778×10^{1}	8.236×10^{-1}	7.688×10^{1}	1.102	1.642×10^{2}	2.358	1.955×10^{2}	2.738
A2PostCol	2.162×10^{-1}	5.998×10^{-2}	1.248×10^{2}	1.353	1.115×10^{2}	1.253	4.543×10^{1}	7.341×10^{-1}	2.401×10^{1}	5.521×10^{-1}
M2	6.329×10^{-2}	3.236×10^{-2}	7.732	4.017×10^{-1}	6.018	3.584×10^{-1}	2.221	2.115×10^{-1}	1.487	1.781×10^{-1}
T4S	1.326	1.572×10^{-1}	8.680×10^{-1}	1.241×10^{-1}	2.954×10^{-1}	6.843×10^{-2}	2.894×10^{-2}	1.121×10^{-2}	3.705×10^{-2}	2.305×10^{-2}
T4L	1.145×10^{-1}	5.017×10^{-2}	1.066×10^{-1}	5.511×10^{-2}	9.481×10^{-2}	3.805×10^{-2}	3.070×10^{-2}	2.871×10^{-2}	0	0
T4C	0	0	6.525×10^{-3}	4.281×10^{-3}	1.544×10^{-6}	1.253×10^{-6}	0	0	2.832×10^{-6}	2.832×10^{-6}
T3+T2+T1	1.533×10^{1}	3.999×10^{-1}	1.351	1.058×10^{-1}	1.365	1.042×10^{-1}	1.248	1.010×10^{-1}	1.263	1.037×10^{-1}

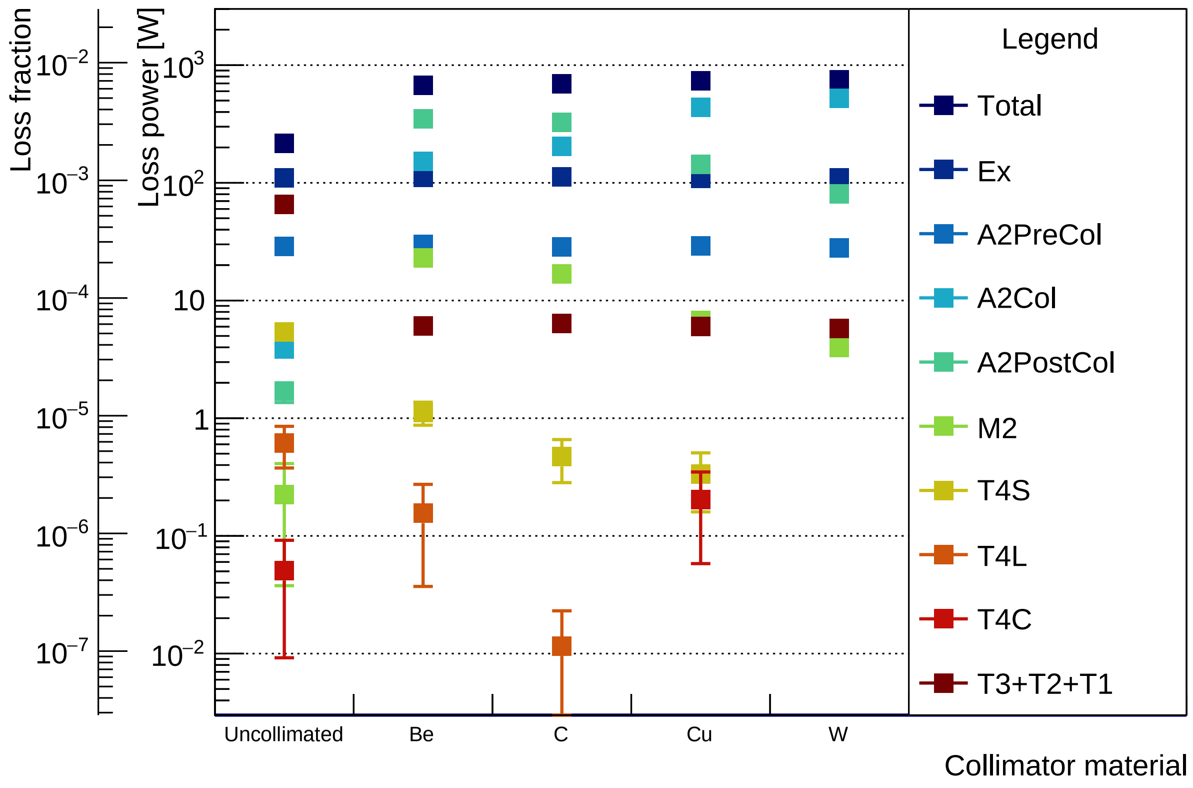

Figure A.14: Power losses for different main collimator materials and a Ar TAIL.

Table A.14: Loss power numbers from Ar TAIL main collimator material sweep in Figure A.14.

Collimator Material	**Uncollimated**		**Be**		**C**		**Cu**		**W**	
Section	P_{loss}[W]	ΔP_{loss}[W]	P_{loss}[W]	ΔP_{loss}[W]	P_{loss}[W]	ΔP_{loss}[W]	P_{loss}[W]	ΔP_{loss}[W]	P_{loss}[W]	ΔP_{loss}[W]
Total	2.159×10^{2}	4.333	6.756×10^{2}	7.350	6.958×10^{2}	7.704	7.349×10^{2}	1.003×10^{1}	7.543×10^{2}	1.102×10^{1}
Ex	1.097×10^{2}	3.385	1.110×10^{2}	3.410	1.128×10^{2}	3.505	1.094×10^{2}	3.401	1.106×10^{2}	3.419
A2PreCol	2.892×10^{1}	1.677	3.004×10^{1}	1.667	2.848×10^{1}	1.651	2.898×10^{1}	1.683	2.802×10^{1}	1.648
A2Col	3.877	5.455×10^{-1}	1.525×10^{2}	2.951	2.039×10^{2}	4.011	4.396×10^{2}	8.559	5.250×10^{2}	9.914
A2PostCol	1.710	3.503×10^{-1}	3.515×10^{2}	4.998	3.269×10^{2}	4.769	1.436×10^{2}	2.918	8.083×10^{1}	2.285
M2	2.247×10^{-1}	1.869×10^{-1}	2.313×10^{1}	1.573	1.690×10^{1}	1.342	6.777	8.516×10^{-1}	3.983	6.195×10^{-1}
T4S	5.410	6.565×10^{-1}	1.120	2.479×10^{-1}	4.709×10^{-1}	1.874×10^{-1}	3.339×10^{-1}	1.738×10^{-1}	4.762×10^{-4}	3.488×10^{-4}
T4L	6.153×10^{-1}	2.377×10^{-1}	1.556×10^{-1}	1.184×10^{-1}	1.155×10^{-2}	1.155×10^{-2}	0	0	0	0
T4C	5.050×10^{-2}	4.128×10^{-2}	5.942×10^{-5}	5.942×10^{-5}	2.669×10^{-4}	2.669×10^{-4}	2.037×10^{-1}	1.455×10^{-1}	0	0
T3+T2+T1	6.544×10^{1}	1.802	6.101	5.036×10^{-1}	6.397	5.167×10^{-1}	6.023	4.938×10^{-1}	5.813	5.083×10^{-1}

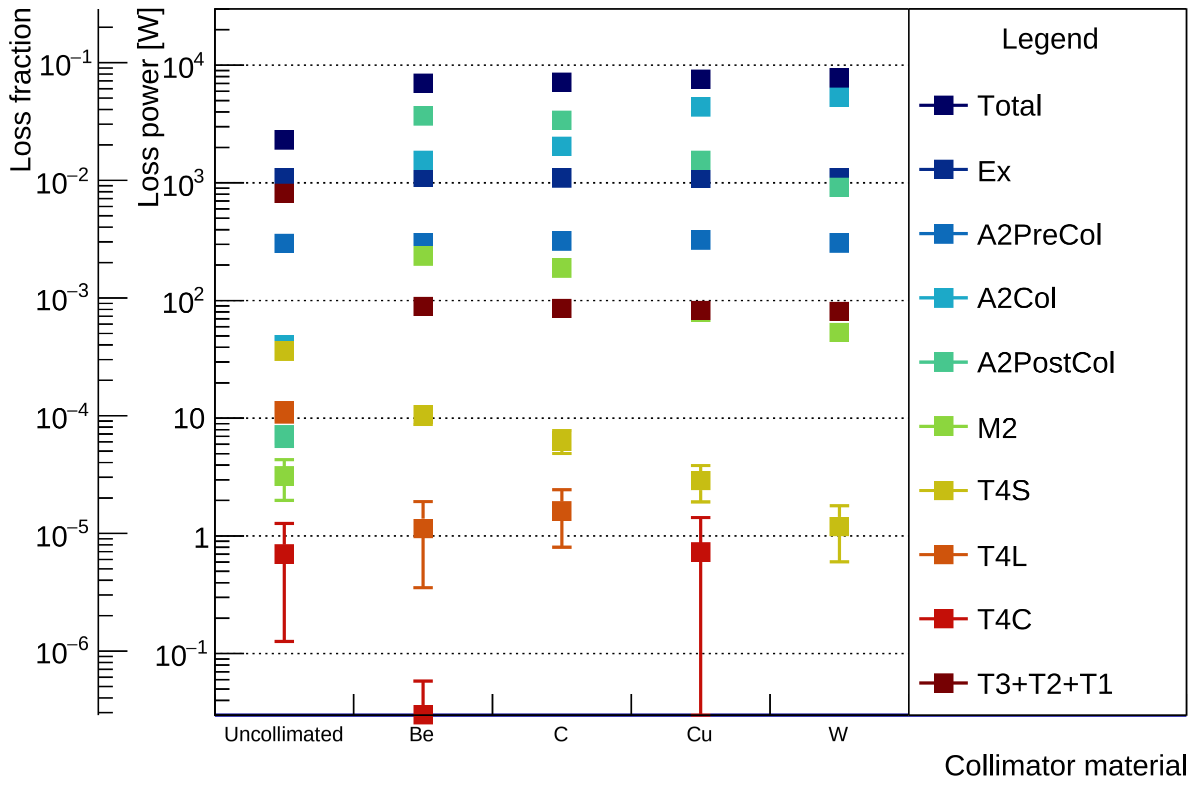

Figure A.15: Power losses for different main collimator materials and a Xe TAIL.

Table A.15: Loss power numbers from Xe TAIL main collimator material sweep in Figure A.15.

Collimator Material	**Uncollimated**		**Be**		**C**		**Cu**		**W**	
Section	P_{loss}[W]	ΔP_{loss}[W]	P_{loss}[W]	ΔP_{loss}[W]	P_{loss}[W]	ΔP_{loss}[W]	P_{loss}[W]	ΔP_{loss}[W]	P_{loss}[W]	ΔP_{loss}[W]
Total	2.325×10^{3}	3.016×10^{1}	7.035×10^{3}	5.540×10^{1}	7.150×10^{3}	5.666×10^{1}	7.567×10^{3}	7.035×10^{1}	7.802×10^{3}	7.670×10^{1}
Ex	1.103×10^{3}	2.257×10^{1}	1.111×10^{3}	2.269×10^{1}	1.097×10^{3}	2.238×10^{1}	1.095×10^{3}	2.227×10^{1}	1.102×10^{3}	2.246×10^{1}
A2PreCol	3.059×10^{2}	1.112×10^{1}	3.078×10^{2}	1.126×10^{1}	3.225×10^{2}	1.152×10^{1}	3.279×10^{2}	1.155×10^{1}	3.089×10^{2}	1.145×10^{1}
A2Col	4.210×10^{1}	3.522	1.551×10^{3}	1.988×10^{1}	2.043×10^{3}	2.656×10^{1}	4.428×10^{3}	5.667×10^{1}	5.337×10^{3}	6.630×10^{1}
A2PostCol	7.192	1.430	3.725×10^{3}	3.632×10^{1}	3.405×10^{3}	3.379×10^{1}	1.551×10^{3}	2.077×10^{1}	9.186×10^{2}	1.597×10^{1}
M2	3.221	1.214	2.386×10^{2}	1.029×10^{1}	1.888×10^{2}	9.201	7.948×10^{1}	5.845	5.365×10^{1}	4.939
T4S	3.737×10^{1}	3.310	1.073×10^{1}	1.865	6.430	1.408	2.950	1.008	1.201	5.998×10^{-1}
T4L	1.153×10^{1}	2.246	1.158	7.958×10^{-1}	1.633	8.309×10^{-1}	2.763×10^{-2}	2.058×10^{-2}	0	0
T4C	7.025×10^{-1}	5.756×10^{-1}	3.027×10^{-2}	2.811×10^{-2}	8.281×10^{-4}	8.281×10^{-4}	7.277×10^{-1}	7.049×10^{-1}	0	0
T3+T2+T1	8.134×10^{2}	1.344×10^{1}	8.918×10^{1}	3.776	8.563×10^{1}	3.589	8.240×10^{1}	3.516	8.116×10^{1}	3.520

A.4 Spoiler Aperture Sweeps

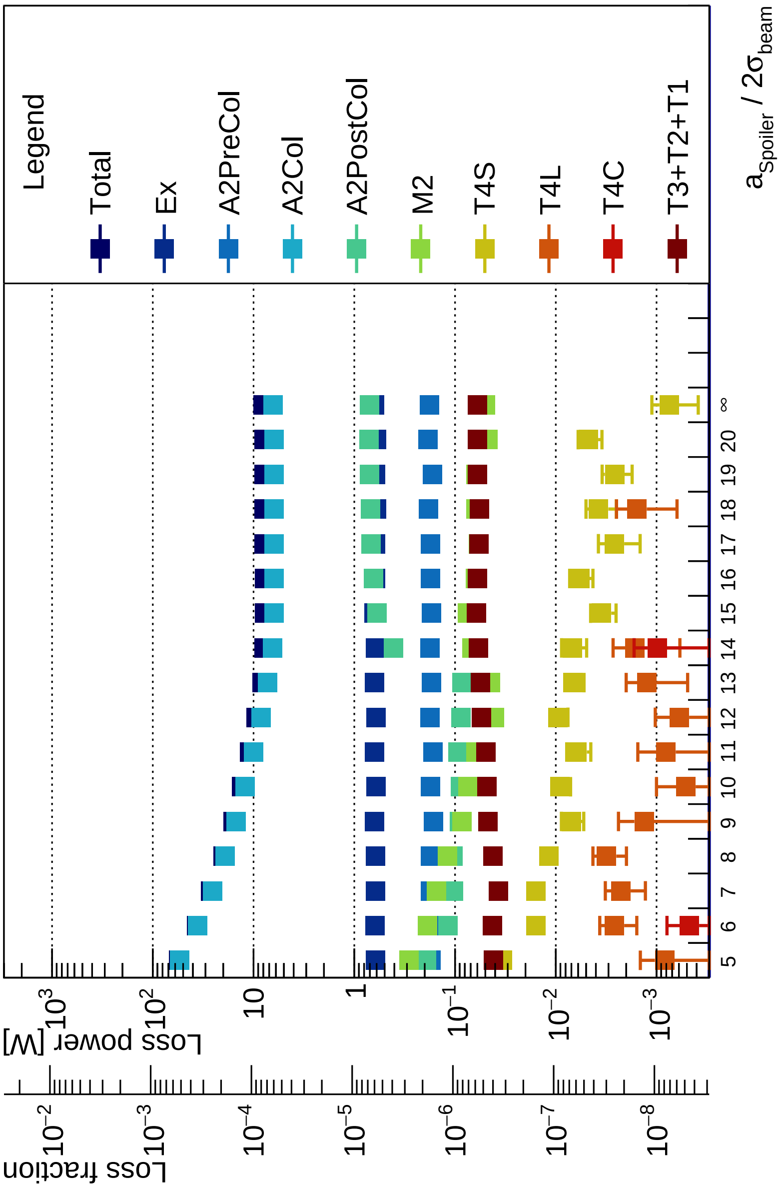

Figure A.16: Spoiler aperture sweep for a H target induced halo.

Table A.16: Loss power numbers from H TAIL spoiler aperture sweep in Figure A.16.

$\frac{a_{\text{Spoiler}}}{2\sigma_{\text{beam}}}$	**5**		**6**		**7**		**8**		**9**		**10**	
Section	P_{loss}[W]	ΔP_{loss}[W]	P_{loss}[W]	ΔP_{loss}[W]	P_{loss}[W]	ΔP_{loss}[W]	P_{loss}[W]	ΔP_{loss}[W]	P_{loss}[W]	ΔP_{loss}[W]	P_{loss}[W]	ΔP_{loss}[W]
Total	5.534×10^{1}	2.400×10^{-1}	3.687×10^{1}	1.849×10^{-1}	2.654×10^{1}	1.519×10^{-1}	2.015×10^{1}	1.297×10^{-1}	1.598×10^{1}	1.140×10^{-1}	1.308×10^{1}	1.024×10^{-1}
Ex	6.155×10^{-1}	1.810×10^{-2}	6.244×10^{-1}	1.819×10^{-2}	6.186×10^{-1}	1.825×10^{-2}	6.176×10^{-1}	1.810×10^{-2}	6.272×10^{-1}	1.828×10^{-2}	6.082×10^{-1}	1.792×10^{-2}
A2PreCol	1.732×10^{-1}	9.071×10^{-3}	1.728×10^{-1}	8.765×10^{-3}	1.753×10^{-1}	9.137×10^{-3}	1.748×10^{-1}	9.141×10^{-3}	1.629×10^{-1}	9.080×10^{-3}	1.745×10^{-1}	9.029×10^{-3}
A2Col	5.400×10^{1}	2.356×10^{-1}	3.570×10^{1}	1.811×10^{-1}	2.544×10^{1}	1.482×10^{-1}	1.907×10^{1}	1.260×10^{-1}	1.496×10^{1}	1.104×10^{-1}	1.208×10^{1}	9.869×10^{-2}
A2PostCol	1.926×10^{-1}	8.440×10^{-3}	1.181×10^{-1}	6.594×10^{-3}	1.035×10^{-1}	5.984×10^{-3}	1.046×10^{-1}	6.060×10^{-3}	9.046×10^{-2}	5.497×10^{-3}	8.801×10^{-2}	5.769×10^{-3}
M2	2.851×10^{-1}	1.259×10^{-2}	1.873×10^{-1}	1.022×10^{-2}	1.532×10^{-1}	9.315×10^{-3}	1.183×10^{-1}	8.082×10^{-3}	8.568×10^{-2}	6.944×10^{-3}	7.473×10^{-2}	6.501×10^{-3}
T4S	3.375×10^{-2}	3.581×10^{-3}	1.575×10^{-2}	2.236×10^{-3}	1.577×10^{-2}	2.378×10^{-3}	1.175×10^{-2}	2.042×10^{-3}	7.035×10^{-3}	1.758×10^{-3}	9.116×10^{-3}	1.984×10^{-3}
T4L	8.320×10^{-4}	6.162×10^{-4}	2.615×10^{-3}	1.045×10^{-3}	2.257×10^{-3}	9.669×10^{-4}	3.135×10^{-3}	1.145×10^{-3}	1.328×10^{-3}	1.059×10^{-3}	5.109×10^{-4}	4.902×10^{-4}
T4C	3.792×10^{-5}	3.151×10^{-5}	4.717×10^{-4}	3.161×10^{-4}	2.750×10^{-6}	1.524×10^{-6}	3.333×10^{-6}	1.842×10^{-6}	0	0	1.316×10^{-6}	1.316×10^{-6}
T3+T2+T1	4.140×10^{-2}	3.001×10^{-3}	4.241×10^{-2}	2.931×10^{-3}	3.719×10^{-2}	2.810×10^{-3}	4.193×10^{-2}	2.950×10^{-3}	4.689×10^{-2}	3.010×10^{-3}	4.839×10^{-2}	3.141×10^{-3}

$\frac{a_{\text{Spoiler}}}{2\sigma_{\text{beam}}}$	**11**		**12**		**13**		**14**		**15**		**16**	
Section	P_{loss}[W]	ΔP_{loss}[W]	P_{loss}[W]	ΔP_{loss}[W]	P_{loss}[W]	ΔP_{loss}[W]	P_{loss}[W]	ΔP_{loss}[W]	P_{loss}[W]	ΔP_{loss}[W]	P_{loss}[W]	ΔP_{loss}[W]
Total	1.099×10^{1}	9.343×10^{-2}	9.410	8.611×10^{-2}	8.217	8.008×10^{-2}	7.833	7.746×10^{-2}	7.808	7.760×10^{-2}	7.807	7.825×10^{-2}
Ex	6.283×10^{-1}	1.837×10^{-2}	6.119×10^{-1}	1.795×10^{-2}	6.266×10^{-1}	1.845×10^{-2}	6.151×10^{-1}	1.808×10^{-2}	6.363×10^{-1}	1.841×10^{-2}	6.141×10^{-1}	1.790×10^{-2}
A2PreCol	1.660×10^{-1}	8.740×10^{-3}	1.769×10^{-1}	8.988×10^{-3}	1.704×10^{-1}	9.095×10^{-3}	1.768×10^{-1}	9.051×10^{-3}	1.720×10^{-1}	9.003×10^{-3}	1.746×10^{-1}	8.994×10^{-3}
A2Col	9.985	8.962×10^{-2}	8.428	8.231×10^{-2}	7.225	7.602×10^{-2}	6.495	7.213×10^{-2}	6.265	7.165×10^{-2}	6.244	7.244×10^{-2}
A2PostCol	9.332×10^{-2}	5.849×10^{-3}	8.739×10^{-2}	5.731×10^{-3}	8.539×10^{-2}	5.397×10^{-3}	4.104×10^{-1}	1.234×10^{-2}	5.945×10^{-1}	1.446×10^{-2}	6.459×10^{-1}	1.484×10^{-2}
M2	6.229×10^{-2}	5.908×10^{-3}	4.082×10^{-2}	4.755×10^{-3}	4.478×10^{-2}	4.774×10^{-3}	6.761×10^{-2}	6.140×10^{-3}	7.566×10^{-2}	6.448×10^{-3}	6.273×10^{-2}	5.753×10^{-3}
T4S	6.141×10^{-3}	1.649×10^{-3}	9.496×10^{-3}	1.926×10^{-3}	6.737×10^{-3}	1.491×10^{-3}	6.848×10^{-3}	1.907×10^{-3}	3.515×10^{-3}	9.935×10^{-4}	5.779×10^{-3}	1.501×10^{-3}
T4L	8.055×10^{-4}	7.284×10^{-4}	5.927×10^{-4}	4.365×10^{-4}	1.246×10^{-3}	7.551×10^{-4}	1.643×10^{-3}	1.057×10^{-3}	0	0	0	0
T4C	3.441×10^{-7}	3.441×10^{-7}	2.773×10^{-6}	1.978×10^{-6}	6.407×10^{-6}	6.407×10^{-6}	9.858×10^{-4}	6.845×10^{-4}	0	0	1.003×10^{-6}	1.003×10^{-6}
T3+T2+T1	4.943×10^{-2}	2.934×10^{-3}	5.454×10^{-2}	3.187×10^{-3}	5.597×10^{-2}	3.132×10^{-3}	5.883×10^{-2}	3.371×10^{-3}	6.153×10^{-2}	3.387×10^{-3}	6.020×10^{-2}	3.398×10^{-3}

$\frac{a_{\text{Spoiler}}}{2\sigma_{\text{beam}}}$	**17**		**18**		**19**		**20**		∞	
Section	P_{loss}[W]	ΔP_{loss}[W]	P_{loss}[W]	ΔP_{loss}[W]	P_{loss}[W]	ΔP_{loss}[W]	P_{loss}[W]	ΔP_{loss}[W]	P_{loss}[W]	ΔP_{loss}[W]
Total	7.838	7.905×10^{-2}	7.842	7.960×10^{-2}	7.868	8.021×10^{-2}	7.872	8.079×10^{-2}	8.029	8.440×10^{-2}
Ex	6.160×10^{-1}	1.801×10^{-2}	6.025×10^{-1}	1.788×10^{-2}	6.155×10^{-1}	1.806×10^{-2}	6.006×10^{-1}	1.772×10^{-2}	6.288×10^{-1}	1.836×10^{-2}
A2PreCol	1.751×10^{-1}	8.964×10^{-3}	1.835×10^{-1}	9.196×10^{-3}	1.676×10^{-1}	9.009×10^{-3}	1.859×10^{-1}	9.288×10^{-3}	1.797×10^{-1}	9.202×10^{-3}
A2Col	6.247	7.323×10^{-2}	6.244	7.378×10^{-2}	6.255	7.440×10^{-2}	6.257	7.507×10^{-2}	6.406	7.883×10^{-2}
A2PostCol	6.802×10^{-1}	1.507×10^{-2}	6.868×10^{-1}	1.516×10^{-2}	7.044×10^{-1}	1.523×10^{-2}	7.174×10^{-1}	1.549×10^{-2}	7.036×10^{-1}	1.511×10^{-2}
M2	5.861×10^{-2}	5.607×10^{-3}	6.201×10^{-2}	5.715×10^{-3}	6.215×10^{-2}	5.775×10^{-3}	4.707×10^{-2}	4.951×10^{-3}	5.014×10^{-2}	5.149×10^{-3}
T4S	2.616×10^{-3}	1.161×10^{-3}	3.760×10^{-3}	1.254×10^{-3}	2.607×10^{-3}	8.606×10^{-4}	4.741×10^{-3}	1.259×10^{-3}	7.491×10^{-4}	3.635×10^{-4}
T4L	0	0	1.562×10^{-3}	9.355×10^{-4}	0	0	0	0	0	0
T4C	1.017×10^{-6}	7.291×10^{-7}	4.155×10^{-7}	4.155×10^{-7}	4.404×10^{-7}	4.404×10^{-7}	0	0	0	0
T3+T2+T1	5.784×10^{-2}	3.326×10^{-3}	5.742×10^{-2}	3.346×10^{-3}	6.000×10^{-2}	3.360×10^{-3}	5.985×10^{-2}	3.366×10^{-3}	6.006×10^{-2}	3.329×10^{-3}

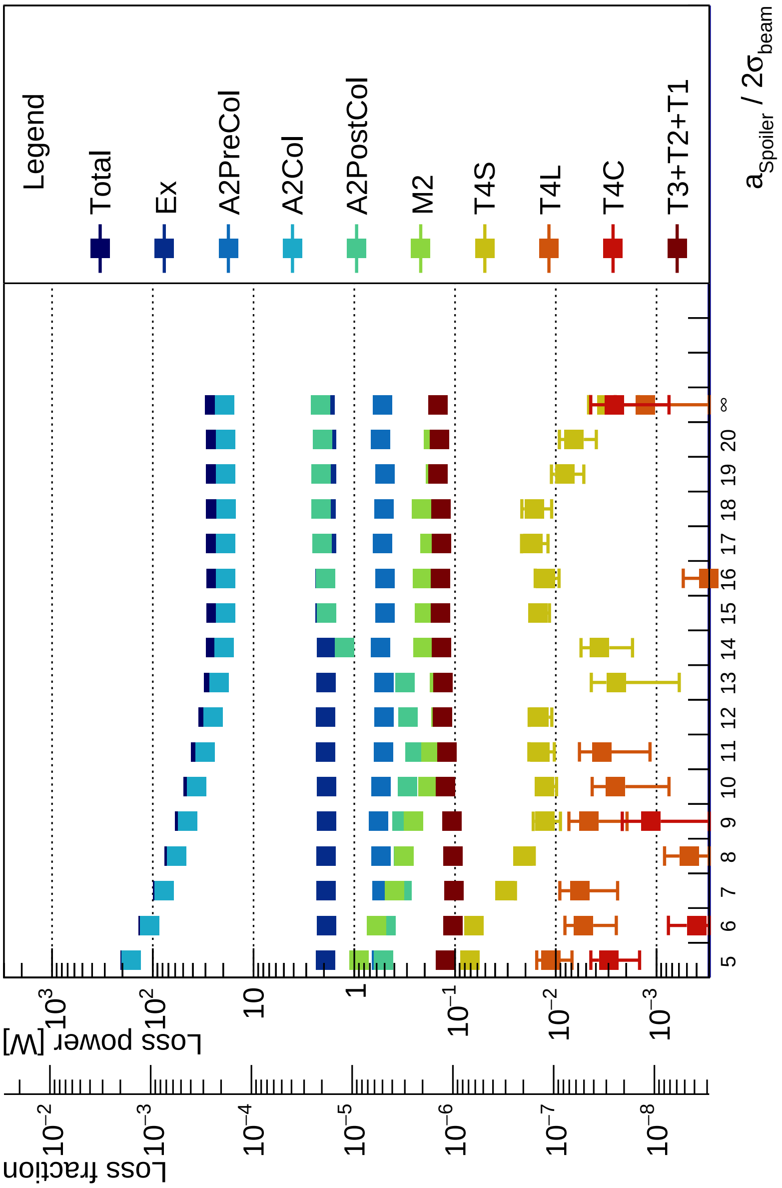

Figure A.17: Spoiler aperture sweep for a He target induced halo.

Table A.17: Loss power numbers from H TAIL spoiler aperture sweep in Figure A.17.

$\frac{a_{\text{Spoiler}}}{2\sigma_{\text{beam}}}$	**5**		**6**		**7**		**8**		**9**		**10**	
Section	P_{loss}[W]	ΔP_{loss}[W]	P_{loss}[W]	ΔP_{loss}[W]	P_{loss}[W]	ΔP_{loss}[W]	P_{loss}[W]	ΔP_{loss}[W]	P_{loss}[W]	ΔP_{loss}[W]	P_{loss}[W]	ΔP_{loss}[W]
Total	1.684×10^{2}	7.658×10^{-1}	1.112×10^{2}	5.861×10^{-1}	8.028×10^{1}	4.812×10^{-1}	6.142×10^{1}	4.135×10^{-1}	4.846×10^{1}	3.619×10^{-1}	3.974×10^{1}	3.258×10^{-1}
Ex	1.932	5.854×10^{-2}	1.883	5.710×10^{-2}	1.902	5.794×10^{-2}	1.912	5.805×10^{-2}	1.882	5.752×10^{-2}	1.893	5.837×10^{-2}
A2PreCol	5.383×10^{-1}	2.920×10^{-2}	5.461×10^{-1}	2.993×10^{-2}	5.282×10^{-1}	2.834×10^{-2}	5.401×10^{-1}	2.956×10^{-2}	5.739×10^{-1}	3.060×10^{-2}	5.453×10^{-1}	2.998×10^{-2}
A2Col	1.643×10^{2}	7.517×10^{-1}	1.075×10^{2}	5.735×10^{-1}	7.697×10^{1}	4.697×10^{-1}	5.820×10^{1}	4.019×10^{-1}	4.528×10^{1}	3.502×10^{-1}	3.668×10^{1}	3.139×10^{-1}
A2PostCol	5.144×10^{-1}	2.521×10^{-2}	4.871×10^{-1}	2.473×10^{-2}	3.347×10^{-1}	1.919×10^{-2}	3.251×10^{-1}	1.981×10^{-2}	3.347×10^{-1}	2.010×10^{-2}	2.969×10^{-1}	1.941×10^{-2}
M2	8.943×10^{-1}	4.044×10^{-2}	6.053×10^{-1}	3.306×10^{-2}	3.996×10^{-1}	2.677×10^{-2}	3.214×10^{-1}	2.425×10^{-2}	2.578×10^{-1}	2.133×10^{-2}	1.861×10^{-1}	1.826×10^{-2}
T4S	7.121×10^{-2}	9.021×10^{-3}	6.478×10^{-2}	8.358×10^{-3}	3.198×10^{-2}	6.834×10^{-3}	2.122×10^{-2}	4.858×10^{-3}	1.287×10^{-2}	3.879×10^{-3}	1.303×10^{-2}	3.208×10^{-3}
T4L	1.118×10^{-2}	4.276×10^{-3}	5.312×10^{-3}	2.803×10^{-3}	5.776×10^{-3}	3.341×10^{-3}	4.740×10^{-4}	3.586×10^{-4}	4.687×10^{-3}	2.724×10^{-3}	2.553×10^{-3}	1.801×10^{-3}
T4C	2.981×10^{-3}	1.507×10^{-3}	4.005×10^{-4}	3.620×10^{-4}	1.230×10^{-5}	6.923×10^{-6}	1.894×10^{-4}	1.368×10^{-4}	1.136×10^{-3}	1.053×10^{-3}	0	0
T3+T2+T1	1.252×10^{-1}	9.334×10^{-3}	1.047×10^{-1}	8.232×10^{-3}	1.031×10^{-1}	8.443×10^{-3}	1.054×10^{-1}	8.237×10^{-3}	1.072×10^{-1}	8.165×10^{-3}	1.241×10^{-1}	9.184×10^{-3}

$\frac{a_{\text{Spoiler}}}{2\sigma_{\text{beam}}}$	**11**		**12**		**13**		**14**		**15**		**16**	
Section	P_{loss}[W]	ΔP_{loss}[W]	P_{loss}[W]	ΔP_{loss}[W]	P_{loss}[W]	ΔP_{loss}[W]	P_{loss}[W]	ΔP_{loss}[W]	P_{loss}[W]	ΔP_{loss}[W]	P_{loss}[W]	ΔP_{loss}[W]
Total	3.342×10^{1}	2.976×10^{-1}	2.834×10^{1}	2.722×10^{-1}	2.491×10^{1}	2.542×10^{-1}	2.367×10^{1}	2.454×10^{-1}	2.361×10^{1}	2.458×10^{-1}	2.363×10^{1}	2.489×10^{-1}
Ex	1.924	5.816×10^{-2}	1.926	5.860×10^{-2}	1.916	5.832×10^{-2}	1.891	5.788×10^{-2}	1.960	5.910×10^{-2}	1.946	5.868×10^{-2}
A2PreCol	5.147×10^{-1}	2.883×10^{-2}	5.073×10^{-1}	2.847×10^{-2}	5.060×10^{-1}	2.809×10^{-2}	5.489×10^{-1}	2.974×10^{-2}	4.963×10^{-1}	2.820×10^{-2}	4.981×10^{-1}	2.811×10^{-2}
A2Col	3.042×10^{1}	2.857×10^{-1}	2.533×10^{1}	2.597×10^{-1}	2.190×10^{1}	2.413×10^{-1}	1.963×10^{1}	2.284×10^{-1}	1.891×10^{1}	2.266×10^{-1}	1.891×10^{1}	2.301×10^{-1}
A2PostCol	2.503×10^{-1}	1.728×10^{-2}	2.917×10^{-1}	1.907×10^{-2}	3.133×10^{-1}	2.000×10^{-2}	1.247	3.861×10^{-2}	1.885	4.700×10^{-2}	1.923	4.691×10^{-2}
M2	1.727×10^{-1}	1.803×10^{-2}	1.386×10^{-1}	1.595×10^{-2}	1.424×10^{-1}	1.620×10^{-2}	2.093×10^{-1}	1.925×10^{-2}	2.021×10^{-1}	1.933×10^{-2}	2.094×10^{-1}	1.940×10^{-2}
T4S	1.442×10^{-2}	4.079×10^{-3}	1.466×10^{-2}	3.712×10^{-3}	2.518×10^{-3}	1.923×10^{-3}	3.675×10^{-3}	1.943×10^{-3}	1.506×10^{-2}	3.500×10^{-3}	1.265×10^{-2}	3.363×10^{-3}
T4L	3.493×10^{-3}	2.332×10^{-3}	1.927×10^{-4}	1.651×10^{-4}	0	0	3.992×10^{-6}	3.992×10^{-6}	0	0	3.024×10^{-4}	2.407×10^{-4}
T4C	4.514×10^{-6}	4.514×10^{-6}	0	0	0	0	1.067×10^{-5}	1.067×10^{-5}	0	0	1.064×10^{-5}	9.241×10^{-6}
T3+T2+T1	1.209×10^{-1}	8.988×10^{-3}	1.331×10^{-1}	9.000×10^{-3}	1.312×10^{-1}	9.177×10^{-3}	1.360×10^{-1}	9.251×10^{-3}	1.401×10^{-1}	9.577×10^{-3}	1.395×10^{-1}	9.503×10^{-3}

$\frac{a_{\text{Spoiler}}}{2\sigma_{\text{beam}}}$	**17**		**18**		**19**		**20**		∞	
Section	P_{loss}[W]	ΔP_{loss}[W]	P_{loss}[W]	ΔP_{loss}[W]	P_{loss}[W]	ΔP_{loss}[W]	P_{loss}[W]	ΔP_{loss}[W]	P_{loss}[W]	ΔP_{loss}[W]
Total	2.370×10^{1}	2.500×10^{-1}	2.367×10^{1}	2.521×10^{-1}	2.386×10^{1}	2.550×10^{-1}	2.387×10^{1}	2.567×10^{-1}	2.424×10^{1}	2.670×10^{-1}
Ex	1.896	5.739×10^{-2}	1.907	5.849×10^{-2}	1.888	5.730×10^{-2}	1.895	5.829×10^{-2}	1.953	5.920×10^{-2}
A2PreCol	5.257×10^{-1}	2.893×10^{-2}	5.064×10^{-1}	2.815×10^{-2}	4.948×10^{-1}	2.772×10^{-2}	5.485×10^{-1}	2.888×10^{-2}	5.251×10^{-1}	2.883×10^{-2}
A2Col	1.885×10^{1}	2.313×10^{-1}	1.875×10^{1}	2.330×10^{-1}	1.903×10^{1}	2.369×10^{-1}	1.905×10^{1}	2.386×10^{-1}	1.929×10^{1}	2.490×10^{-1}
A2PostCol	2.092	4.817×10^{-2}	2.143	4.865×10^{-2}	2.139	4.783×10^{-2}	2.067	4.679×10^{-2}	2.162	4.819×10^{-2}
M2	1.777×10^{-1}	1.785×10^{-2}	2.148×10^{-1}	1.988×10^{-2}	1.561×10^{-1}	1.699×10^{-2}	1.629×10^{-1}	1.689×10^{-2}	1.477×10^{-1}	1.638×10^{-2}
T4S	1.691×10^{-2}	4.956×10^{-3}	1.636×10^{-2}	5.364×10^{-3}	8.160×10^{-3}	2.890×10^{-3}	6.587×10^{-3}	2.626×10^{-3}	3.118×10^{-3}	1.608×10^{-3}
T4L	0	0	0	0	0	0	0	0	1.286×10^{-3}	1.286×10^{-3}
T4C	5.840×10^{-8}	5.840×10^{-8}	1.785×10^{-6}	1.785×10^{-6}	4.087×10^{-7}	4.087×10^{-7}	5.659×10^{-7}	5.659×10^{-7}	2.625×10^{-3}	1.873×10^{-3}
T3+T2+T1	1.368×10^{-1}	9.259×10^{-3}	1.383×10^{-1}	9.495×10^{-3}	1.480×10^{-1}	9.587×10^{-3}	1.434×10^{-1}	1.003×10^{-2}	1.476×10^{-1}	9.894×10^{-3}

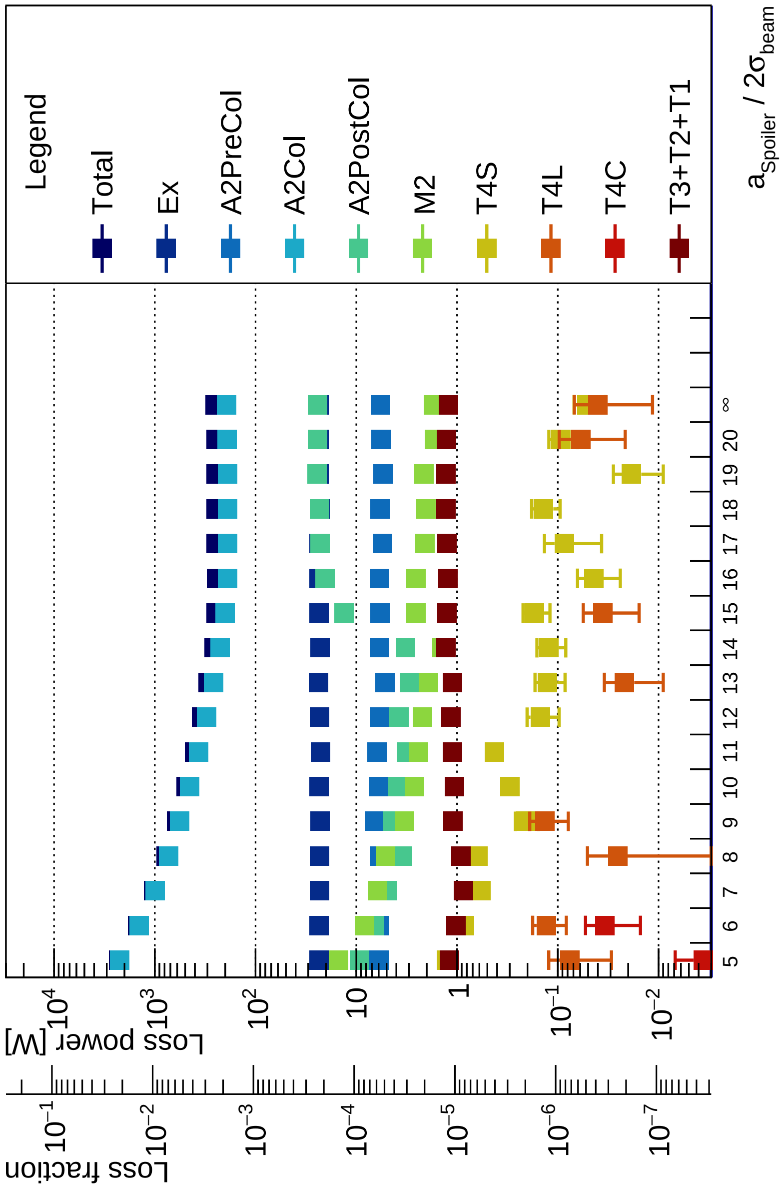

Figure A.18: Spoiler aperture sweep for a O target induced halo.

Table A.18: Loss power numbers from O TAIL spoiler aperture sweep in Figure A.18.

$\frac{a_{\text{Spoiler}}}{2\sigma_{\text{beam}}}$	**5**		**6**		**7**		**8**		**9**		**10**	
Section	P_{loss}[W]	ΔP_{loss}[W]	P_{loss}[W]	ΔP_{loss}[W]	P_{loss}[W]	ΔP_{loss}[W]	P_{loss}[W]	ΔP_{loss}[W]	P_{loss}[W]	ΔP_{loss}[W]	P_{loss}[W]	ΔP_{loss}[W]
Total	2.297×10^{3}	9.870	1.477×10^{3}	7.421	1.032×10^{3}	5.967	7.708×10^{2}	5.061	6.046×10^{2}	4.419	4.891×10^{2}	3.934
Ex	2.343×10^{1}	7.092×10^{-1}	2.330×10^{1}	7.052×10^{-1}	2.312×10^{1}	6.959×10^{-1}	2.320×10^{1}	7.069×10^{-1}	2.286×10^{1}	6.972×10^{-1}	2.354×10^{1}	7.100×10^{-1}
A2PreCol	5.966	3.386×10^{-1}	5.964	3.402×10^{-1}	5.642	3.262×10^{-1}	5.852	3.391×10^{-1}	6.614	3.663×10^{-1}	6.016	3.356×10^{-1}
A2Col	2.240×10^{3}	9.686	1.431×10^{3}	7.270	9.907×10^{2}	5.830	7.316×10^{2}	4.925	5.660×10^{2}	4.280	4.517×10^{2}	3.795
A2PostCol	9.259	3.719×10^{-1}	6.606	3.097×10^{-1}	4.897	2.656×10^{-1}	3.469	2.064×10^{-1}	4.381	2.560×10^{-1}	3.840	2.334×10^{-1}
M2	1.503×10^{1}	5.734×10^{-1}	8.293	4.264×10^{-1}	6.163	3.647×10^{-1}	5.120	3.370×10^{-1}	3.341	2.772×10^{-1}	2.633	2.370×10^{-1}
T4S	1.273	1.368×10^{-1}	8.450×10^{-1}	1.053×10^{-1}	5.787×10^{-1}	8.750×10^{-2}	6.193×10^{-1}	9.434×10^{-2}	2.099×10^{-1}	5.392×10^{-2}	2.982×10^{-1}	5.454×10^{-2}
T4L	7.615×10^{-2}	4.682×10^{-2}	1.299×10^{-1}	4.758×10^{-2}	0	0	2.538×10^{-2}	2.538×10^{-2}	1.343×10^{-1}	5.557×10^{-2}	0	0
T4C	3.603×10^{-3}	3.233×10^{-3}	3.409×10^{-2}	1.897×10^{-2}	2.832×10^{-6}	2.832×10^{-6}	3.046×10^{-4}	2.459×10^{-4}	1.453×10^{-4}	8.765×10^{-5}	0	0
T3+T2+T1	1.193	1.069×10^{-1}	1.024	9.470×10^{-2}	8.618×10^{-1}	8.839×10^{-2}	9.103×10^{-1}	9.537×10^{-2}	1.101	9.932×10^{-2}	1.067	9.486×10^{-2}

$\frac{a_{\text{Spoiler}}}{2\sigma_{\text{beam}}}$	**11**		**12**		**13**		**14**		**15**		**16**	
Section	P_{loss}[W]	ΔP_{loss}[W]	P_{loss}[W]	ΔP_{loss}[W]	P_{loss}[W]	ΔP_{loss}[W]	P_{loss}[W]	ΔP_{loss}[W]	P_{loss}[W]	ΔP_{loss}[W]	P_{loss}[W]	ΔP_{loss}[W]
Total	4.029×10^{2}	3.541	3.432×10^{2}	3.259	2.963×10^{2}	3.019	2.592×10^{2}	2.814	2.463×10^{2}	2.724	2.439×10^{2}	2.699
Ex	2.276×10^{1}	6.933×10^{-1}	2.311×10^{1}	6.993×10^{-1}	2.365×10^{1}	7.036×10^{-1}	2.303×10^{1}	6.931×10^{-1}	2.353×10^{1}	7.071×10^{-1}	2.335×10^{1}	7.022×10^{-1}
A2PreCol	6.239	3.521×10^{-1}	5.914	3.363×10^{-1}	5.210	3.168×10^{-1}	5.891	3.377×10^{-1}	5.799	3.512×10^{-1}	5.916	3.337×10^{-1}
A2Col	3.668×10^{2}	3.399	3.069×10^{2}	3.112	2.613×10^{2}	2.871	2.243×10^{2}	2.661	1.997×10^{2}	2.517	1.904×10^{2}	2.470
A2PostCol	3.186	2.164×10^{-1}	3.783	2.281×10^{-1}	2.960	1.969×10^{-1}	3.231	2.114×10^{-1}	1.326×10^{1}	4.446×10^{-1}	2.042×10^{1}	5.449×10^{-1}
M2	2.414	2.267×10^{-1}	2.197	2.155×10^{-1}	1.917	2.074×10^{-1}	1.410	1.716×10^{-1}	2.556	2.404×10^{-1}	2.557	2.340×10^{-1}
T4S	4.266×10^{-1}	7.641×10^{-2}	1.494×10^{-1}	5.233×10^{-2}	1.265×10^{-1}	4.180×10^{-2}	1.222×10^{-1}	3.893×10^{-2}	1.704×10^{-1}	5.083×10^{-2}	4.384×10^{-2}	1.986×10^{-2}
T4L	0	0	0	0	2.175×10^{-2}	1.276×10^{-2}	0	0	3.576×10^{-2}	2.017×10^{-2}	1.731×10^{-4}	1.731×10^{-4}
T4C	0	0	1.046×10^{-4}	1.046×10^{-4}	0	0	0	0	0	0	0	0
T3+T2+T1	1.112	9.477×10^{-2}	1.154	9.896×10^{-2}	1.108	9.190×10^{-2}	1.284	1.002×10^{-1}	1.265	9.967×10^{-2}	1.231	9.823×10^{-2}

$\frac{a_{\text{Spoiler}}}{2\sigma_{\text{beam}}}$	**17**		**18**		**19**		**20**		∞	
Section	P_{loss}[W]	ΔP_{loss}[W]	P_{loss}[W]	ΔP_{loss}[W]	P_{loss}[W]	ΔP_{loss}[W]	P_{loss}[W]	ΔP_{loss}[W]	P_{loss}[W]	ΔP_{loss}[W]
Total	2.452×10^{2}	2.731	2.453×10^{2}	2.747	2.464×10^{2}	2.774	2.471×10^{2}	2.802	2.513×10^{2}	2.943
Ex	2.330×10^{1}	7.048×10^{-1}	2.288×10^{1}	6.896×10^{-1}	2.334×10^{1}	7.022×10^{-1}	2.337×10^{1}	7.006×10^{-1}	2.352×10^{1}	7.110×10^{-1}
A2PreCol	5.500	3.164×10^{-1}	5.813	3.254×10^{-1}	5.445	3.196×10^{-1}	5.689	3.404×10^{-1}	5.754	3.369×10^{-1}
A2Col	1.902×10^{2}	2.503	1.900×10^{2}	2.526	1.896×10^{2}	2.547	1.908×10^{2}	2.579	1.948×10^{2}	2.730
A2PostCol	2.282×10^{1}	5.609×10^{-1}	2.316×10^{1}	5.533×10^{-1}	2.449×10^{1}	5.716×10^{-1}	2.415×10^{1}	5.630×10^{-1}	2.427×10^{1}	5.549×10^{-1}
M2	2.088	2.079×10^{-1}	2.027	2.037×10^{-1}	2.120	2.170×10^{-1}	1.682	1.858×10^{-1}	1.705	1.908×10^{-1}
T4S	8.623×10^{-2}	4.951×10^{-2}	1.383×10^{-1}	4.332×10^{-2}	1.852×10^{-2}	9.544×10^{-3}	9.326×10^{-2}	2.939×10^{-2}	5.135×10^{-2}	1.765×10^{-2}
T4L	0	0	0	0	0	0	5.912×10^{-2}	3.769×10^{-2}	3.995×10^{-2}	2.848×10^{-2}
T4C	2.459×10^{-6}	2.459×10^{-6}	0	0	5.196×10^{-5}	5.196×10^{-5}	2.004×10^{-5}	2.004×10^{-5}	0	0
T3+T2+T1	1.258	1.010×10^{-1}	1.284	1.026×10^{-1}	1.285	1.074×10^{-1}	1.279	1.001×10^{-1}	1.211	9.571×10^{-2}

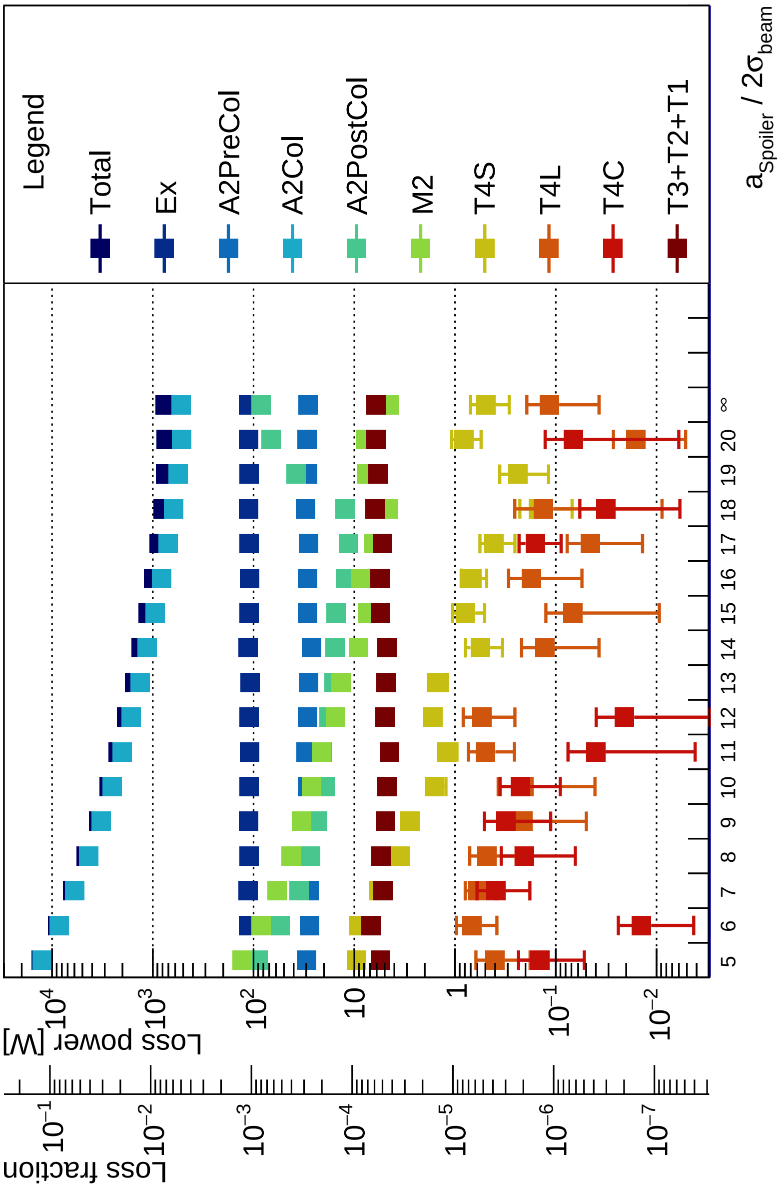

Figure A.19: Spoiler aperture sweep for a Ar target induced halo.

Table A.19: Loss power numbers from Ar TAIL spoiler aperture sweep in Figure A.19.

$\frac{a_{\text{Spoiler}}}{2\sigma_{\text{beam}}}$	**5**		**6**		**7**		**8**		**9**		**10**	
Section	P_{loss}[W]	ΔP_{loss}[W]	P_{loss}[W]	ΔP_{loss}[W]	P_{loss}[W]	ΔP_{loss}[W]	P_{loss}[W]	ΔP_{loss}[W]	P_{loss}[W]	ΔP_{loss}[W]	P_{loss}[W]	ΔP_{loss}[W]
Total	1.285×10^{4}	5.505×10^{1}	8.799×10^{3}	4.243×10^{1}	6.223×10^{3}	3.401×10^{1}	4.570×10^{3}	2.821×10^{1}	3.460×10^{3}	2.401×10^{1}	2.710×10^{3}	2.093×10^{1}
Ex	1.110×10^{2}	3.460	1.121×10^{2}	3.477	1.134×10^{2}	3.478	1.105×10^{2}	3.413	1.115×10^{2}	3.451	1.106×10^{2}	3.407
A2PreCol	2.995×10^{1}	1.688	2.784×10^{1}	1.581	2.820×10^{1}	1.653	2.864×10^{1}	1.672	2.811×10^{1}	1.624	2.913×10^{1}	1.670
A2Col	1.247×10^{4}	5.379×10^{1}	8.504×10^{3}	4.144×10^{1}	5.976×10^{3}	3.317×10^{1}	4.352×10^{3}	2.746×10^{1}	3.256×10^{3}	2.328×10^{1}	2.518×10^{3}	2.021×10^{1}
A2PostCol	8.997×10^{1}	2.559	5.427×10^{1}	1.972	3.530×10^{1}	1.599	2.722×10^{1}	1.349	2.309×10^{1}	1.268	1.950×10^{1}	1.159
M2	1.304×10^{2}	3.781	8.425×10^{1}	3.042	5.824×10^{1}	2.510	4.242×10^{1}	2.161	3.357×10^{1}	1.909	2.657×10^{1}	1.725
T4S	9.544	8.763×10^{-1}	8.972	8.145×10^{-1}	5.695	6.699×10^{-1}	3.490	4.715×10^{-1}	2.790	4.119×10^{-1}	1.594	3.625×10^{-1}
T4L	4.003×10^{-1}	2.204×10^{-1}	6.769×10^{-1}	2.926×10^{-1}	5.895×10^{-1}	2.026×10^{-1}	4.814×10^{-1}	2.334×10^{-1}	2.132×10^{-1}	1.634×10^{-1}	2.070×10^{-1}	1.661×10^{-1}
T4C	1.432×10^{-1}	9.111×10^{-2}	1.411×10^{-2}	9.837×10^{-3}	3.930×10^{-1}	2.121×10^{-1}	2.059×10^{-1}	1.419×10^{-1}	3.118×10^{-1}	1.994×10^{-1}	2.239×10^{-1}	1.336×10^{-1}
T3+T2+T1	5.512	5.223×10^{-1}	6.818	5.980×10^{-1}	5.168	4.867×10^{-1}	5.404	5.473×10^{-1}	4.912	5.029×10^{-1}	4.740	4.390×10^{-1}

$\frac{a_{\text{Spoiler}}}{2\sigma_{\text{beam}}}$	**11**		**12**		**13**		**14**		**15**		**16**	
Section	P_{loss}[W]	ΔP_{loss}[W]	P_{loss}[W]	ΔP_{loss}[W]	P_{loss}[W]	ΔP_{loss}[W]	P_{loss}[W]	ΔP_{loss}[W]	P_{loss}[W]	ΔP_{loss}[W]	P_{loss}[W]	ΔP_{loss}[W]
Total	2.195×10^{3}	1.859×10^{1}	1.815×10^{3}	1.682×10^{1}	1.515×10^{3}	1.525×10^{1}	1.303×10^{3}	1.402×10^{1}	1.116×10^{3}	1.291×10^{1}	9.798×10^{2}	1.205×10^{1}
Ex	1.096×10^{2}	3.384	1.114×10^{2}	3.432	1.085×10^{2}	3.388	1.130×10^{2}	3.464	1.112×10^{2}	3.413	1.098×10^{2}	3.367
A2PreCol	3.014×10^{1}	1.640	2.921×10^{1}	1.687	2.846×10^{1}	1.621	2.671×10^{1}	1.545	2.909×10^{1}	1.720	2.899×10^{1}	1.673
A2Col	2.008×10^{3}	1.786×10^{1}	1.635×10^{3}	1.608×10^{1}	1.343×10^{3}	1.450×10^{1}	1.133×10^{3}	1.325×10^{1}	9.468×10^{2}	1.210×10^{1}	8.138×10^{2}	1.122×10^{1}
A2PostCol	2.080×10^{1}	1.237	1.782×10^{1}	1.106	1.590×10^{1}	1.068	1.552×10^{1}	1.060	1.524×10^{1}	1.039	1.220×10^{1}	8.624×10^{-1}
M2	2.105×10^{1}	1.545	1.530×10^{1}	1.302	1.349×10^{1}	1.216	9.114	9.834×10^{-1}	7.403	9.051×10^{-1}	8.599	9.873×10^{-1}
T4S	1.208	2.504×10^{-1}	1.663	3.213×10^{-1}	1.532	3.432×10^{-1}	5.623×10^{-1}	2.247×10^{-1}	7.862×10^{-1}	2.777×10^{-1}	6.776×10^{-1}	1.917×10^{-1}
T4L	4.967×10^{-1}	2.390×10^{-1}	5.421×10^{-1}	2.875×10^{-1}	0	0	1.279×10^{-1}	9.062×10^{-2}	6.741×10^{-2}	5.803×10^{-2}	1.745×10^{-1}	1.195×10^{-1}
T4C	3.990×10^{-2}	3.576×10^{-2}	2.079×10^{-2}	1.893×10^{-2}	0	0	5.128×10^{-4}	3.798×10^{-4}	2.831×10^{-4}	2.831×10^{-4}	2.145×10^{-4}	2.145×10^{-4}
T3+T2+T1	4.475	4.466×10^{-1}	4.963	4.578×10^{-1}	4.865	4.657×10^{-1}	4.747	4.511×10^{-1}	5.520	4.944×10^{-1}	5.539	5.142×10^{-1}

$\frac{a_{\text{Spoiler}}}{2\sigma_{\text{beam}}}$	**17**		**18**		**19**		**20**		∞	
Section	P_{loss}[W]	ΔP_{loss}[W]	P_{loss}[W]	ΔP_{loss}[W]	P_{loss}[W]	ΔP_{loss}[W]	P_{loss}[W]	ΔP_{loss}[W]	P_{loss}[W]	ΔP_{loss}[W]
Total	8.686×10^{2}	1.126×10^{1}	7.884×10^{2}	1.072×10^{1}	7.493×10^{2}	1.029×10^{1}	7.404×10^{2}	1.016×10^{1}	7.583×10^{2}	1.105×10^{1}
Ex	1.112×10^{2}	3.456	1.118×10^{2}	3.488	1.112×10^{2}	3.439	1.114×10^{2}	3.457	1.123×10^{2}	3.493
A2PreCol	2.835×10^{1}	1.664	3.042×10^{1}	1.637	2.898×10^{1}	1.623	2.944×10^{1}	1.676	2.867×10^{1}	1.644
A2Col	7.053×10^{2}	1.038×10^{1}	6.227×10^{2}	9.813	5.575×10^{2}	9.218	5.179×10^{2}	8.929	5.216×10^{2}	9.890
A2PostCol	1.143×10^{1}	8.914×10^{-1}	1.235×10^{1}	8.840×10^{-1}	3.794×10^{1}	1.691	6.690×10^{1}	2.223	8.467×10^{1}	2.358
M2	6.389	8.254×10^{-1}	4.560	6.915×10^{-1}	7.539	8.910×10^{-1}	7.712	8.760×10^{-1}	4.456	6.669×10^{-1}
T4S	4.104×10^{-1}	1.560×10^{-1}	1.482×10^{-1}	7.923×10^{-2}	2.389×10^{-1}	1.210×10^{-1}	8.157×10^{-1}	2.643×10^{-1}	4.956×10^{-1}	2.059×10^{-1}
T4L	4.545×10^{-2}	3.169×10^{-2}	1.320×10^{-1}	1.232×10^{-1}	0	0	1.597×10^{-2}	1.083×10^{-2}	1.156×10^{-1}	7.833×10^{-2}
T4C	1.601×10^{-1}	7.151×10^{-2}	3.180×10^{-2}	2.593×10^{-2}	2.079×10^{-5}	2.079×10^{-5}	6.677×10^{-2}	6.075×10^{-2}	2.141×10^{-4}	2.141×10^{-4}
T3+T2+T1	5.271	4.447×10^{-1}	6.219	5.200×10^{-1}	5.842	4.856×10^{-1}	6.100	4.950×10^{-1}	6.056	5.151×10^{-1}

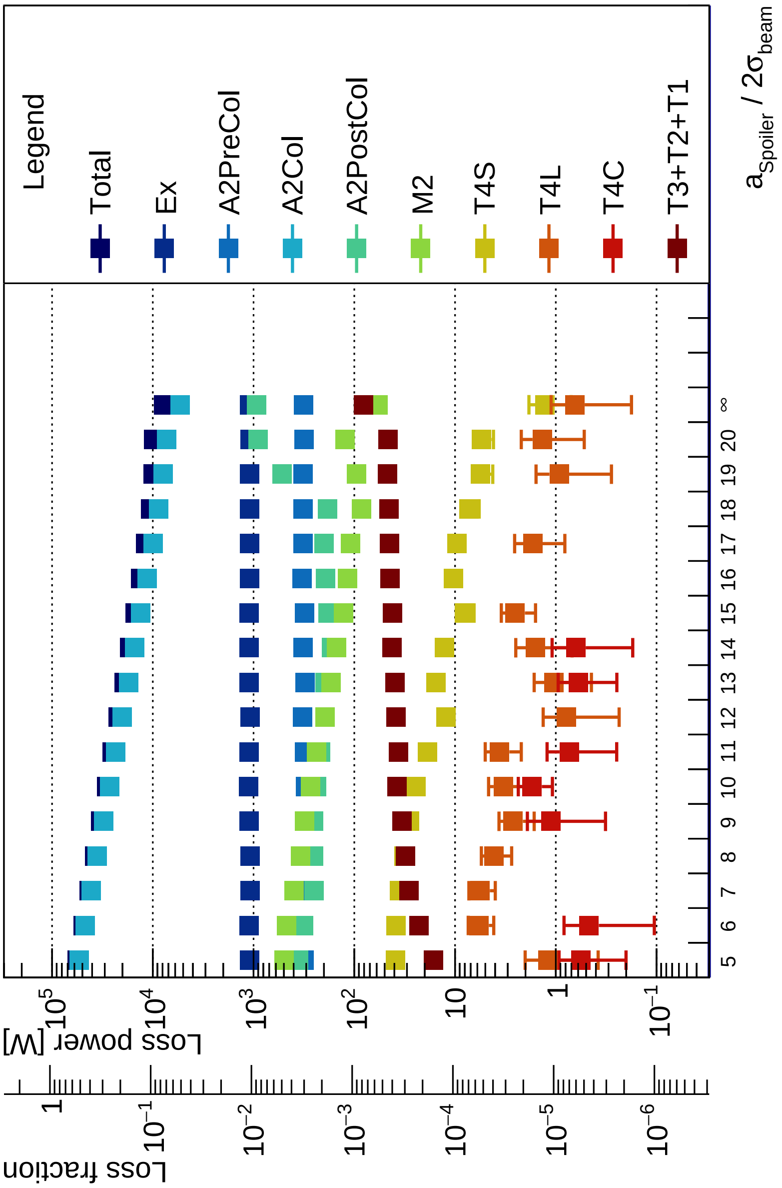

Figure A.20: Spoiler aperture sweep for a Xe target induced halo.

Table A.20: Loss power numbers from Xe TAIL spoiler aperture sweep in Figure A.20.

$\frac{a_{\text{Spoiler}}}{2\sigma_{\text{beam}}}$	**5**		**6**		**7**		**8**		**9**		**10**	
Section	P_{loss}[W]	ΔP_{loss}[W]	P_{loss}[W]	ΔP_{loss}[W]	P_{loss}[W]	ΔP_{loss}[W]	P_{loss}[W]	ΔP_{loss}[W]	P_{loss}[W]	ΔP_{loss}[W]	P_{loss}[W]	ΔP_{loss}[W]
Total	5.638×10^{4}	2.833×10^{2}	4.931×10^{4}	2.549×10^{2}	4.301×10^{4}	2.294×10^{2}	3.766×10^{4}	2.079×10^{2}	3.296×10^{4}	1.884×10^{2}	2.879×10^{4}	1.712×10^{2}
Ex	1.097×10^{3}	2.234×10^{1}	1.107×10^{3}	2.264×10^{1}	1.086×10^{3}	2.220×10^{1}	1.088×10^{3}	2.230×10^{1}	1.112×10^{3}	2.270×10^{1}	1.118×10^{3}	2.265×10^{1}
A2PreCol	3.167×10^{2}	1.122×10^{1}	3.183×10^{2}	1.146×10^{1}	3.260×10^{2}	1.144×10^{1}	3.150×10^{2}	1.136×10^{1}	3.055×10^{2}	1.136×10^{1}	3.053×10^{2}	1.137×10^{1}
A2Col	5.405×10^{4}	2.730×10^{2}	4.702×10^{4}	2.449×10^{2}	4.088×10^{4}	2.201×10^{2}	3.560×10^{4}	1.989×10^{2}	3.091×10^{4}	1.795×10^{2}	2.678×10^{4}	1.625×10^{2}
A2PostCol	3.584×10^{2}	1.054×10^{1}	3.182×10^{2}	9.936	2.508×10^{2}	8.696	2.534×10^{2}	8.549	2.533×10^{2}	8.697	2.378×10^{2}	8.144
M2	5.007×10^{2}	1.513×10^{1}	4.709×10^{2}	1.472×10^{1}	3.962×10^{2}	1.362×10^{1}	3.410×10^{2}	1.253×10^{1}	3.127×10^{2}	1.203×10^{1}	2.728×10^{2}	1.120×10^{1}
T4S	3.892×10^{1}	3.396	3.844×10^{1}	3.406	3.558×10^{1}	3.368	3.216×10^{1}	3.107	2.838×10^{1}	2.754	2.432×10^{1}	2.742
T4L	1.197	8.171×10^{-1}	5.765	1.636	5.637	1.650	4.112	1.369	2.651	1.012	3.315	1.332
T4C	5.645×10^{-1}	3.637×10^{-1}	4.669×10^{-1}	3.617×10^{-1}	1.123×10^{-2}	5.829×10^{-3}	3.141×10^{-3}	1.243×10^{-3}	1.118	7.969×10^{-1}	1.719	6.381×10^{-1}
T3+T2+T1	1.641×10^{1}	1.724	2.276×10^{1}	2.137	2.879×10^{1}	2.394	3.113×10^{1}	2.410	3.372×10^{1}	2.608	3.753×10^{1}	2.741

$\frac{a_{\text{Spoiler}}}{2\sigma_{\text{beam}}}$	**11**		**12**		**13**		**14**		**15**		**16**	
Section	P_{loss}[W]	ΔP_{loss}[W]	P_{loss}[W]	ΔP_{loss}[W]	P_{loss}[W]	ΔP_{loss}[W]	P_{loss}[W]	ΔP_{loss}[W]	P_{loss}[W]	ΔP_{loss}[W]	P_{loss}[W]	ΔP_{loss}[W]
Total	2.518×10^{4}	1.560×10^{2}	2.202×10^{4}	1.425×10^{2}	1.927×10^{4}	1.305×10^{2}	1.699×10^{4}	1.202×10^{2}	1.497×10^{4}	1.107×10^{2}	1.320×10^{4}	1.023×10^{2}
Ex	1.101×10^{3}	2.254×10^{1}	1.084×10^{3}	2.223×10^{1}	1.107×10^{3}	2.242×10^{1}	1.108×10^{3}	2.254×10^{1}	1.105×10^{3}	2.238×10^{1}	1.089×10^{3}	2.237×10^{1}
A2PreCol	3.127×10^{2}	1.102×10^{1}	3.254×10^{2}	1.141×10^{1}	3.097×10^{2}	1.128×10^{1}	3.219×10^{2}	1.171×10^{1}	3.131×10^{2}	1.115×10^{1}	3.292×10^{2}	1.175×10^{1}
A2Col	2.325×10^{4}	1.478×10^{2}	2.017×10^{4}	1.345×10^{2}	1.744×10^{4}	1.226×10^{2}	1.518×10^{4}	1.124×10^{2}	1.319×10^{4}	1.029×10^{2}	1.142×10^{4}	9.440×10^{1}
A2PostCol	2.155×10^{2}	7.801	1.946×10^{2}	7.543	1.953×10^{2}	7.657	1.689×10^{2}	7.035	1.831×10^{2}	7.325	1.921×10^{2}	7.394
M2	2.376×10^{2}	1.049×10^{1}	1.957×10^{2}	9.418	1.697×10^{2}	8.894	1.503×10^{2}	8.219	1.284×10^{2}	7.730	1.173×10^{2}	7.205
T4S	1.883×10^{1}	2.578	1.235×10^{1}	1.802	1.539×10^{1}	2.217	1.267×10^{1}	1.884	8.087	1.613	1.037×10^{1}	1.946
T4L	3.609	1.408	7.846×10^{-1}	5.495×10^{-1}	1.041	5.980×10^{-1}	1.593	9.031×10^{-1}	2.532	9.426×10^{-1}	6.601×10^{-3}	4.766×10^{-3}
T4C	7.344×10^{-1}	4.859×10^{-1}	1.447×10^{-2}	1.206×10^{-2}	5.976×10^{-1}	3.498×10^{-1}	6.302×10^{-1}	4.579×10^{-1}	1.317×10^{-3}	1.259×10^{-3}	1.087×10^{-2}	1.001×10^{-2}
T3+T2+T1	3.656×10^{1}	2.674	3.842×10^{1}	2.678	3.961×10^{1}	2.767	4.208×10^{1}	2.810	4.198×10^{1}	2.825	4.443×10^{1}	2.836

$\frac{a_{\text{Spoiler}}}{2\sigma_{\text{beam}}}$	**17**		**18**		**19**		**20**		∞	
Section	P_{loss}[W]	ΔP_{loss}[W]	P_{loss}[W]	ΔP_{loss}[W]	P_{loss}[W]	ΔP_{loss}[W]	P_{loss}[W]	ΔP_{loss}[W]	P_{loss}[W]	ΔP_{loss}[W]
Total	1.175×10^{4}	9.506×10^{1}	1.047×10^{4}	8.843×10^{1}	9.942×10^{3}	8.529×10^{1}	9.802×10^{3}	8.409×10^{1}	1.008×10^{4}	9.016×10^{1}
Ex	1.093×10^{3}	2.238×10^{1}	1.099×10^{3}	2.234×10^{1}	1.097×10^{3}	2.239×10^{1}	1.088×10^{3}	2.226×10^{1}	1.081×10^{3}	2.215×10^{1}
A2PreCol	3.221×10^{2}	1.139×10^{1}	3.229×10^{2}	1.176×10^{1}	3.215×10^{2}	1.158×10^{1}	3.166×10^{2}	1.145×10^{1}	3.239×10^{2}	1.163×10^{1}
A2Col	9.974×10^{3}	8.711×10^{1}	8.729×10^{3}	8.054×10^{1}	7.855×10^{3}	7.593×10^{1}	7.322×10^{3}	7.314×10^{1}	7.408×10^{3}	7.949×10^{1}
A2PostCol	2.008×10^{2}	7.897	1.848×10^{2}	7.271	5.200×10^{2}	1.271×10^{1}	8.982×10^{2}	1.680×10^{1}	1.157×10^{3}	1.809×10^{1}
M2	1.094×10^{2}	7.182	8.435×10^{1}	6.187	9.547×10^{1}	6.520	1.238×10^{2}	7.366	6.659×10^{1}	5.405
T4S	9.590	1.587	7.312	1.550	5.613	1.390	5.446	1.290	2.981	8.821×10^{-1}
T4L	1.687	8.743×10^{-1}	0	0	9.254×10^{-1}	6.451×10^{-1}	1.361	8.395×10^{-1}	7.225×10^{-1}	4.521×10^{-1}
T4C	1.261×10^{-2}	8.588×10^{-3}	1.027×10^{-3}	9.697×10^{-4}	7.229×10^{-5}	6.036×10^{-5}	0	0	4.875×10^{-3}	4.817×10^{-3}
T3+T2+T1	4.467×10^{1}	2.837	4.506×10^{1}	2.808	4.703×10^{1}	2.988	4.630×10^{1}	2.907	4.482×10^{1}	2.915

A.5 Aperture Sweeps of the Second Collimator

A.5.1 With Halo Spoiler

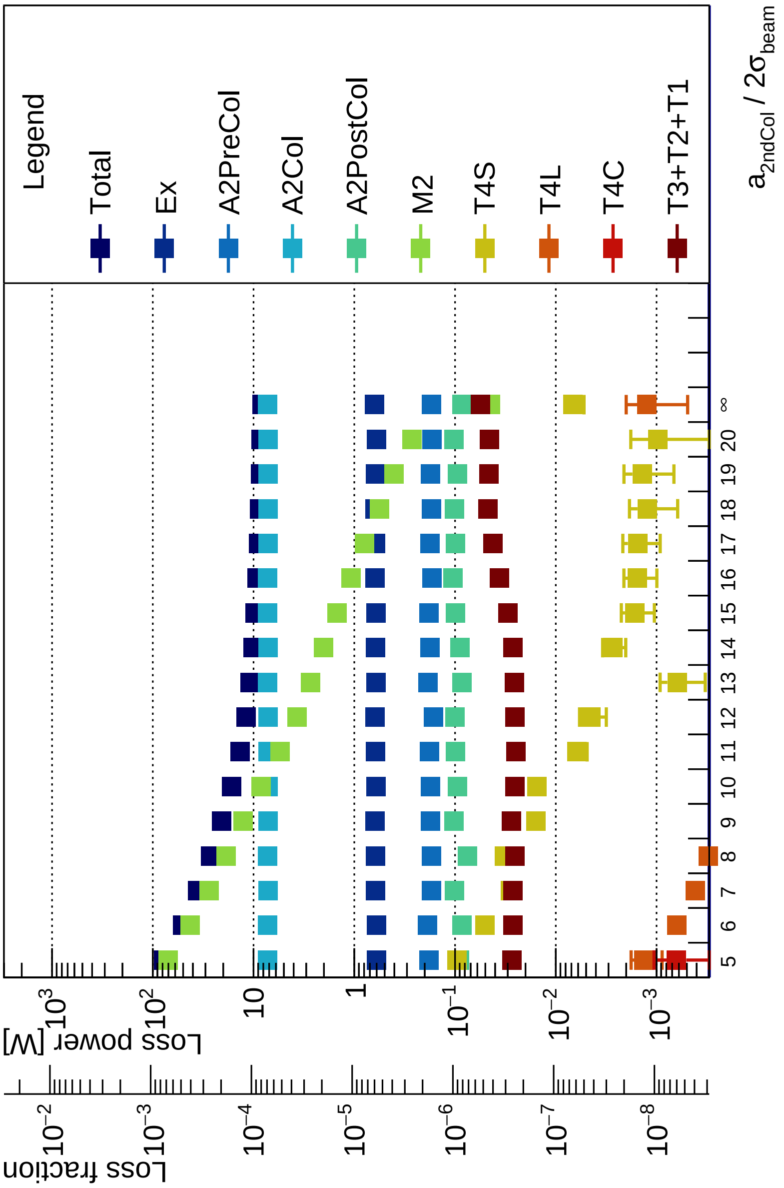

Figure A.21: Second collimator aperture sweep with spoiler for a H target induced halo.

Table A.21: Loss power numbers from H TAIL second collimator aperture sweep with spoiler in Figure A.21.

$\frac{a_{2\text{ndCol}}}{2\sigma_{\text{beam}}}$	**5**		**6**		**7**		**8**		**9**		**10**	
Section	P_{loss}[W]	ΔP_{loss}[W]	P_{loss}[W]	ΔP_{loss}[W]	P_{loss}[W]	ΔP_{loss}[W]	P_{loss}[W]	ΔP_{loss}[W]	P_{loss}[W]	ΔP_{loss}[W]	P_{loss}[W]	ΔP_{loss}[W]
Total	7.842×10^{1}	3.317×10^{-1}	5.086×10^{1}	2.515×10^{-1}	3.590×10^{1}	2.025×10^{-1}	2.679×10^{1}	1.692×10^{-1}	2.081×10^{1}	1.446×10^{-1}	1.659×10^{1}	1.258×10^{-1}
Ex	6.047×10^{-1}	1.777×10^{-2}	6.021×10^{-1}	1.796×10^{-2}	6.154×10^{-1}	1.809×10^{-2}	6.173×10^{-1}	1.821×10^{-2}	6.264×10^{-1}	1.820×10^{-2}	6.093×10^{-1}	1.795×10^{-2}
A2PreCol	1.820×10^{-1}	9.144×10^{-3}	1.886×10^{-1}	9.675×10^{-3}	1.718×10^{-1}	9.192×10^{-3}	1.705×10^{-1}	9.033×10^{-3}	1.763×10^{-1}	8.894×10^{-3}	1.758×10^{-1}	9.225×10^{-3}
A2Col	7.228	7.601×10^{-2}	7.228	7.605×10^{-2}	7.194	7.572×10^{-2}	7.228	7.615×10^{-2}	7.189	7.557×10^{-2}	7.210	7.590×10^{-2}
A2PostCol	9.050×10^{-2}	5.676×10^{-3}	8.551×10^{-2}	5.378×10^{-3}	1.008×10^{-1}	6.077×10^{-3}	7.533×10^{-2}	5.049×10^{-3}	1.020×10^{-1}	6.123×10^{-3}	9.508×10^{-2}	5.711×10^{-3}
M2	7.019×10^{1}	3.038×10^{-1}	4.268×10^{1}	2.236×10^{-1}	2.776×10^{1}	1.739×10^{-1}	1.864×10^{1}	1.387×10^{-1}	1.268×10^{1}	1.122×10^{-1}	8.459	9.010×10^{-2}
T4S	9.552×10^{-2}	5.491×10^{-3}	5.051×10^{-2}	3.558×10^{-3}	2.828×10^{-2}	2.636×10^{-3}	3.230×10^{-2}	3.433×10^{-3}	1.582×10^{-2}	1.835×10^{-3}	1.535×10^{-2}	2.233×10^{-3}
T4L	1.335×10^{-3}	4.538×10^{-4}	6.294×10^{-4}	4.857×10^{-5}	4.143×10^{-4}	6.436×10^{-5}	3.078×10^{-4}	3.414×10^{-5}	1.869×10^{-4}	1.885×10^{-5}	1.501×10^{-4}	1.931×10^{-5}
T4C	6.330×10^{-4}	4.264×10^{-4}	5.470×10^{-5}	2.481×10^{-5}	1.593×10^{-5}	9.051×10^{-6}	3.529×10^{-5}	1.942×10^{-5}	3.879×10^{-6}	1.839×10^{-6}	4.144×10^{-6}	1.993×10^{-6}
T3+T2+T1	2.738×10^{-2}	2.547×10^{-3}	2.669×10^{-2}	2.406×10^{-3}	2.674×10^{-2}	2.348×10^{-3}	2.552×10^{-2}	2.336×10^{-3}	2.745×10^{-2}	2.529×10^{-3}	2.553×10^{-2}	2.345×10^{-3}

$\frac{a_{2\text{ndCol}}}{2\sigma_{\text{beam}}}$	**11**		**12**		**13**		**14**		**15**		**16**	
Section	P_{loss}[W]	ΔP_{loss}[W]	P_{loss}[W]	ΔP_{loss}[W]	P_{loss}[W]	ΔP_{loss}[W]	P_{loss}[W]	ΔP_{loss}[W]	P_{loss}[W]	ΔP_{loss}[W]	P_{loss}[W]	ΔP_{loss}[W]
Total	1.361×10^{1}	1.112×10^{-1}	1.181×10^{1}	1.016×10^{-1}	1.085×10^{1}	9.629×10^{-2}	1.013×10^{1}	9.188×10^{-2}	9.625	8.897×10^{-2}	9.234	8.655×10^{-2}
Ex	6.156×10^{-1}	1.782×10^{-2}	6.255×10^{-1}	1.832×10^{-2}	6.085×10^{-1}	1.799×10^{-2}	6.158×10^{-1}	1.825×10^{-2}	6.083×10^{-1}	1.793×10^{-2}	6.210×10^{-1}	1.808×10^{-2}
A2PreCol	1.792×10^{-1}	9.302×10^{-3}	1.632×10^{-1}	8.751×10^{-3}	1.852×10^{-1}	9.546×10^{-3}	1.783×10^{-1}	9.455×10^{-3}	1.815×10^{-1}	9.143×10^{-3}	1.689×10^{-1}	8.987×10^{-3}
A2Col	7.206	7.608×10^{-2}	7.215	7.591×10^{-2}	7.232	7.609×10^{-2}	7.196	7.565×10^{-2}	7.221	7.610×10^{-2}	7.227	7.615×10^{-2}
A2PostCol	9.951×10^{-2}	5.873×10^{-3}	9.988×10^{-2}	6.017×10^{-3}	8.513×10^{-2}	5.574×10^{-3}	8.920×10^{-2}	5.622×10^{-3}	9.958×10^{-2}	6.045×10^{-3}	1.054×10^{-1}	6.169×10^{-3}
M2	5.479	7.156×10^{-2}	3.681	5.823×10^{-2}	2.714	4.963×10^{-2}	2.019	4.249×10^{-2}	1.484	3.611×10^{-2}	1.073	3.052×10^{-2}
T4S	6.207×10^{-3}	1.321×10^{-3}	4.482×10^{-3}	1.329×10^{-3}	6.251×10^{-4}	2.966×10^{-4}	2.724×10^{-3}	7.029×10^{-4}	1.644×10^{-3}	5.931×10^{-4}	1.551×10^{-3}	5.578×10^{-4}
T4L	8.202×10^{-5}	1.186×10^{-5}	1.020×10^{-4}	2.525×10^{-5}	6.893×10^{-5}	2.252×10^{-5}	9.044×10^{-5}	4.003×10^{-5}	3.462×10^{-5}	7.375×10^{-6}	4.102×10^{-5}	1.556×10^{-5}
T4C	1.221×10^{-6}	1.212×10^{-6}	1.276×10^{-5}	1.200×10^{-5}	0	0	0	0	7.898×10^{-7}	7.898×10^{-7}	7.086×10^{-8}	7.086×10^{-8}
T3+T2+T1	2.489×10^{-2}	2.241×10^{-3}	2.548×10^{-2}	2.315×10^{-3}	2.580×10^{-2}	2.256×10^{-3}	2.672×10^{-2}	2.412×10^{-3}	2.996×10^{-2}	2.587×10^{-3}	3.626×10^{-2}	2.673×10^{-3}

$\frac{a_{2\text{ndCol}}}{2\sigma_{\text{beam}}}$	**17**		**18**		**19**		**20**		∞	
Section	P_{loss}[W]	ΔP_{loss}[W]	P_{loss}[W]	ΔP_{loss}[W]	P_{loss}[W]	ΔP_{loss}[W]	P_{loss}[W]	ΔP_{loss}[W]	P_{loss}[W]	ΔP_{loss}[W]
Total	8.931	8.460×10^{-2}	8.723	8.330×10^{-2}	8.545	8.202×10^{-2}	8.391	8.103×10^{-2}	8.217	8.008×10^{-2}
Ex	6.157×10^{-1}	1.801×10^{-2}	6.247×10^{-1}	1.856×10^{-2}	6.172×10^{-1}	1.815×10^{-2}	6.048×10^{-1}	1.782×10^{-2}	6.266×10^{-1}	1.845×10^{-2}
A2PreCol	1.765×10^{-1}	9.113×10^{-3}	1.708×10^{-1}	8.915×10^{-3}	1.748×10^{-1}	9.224×10^{-3}	1.695×10^{-1}	9.101×10^{-3}	1.704×10^{-1}	9.095×10^{-3}
A2Col	7.201	7.594×10^{-2}	7.216	7.590×10^{-2}	7.206	7.580×10^{-2}	7.200	7.567×10^{-2}	7.225	7.602×10^{-2}
A2PostCol	9.902×10^{-2}	5.866×10^{-3}	1.019×10^{-1}	6.172×10^{-3}	9.500×10^{-2}	5.614×10^{-3}	1.020×10^{-1}	6.222×10^{-3}	8.539×10^{-2}	5.397×10^{-3}
M2	7.954×10^{-1}	2.600×10^{-2}	5.611×10^{-1}	2.183×10^{-2}	4.047×10^{-1}	1.804×10^{-2}	2.684×10^{-1}	1.460×10^{-2}	4.478×10^{-2}	4.774×10^{-3}
T4S	1.540×10^{-3}	6.204×10^{-4}	1.237×10^{-3}	6.199×10^{-4}	1.389×10^{-3}	7.167×10^{-4}	9.705×10^{-4}	8.307×10^{-4}	6.737×10^{-3}	1.491×10^{-3}
T4L	1.860×10^{-5}	4.402×10^{-6}	1.252×10^{-5}	4.565×10^{-6}	1.395×10^{-5}	1.035×10^{-5}	1.864×10^{-5}	1.392×10^{-5}	1.246×10^{-3}	7.551×10^{-4}
T4C	8.692×10^{-7}	8.692×10^{-7}	6.928×10^{-8}	5.096×10^{-8}	5.112×10^{-6}	5.112×10^{-6}	0	0	6.407×10^{-6}	6.407×10^{-6}
T3+T2+T1	4.209×10^{-2}	2.799×10^{-3}	4.733×10^{-2}	3.114×10^{-3}	4.630×10^{-2}	2.872×10^{-3}	4.578×10^{-2}	2.838×10^{-3}	5.597×10^{-2}	3.132×10^{-3}

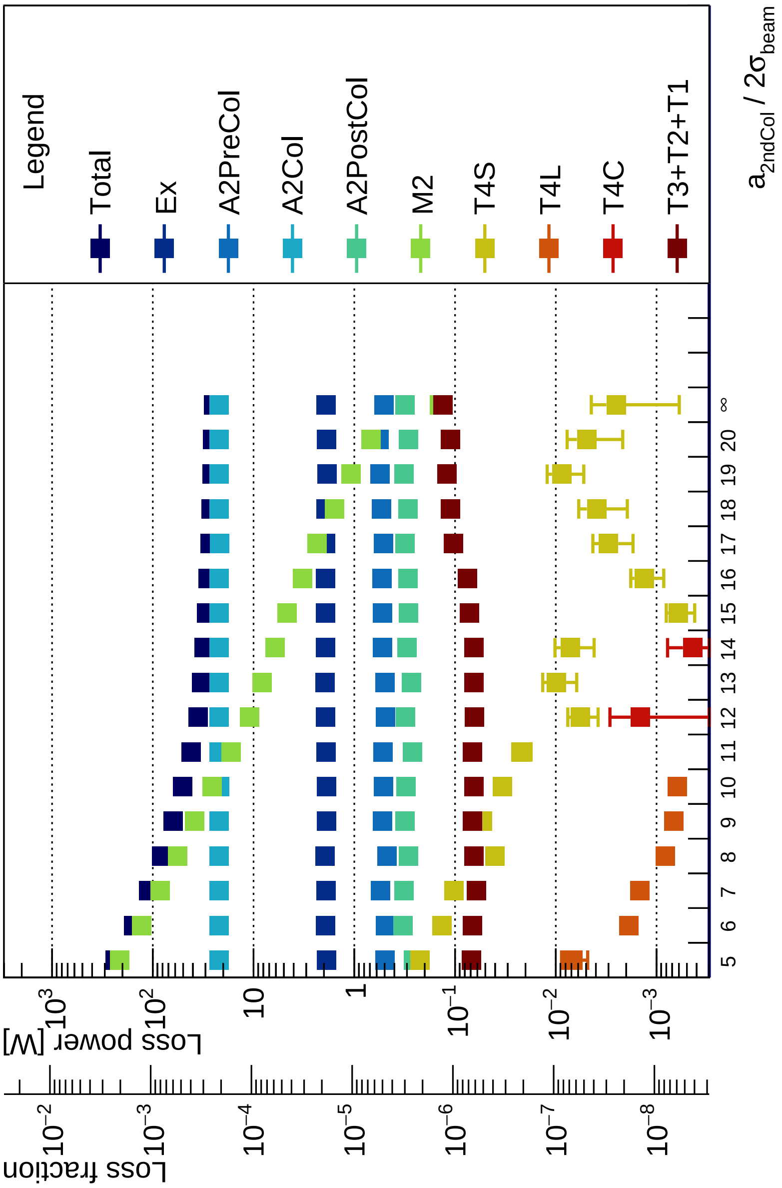

Figure A.22: Second collimator aperture sweep with spoiler for a He target induced halo.

Table A.22: Loss power numbers from He TAIL second collimator aperture sweep with spoiler in Figure A.22.

$\frac{a_{\text{2ndCol}}}{2\sigma_{\text{beam}}}$	**5**		**6**		**7**		**8**		**9**		**10**	
Section	P_{loss}[W]	ΔP_{loss}[W]	P_{loss}[W]	ΔP_{loss}[W]	P_{loss}[W]	ΔP_{loss}[W]	P_{loss}[W]	ΔP_{loss}[W]	P_{loss}[W]	ΔP_{loss}[W]	P_{loss}[W]	ΔP_{loss}[W]
Total	2.375×10^{2}	1.054	1.544×10^{2}	8.001×10^{-1}	1.094×10^{2}	6.455×10^{-1}	8.159×10^{1}	5.386×10^{-1}	6.318×10^{1}	4.599×10^{-1}	5.049×10^{1}	3.995×10^{-1}
Ex	1.877	5.691×10^{-2}	1.928	5.871×10^{-2}	1.909	5.837×10^{-2}	1.957	5.908×10^{-2}	1.883	5.708×10^{-2}	1.883	5.735×10^{-2}
A2PreCol	4.951×10^{-1}	2.737×10^{-2}	4.910×10^{-1}	2.812×10^{-2}	5.516×10^{-1}	2.953×10^{-2}	4.750×10^{-1}	2.796×10^{-2}	5.258×10^{-1}	2.878×10^{-2}	5.117×10^{-1}	2.801×10^{-2}
A2Col	2.195×10^{1}	2.416×10^{-1}	2.192×10^{1}	2.414×10^{-1}	2.186×10^{1}	2.409×10^{-1}	2.193×10^{1}	2.402×10^{-1}	2.190×10^{1}	2.409×10^{-1}	2.184×10^{1}	2.403×10^{-1}
A2PostCol	2.585×10^{-1}	1.647×10^{-2}	3.288×10^{-1}	1.942×10^{-2}	3.207×10^{-1}	1.938×10^{-2}	2.905×10^{-1}	1.830×10^{-2}	3.148×10^{-1}	1.899×10^{-2}	3.067×10^{-1}	1.853×10^{-2}
M2	2.127×10^{2}	9.653×10^{-1}	1.296×10^{2}	7.113×10^{-1}	8.457×10^{1}	5.540×10^{-1}	5.684×10^{1}	4.426×10^{-1}	3.844×10^{1}	3.563×10^{-1}	2.585×10^{1}	2.868×10^{-1}
T4S	2.227×10^{-1}	1.480×10^{-2}	1.354×10^{-1}	1.150×10^{-2}	1.026×10^{-1}	9.716×10^{-3}	4.001×10^{-2}	5.219×10^{-3}	5.325×10^{-2}	6.441×10^{-3}	3.381×10^{-2}	5.336×10^{-3}
T4L	6.792×10^{-3}	1.970×10^{-3}	1.883×10^{-3}	1.422×10^{-4}	1.472×10^{-3}	1.496×10^{-4}	8.174×10^{-4}	8.852×10^{-5}	6.720×10^{-4}	1.092×10^{-4}	6.197×10^{-4}	1.076×10^{-4}
T4C	1.680×10^{-4}	8.417×10^{-5}	3.189×10^{-5}	9.402×10^{-6}	7.197×10^{-5}	4.760×10^{-5}	1.650×10^{-5}	8.890×10^{-6}	8.848×10^{-5}	5.418×10^{-5}	8.398×10^{-5}	5.316×10^{-5}
T3+T2+T1	6.905×10^{-2}	7.024×10^{-3}	6.687×10^{-2}	6.606×10^{-3}	6.111×10^{-2}	6.072×10^{-3}	6.467×10^{-2}	6.435×10^{-3}	6.756×10^{-2}	7.241×10^{-3}	6.463×10^{-2}	6.946×10^{-3}

$\frac{a_{\text{2ndCol}}}{2\sigma_{\text{beam}}}$	**11**		**12**		**13**		**14**		**15**		**16**	
Section	P_{loss}[W]	ΔP_{loss}[W]	P_{loss}[W]	ΔP_{loss}[W]	P_{loss}[W]	ΔP_{loss}[W]	P_{loss}[W]	ΔP_{loss}[W]	P_{loss}[W]	ΔP_{loss}[W]	P_{loss}[W]	ΔP_{loss}[W]
Total	4.150×10^{1}	3.540×10^{-1}	3.565×10^{1}	3.219×10^{-1}	3.295×10^{1}	3.059×10^{-1}	3.090×10^{1}	2.932×10^{-1}	2.940×10^{1}	2.834×10^{-1}	2.810×10^{1}	2.749×10^{-1}
Ex	1.911	5.788×10^{-2}	1.925	5.835×10^{-2}	1.956	5.944×10^{-2}	1.921	5.851×10^{-2}	1.926	5.838×10^{-2}	1.922	5.802×10^{-2}
A2PreCol	5.184×10^{-1}	2.920×10^{-2}	4.907×10^{-1}	2.790×10^{-2}	4.957×10^{-1}	2.779×10^{-2}	5.228×10^{-1}	2.895×10^{-2}	5.254×10^{-1}	2.865×10^{-2}	5.299×10^{-1}	2.871×10^{-2}
A2Col	2.203×10^{1}	2.422×10^{-1}	2.191×10^{1}	2.414×10^{-1}	2.196×10^{1}	2.415×10^{-1}	2.195×10^{1}	2.414×10^{-1}	2.195×10^{1}	2.415×10^{-1}	2.199×10^{1}	2.419×10^{-1}
A2PostCol	2.647×10^{-1}	1.723×10^{-2}	3.110×10^{-1}	1.940×10^{-2}	2.700×10^{-1}	1.888×10^{-2}	2.984×10^{-1}	1.899×10^{-2}	2.911×10^{-1}	1.901×10^{-2}	2.933×10^{-1}	1.846×10^{-2}
M2	1.668×10^{1}	2.275×10^{-1}	1.095×10^{1}	1.830×10^{-1}	8.193	1.575×10^{-1}	6.135	1.354×10^{-1}	4.635	1.161×10^{-1}	3.280	9.665×10^{-2}
T4S	2.210×10^{-2}	4.496×10^{-3}	5.699×10^{-3}	1.898×10^{-3}	9.842×10^{-3}	3.638×10^{-3}	7.178×10^{-3}	3.014×10^{-3}	6.094×10^{-4}	1.914×10^{-4}	1.325×10^{-3}	4.773×10^{-4}
T4L	2.936×10^{-4}	4.734×10^{-5}	1.794×10^{-4}	3.301×10^{-5}	2.233×10^{-4}	9.666×10^{-5}	1.031×10^{-4}	3.481×10^{-5}	2.188×10^{-4}	8.149×10^{-5}	1.215×10^{-4}	5.374×10^{-5}
T4C	2.648×10^{-6}	2.648×10^{-6}	1.450×10^{-3}	1.450×10^{-3}	0	0	4.378×10^{-4}	3.394×10^{-4}	0	0	2.357×10^{-7}	2.357×10^{-7}
T3+T2+T1	6.731×10^{-2}	7.098×10^{-3}	6.386×10^{-2}	7.055×10^{-3}	6.461×10^{-2}	6.726×10^{-3}	6.482×10^{-2}	6.663×10^{-3}	7.159×10^{-2}	7.252×10^{-3}	7.562×10^{-2}	7.241×10^{-3}

$\frac{a_{\text{2ndCol}}}{2\sigma_{\text{beam}}}$	**17**		**18**		**19**		**20**		∞	
Section	P_{loss}[W]	ΔP_{loss}[W]	P_{loss}[W]	ΔP_{loss}[W]	P_{loss}[W]	ΔP_{loss}[W]	P_{loss}[W]	ΔP_{loss}[W]	P_{loss}[W]	ΔP_{loss}[W]
Total	2.702×10^{1}	2.675×10^{-1}	2.635×10^{1}	2.632×10^{-1}	2.581×10^{1}	2.603×10^{-1}	2.542×10^{1}	2.567×10^{-1}	2.491×10^{1}	2.542×10^{-1}
Ex	1.924	5.806×10^{-2}	1.907	5.744×10^{-2}	1.861	5.763×10^{-2}	1.882	5.669×10^{-2}	1.916	5.832×10^{-2}
A2PreCol	5.131×10^{-1}	2.843×10^{-2}	5.374×10^{-1}	2.966×10^{-2}	5.569×10^{-1}	3.033×10^{-2}	5.659×10^{-1}	2.997×10^{-2}	5.060×10^{-1}	2.809×10^{-2}
A2Col	2.182×10^{1}	2.402×10^{-1}	2.194×10^{1}	2.412×10^{-1}	2.186×10^{1}	2.411×10^{-1}	2.188×10^{1}	2.405×10^{-1}	2.190×10^{1}	2.413×10^{-1}
A2PostCol	3.151×10^{-1}	1.914×10^{-2}	2.918×10^{-1}	1.910×10^{-2}	3.217×10^{-1}	1.994×10^{-2}	2.902×10^{-1}	1.877×10^{-2}	3.133×10^{-1}	2.000×10^{-2}
M2	2.340	8.127×10^{-2}	1.563	6.527×10^{-2}	1.073	5.404×10^{-2}	6.797×10^{-1}	4.163×10^{-2}	1.424×10^{-1}	1.620×10^{-2}
T4S	2.999×10^{-3}	1.287×10^{-3}	3.933×10^{-3}	1.983×10^{-3}	8.729×10^{-3}	3.455×10^{-3}	4.941×10^{-3}	2.775×10^{-3}	2.518×10^{-3}	1.923×10^{-3}
T4L	3.564×10^{-5}	1.380×10^{-5}	3.731×10^{-5}	1.508×10^{-5}	3.788×10^{-5}	1.312×10^{-5}	3.530×10^{-6}	2.549×10^{-6}	0	0
T4C	2.773×10^{-6}	2.773×10^{-6}	7.673×10^{-5}	7.673×10^{-5}	0	0	0	0	0	0
T3+T2+T1	1.034×10^{-1}	8.032×10^{-3}	1.114×10^{-1}	8.479×10^{-3}	1.203×10^{-1}	8.642×10^{-3}	1.113×10^{-1}	8.075×10^{-3}	1.312×10^{-1}	9.177×10^{-3}

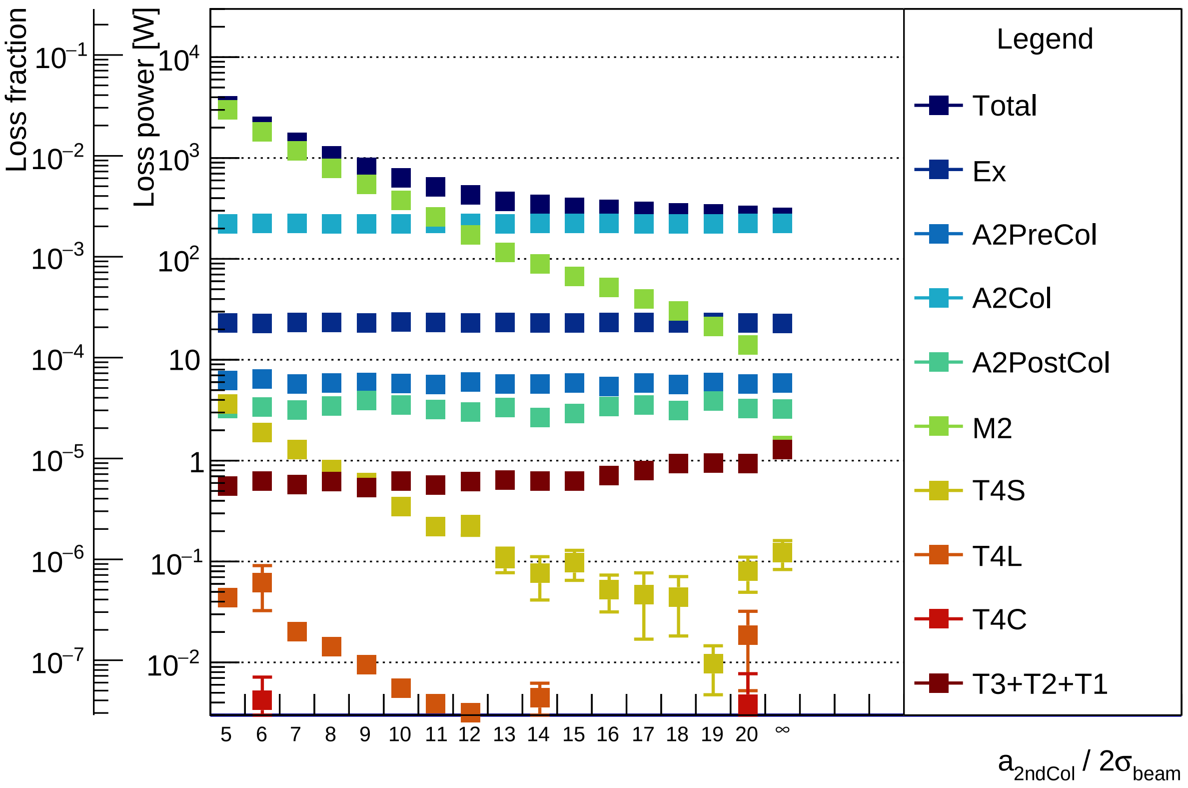

Figure A.23: Second collimator aperture sweep with spoiler for a O target induced halo.

Table A.23: Loss power numbers from O TAIL second collimator aperture sweep with spoiler in Figure A.23.

$\frac{a_{\mathrm{2ndCol}}}{2\sigma_{\mathrm{beam}}}$	**5**		**6**		**7**		**8**		**9**		**10**	
Section	P_{loss}[W]	ΔP_{loss}[W]	P_{loss}[W]	ΔP_{loss}[W]	P_{loss}[W]	ΔP_{loss}[W]	P_{loss}[W]	ΔP_{loss}[W]	P_{loss}[W]	ΔP_{loss}[W]	P_{loss}[W]	ΔP_{loss}[W]
Total	3.273×10^{3}	1.364×10^{1}	2.068×10^{3}	1.016×10^{1}	1.429×10^{3}	8.089	1.048×10^{3}	6.702	8.053×10^{2}	5.718	6.367×10^{2}	4.952
Ex	2.305×10^{1}	7.003×10^{-1}	2.295×10^{1}	7.004×10^{-1}	2.330×10^{1}	7.041×10^{-1}	2.334×10^{1}	7.085×10^{-1}	2.321×10^{1}	7.005×10^{-1}	2.358×10^{1}	7.119×10^{-1}
A2PreCol	6.195	3.461×10^{-1}	6.478	3.521×10^{-1}	5.727	3.403×10^{-1}	5.915	3.375×10^{-1}	5.928	3.413×10^{-1}	5.787	3.282×10^{-1}
A2Col	2.232×10^{2}	2.653	2.236×10^{2}	2.664	2.236×10^{2}	2.658	2.229×10^{2}	2.647	2.220×10^{2}	2.647	2.232×10^{2}	2.655
A2PostCol	3.282	2.016×10^{-1}	3.405	2.098×10^{-1}	3.177	2.151×10^{-1}	3.496	2.201×10^{-1}	3.942	2.489×10^{-1}	3.547	2.213×10^{-1}
M2	3.013×10^{3}	1.276×10^{1}	1.809×10^{3}	9.283	1.171×10^{3}	7.187	7.911×10^{2}	5.754	5.491×10^{2}	4.702	3.796×10^{2}	3.840
T4S	3.646	1.936×10^{-1}	1.903	1.441×10^{-1}	1.288	1.239×10^{-1}	8.180×10^{-1}	9.551×10^{-2}	6.028×10^{-1}	7.608×10^{-2}	3.506×10^{-1}	5.939×10^{-2}
T4L	4.408×10^{-2}	2.586×10^{-3}	6.183×10^{-2}	2.924×10^{-2}	2.020×10^{-2}	1.984×10^{-3}	1.426×10^{-2}	1.881×10^{-3}	9.491×10^{-3}	9.437×10^{-4}	5.564×10^{-3}	7.365×10^{-4}
T4C	2.462×10^{-3}	1.236×10^{-3}	4.204×10^{-3}	2.941×10^{-3}	3.257×10^{-4}	1.131×10^{-4}	2.825×10^{-4}	1.038×10^{-4}	3.774×10^{-4}	1.960×10^{-4}	1.468×10^{-4}	8.262×10^{-5}
T3+T2+T1	5.615×10^{-1}	6.612×10^{-2}	6.296×10^{-1}	7.611×10^{-2}	5.768×10^{-1}	7.029×10^{-2}	6.213×10^{-1}	7.481×10^{-2}	5.411×10^{-1}	6.952×10^{-2}	6.252×10^{-1}	7.491×10^{-2}

$\frac{a_{\mathrm{2ndCol}}}{2\sigma_{\mathrm{beam}}}$	**11**		**12**		**13**		**14**		**15**		**16**	
Section	P_{loss}[W]	ΔP_{loss}[W]	P_{loss}[W]	ΔP_{loss}[W]	P_{loss}[W]	ΔP_{loss}[W]	P_{loss}[W]	ΔP_{loss}[W]	P_{loss}[W]	ΔP_{loss}[W]	P_{loss}[W]	ΔP_{loss}[W]
Total	5.170×10^{2}	4.356	4.288×10^{2}	3.887	3.712×10^{2}	3.555	3.456×10^{2}	3.405	3.239×10^{2}	3.261	3.091×10^{2}	3.157
Ex	2.352×10^{1}	7.113×10^{-1}	2.316×10^{1}	6.998×10^{-1}	2.330×10^{1}	6.987×10^{-1}	2.326×10^{1}	7.023×10^{-1}	2.321×10^{1}	7.042×10^{-1}	2.353×10^{1}	7.038×10^{-1}
A2PreCol	5.686	3.321×10^{-1}	6.026	3.456×10^{-1}	5.754	3.359×10^{-1}	5.771	3.388×10^{-1}	5.852	3.370×10^{-1}	5.448	3.156×10^{-1}
A2Col	2.238×10^{2}	2.655	2.236×10^{2}	2.668	2.227×10^{2}	2.649	2.242×10^{2}	2.667	2.244×10^{2}	2.667	2.238×10^{2}	2.656
A2PostCol	3.224	2.212×10^{-1}	3.036	2.076×10^{-1}	3.379	2.204×10^{-1}	2.685	1.939×10^{-1}	2.945	2.104×10^{-1}	3.428	2.304×10^{-1}
M2	2.599×10^{2}	3.130	1.721×10^{2}	2.515	1.154×10^{2}	2.060	8.897×10^{1}	1.799	6.680×10^{1}	1.543	5.209×10^{1}	1.359
T4S	2.228×10^{-1}	4.112×10^{-2}	2.317×10^{-1}	4.997×10^{-2}	1.065×10^{-1}	2.909×10^{-2}	7.654×10^{-2}	3.502×10^{-2}	9.701×10^{-2}	3.198×10^{-2}	5.250×10^{-2}	2.086×10^{-2}
T4L	3.911×10^{-3}	5.636×10^{-4}	3.155×10^{-3}	5.061×10^{-4}	2.953×10^{-3}	9.289×10^{-4}	4.452×10^{-3}	1.764×10^{-3}	1.642×10^{-3}	4.954×10^{-4}	6.510×10^{-4}	1.593×10^{-4}
T4C	1.368×10^{-4}	9.111×10^{-5}	5.969×10^{-4}	5.012×10^{-4}	1.122×10^{-4}	1.122×10^{-4}	0	0	0	0	0	0
T3+T2+T1	5.712×10^{-1}	6.584×10^{-2}	6.219×10^{-1}	6.970×10^{-2}	6.438×10^{-1}	7.174×10^{-2}	6.266×10^{-1}	7.129×10^{-2}	6.306×10^{-1}	7.308×10^{-2}	7.117×10^{-1}	7.709×10^{-2}

$\frac{a_{\mathrm{2ndCol}}}{2\sigma_{\mathrm{beam}}}$	**17**		**18**		**19**		**20**		∞	
Section	P_{loss}[W]	ΔP_{loss}[W]	P_{loss}[W]	ΔP_{loss}[W]	P_{loss}[W]	ΔP_{loss}[W]	P_{loss}[W]	ΔP_{loss}[W]	P_{loss}[W]	ΔP_{loss}[W]
Total	2.962×10^{2}	3.074	2.869×10^{2}	3.005	2.780×10^{2}	2.938	2.708×10^{2}	2.896	2.592×10^{2}	2.814
Ex	2.336×10^{1}	7.074×10^{-1}	2.325×10^{1}	6.975×10^{-1}	2.334×10^{1}	7.086×10^{-1}	2.309×10^{1}	7.005×10^{-1}	2.303×10^{1}	6.931×10^{-1}
A2PreCol	5.897	3.363×10^{-1}	5.690	3.268×10^{-1}	5.956	3.408×10^{-1}	5.752	3.419×10^{-1}	5.891	3.377×10^{-1}
A2Col	2.225×10^{2}	2.653	2.234×10^{2}	2.656	2.226×10^{2}	2.645	2.236×10^{2}	2.657	2.243×10^{2}	2.661
A2PostCol	3.579	2.284×10^{-1}	3.126	2.055×10^{-1}	3.921	2.422×10^{-1}	3.289	2.152×10^{-1}	3.231	2.114×10^{-1}
M2	3.999×10^{1}	1.176	3.043×10^{1}	1.015	2.128×10^{1}	8.312×10^{-1}	1.406×10^{1}	6.679×10^{-1}	1.410	1.716×10^{-1}
T4S	4.705×10^{-2}	3.006×10^{-2}	4.457×10^{-2}	2.630×10^{-2}	9.688×10^{-3}	4.913×10^{-3}	8.001×10^{-2}	3.047×10^{-2}	1.222×10^{-1}	3.893×10^{-2}
T4L	5.955×10^{-4}	1.671×10^{-4}	4.356×10^{-4}	1.692×10^{-4}	4.850×10^{-4}	1.698×10^{-4}	1.867×10^{-2}	1.343×10^{-2}	0	0
T4C	0	0	3.111×10^{-4}	2.375×10^{-4}	0	0	3.859×10^{-3}	3.859×10^{-3}	0	0
T3+T2+T1	7.965×10^{-1}	8.022×10^{-2}	9.319×10^{-1}	8.713×10^{-2}	9.416×10^{-1}	8.521×10^{-2}	9.331×10^{-1}	8.399×10^{-2}	1.284	1.002×10^{-1}

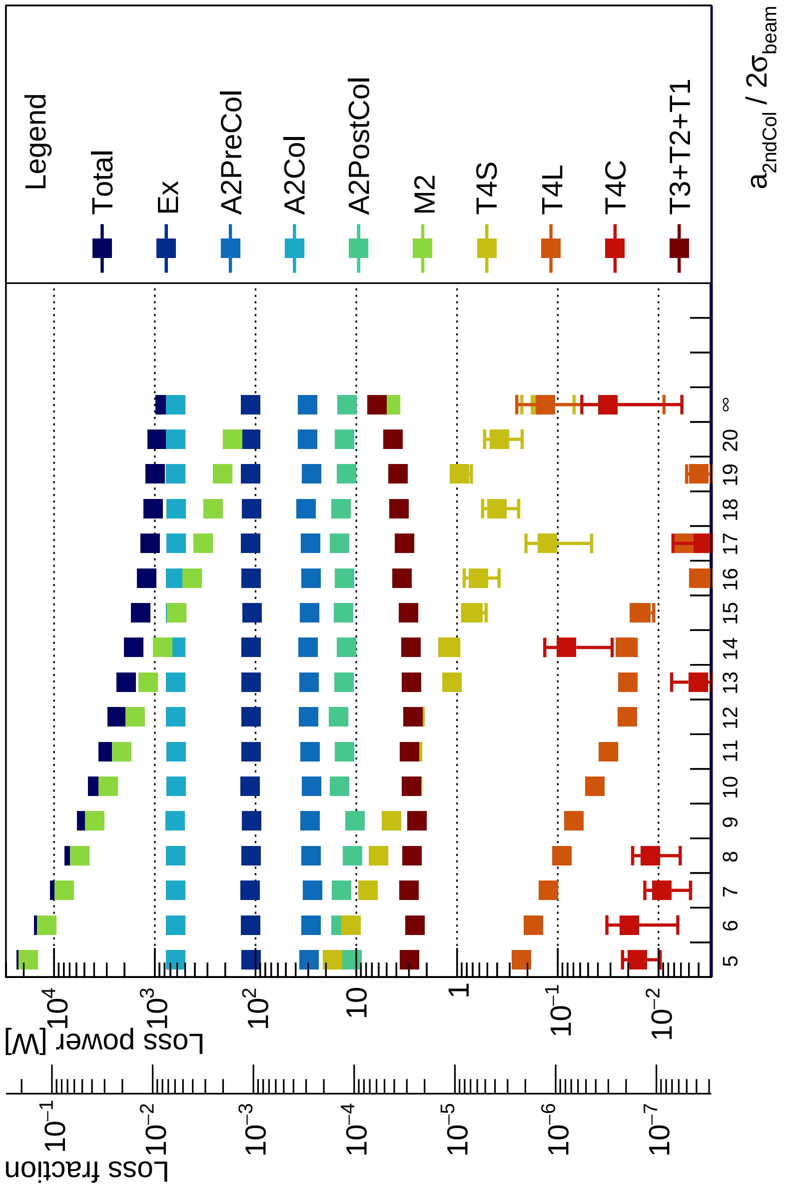

Figure A.24: Second collimator aperture sweep with spoiler for a Ar target induced halo.

Table A.24: Loss power numbers from Ar TAIL second collimator aperture sweep with spoiler in Figure A.24.

$\frac{a_{\text{2ndCol}}}{2\sigma_{\text{beam}}}$	**5**		**6**		**7**		**8**		**9**		**10**	
Section	P_{loss}[W]	ΔP_{loss}[W]	P_{loss}[W]	ΔP_{loss}[W]	P_{loss}[W]	ΔP_{loss}[W]	P_{loss}[W]	ΔP_{loss}[W]	P_{loss}[W]	ΔP_{loss}[W]	P_{loss}[W]	ΔP_{loss}[W]
Total	1.886×10^{4}	7.734×10^{1}	1.264×10^{4}	5.901×10^{1}	8.755×10^{3}	4.660×10^{1}	6.329×10^{3}	3.813×10^{1}	4.749×10^{3}	3.207×10^{1}	3.669×10^{3}	2.748×10^{1}
Ex	1.103×10^{2}	3.423	1.114×10^{2}	3.466	1.131×10^{2}	3.478	1.105×10^{2}	3.429	1.101×10^{2}	3.432	1.138×10^{2}	3.495
A2PreCol	2.947×10^{1}	1.698	2.821×10^{1}	1.674	2.703×10^{1}	1.614	2.816×10^{1}	1.661	2.892×10^{1}	1.688	2.780×10^{1}	1.626
A2Col	6.185×10^{2}	9.781	6.179×10^{2}	9.714	6.207×10^{2}	9.744	6.216×10^{2}	9.812	6.263×10^{2}	9.882	6.167×10^{2}	9.726
A2PostCol	1.109×10^{1}	9.211×10^{-1}	1.410×10^{1}	9.812×10^{-1}	1.409×10^{1}	9.599×10^{-1}	1.091×10^{1}	8.813×10^{-1}	1.029×10^{1}	8.299×10^{-1}	1.468×10^{1}	9.855×10^{-1}
M2	1.807×10^{4}	7.460×10^{1}	1.186×10^{4}	5.632×10^{1}	7.970×10^{3}	4.388×10^{1}	5.549×10^{3}	3.533×10^{1}	3.966×10^{3}	2.910×10^{1}	2.891×10^{3}	2.438×10^{1}
T4S	1.730×10^{1}	9.563×10^{-1}	1.134×10^{1}	7.529×10^{-1}	7.629	6.281×10^{-1}	6.032	5.837×10^{-1}	4.489	5.321×10^{-1}	2.759	3.614×10^{-1}
T4L	2.306×10^{-1}	1.278×10^{-2}	1.741×10^{-1}	1.265×10^{-2}	1.235×10^{-1}	1.077×10^{-2}	9.092×10^{-2}	7.133×10^{-3}	6.903×10^{-2}	7.688×10^{-3}	4.284×10^{-2}	4.121×10^{-3}
T4C	1.621×10^{-2}	6.578×10^{-3}	1.950×10^{-2}	1.306×10^{-2}	9.247×10^{-3}	4.431×10^{-3}	1.209×10^{-2}	5.994×10^{-3}	2.104×10^{-3}	1.331×10^{-3}	1.770×10^{-3}	1.458×10^{-3}
T3+T2+T1	2.961	3.497×10^{-1}	2.624	3.210×10^{-1}	2.992	3.697×10^{-1}	2.793	3.563×10^{-1}	2.502	3.095×10^{-1}	2.835	3.385×10^{-1}

$\frac{a_{\text{2ndCol}}}{2\sigma_{\text{beam}}}$	**11**		**12**		**13**		**14**		**15**		**16**	
Section	P_{loss}[W]	ΔP_{loss}[W]	P_{loss}[W]	ΔP_{loss}[W]	P_{loss}[W]	ΔP_{loss}[W]	P_{loss}[W]	ΔP_{loss}[W]	P_{loss}[W]	ΔP_{loss}[W]	P_{loss}[W]	ΔP_{loss}[W]
Total	2.903×10^{3}	2.395×10^{1}	2.350×10^{3}	2.109×10^{1}	1.933×10^{3}	1.877×10^{1}	1.620×10^{3}	1.687×10^{1}	1.378×10^{3}	1.527×10^{1}	1.207×10^{3}	1.412×10^{1}
Ex	1.113×10^{2}	3.434	1.107×10^{2}	3.413	1.109×10^{2}	3.421	1.113×10^{2}	3.451	1.087×10^{2}	3.392	1.111×10^{2}	3.408
A2PreCol	2.890×10^{1}	1.682	2.989×10^{1}	1.730	2.955×10^{1}	1.692	3.002×10^{1}	1.743	2.915×10^{1}	1.644	2.798×10^{1}	1.652
A2Col	6.176×10^{2}	9.807	6.191×10^{2}	9.770	6.177×10^{2}	9.749	6.213×10^{2}	9.804	6.186×10^{2}	9.766	6.222×10^{2}	9.834
A2PostCol	1.305×10^{1}	9.926×10^{-1}	1.506×10^{1}	9.838×10^{-1}	1.326×10^{1}	9.999×10^{-1}	1.246×10^{1}	9.442×10^{-1}	1.338×10^{1}	9.849×10^{-1}	1.313×10^{1}	9.830×10^{-1}
M2	2.126×10^{3}	2.060×10^{1}	1.570×10^{3}	1.747×10^{1}	1.158×10^{3}	1.484×10^{1}	8.402×10^{2}	1.251×10^{1}	6.039×10^{2}	1.051×10^{1}	4.284×10^{2}	8.836
T4S	2.774	3.818×10^{-1}	2.610	4.094×10^{-1}	1.124	2.046×10^{-1}	1.225	2.625×10^{-1}	6.975×10^{-1}	1.830×10^{-1}	6.159×10^{-1}	2.334×10^{-1}
T4L	3.166×10^{-2}	4.051×10^{-3}	2.033×10^{-2}	2.760×10^{-3}	2.018×10^{-2}	2.811×10^{-3}	2.138×10^{-2}	4.713×10^{-3}	1.491×10^{-2}	3.746×10^{-3}	3.804×10^{-3}	9.943×10^{-4}
T4C	1.744×10^{-3}	1.225×10^{-3}	5.431×10^{-4}	2.796×10^{-4}	4.049×10^{-3}	3.369×10^{-3}	8.171×10^{-2}	5.287×10^{-2}	8.265×10^{-4}	8.221×10^{-4}	2.422×10^{-4}	2.422×10^{-4}
T3+T2+T1	2.973	3.765×10^{-1}	2.727	3.235×10^{-1}	2.833	3.499×10^{-1}	2.858	3.547×10^{-1}	3.020	3.465×10^{-1}	3.531	3.781×10^{-1}

$\frac{a_{\text{2ndCol}}}{2\sigma_{\text{beam}}}$	**17**		**18**		**19**		**20**		∞	
Section	P_{loss}[W]	ΔP_{loss}[W]	P_{loss}[W]	ΔP_{loss}[W]	P_{loss}[W]	ΔP_{loss}[W]	P_{loss}[W]	ΔP_{loss}[W]	P_{loss}[W]	ΔP_{loss}[W]
Total	1.107×10^{3}	1.333×10^{1}	1.040×10^{3}	1.279×10^{1}	9.877×10^{2}	1.244×10^{1}	9.497×10^{2}	1.205×10^{1}	7.884×10^{2}	1.072×10^{1}
Ex	1.119×10^{2}	3.470	1.091×10^{2}	3.404	1.117×10^{2}	3.489	1.115×10^{2}	3.465	1.118×10^{2}	3.488
A2PreCol	2.859×10^{1}	1.622	3.171×10^{1}	1.772	2.787×10^{1}	1.631	3.042×10^{1}	1.679	3.042×10^{1}	1.637
A2Col	6.161×10^{2}	9.723	6.165×10^{2}	9.692	6.185×10^{2}	9.782	6.213×10^{2}	9.735	6.227×10^{2}	9.813
A2PostCol	1.468×10^{1}	1.019	1.416×10^{1}	9.855×10^{-1}	1.255×10^{1}	9.559×10^{-1}	1.306×10^{1}	9.590×10^{-1}	1.235×10^{1}	8.840×10^{-1}
M2	3.319×10^{2}	7.733	2.647×10^{2}	6.865	2.123×10^{2}	6.116	1.687×10^{2}	5.437	4.560	6.915×10^{-1}
T4S	1.266×10^{-1}	8.036×10^{-2}	4.010×10^{-1}	1.565×10^{-1}	9.502×10^{-1}	2.294×10^{-1}	3.793×10^{-1}	1.534×10^{-1}	1.482×10^{-1}	7.923×10^{-2}
T4L	5.517×10^{-3}	1.344×10^{-3}	2.740×10^{-3}	7.907×10^{-4}	3.971×10^{-3}	1.290×10^{-3}	2.876×10^{-3}	8.205×10^{-4}	1.320×10^{-1}	1.232×10^{-1}
T4C	3.593×10^{-3}	3.590×10^{-3}	1.785×10^{-5}	1.785×10^{-5}	1.810×10^{-4}	1.810×10^{-4}	3.868×10^{-4}	2.856×10^{-4}	3.180×10^{-2}	2.593×10^{-2}
T3+T2+T1	3.334	3.703×10^{-1}	3.769	4.015×10^{-1}	3.863	4.019×10^{-1}	4.344	4.147×10^{-1}	6.219	5.200×10^{-1}

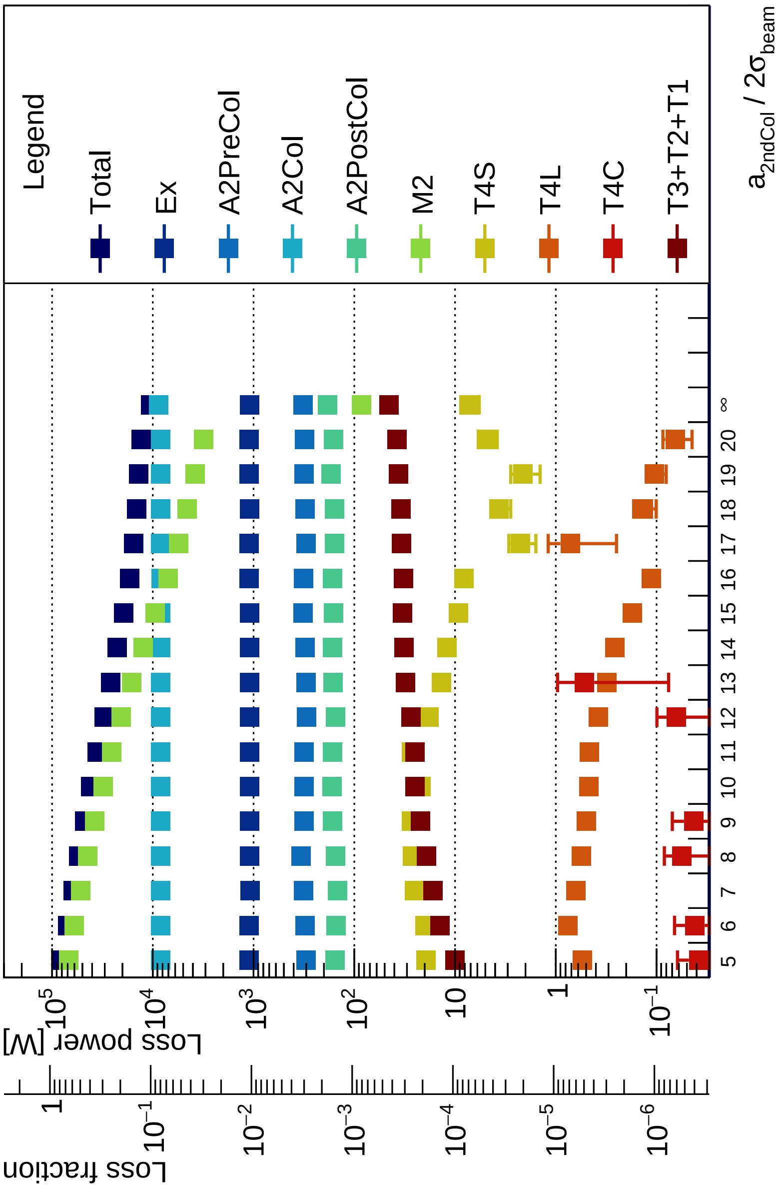

Figure A.25: Second collimator aperture sweep with spoiler for a Xe target induced halo.

Table A.25: Loss power numbers from Xe TAIL second collimator aperture sweep with spoiler in Figure A.25.

$\frac{a_{\mathrm{2ndCol}}}{2\sigma_{\mathrm{beam}}}$	**5**		**6**		**7**		**8**		**9**		**10**	
Section	P_{loss}[W]	ΔP_{loss}[W]	P_{loss}[W]	ΔP_{loss}[W]	P_{loss}[W]	ΔP_{loss}[W]	P_{loss}[W]	ΔP_{loss}[W]	P_{loss}[W]	ΔP_{loss}[W]	P_{loss}[W]	ΔP_{loss}[W]
Total	7.802×10^{4}	3.844×10^{2}	6.994×10^{4}	3.539×10^{2}	6.196×10^{4}	3.228×10^{2}	5.447×10^{4}	2.928×10^{2}	4.758×10^{4}	2.645×10^{2}	4.117×10^{4}	2.376×10^{2}
Ex	1.109×10^{3}	2.235×10^{1}	1.108×10^{3}	2.234×10^{1}	1.086×10^{3}	2.224×10^{1}	1.091×10^{3}	2.225×10^{1}	1.094×10^{3}	2.242×10^{1}	1.094×10^{3}	2.238×10^{1}
A2PreCol	3.015×10^{2}	1.092×10^{1}	3.078×10^{2}	1.131×10^{1}	3.193×10^{2}	1.129×10^{1}	3.393×10^{2}	1.190×10^{1}	3.139×10^{2}	1.119×10^{1}	3.162×10^{2}	1.140×10^{1}
A2Col	8.315×10^{3}	7.791×10^{1}	8.346×10^{3}	7.828×10^{1}	8.339×10^{3}	7.833×10^{1}	8.371×10^{3}	7.827×10^{1}	8.358×10^{3}	7.822×10^{1}	8.326×10^{3}	7.806×10^{1}
A2PostCol	1.554×10^{2}	6.755	1.519×10^{2}	7.002	1.472×10^{2}	6.651	1.539×10^{2}	6.827	1.635×10^{2}	7.026	1.662×10^{2}	7.121
M2	6.811×10^{4}	3.399×10^{2}	5.999×10^{4}	3.096×10^{2}	5.202×10^{4}	2.789×10^{2}	4.446×10^{4}	2.488×10^{2}	3.760×10^{4}	2.208×10^{2}	3.122×10^{4}	1.940×10^{2}
T4S	1.948×10^{1}	2.020	1.984×10^{1}	1.965	2.535×10^{1}	2.571	2.642×10^{1}	2.627	2.716×10^{1}	2.400	2.171×10^{1}	2.122
T4L	5.473×10^{-1}	4.691×10^{-2}	7.577×10^{-1}	6.427×10^{-2}	6.304×10^{-1}	3.844×10^{-2}	5.548×10^{-1}	4.265×10^{-2}	4.989×10^{-1}	3.432×10^{-2}	4.712×10^{-1}	3.120×10^{-2}
T4C	3.818×10^{-2}	2.378×10^{-2}	4.156×10^{-2}	2.473×10^{-2}	2.805×10^{-2}	1.834×10^{-2}	5.611×10^{-2}	2.753×10^{-2}	4.277×10^{-2}	2.696×10^{-2}	2.089×10^{-2}	1.491×10^{-2}
T3+T2+T1	9.964	1.437	1.417×10^{1}	1.577	1.654×10^{1}	1.718	1.930×10^{1}	1.770	2.213×10^{1}	2.032	2.489×10^{1}	2.090

$\frac{a_{\mathrm{2ndCol}}}{2\sigma_{\mathrm{beam}}}$	**11**		**12**		**13**		**14**		**15**		**16**	
Section	P_{loss}[W]	ΔP_{loss}[W]	P_{loss}[W]	ΔP_{loss}[W]	P_{loss}[W]	ΔP_{loss}[W]	P_{loss}[W]	ΔP_{loss}[W]	P_{loss}[W]	ΔP_{loss}[W]	P_{loss}[W]	ΔP_{loss}[W]
Total	3.551×10^{4}	2.131×10^{2}	3.055×10^{4}	1.910×10^{2}	2.619×10^{4}	1.709×10^{2}	2.248×10^{4}	1.531×10^{2}	1.946×10^{4}	1.381×10^{2}	1.700×10^{4}	1.255×10^{2}
Ex	1.097×10^{3}	2.239×10^{1}	1.100×10^{3}	2.247×10^{1}	1.089×10^{3}	2.233×10^{1}	1.094×10^{3}	2.241×10^{1}	1.094×10^{3}	2.228×10^{1}	1.106×10^{3}	2.250×10^{1}
A2PreCol	3.168×10^{2}	1.125×10^{1}	2.969×10^{2}	1.100×10^{1}	3.015×10^{2}	1.104×10^{1}	3.095×10^{2}	1.141×10^{1}	3.225×10^{2}	1.167×10^{1}	3.181×10^{2}	1.131×10^{1}
A2Col	8.328×10^{3}	7.805×10^{1}	8.346×10^{3}	7.825×10^{1}	8.336×10^{3}	7.824×10^{1}	8.339×10^{3}	7.809×10^{1}	8.341×10^{3}	7.823×10^{1}	8.299×10^{3}	7.798×10^{1}
A2PostCol	1.651×10^{2}	7.058	1.537×10^{2}	6.703	1.617×10^{2}	6.905	1.648×10^{2}	7.160	1.613×10^{2}	6.711	1.650×10^{2}	6.842
M2	2.555×10^{4}	1.693×10^{2}	2.061×10^{4}	1.469×10^{2}	1.625×10^{4}	1.262×10^{2}	1.253×10^{4}	1.074×10^{2}	9.502×10^{3}	9.079×10^{1}	7.068×10^{3}	7.657×10^{1}
T4S	2.698×10^{1}	2.598	1.810×10^{1}	1.986	1.368×10^{1}	1.645	1.201×10^{1}	1.427	9.241	1.477	8.152	1.513
T4L	4.635×10^{-1}	3.418×10^{-2}	3.800×10^{-1}	3.880×10^{-2}	3.119×10^{-1}	3.157×10^{-2}	2.600×10^{-1}	3.957×10^{-2}	1.744×10^{-1}	2.664×10^{-2}	1.126×10^{-1}	1.899×10^{-2}
T4C	1.249×10^{-2}	3.597×10^{-3}	6.371×10^{-2}	3.544×10^{-2}	5.184×10^{-1}	4.425×10^{-1}	1.774×10^{-2}	1.384×10^{-2}	5.452×10^{-3}	4.412×10^{-3}	1.008×10^{-2}	8.125×10^{-3}
T3+T2+T1	2.510×10^{1}	2.131	2.747×10^{1}	2.275	3.092×10^{1}	2.294	3.218×10^{1}	2.385	3.331×10^{1}	2.489	3.246×10^{1}	2.454

$\frac{a_{\mathrm{2ndCol}}}{2\sigma_{\mathrm{beam}}}$	**17**		**18**		**19**		**20**		∞	
Section	P_{loss}[W]	ΔP_{loss}[W]	P_{loss}[W]	ΔP_{loss}[W]	P_{loss}[W]	ΔP_{loss}[W]	P_{loss}[W]	ΔP_{loss}[W]	P_{loss}[W]	ΔP_{loss}[W]
Total	1.552×10^{4}	1.177×10^{2}	1.452×10^{4}	1.124×10^{2}	1.375×10^{4}	1.081×10^{2}	1.307×10^{4}	1.043×10^{2}	1.047×10^{4}	8.843×10^{1}
Ex	1.112×10^{3}	2.241×10^{1}	1.093×10^{3}	2.218×10^{1}	1.101×10^{3}	2.243×10^{1}	1.108×10^{3}	2.241×10^{1}	1.099×10^{3}	2.234×10^{1}
A2PreCol	3.008×10^{2}	1.122×10^{1}	3.088×10^{2}	1.116×10^{1}	3.157×10^{2}	1.148×10^{1}	3.120×10^{2}	1.129×10^{1}	3.229×10^{2}	1.176×10^{1}
A2Col	8.340×10^{3}	7.806×10^{1}	8.347×10^{3}	7.821×10^{1}	8.314×10^{3}	7.795×10^{1}	8.329×10^{3}	7.818×10^{1}	8.729×10^{3}	8.054×10^{1}
A2PostCol	1.575×10^{2}	6.834	1.566×10^{2}	6.702	1.693×10^{2}	7.140	1.606×10^{2}	6.701	1.848×10^{2}	7.271
M2	5.569×10^{3}	6.722×10^{1}	4.573×10^{3}	6.036×10^{1}	3.813×10^{3}	5.472×10^{1}	3.121×10^{3}	4.905×10^{1}	8.435×10^{1}	6.187
T4S	2.251	6.742×10^{-1}	3.671	8.693×10^{-1}	2.114	6.817×10^{-1}	4.897	1.084	7.312	1.550
T4L	7.198×10^{-1}	4.700×10^{-1}	1.347×10^{-1}	3.397×10^{-2}	1.049×10^{-1}	2.470×10^{-2}	6.545×10^{-2}	2.102×10^{-2}	0	0
T4C	0	0	0	0	8.542×10^{-3}	8.088×10^{-3}	4.380×10^{-4}	4.380×10^{-4}	1.027×10^{-3}	9.697×10^{-4}
T3+T2+T1	3.403×10^{1}	2.581	3.447×10^{1}	2.436	3.651×10^{1}	2.610	3.772×10^{1}	2.625	4.506×10^{1}	2.808

A.5.2 Without Halo Spoiler

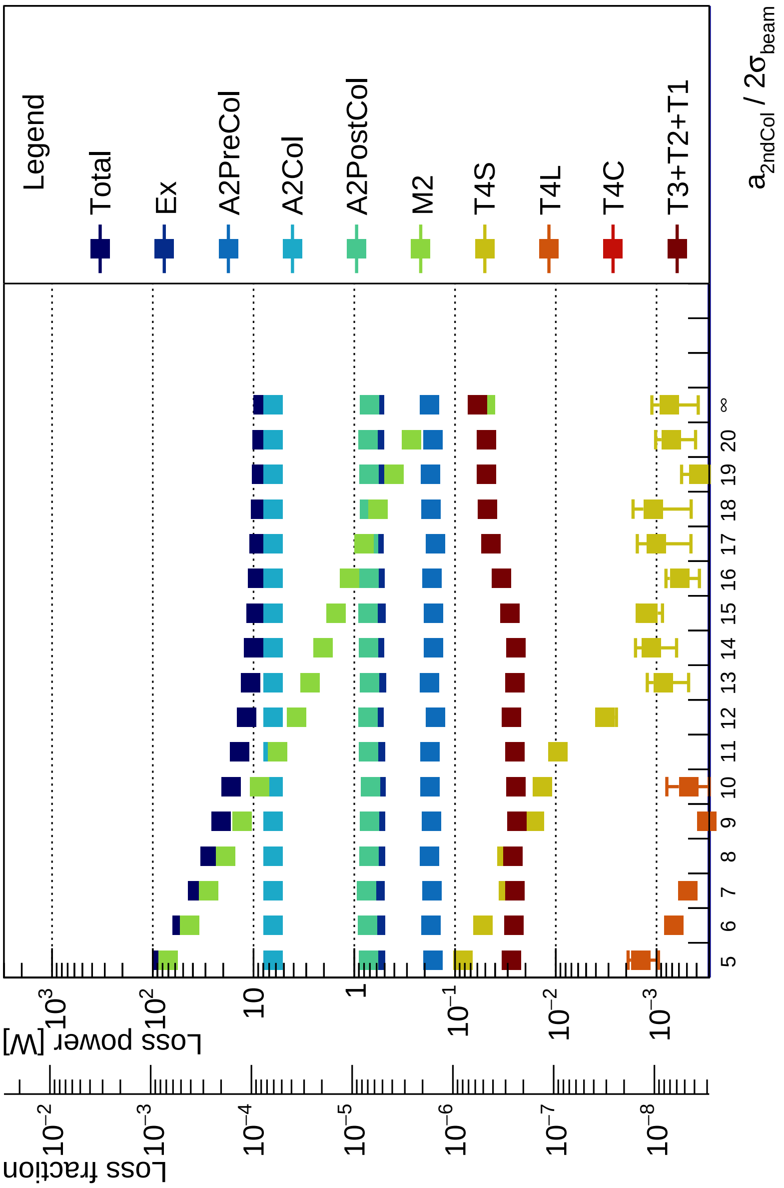

Figure A.26: Second collimator aperture sweep without spoiler for a H target induced halo.

Table A.26: Loss power numbers from H TAIL second collimator aperture sweep without spoiler in Figure A.26.

$\frac{a_{\text{2ndCol}}}{2\sigma_{\text{beam}}}$	**5**		**6**		**7**		**8**		**9**		**10**	
Section	P_{loss}[W]	ΔP_{loss}[W]	P_{loss}[W]	ΔP_{loss}[W]	P_{loss}[W]	ΔP_{loss}[W]	P_{loss}[W]	ΔP_{loss}[W]	P_{loss}[W]	ΔP_{loss}[W]	P_{loss}[W]	ΔP_{loss}[W]
Total	7.851×10^{1}	3.331×10^{-1}	5.098×10^{1}	2.534×10^{-1}	3.602×10^{1}	2.050×10^{-1}	2.694×10^{1}	1.725×10^{-1}	2.093×10^{1}	1.484×10^{-1}	1.668×10^{1}	1.297×10^{-1}
Ex	6.159×10^{-1}	1.804×10^{-2}	6.125×10^{-1}	1.790×10^{-2}	6.205×10^{-1}	1.811×10^{-2}	6.130×10^{-1}	1.820×10^{-2}	6.193×10^{-1}	1.821×10^{-2}	6.104×10^{-1}	1.789×10^{-2}
A2PreCol	1.663×10^{-1}	8.881×10^{-3}	1.740×10^{-1}	9.076×10^{-3}	1.704×10^{-1}	9.045×10^{-3}	1.795×10^{-1}	9.430×10^{-3}	1.714×10^{-1}	9.148×10^{-3}	1.780×10^{-1}	9.228×10^{-3}
A2Col	6.404	7.880×10^{-2}	6.374	7.867×10^{-2}	6.370	7.865×10^{-2}	6.410	7.886×10^{-2}	6.411	7.886×10^{-2}	6.422	7.888×10^{-2}
A2PostCol	7.256×10^{-1}	1.518×10^{-2}	7.394×10^{-1}	1.560×10^{-2}	7.550×10^{-1}	1.588×10^{-2}	7.157×10^{-1}	1.507×10^{-2}	7.090×10^{-1}	1.512×10^{-2}	6.871×10^{-1}	1.475×10^{-2}
M2	7.049×10^{1}	3.046×10^{-1}	4.300×10^{1}	2.245×10^{-1}	2.804×10^{1}	1.749×10^{-1}	1.897×10^{1}	1.403×10^{-1}	1.298×10^{1}	1.137×10^{-1}	8.740	9.159×10^{-2}
T4S	8.349×10^{-2}	4.885×10^{-3}	5.273×10^{-2}	4.020×10^{-3}	2.952×10^{-2}	2.603×10^{-3}	3.051×10^{-2}	3.026×10^{-3}	1.624×10^{-2}	2.213×10^{-3}	1.357×10^{-2}	1.913×10^{-3}
T4L	1.436×10^{-3}	4.795×10^{-4}	6.767×10^{-4}	6.869×10^{-5}	4.879×10^{-4}	6.257×10^{-5}	2.893×10^{-4}	2.990×10^{-5}	3.181×10^{-4}	4.459×10^{-5}	4.803×10^{-4}	3.098×10^{-4}
T4C	2.355×10^{-4}	1.870×10^{-4}	4.290×10^{-5}	3.519×10^{-5}	4.652×10^{-5}	2.035×10^{-5}	3.380×10^{-5}	2.239×10^{-5}	2.763×10^{-5}	2.438×10^{-5}	1.200×10^{-6}	1.063×10^{-6}
T3+T2+T1	2.756×10^{-2}	2.361×10^{-3}	2.611×10^{-2}	2.335×10^{-3}	2.557×10^{-2}	2.293×10^{-3}	2.670×10^{-2}	2.262×10^{-3}	2.432×10^{-2}	2.302×10^{-3}	2.477×10^{-2}	2.315×10^{-3}

$\frac{a_{\text{2ndCol}}}{2\sigma_{\text{beam}}}$	**11**		**12**		**13**		**14**		**15**		**16**	
Section	P_{loss}[W]	ΔP_{loss}[W]	P_{loss}[W]	ΔP_{loss}[W]	P_{loss}[W]	ΔP_{loss}[W]	P_{loss}[W]	ΔP_{loss}[W]	P_{loss}[W]	ΔP_{loss}[W]	P_{loss}[W]	ΔP_{loss}[W]
Total	1.371×10^{1}	1.156×10^{-1}	1.167×10^{1}	1.052×10^{-1}	1.065×10^{1}	9.985×10^{-2}	9.969	9.600×10^{-2}	9.445	9.281×10^{-2}	9.070	9.075×10^{-2}
Ex	6.152×10^{-1}	1.805×10^{-2}	6.402×10^{-1}	1.866×10^{-2}	5.991×10^{-1}	1.793×10^{-2}	6.284×10^{-1}	1.852×10^{-2}	6.118×10^{-1}	1.789×10^{-2}	6.209×10^{-1}	1.817×10^{-2}
A2PreCol	1.769×10^{-1}	9.116×10^{-3}	1.571×10^{-1}	8.473×10^{-3}	1.785×10^{-1}	9.067×10^{-3}	1.633×10^{-1}	8.841×10^{-3}	1.644×10^{-1}	8.643×10^{-3}	1.688×10^{-1}	8.912×10^{-3}
A2Col	6.397	7.887×10^{-2}	6.369	7.857×10^{-2}	6.395	7.880×10^{-2}	6.397	7.885×10^{-2}	6.390	7.873×10^{-2}	6.419	7.901×10^{-2}
A2PostCol	7.205×10^{-1}	1.527×10^{-2}	7.336×10^{-1}	1.544×10^{-2}	7.096×10^{-1}	1.516×10^{-2}	7.220×10^{-1}	1.526×10^{-2}	7.274×10^{-1}	1.545×10^{-2}	7.146×10^{-1}	1.516×10^{-2}
M2	5.768	7.340×10^{-2}	3.739	5.865×10^{-2}	2.746	4.991×10^{-2}	2.032	4.262×10^{-2}	1.521	3.652×10^{-2}	1.111	3.105×10^{-2}
T4S	9.510×10^{-3}	1.638×10^{-3}	3.243×10^{-3}	7.407×10^{-4}	8.580×10^{-4}	3.776×10^{-4}	1.125×10^{-3}	4.922×10^{-4}	1.214×10^{-3}	3.410×10^{-4}	5.907×10^{-4}	2.152×10^{-4}
T4L	1.175×10^{-4}	2.443×10^{-5}	9.155×10^{-5}	2.341×10^{-5}	7.382×10^{-5}	1.993×10^{-5}	4.399×10^{-5}	1.146×10^{-5}	4.050×10^{-5}	1.286×10^{-5}	3.240×10^{-5}	8.626×10^{-6}
T4C	2.521×10^{-7}	1.946×10^{-7}	1.039×10^{-5}	1.039×10^{-5}	0	0	0	0	1.763×10^{-8}	1.763×10^{-8}	0	0
T3+T2+T1	2.544×10^{-2}	2.398×10^{-3}	2.758×10^{-2}	2.564×10^{-3}	2.535×10^{-2}	2.319×10^{-3}	2.494×10^{-2}	2.297×10^{-3}	2.839×10^{-2}	2.345×10^{-3}	3.461×10^{-2}	2.632×10^{-3}

$\frac{a_{\text{2ndCol}}}{2\sigma_{\text{beam}}}$	**17**		**18**		**19**		**20**		∞	
Section	P_{loss}[W]	ΔP_{loss}[W]	P_{loss}[W]	ΔP_{loss}[W]	P_{loss}[W]	ΔP_{loss}[W]	P_{loss}[W]	ΔP_{loss}[W]	P_{loss}[W]	ΔP_{loss}[W]
Total	8.766	8.877×10^{-2}	8.525	8.738×10^{-2}	8.364	8.642×10^{-2}	8.214	8.545×10^{-2}	8.029	8.440×10^{-2}
Ex	6.383×10^{-1}	1.848×10^{-2}	6.180×10^{-1}	1.795×10^{-2}	6.026×10^{-1}	1.764×10^{-2}	6.269×10^{-1}	1.817×10^{-2}	6.288×10^{-1}	1.836×10^{-2}
A2PreCol	1.564×10^{-1}	8.440×10^{-3}	1.735×10^{-1}	9.175×10^{-3}	1.745×10^{-1}	9.039×10^{-3}	1.662×10^{-1}	8.895×10^{-3}	1.797×10^{-1}	9.202×10^{-3}
A2Col	6.404	7.881×10^{-2}	6.396	7.883×10^{-2}	6.421	7.894×10^{-2}	6.372	7.862×10^{-2}	6.406	7.883×10^{-2}
A2PostCol	7.246×10^{-1}	1.527×10^{-2}	7.061×10^{-1}	1.493×10^{-2}	7.134×10^{-1}	1.526×10^{-2}	7.295×10^{-1}	1.529×10^{-2}	7.036×10^{-1}	1.511×10^{-2}
M2	7.973×10^{-1}	2.606×10^{-2}	5.825×10^{-1}	2.198×10^{-2}	4.035×10^{-1}	1.817×10^{-2}	2.699×10^{-1}	1.465×10^{-2}	5.014×10^{-2}	5.149×10^{-3}
T4S	1.004×10^{-3}	5.486×10^{-4}	1.082×10^{-3}	6.286×10^{-4}	3.801×10^{-4}	1.841×10^{-4}	7.153×10^{-4}	3.055×10^{-4}	7.491×10^{-4}	3.635×10^{-4}
T4L	1.303×10^{-5}	4.735×10^{-6}	2.202×10^{-5}	8.582×10^{-6}	1.473×10^{-5}	8.009×10^{-6}	3.999×10^{-6}	2.068×10^{-6}	0	0
T4C	0	0	0	0	0	0	4.235×10^{-8}	4.235×10^{-8}	0	0
T3+T2+T1	4.404×10^{-2}	2.906×10^{-3}	4.761×10^{-2}	2.894×10^{-3}	4.890×10^{-2}	2.958×10^{-3}	4.900×10^{-2}	2.951×10^{-3}	6.006×10^{-2}	3.329×10^{-3}

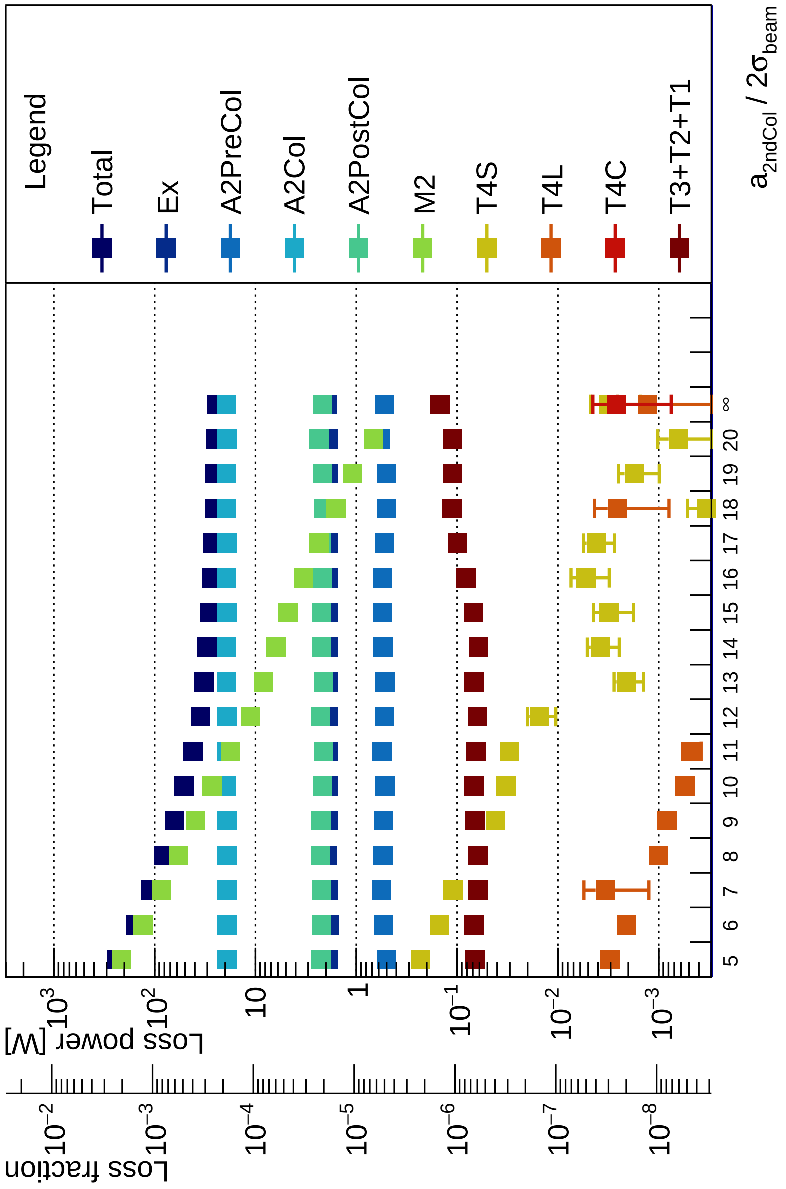

Figure A.27: Second collimator aperture sweep without spoiler for a He target induced halo.

Table A.27: Loss power numbers from He TAIL second collimator aperture sweep without spoiler in Figure A.27.

$\frac{a_{\mathrm{2ndCol}}}{2\sigma_{\mathrm{beam}}}$	**5**		**6**		**7**		**8**		**9**		**10**	
Section	P_{loss}[W]	ΔP_{loss}[W]	P_{loss}[W]	ΔP_{loss}[W]	P_{loss}[W]	ΔP_{loss}[W]	P_{loss}[W]	ΔP_{loss}[W]	P_{loss}[W]	ΔP_{loss}[W]	P_{loss}[W]	ΔP_{loss}[W]
Total	2.380×10^{2}	1.059	1.547×10^{2}	8.061×10^{-1}	1.096×10^{2}	6.534×10^{-1}	8.199×10^{1}	5.485×10^{-1}	6.356×10^{1}	4.717×10^{-1}	5.092×10^{1}	4.137×10^{-1}
Ex	1.917	5.793×10^{-2}	1.855	5.688×10^{-2}	1.888	5.805×10^{-2}	1.933	5.870×10^{-2}	1.885	5.713×10^{-2}	1.901	5.792×10^{-2}
A2PreCol	5.010×10^{-1}	2.793×10^{-2}	5.370×10^{-1}	2.926×10^{-2}	5.619×10^{-1}	3.019×10^{-2}	5.440×10^{-1}	2.878×10^{-2}	5.349×10^{-1}	2.918×10^{-2}	5.168×10^{-1}	2.859×10^{-2}
A2Col	1.925×10^{1}	2.494×10^{-1}	1.925×10^{1}	2.491×10^{-1}	1.926×10^{1}	2.494×10^{-1}	1.926×10^{1}	2.491×10^{-1}	1.925×10^{1}	2.490×10^{-1}	1.938×10^{1}	2.498×10^{-1}
A2PostCol	2.236	5.009×10^{-2}	2.225	4.907×10^{-2}	2.216	4.871×10^{-2}	2.252	4.956×10^{-2}	2.227	4.913×10^{-2}	2.155	4.819×10^{-2}
M2	2.138×10^{2}	9.691×10^{-1}	1.306×10^{2}	7.146×10^{-1}	8.553×10^{1}	5.578×10^{-1}	5.787×10^{1}	4.467×10^{-1}	3.955×10^{1}	3.621×10^{-1}	2.687×10^{1}	2.934×10^{-1}
T4S	2.309×10^{-1}	1.466×10^{-2}	1.501×10^{-1}	1.205×10^{-2}	1.094×10^{-1}	1.052×10^{-2}	6.120×10^{-2}	7.392×10^{-3}	4.165×10^{-2}	6.008×10^{-3}	3.285×10^{-2}	5.491×10^{-3}
T4L	3.028×10^{-3}	2.051×10^{-4}	2.077×10^{-3}	1.512×10^{-4}	3.386×10^{-3}	2.134×10^{-3}	1.005×10^{-3}	1.051×10^{-4}	8.263×10^{-4}	1.016×10^{-4}	5.466×10^{-4}	7.411×10^{-5}
T4C	2.793×10^{-4}	1.166×10^{-4}	2.337×10^{-4}	9.690×10^{-5}	8.697×10^{-5}	7.147×10^{-5}	7.472×10^{-5}	3.908×10^{-5}	1.285×10^{-4}	1.092×10^{-4}	3.551×10^{-5}	1.945×10^{-5}
T3+T2+T1	6.656×10^{-2}	6.688×10^{-3}	6.762×10^{-2}	6.880×10^{-3}	6.203×10^{-2}	6.388×10^{-3}	6.226×10^{-2}	6.984×10^{-3}	6.628×10^{-2}	7.136×10^{-3}	6.820×10^{-2}	6.842×10^{-3}

$\frac{a_{\mathrm{2ndCol}}}{2\sigma_{\mathrm{beam}}}$	**11**		**12**		**13**		**14**		**15**		**16**	
Section	P_{loss}[W]	ΔP_{loss}[W]	P_{loss}[W]	ΔP_{loss}[W]	P_{loss}[W]	ΔP_{loss}[W]	P_{loss}[W]	ΔP_{loss}[W]	P_{loss}[W]	ΔP_{loss}[W]	P_{loss}[W]	ΔP_{loss}[W]
Total	4.171×10^{1}	3.679×10^{-1}	3.525×10^{1}	3.334×10^{-1}	3.228×10^{1}	3.167×10^{-1}	3.031×10^{1}	3.050×10^{-1}	2.870×10^{1}	2.951×10^{-1}	2.735×10^{1}	2.871×10^{-1}
Ex	1.887	5.798×10^{-2}	1.906	5.780×10^{-2}	1.882	5.730×10^{-2}	1.908	5.837×10^{-2}	1.888	5.786×10^{-2}	1.908	5.854×10^{-2}
A2PreCol	5.531×10^{-1}	3.076×10^{-2}	5.228×10^{-1}	2.868×10^{-2}	5.160×10^{-1}	2.825×10^{-2}	5.403×10^{-1}	2.887×10^{-2}	5.519×10^{-1}	3.012×10^{-2}	5.507×10^{-1}	2.973×10^{-2}
A2Col	1.938×10^{1}	2.501×10^{-1}	1.923×10^{1}	2.490×10^{-1}	1.934×10^{1}	2.495×10^{-1}	1.931×10^{1}	2.495×10^{-1}	1.923×10^{1}	2.491×10^{-1}	1.930×10^{1}	2.497×10^{-1}
A2PostCol	2.115	4.748×10^{-2}	2.257	5.000×10^{-2}	2.124	4.816×10^{-2}	2.201	4.871×10^{-2}	2.223	4.772×10^{-2}	2.174	4.860×10^{-2}
M2	1.768×10^{1}	2.343×10^{-1}	1.125×10^{1}	1.856×10^{-1}	8.347	1.588×10^{-1}	6.280	1.370×10^{-1}	4.738	1.177×10^{-1}	3.332	9.760×10^{-2}
T4S	3.022×10^{-2}	4.722×10^{-3}	1.526×10^{-2}	4.775×10^{-3}	2.094×10^{-3}	6.797×10^{-4}	3.788×10^{-3}	1.325×10^{-3}	3.106×10^{-3}	1.325×10^{-3}	5.256×10^{-3}	2.159×10^{-3}
T4L	4.851×10^{-4}	1.055×10^{-4}	1.977×10^{-4}	4.358×10^{-5}	2.181×10^{-4}	6.877×10^{-5}	1.778×10^{-4}	9.043×10^{-5}	5.836×10^{-5}	1.801×10^{-5}	6.069×10^{-5}	2.084×10^{-5}
T4C	1.358×10^{-5}	7.263×10^{-6}	1.071×10^{-6}	1.071×10^{-6}	0	0	0	0	1.334×10^{-6}	1.334×10^{-6}	4.058×10^{-6}	4.058×10^{-6}
T3+T2+T1	6.473×10^{-2}	6.850×10^{-3}	6.295×10^{-2}	6.781×10^{-3}	6.800×10^{-2}	6.861×10^{-3}	6.154×10^{-2}	6.134×10^{-3}	6.903×10^{-2}	6.957×10^{-3}	8.149×10^{-2}	7.370×10^{-3}

$\frac{a_{\mathrm{2ndCol}}}{2\sigma_{\mathrm{beam}}}$	**17**		**18**		**19**		**20**		∞	
Section	P_{loss}[W]	ΔP_{loss}[W]	P_{loss}[W]	ΔP_{loss}[W]	P_{loss}[W]	ΔP_{loss}[W]	P_{loss}[W]	ΔP_{loss}[W]	P_{loss}[W]	ΔP_{loss}[W]
Total	2.632×10^{1}	2.799×10^{-1}	2.564×10^{1}	2.766×10^{-1}	2.511×10^{1}	2.729×10^{-1}	2.474×10^{1}	2.699×10^{-1}	2.424×10^{1}	2.670×10^{-1}
Ex	1.885	5.727×10^{-2}	1.921	5.876×10^{-2}	1.914	5.780×10^{-2}	1.877	5.773×10^{-2}	1.953	5.920×10^{-2}
A2PreCol	5.260×10^{-1}	2.933×10^{-2}	5.032×10^{-1}	2.876×10^{-2}	5.034×10^{-1}	2.842×10^{-2}	5.730×10^{-1}	3.139×10^{-2}	5.251×10^{-1}	2.883×10^{-2}
A2Col	1.921×10^{1}	2.486×10^{-1}	1.938×10^{1}	2.501×10^{-1}	1.933×10^{1}	2.499×10^{-1}	1.918×10^{1}	2.483×10^{-1}	1.929×10^{1}	2.490×10^{-1}
A2PostCol	2.246	4.937×10^{-2}	2.119	4.803×10^{-2}	2.164	4.825×10^{-2}	2.330	5.015×10^{-2}	2.162	4.819×10^{-2}
M2	2.341	8.089×10^{-2}	1.594	6.640×10^{-2}	1.090	5.333×10^{-2}	6.719×10^{-1}	4.206×10^{-2}	1.477×10^{-1}	1.638×10^{-2}
T4S	4.157×10^{-3}	1.416×10^{-3}	3.346×10^{-4}	1.846×10^{-4}	1.747×10^{-3}	7.588×10^{-4}	6.383×10^{-4}	3.828×10^{-4}	3.118×10^{-3}	1.608×10^{-3}
T4L	3.669×10^{-5}	1.349×10^{-5}	2.570×10^{-3}	1.779×10^{-3}	2.434×10^{-5}	9.508×10^{-6}	5.028×10^{-5}	2.673×10^{-5}	1.286×10^{-3}	1.286×10^{-3}
T4C	0	0	0	0	1.700×10^{-5}	1.700×10^{-5}	1.589×10^{-6}	1.589×10^{-6}	2.625×10^{-3}	1.873×10^{-3}
T3+T2+T1	9.908×10^{-2}	7.751×10^{-3}	1.120×10^{-1}	8.436×10^{-3}	1.113×10^{-1}	8.134×10^{-3}	1.110×10^{-1}	7.901×10^{-3}	1.476×10^{-1}	9.894×10^{-3}

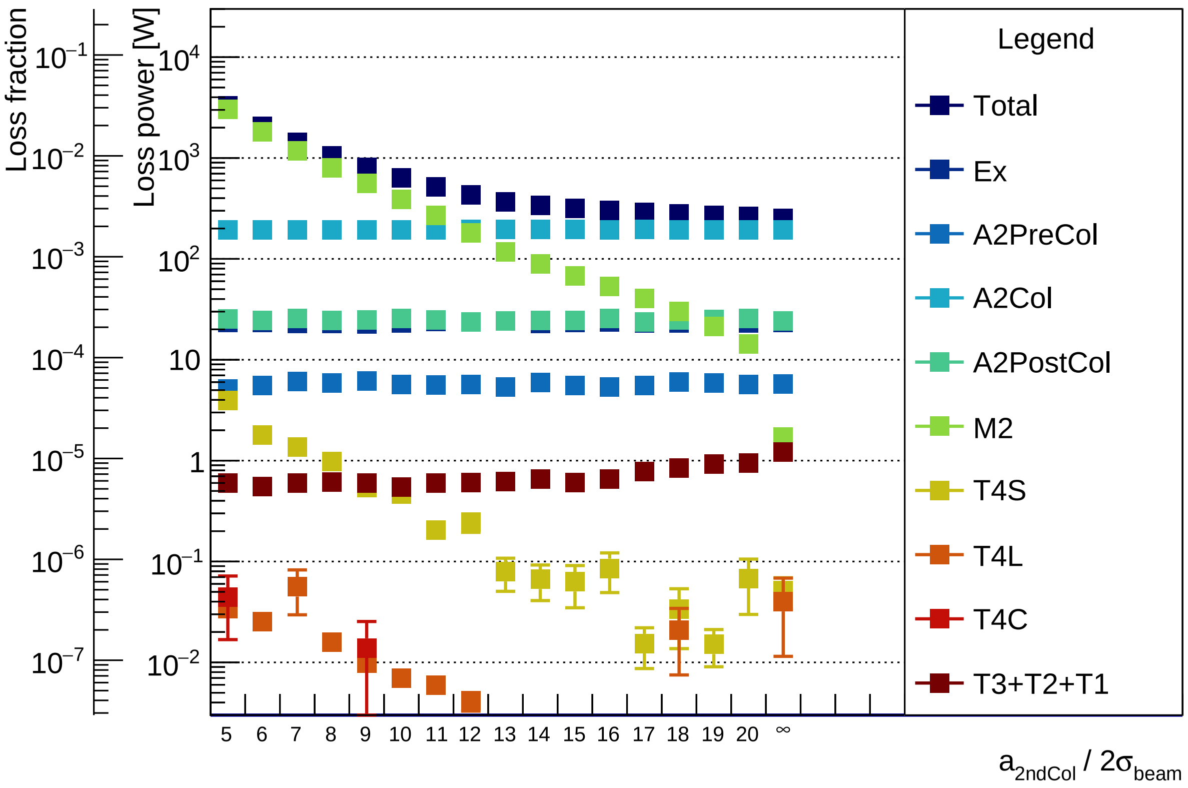

Figure A.28: Second collimator aperture sweep without spoiler for a O target induced halo.

Table A.28: Loss power numbers from O TAIL second collimator aperture sweep without spoiler in Figure A.28.

$\frac{a_{\text{2ndCol}}}{2\sigma_{\text{beam}}}$	**5**		**6**		**7**		**8**		**9**		**10**	
Section	P_{loss}[W]	ΔP_{loss}[W]	P_{loss}[W]	ΔP_{loss}[W]	P_{loss}[W]	ΔP_{loss}[W]	P_{loss}[W]	ΔP_{loss}[W]	P_{loss}[W]	ΔP_{loss}[W]	P_{loss}[W]	ΔP_{loss}[W]
Total	$3.277{\times}10^{3}$	$1.369{\times}10^{1}$	$2.069{\times}10^{3}$	$1.021{\times}10^{1}$	$1.431{\times}10^{3}$	8.155	$1.052{\times}10^{3}$	6.796	$8.091{\times}10^{2}$	5.822	$6.391{\times}10^{2}$	5.068
Ex	$2.349{\times}10^{1}$	$7.006{\times}10^{-1}$	$2.353{\times}10^{1}$	$7.076{\times}10^{-1}$	$2.303{\times}10^{1}$	$6.996{\times}10^{-1}$	$2.291{\times}10^{1}$	$6.916{\times}10^{-1}$	$2.270{\times}10^{1}$	$6.884{\times}10^{-1}$	$2.306{\times}10^{1}$	$6.930{\times}10^{-1}$
A2PreCol	5.151	$3.192{\times}10^{-1}$	5.532	$3.273{\times}10^{-1}$	6.072	$3.481{\times}10^{-1}$	5.867	$3.346{\times}10^{-1}$	6.188	$3.466{\times}10^{-1}$	5.677	$3.264{\times}10^{-1}$
A2Col	$1.943{\times}10^{2}$	2.729	$1.948{\times}10^{2}$	2.737	$1.933{\times}10^{2}$	2.720	$1.942{\times}10^{2}$	2.726	$1.945{\times}10^{2}$	2.735	$1.940{\times}10^{2}$	2.730
A2PostCol	$2.525{\times}10^{1}$	$5.813{\times}10^{-1}$	$2.456{\times}10^{1}$	$5.723{\times}10^{-1}$	$2.563{\times}10^{1}$	$5.858{\times}10^{-1}$	$2.464{\times}10^{1}$	$5.760{\times}10^{-1}$	$2.486{\times}10^{1}$	$5.785{\times}10^{-1}$	$2.559{\times}10^{1}$	$5.765{\times}10^{-1}$
M2	$3.024{\times}10^{3}$	$1.280{\times}10^{1}$	$1.818{\times}10^{3}$	9.311	$1.181{\times}10^{3}$	7.221	$8.029{\times}10^{2}$	5.804	$5.596{\times}10^{2}$	4.747	$3.898{\times}10^{2}$	3.895
T4S	3.930	$2.110{\times}10^{-1}$	1.797	$1.266{\times}10^{-1}$	1.360	$1.254{\times}10^{-1}$	$9.838{\times}10^{-1}$	$1.105{\times}10^{-1}$	$5.417{\times}10^{-1}$	$6.001{\times}10^{-2}$	$4.668{\times}10^{-1}$	$8.027{\times}10^{-2}$
T4L	$3.403{\times}10^{-2}$	$1.959{\times}10^{-3}$	$2.546{\times}10^{-2}$	$1.929{\times}10^{-3}$	$5.607{\times}10^{-2}$	$2.645{\times}10^{-2}$	$1.595{\times}10^{-2}$	$2.101{\times}10^{-3}$	$9.808{\times}10^{-3}$	$1.679{\times}10^{-3}$	$6.942{\times}10^{-3}$	$1.077{\times}10^{-3}$
T4C	$4.430{\times}10^{-2}$	$2.749{\times}10^{-2}$	$2.473{\times}10^{-3}$	$1.508{\times}10^{-3}$	$6.421{\times}10^{-4}$	$5.061{\times}10^{-4}$	$1.388{\times}10^{-4}$	$8.635{\times}10^{-5}$	$1.387{\times}10^{-2}$	$1.156{\times}10^{-2}$	$1.080{\times}10^{-3}$	$8.486{\times}10^{-4}$
T3+T2+T1	$5.995{\times}10^{-1}$	$6.943{\times}10^{-2}$	$5.516{\times}10^{-1}$	$6.721{\times}10^{-2}$	$5.971{\times}10^{-1}$	$7.062{\times}10^{-2}$	$6.133{\times}10^{-1}$	$7.586{\times}10^{-2}$	$5.996{\times}10^{-1}$	$7.396{\times}10^{-2}$	$5.456{\times}10^{-1}$	$7.022{\times}10^{-2}$

$\frac{a_{\text{2ndCol}}}{2\sigma_{\text{beam}}}$	**11**		**12**		**13**		**14**		**15**		**16**	
Section	P_{loss}[W]	ΔP_{loss}[W]	P_{loss}[W]	ΔP_{loss}[W]	P_{loss}[W]	ΔP_{loss}[W]	P_{loss}[W]	ΔP_{loss}[W]	P_{loss}[W]	ΔP_{loss}[W]	P_{loss}[W]	ΔP_{loss}[W]
Total	$5.191{\times}10^{2}$	4.488	$4.314{\times}10^{2}$	4.025	$3.666{\times}10^{2}$	3.677	$3.388{\times}10^{2}$	3.508	$3.173{\times}10^{2}$	3.377	$3.024{\times}10^{2}$	3.278
Ex	$2.388{\times}10^{1}$	$7.145{\times}10^{-1}$	$2.380{\times}10^{1}$	$7.078{\times}10^{-1}$	$2.416{\times}10^{1}$	$7.301{\times}10^{-1}$	$2.290{\times}10^{1}$	$6.936{\times}10^{-1}$	$2.339{\times}10^{1}$	$7.045{\times}10^{-1}$	$2.358{\times}10^{1}$	$7.148{\times}10^{-1}$
A2PreCol	5.630	$3.338{\times}10^{-1}$	5.706	$3.243{\times}10^{-1}$	5.361	$3.143{\times}10^{-1}$	5.923	$3.424{\times}10^{-1}$	5.579	$3.299{\times}10^{-1}$	5.356	$3.142{\times}10^{-1}$
A2Col	$1.931{\times}10^{2}$	2.720	$1.956{\times}10^{2}$	2.737	$1.951{\times}10^{2}$	2.735	$1.953{\times}10^{2}$	2.736	$1.953{\times}10^{2}$	2.738	$1.939{\times}10^{2}$	2.727
A2PostCol	$2.492{\times}10^{1}$	$5.632{\times}10^{-1}$	$2.371{\times}10^{1}$	$5.407{\times}10^{-1}$	$2.412{\times}10^{1}$	$5.636{\times}10^{-1}$	$2.447{\times}10^{1}$	$5.571{\times}10^{-1}$	$2.452{\times}10^{1}$	$5.488{\times}10^{-1}$	$2.560{\times}10^{1}$	$5.795{\times}10^{-1}$
M2	$2.707{\times}10^{2}$	3.203	$1.817{\times}10^{2}$	2.587	$1.172{\times}10^{2}$	2.071	$8.944{\times}10^{1}$	1.800	$6.784{\times}10^{1}$	1.562	$5.317{\times}10^{1}$	1.369
T4S	$2.047{\times}10^{-1}$	$3.436{\times}10^{-2}$	$2.467{\times}10^{-1}$	$5.209{\times}10^{-2}$	$7.921{\times}10^{-2}$	$2.860{\times}10^{-2}$	$6.665{\times}10^{-2}$	$2.568{\times}10^{-2}$	$6.298{\times}10^{-2}$	$2.819{\times}10^{-2}$	$8.543{\times}10^{-2}$	$3.624{\times}10^{-2}$
T4L	$5.951{\times}10^{-3}$	$9.806{\times}10^{-4}$	$4.147{\times}10^{-3}$	$8.602{\times}10^{-4}$	$2.365{\times}10^{-3}$	$6.780{\times}10^{-4}$	$1.071{\times}10^{-3}$	$2.456{\times}10^{-4}$	$2.274{\times}10^{-3}$	$8.031{\times}10^{-4}$	$1.109{\times}10^{-3}$	$2.972{\times}10^{-4}$
T4C	$1.122{\times}10^{-3}$	$8.816{\times}10^{-4}$	$1.636{\times}10^{-4}$	$7.880{\times}10^{-5}$	$3.517{\times}10^{-5}$	$3.517{\times}10^{-5}$	0	0	0	0	0	0
T3+T2+T1	$6.000{\times}10^{-1}$	$7.195{\times}10^{-2}$	$6.082{\times}10^{-1}$	$7.403{\times}10^{-2}$	$6.214{\times}10^{-1}$	$7.378{\times}10^{-2}$	$6.536{\times}10^{-1}$	$7.756{\times}10^{-2}$	$6.057{\times}10^{-1}$	$6.730{\times}10^{-2}$	$6.593{\times}10^{-1}$	$6.511{\times}10^{-2}$

$\frac{a_{\text{2ndCol}}}{2\sigma_{\text{beam}}}$	**17**		**18**		**19**		**20**		∞	
Section	P_{loss}[W]	ΔP_{loss}[W]	P_{loss}[W]	ΔP_{loss}[W]	P_{loss}[W]	ΔP_{loss}[W]	P_{loss}[W]	ΔP_{loss}[W]	P_{loss}[W]	ΔP_{loss}[W]
Total	$2.895{\times}10^{2}$	3.199	$2.796{\times}10^{2}$	3.125	$2.711{\times}10^{2}$	3.071	$2.633{\times}10^{2}$	3.017	$2.513{\times}10^{2}$	2.943
Ex	$2.312{\times}10^{1}$	$7.012{\times}10^{-1}$	$2.322{\times}10^{1}$	$7.137{\times}10^{-1}$	$2.316{\times}10^{1}$	$7.021{\times}10^{-1}$	$2.320{\times}10^{1}$	$7.037{\times}10^{-1}$	$2.352{\times}10^{1}$	$7.110{\times}10^{-1}$
A2PreCol	5.566	$3.257{\times}10^{-1}$	6.044	$3.367{\times}10^{-1}$	5.898	$3.389{\times}10^{-1}$	5.712	$3.335{\times}10^{-1}$	5.754	$3.369{\times}10^{-1}$
A2Col	$1.958{\times}10^{2}$	2.742	$1.946{\times}10^{2}$	2.728	$1.945{\times}10^{2}$	2.732	$1.934{\times}10^{2}$	2.721	$1.948{\times}10^{2}$	2.730
A2PostCol	$2.381{\times}10^{1}$	$5.552{\times}10^{-1}$	$2.474{\times}10^{1}$	$5.620{\times}10^{-1}$	$2.522{\times}10^{1}$	$5.748{\times}10^{-1}$	$2.563{\times}10^{1}$	$5.760{\times}10^{-1}$	$2.427{\times}10^{1}$	$5.549{\times}10^{-1}$
M2	$4.042{\times}10^{1}$	1.179	$3.012{\times}10^{1}$	1.003	$2.129{\times}10^{1}$	$8.334{\times}10^{-1}$	$1.434{\times}10^{1}$	$6.717{\times}10^{-1}$	1.705	$1.908{\times}10^{-1}$
T4S	$1.536{\times}10^{-2}$	$6.672{\times}10^{-3}$	$3.369{\times}10^{-2}$	$2.000{\times}10^{-2}$	$1.510{\times}10^{-2}$	$6.052{\times}10^{-3}$	$6.773{\times}10^{-2}$	$3.786{\times}10^{-2}$	$5.135{\times}10^{-2}$	$1.765{\times}10^{-2}$
T4L	$8.575{\times}10^{-4}$	$2.581{\times}10^{-4}$	$2.089{\times}10^{-2}$	$1.338{\times}10^{-2}$	$4.436{\times}10^{-4}$	$1.938{\times}10^{-4}$	$1.208{\times}10^{-3}$	$9.794{\times}10^{-4}$	$3.995{\times}10^{-2}$	$2.848{\times}10^{-2}$
T4C	0	0	0	0	0	0	0	0	0	0
T3+T2+T1	$7.805{\times}10^{-1}$	$7.793{\times}10^{-2}$	$8.467{\times}10^{-1}$	$8.308{\times}10^{-2}$	$9.235{\times}10^{-1}$	$8.135{\times}10^{-2}$	$9.445{\times}10^{-1}$	$8.168{\times}10^{-2}$	1.211	$9.571{\times}10^{-2}$

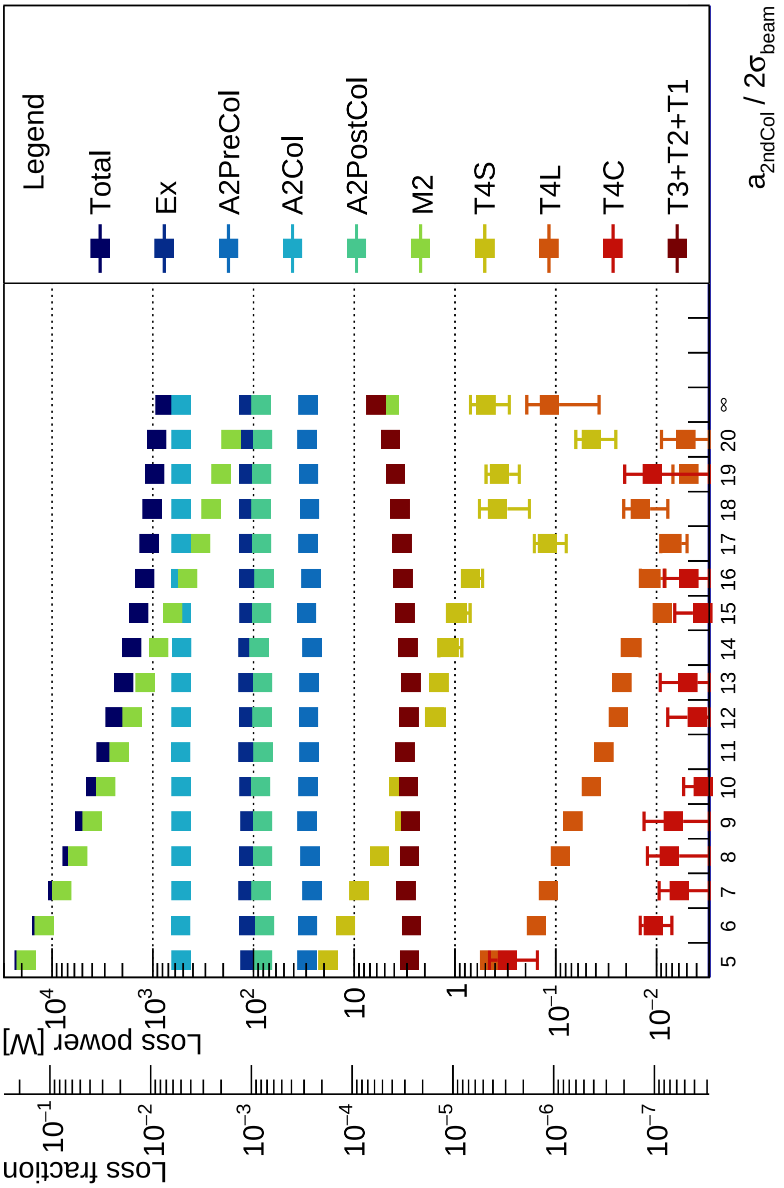

Figure A.29: Second collimator aperture sweep without spoiler for a Ar target induced halo.

Table A.29: Loss power numbers from Ar TAIL second collimator aperture sweep without spoiler in Figure A.29.

$\frac{a_{\mathrm{2ndCol}}}{2\sigma_{\mathrm{beam}}}$	**5**		**6**		**7**		**8**		**9**		**10**	
Section	P_{loss}[W]	ΔP_{loss}[W]	P_{loss}[W]	ΔP_{loss}[W]	P_{loss}[W]	ΔP_{loss}[W]	P_{loss}[W]	ΔP_{loss}[W]	P_{loss}[W]	ΔP_{loss}[W]	P_{loss}[W]	ΔP_{loss}[W]
Total	1.888×10^{4}	7.746×10^{1}	1.266×10^{4}	5.918×10^{1}	8.757×10^{3}	4.675×10^{1}	6.337×10^{3}	3.831×10^{1}	4.749×10^{3}	3.224×10^{1}	3.675×10^{3}	2.775×10^{1}
Ex	1.086×10^{2}	3.385	1.114×10^{2}	3.455	1.130×10^{2}	3.524	1.125×10^{2}	3.487	1.087×10^{2}	3.372	1.104×10^{2}	3.412
A2PreCol	2.931×10^{1}	1.711	2.923×10^{1}	1.679	2.625×10^{1}	1.595	2.735×10^{1}	1.611	2.935×10^{1}	1.646	2.884×10^{1}	1.686
A2Col	5.232×10^{2}	9.904	5.291×10^{2}	9.979	5.210×10^{2}	9.892	5.260×10^{2}	9.912	5.263×10^{2}	9.915	5.214×10^{2}	9.895
A2PostCol	8.164×10^{1}	2.286	7.753×10^{1}	2.211	8.443×10^{1}	2.371	8.158×10^{1}	2.314	8.094×10^{1}	2.258	8.499×10^{1}	2.396
M2	1.811×10^{4}	7.473×10^{1}	1.190×10^{4}	5.646×10^{1}	8.001×10^{3}	4.400×10^{1}	5.581×10^{3}	3.545×10^{1}	3.998×10^{3}	2.924×10^{1}	2.922×10^{3}	2.454×10^{1}
T4S	1.826×10^{1}	1.034	1.221×10^{1}	7.990×10^{-1}	8.953	6.996×10^{-1}	5.594	5.833×10^{-1}	3.170	3.742×10^{-1}	3.607	4.295×10^{-1}
T4L	4.371×10^{-1}	1.095×10^{-1}	1.555×10^{-1}	9.342×10^{-3}	1.184×10^{-1}	8.967×10^{-3}	9.032×10^{-2}	7.185×10^{-3}	6.766×10^{-2}	1.011×10^{-2}	4.442×10^{-2}	5.248×10^{-3}
T4C	3.034×10^{-1}	1.511×10^{-1}	1.078×10^{-2}	3.738×10^{-3}	5.949×10^{-3}	3.481×10^{-3}	7.441×10^{-3}	4.865×10^{-3}	6.794×10^{-3}	6.522×10^{-3}	3.427×10^{-3}	1.954×10^{-3}
T3+T2+T1	2.834	3.506×10^{-1}	2.694	3.394×10^{-1}	3.065	3.724×10^{-1}	2.845	3.326×10^{-1}	2.771	3.429×10^{-1}	2.898	3.444×10^{-1}

$\frac{a_{\mathrm{2ndCol}}}{2\sigma_{\mathrm{beam}}}$	**11**		**12**		**13**		**14**		**15**		**16**	
Section	P_{loss}[W]	ΔP_{loss}[W]	P_{loss}[W]	ΔP_{loss}[W]	P_{loss}[W]	ΔP_{loss}[W]	P_{loss}[W]	ΔP_{loss}[W]	P_{loss}[W]	ΔP_{loss}[W]	P_{loss}[W]	ΔP_{loss}[W]
Total	2.911×10^{3}	2.425×10^{1}	2.356×10^{3}	2.143×10^{1}	1.940×10^{3}	1.915×10^{1}	1.622×10^{3}	1.725×10^{1}	1.383×10^{3}	1.571×10^{1}	1.200×10^{3}	1.449×10^{1}
Ex	1.127×10^{2}	3.478	1.119×10^{2}	3.478	1.132×10^{2}	3.510	1.128×10^{2}	3.457	1.113×10^{2}	3.446	1.123×10^{2}	3.445
A2PreCol	2.803×10^{1}	1.654	2.830×10^{1}	1.677	2.804×10^{1}	1.636	2.629×10^{1}	1.560	2.962×10^{1}	1.699	2.688×10^{1}	1.628
A2Col	5.265×10^{2}	9.955	5.242×10^{2}	9.913	5.252×10^{2}	9.941	5.177×10^{2}	9.868	5.220×10^{2}	9.897	5.274×10^{2}	9.951
A2PostCol	8.048×10^{1}	2.292	8.187×10^{1}	2.328	8.176×10^{1}	2.305	8.791×10^{1}	2.444	8.352×10^{1}	2.348	7.878×10^{1}	2.292
M2	2.157×10^{3}	2.077×10^{1}	1.605×10^{3}	1.766×10^{1}	1.188×10^{3}	1.503×10^{1}	8.734×10^{2}	1.277×10^{1}	6.328×10^{2}	1.075×10^{1}	4.509×10^{2}	9.006
T4S	3.144	4.139×10^{-1}	1.598	3.270×10^{-1}	1.450	2.580×10^{-1}	1.151	2.956×10^{-1}	9.516×10^{-1}	2.419×10^{-1}	7.042×10^{-1}	1.724×10^{-1}
T4L	3.344×10^{-2}	5.049×10^{-3}	2.396×10^{-2}	3.470×10^{-3}	2.222×10^{-2}	3.238×10^{-3}	1.821×10^{-2}	3.635×10^{-3}	8.797×10^{-3}	1.707×10^{-3}	1.136×10^{-2}	3.106×10^{-3}
T4C	8.921×10^{-4}	4.470×10^{-4}	3.961×10^{-3}	3.777×10^{-3}	4.872×10^{-3}	4.316×10^{-3}	8.205×10^{-4}	4.318×10^{-4}	3.483×10^{-3}	3.113×10^{-3}	4.788×10^{-3}	3.607×10^{-3}
T3+T2+T1	3.151	3.784×10^{-1}	2.867	3.280×10^{-1}	2.744	3.410×10^{-1}	2.945	3.632×10^{-1}	3.134	3.560×10^{-1}	3.270	3.642×10^{-1}

$\frac{a_{\mathrm{2ndCol}}}{2\sigma_{\mathrm{beam}}}$	**17**		**18**		**19**		**20**		∞	
Section	P_{loss}[W]	ΔP_{loss}[W]	P_{loss}[W]	ΔP_{loss}[W]	P_{loss}[W]	ΔP_{loss}[W]	P_{loss}[W]	ΔP_{loss}[W]	P_{loss}[W]	ΔP_{loss}[W]
Total	1.085×10^{3}	1.368×10^{1}	1.019×10^{3}	1.319×10^{1}	9.613×10^{2}	1.272×10^{1}	9.195×10^{2}	1.241×10^{1}	7.583×10^{2}	1.105×10^{1}
Ex	1.115×10^{2}	3.419	1.119×10^{2}	3.439	1.114×10^{2}	3.428	1.099×10^{2}	3.403	1.123×10^{2}	3.493
A2PreCol	2.862×10^{1}	1.660	2.790×10^{1}	1.646	2.853×10^{1}	1.643	2.957×10^{1}	1.684	2.867×10^{1}	1.644
A2Col	5.241×10^{2}	9.934	5.257×10^{2}	9.945	5.233×10^{2}	9.899	5.261×10^{2}	9.946	5.216×10^{2}	9.890
A2PostCol	8.311×10^{1}	2.329	8.461×10^{1}	2.375	8.281×10^{1}	2.308	8.168×10^{1}	2.292	8.467×10^{1}	2.358
M2	3.337×10^{2}	7.764	2.651×10^{2}	6.906	2.110×10^{2}	6.129	1.678×10^{2}	5.453	4.456	6.669×10^{-1}
T4S	1.212×10^{-1}	4.234×10^{-2}	3.776×10^{-1}	1.951×10^{-1}	3.618×10^{-1}	1.311×10^{-1}	4.432×10^{-2}	1.896×10^{-2}	4.956×10^{-1}	2.059×10^{-1}
T4L	7.029×10^{-3}	2.048×10^{-3}	1.444×10^{-2}	6.716×10^{-3}	4.799×10^{-3}	2.079×10^{-3}	5.124×10^{-3}	3.793×10^{-3}	1.156×10^{-1}	7.833×10^{-2}
T4C	0	0	2.814×10^{-4}	2.797×10^{-4}	1.101×10^{-2}	9.687×10^{-3}	4.369×10^{-5}	4.369×10^{-5}	2.141×10^{-4}	2.141×10^{-4}
T3+T2+T1	3.361	3.667×10^{-1}	3.503	3.610×10^{-1}	3.894	3.727×10^{-1}	4.384	4.279×10^{-1}	6.056	5.151×10^{-1}

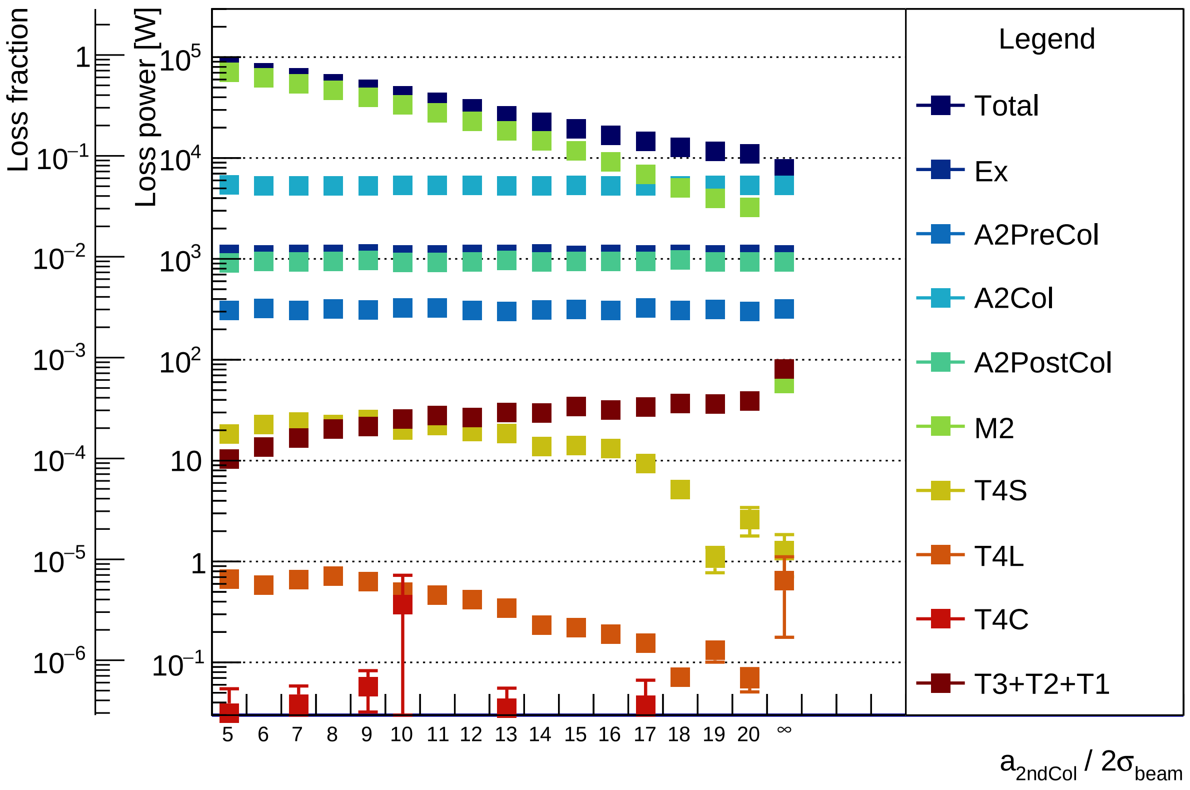

Figure A.30: Second collimator aperture sweep without spoiler for a Xe target induced halo.

Table A.30: Loss power numbers from Xe TAIL second collimator aperture sweep without spoiler in Figure A.30.

$\frac{a_{\mathrm{2ndCol}}}{2\sigma_{\mathrm{beam}}}$	**5**		**6**		**7**		**8**		**9**		**10**	
Section	P_{loss}[W]	ΔP_{loss}[W]	P_{loss}[W]	ΔP_{loss}[W]	P_{loss}[W]	ΔP_{loss}[W]	P_{loss}[W]	ΔP_{loss}[W]	P_{loss}[W]	ΔP_{loss}[W]	P_{loss}[W]	ΔP_{loss}[W]
Total	7.824×10^{4}	3.845×10^{2}	7.016×10^{4}	3.543×10^{2}	6.217×10^{4}	3.235×10^{2}	5.464×10^{4}	2.938×10^{2}	4.773×10^{4}	2.657×10^{2}	4.136×10^{4}	2.393×10^{2}
Ex	1.107×10^{3}	2.260×10^{1}	1.096×10^{3}	2.251×10^{1}	1.107×10^{3}	2.259×10^{1}	1.109×10^{3}	2.257×10^{1}	1.115×10^{3}	2.262×10^{1}	1.091×10^{3}	2.222×10^{1}
A2PreCol	3.070×10^{2}	1.102×10^{1}	3.214×10^{2}	1.152×10^{1}	3.088×10^{2}	1.130×10^{1}	3.192×10^{2}	1.141×10^{1}	3.127×10^{2}	1.142×10^{1}	3.271×10^{2}	1.156×10^{1}
A2Col	5.389×10^{3}	6.666×10^{1}	5.319×10^{3}	6.615×10^{1}	5.296×10^{3}	6.597×10^{1}	5.324×10^{3}	6.619×10^{1}	5.278×10^{3}	6.596×10^{1}	5.342×10^{3}	6.633×10^{1}
A2PostCol	9.092×10^{2}	1.617×10^{1}	9.406×10^{2}	1.641×10^{1}	9.373×10^{2}	1.611×10^{1}	9.465×10^{2}	1.649×10^{1}	9.664×10^{2}	1.672×10^{1}	9.239×10^{2}	1.606×10^{1}
M2	7.050×10^{4}	3.490×10^{2}	6.245×10^{4}	3.192×10^{2}	5.448×10^{4}	2.887×10^{2}	4.690×10^{4}	2.589×10^{2}	4.001×10^{4}	2.309×10^{2}	3.363×10^{4}	2.045×10^{2}
T4S	1.846×10^{1}	2.034	2.291×10^{1}	2.194	2.426×10^{1}	2.338	2.287×10^{1}	2.143	2.555×10^{1}	2.351	2.007×10^{1}	1.984
T4L	6.700×10^{-1}	5.592×10^{-2}	5.812×10^{-1}	4.574×10^{-2}	6.590×10^{-1}	3.864×10^{-2}	7.201×10^{-1}	6.225×10^{-2}	6.349×10^{-1}	4.732×10^{-2}	4.955×10^{-1}	3.713×10^{-2}
T4C	3.147×10^{-2}	2.329×10^{-2}	1.889×10^{-2}	8.670×10^{-3}	3.858×10^{-2}	1.975×10^{-2}	2.303×10^{-2}	1.963×10^{-2}	5.745×10^{-2}	2.527×10^{-2}	3.741×10^{-1}	3.559×10^{-1}
T3+T2+T1	1.038×10^{1}	1.312	1.370×10^{1}	1.623	1.684×10^{1}	1.775	2.059×10^{1}	1.876	2.170×10^{1}	2.027	2.584×10^{1}	2.167

$\frac{a_{\mathrm{2ndCol}}}{2\sigma_{\mathrm{beam}}}$	**11**		**12**		**13**		**14**		**15**		**16**	
Section	P_{loss}[W]	ΔP_{loss}[W]	P_{loss}[W]	ΔP_{loss}[W]	P_{loss}[W]	ΔP_{loss}[W]	P_{loss}[W]	ΔP_{loss}[W]	P_{loss}[W]	ΔP_{loss}[W]	P_{loss}[W]	ΔP_{loss}[W]
Total	3.571×10^{4}	2.153×10^{2}	3.076×10^{4}	1.936×10^{2}	2.632×10^{4}	1.736×10^{2}	2.260×10^{4}	1.563×10^{2}	1.950×10^{4}	1.413×10^{2}	1.686×10^{4}	1.280×10^{2}
Ex	1.089×10^{3}	2.226×10^{1}	1.104×10^{3}	2.261×10^{1}	1.102×10^{3}	2.254×10^{1}	1.114×10^{3}	2.252×10^{1}	1.078×10^{3}	2.226×10^{1}	1.106×10^{3}	2.235×10^{1}
A2PreCol	3.251×10^{2}	1.152×10^{1}	3.075×10^{2}	1.124×10^{1}	3.015×10^{2}	1.106×10^{1}	3.117×10^{2}	1.122×10^{1}	3.137×10^{2}	1.135×10^{1}	3.085×10^{2}	1.123×10^{1}
A2Col	5.344×10^{3}	6.637×10^{1}	5.335×10^{3}	6.621×10^{1}	5.303×10^{3}	6.605×10^{1}	5.312×10^{3}	6.610×10^{1}	5.327×10^{3}	6.617×10^{1}	5.317×10^{3}	6.627×10^{1}
A2PostCol	9.257×10^{2}	1.614×10^{1}	9.303×10^{2}	1.595×10^{1}	9.660×10^{2}	1.666×10^{1}	9.378×10^{2}	1.639×10^{1}	9.385×10^{2}	1.620×10^{1}	9.404×10^{2}	1.646×10^{1}
M2	2.797×10^{4}	1.803×10^{2}	2.304×10^{4}	1.583×10^{2}	1.860×10^{4}	1.379×10^{2}	1.488×10^{4}	1.199×10^{2}	1.180×10^{4}	1.038×10^{2}	9.147×10^{3}	8.909×10^{1}
T4S	2.218×10^{1}	2.233	1.954×10^{1}	1.900	1.855×10^{1}	1.950	1.383×10^{1}	1.802	1.404×10^{1}	1.674	1.312×10^{1}	1.612
T4L	4.651×10^{-1}	4.297×10^{-2}	4.166×10^{-1}	3.781×10^{-2}	3.449×10^{-1}	3.628×10^{-2}	2.346×10^{-1}	2.182×10^{-2}	2.198×10^{-1}	2.821×10^{-2}	1.910×10^{-1}	3.024×10^{-2}
T4C	1.744×10^{-2}	1.138×10^{-2}	1.633×10^{-2}	1.013×10^{-2}	3.496×10^{-2}	2.054×10^{-2}	1.913×10^{-2}	1.549×10^{-2}	2.902×10^{-2}	2.122×10^{-2}	4.436×10^{-3}	1.910×10^{-3}
T3+T2+T1	2.801×10^{1}	2.183	2.677×10^{1}	2.184	3.007×10^{1}	2.259	2.970×10^{1}	2.332	3.422×10^{1}	2.557	3.184×10^{1}	2.435

$\frac{a_{\mathrm{2ndCol}}}{2\sigma_{\mathrm{beam}}}$	**17**		**18**		**19**		**20**		∞	
Section	P_{loss}[W]	ΔP_{loss}[W]	P_{loss}[W]	ΔP_{loss}[W]	P_{loss}[W]	ΔP_{loss}[W]	P_{loss}[W]	ΔP_{loss}[W]	P_{loss}[W]	ΔP_{loss}[W]
Total	1.462×10^{4}	1.163×10^{2}	1.279×10^{4}	1.064×10^{2}	1.169×10^{4}	1.005×10^{2}	1.096×10^{4}	9.638×10^{1}	7.824×10^{3}	7.673×10^{1}
Ex	1.098×10^{3}	2.245×10^{1}	1.106×10^{3}	2.252×10^{1}	1.094×10^{3}	2.225×10^{1}	1.103×10^{3}	2.266×10^{1}	1.097×10^{3}	2.232×10^{1}
A2PreCol	3.266×10^{2}	1.153×10^{1}	3.088×10^{2}	1.121×10^{1}	3.171×10^{2}	1.127×10^{1}	3.014×10^{2}	1.126×10^{1}	3.199×10^{2}	1.135×10^{1}
A2Col	5.324×10^{3}	6.621×10^{1}	5.304×10^{3}	6.600×10^{1}	5.347×10^{3}	6.642×10^{1}	5.336×10^{3}	6.632×10^{1}	5.333×10^{3}	6.628×10^{1}
A2PostCol	9.417×10^{2}	1.634×10^{1}	9.743×10^{2}	1.653×10^{1}	9.331×10^{2}	1.625×10^{1}	9.363×10^{2}	1.628×10^{1}	9.335×10^{2}	1.619×10^{1}
M2	6.889×10^{3}	7.556×10^{1}	5.056×10^{3}	6.378×10^{1}	3.965×10^{3}	5.589×10^{1}	3.243×10^{3}	5.016×10^{1}	5.824×10^{1}	5.083
T4S	9.366	1.286	5.181	9.371×10^{-1}	1.076	3.026×10^{-1}	2.610	8.195×10^{-1}	1.277	5.708×10^{-1}
T4L	1.546×10^{-1}	2.159×10^{-2}	7.111×10^{-2}	1.029×10^{-2}	1.314×10^{-1}	3.091×10^{-2}	6.882×10^{-2}	1.785×10^{-2}	6.452×10^{-1}	4.678×10^{-1}
T4C	3.756×10^{-2}	2.901×10^{-2}	1.752×10^{-3}	1.016×10^{-3}	7.107×10^{-4}	7.107×10^{-4}	7.649×10^{-4}	6.946×10^{-4}	0	0
T3+T2+T1	3.417×10^{1}	2.484	3.692×10^{1}	2.655	3.623×10^{1}	2.639	3.895×10^{1}	2.675	8.076×10^{1}	3.452

B Abbreviations

BDSIM	Beam Delivery Simulation, page 31
c.w.	Continuous Wave, page 2
CSDA	Continuous Slowing Down Approximation, page 26
CSV	Comma Separated Value, page 52
EC	Electron Capture, page 27
ERL	Energy Recovery Linac, page 2
Geant4	Geometry And Tracking, page 31
LHC	Large Hadron Collider, page 31
Linac	Linear Accelerator, page 2
MAD-X	Methodical Accelerator Design, page 31
MAGIX	MESA Gas Internal Target Experiment, page 3
MAMI	Mainz Microtron, page 37
NIST	National Institute of Science and Technology, page 37
PDF	Probability Density Function, page 22
TAIL	Target Induced Halo, page 6

C Tables

D Figures

Associated Publications

[Ledroit & Aulenbacher 2017]
Ledroit, B. & Aulenbacher, K.
Beam Dynamics and Collimation Following MAGIX at MESA
in *Proc. 59th Advanced ICFA Beam Dynamics Workshop on Energy Recovery Linacs (ERL'17)*
(Geneva, Switzerland, 2017),
17–19.

[Ledroit & Aulenbacher 2018]
Ledroit, B. & Aulenbacher, K.
*Beam Dynamics and Collimation Following MAGIX at MESA**
in *Proc. 29th Linear Accelerator Conference (LINAC'18)*
(Beijing, China, 2018),
540–542.

[Ledroit & Aulenbacher 2019]
Ledroit, B. & Aulenbacher, K.
Collimation of Target Induced Halo Following MAGIX at MESA
in *Proc. 10th Int. Particle Accelerator Conf. (IPAC'19)*
(Melbourne, Australia, 2019),
3839–3842.

References

[Agostinelli *et al.* 2003]
Agostinelli, S. *et al.*
Geant4 — a simulation toolkit.
Nuclear Instruments and Methods in Physics Research Section A: Accelerators, Spectrometers, Detectors and Associated Equipment **506,** 250 –303. ISSN: 0168-9002
(2003).

[Alexander 2018]
Alexander, I. C.
Experimental Investigation of the Beam Dynamics of the MESA Photoinjector
PhD thesis (Johannes Gutenberg-University Mainz, 2018).

[Allison *et al.* 2016]
Allison, J. *et al.*
Recent developments in Geant4.
Nuclear Instruments and Methods in Physics Research Section A: Accelerators, Spectrometers, Detectors and Associated Equipment **835,** 186 –225. ISSN: 0168-9002
(2016).

[Aulenbacher 2014]
Aulenbacher, S.
Design and Simulation of the Internal Gas-Target for MAGIX
Diploma thesis (Johannes Gutenberg-University Mainz, 2014).

[Barletta *et al.* 2012]
Barletta, W., Spentzouris, L. & Harms, E.
USPAS notes
2012.
`https://uspas.fnal.gov/materials/12MSU/emitlect.pdf`.

[Baumgarten *et al.* 2003]
Baumgarten, C. *et al.*
The storage cell of the polarized H/D internal gas target of the HERMES experiment at HERA.
Nuclear Instruments and Methods in Physics Research Section A: Accelerators, Spectrometers, Detectors and Associated Equipment **496,** 277 –285. ISSN: 0168-9002
(2003).

[Berger & Seltzer 1982]
Berger, M. J. & Seltzer, S. M.
Stopping Powers and Ranges of Electrons and Positrons 2nd Edition
(U.S. Department of Commerce, 1982).

[Berger *et al.* 2020]
Berger, M. J. *et al.*
ESTAR, PSTAR, and ASTAR: Computer Programs for Calculating Stopping-Power and Range Tables for Electrons, Protons, and Helium Ions (Version 2.0.0)
visited 07.05.2020.
2020.
`https://physics.nist.gov/PhysRefData/Star/Text/ESTAR.html`.

[Bernauer 2020]
Bernauer, J. C.
The proton radius puzzle – 9 years later.
EPJ Web Conf. **234** (eds D'Ambrosio, G. *et al.*) 01001
(2020).

[Böhlen *et al.* 2014]
Böhlen, T. *et al.*
The FLUKA Code: Developments and Challenges for High Energy and Medical Applications.
Nuclear Data Sheets **120,** 211 –214. ISSN: 0090-3752
(2014).

[Bundesamt für Strahlenschutz 2018]
Bundesamt für Strahlenschutz.
Verordnung zum Schutz vor der schädlichen Wirkung ionisierender Strahlung (Strahlenschutzverordnung - StrlSchV)
2018.

[Chao *et al.* 2013]
Chao, A. *et al.*
Handbook of Accelerator Physics and Engineering: 2nd Edition 2nd Edition.
ISBN: 978-981-4415-84-2, 978-981-4417-17-4
(Jan. 2013).

[Crawford 2005]
Crawford, C.
Precision measurement of the proton electric to magnetic form factor ratio with BLAST
PhD thesis (Massachusetts Institute of Technology, 2005).

[Deniau *et al.* 2019]
Deniau, L. *et al.*
The MAD-X Program: User's Reference Manual
CERN (Geneva, Switzerland, 2019).

[Diefenbach 2020a]
Diefenbach, J.
Criteria for radiation limits in the experimental area
Email from 18.08.2020.
2020.

[Diefenbach 2020b]
Diefenbach, J.
FLUKA simulations of the MAGIX jet target
unpublished.
2020.

[Doria *et al.* 2018]
Doria, L. *et al.*
Search for light dark matter with the MESA accelerator
in *13th Conference on the Intersections of Particle and Nuclear Physics*
(Sept. 2018).
arXiv: `1809.07168 [hep-ex]`.

[Edwards & Syphers 1992]
Edwards, D. & Syphers, M.
An Introduction to the Physics of High-Energy Accelerators
ISBN: 978-0-471-55163-8
(Wiley, New York, 1992).

[Ferrari *et al.* 2005]
Ferrari, A. *et al.*
FLUKA: A multi-particle transport code (Program version 2005)
(2005).

[Friščić *et al.* 2019]
Friščić, I., Donnelly, T. & Milner, R.
New approach to determining radiative capture reaction rates at astrophysical energies.
Phys. Rev. C **100,** 025804.
arXiv: `1904.05819 [nucl-ex]`
(2019).

[Gagneur 2018]
Gagneur, S.
Strahlprofilmessung des Gas-Jet-Targets für das MAGIX-Experiment
bachelor's thesis (Johannes Gutenberg-University Mainz, 2018).

[Geant4 Collaboration 2017]
Geant4 Collaboration.
Geant4 Book For Application Developers
(2017).

[Geant4 Collaboration 2019]
Geant4 Collaboration.

Geant4 Physics Reference Manual
Version 10.4
(2019).

[Grieser *et al.* 2018]
Grieser, S. *et al.*
A cryogenic supersonic jet target for electron scattering experiments at MAGIX@MESA and MAMI.
Nuclear Instruments and Methods in Physics Research Section A: Accelerators, Spectrometers, Detectors and Associated Equipment **906,** 120–126. ISSN: 0168-9002
(2018).

[Heinemeyer *et al.* 2007]
Heinemeyer, S. *et al.*
An Experiment to Search for Light Dark Matter in Low-Energy ep Scattering
2007.
arXiv: `0705.4056 [hep-ex]`.

[Karr & Marchand 2019]
Karr, J.-P. & Marchand, D.
Progress on the proton-radius puzzle.
Nature **575,** 61–62
(2019).

[Krieger 2017]
Krieger, H.
Grundlagen der Strahlungsphysik und des Strahlenschutzes 4th Edition
(Springer Spektrum, Ingolstadt, 2017).

[Ledroit 2016]
Ledroit, B.
Aufbau und Test des MESA-Choppers
master's thesis (Johannes Gutenberg-University Mainz, 2016).

[Lee *et al.* 2019]
Lee, S. *et al.*
Design and operation of a windowless gas target internal to a solenoidal magnet for use with a megawatt electron beam.
Nuclear Instruments and Methods in Physics Research Section A: Accelerators, Spectrometers, Detectors and Associated Equipment **939,** 46 –54. ISSN: 0168-9002
(2019).

[Leo 1994]
Leo, W. R.
Techniques for Nuclear and Particle Physics Experiments 2nd Edition
(Springer-Verlag Berlin Heidelberg, 1994).

[Lide 2004]
Lide, D. R.

CRC Handbook of Chemistry and Physics 84th Edition
(CRC Press, Boca Raton, FL, 2004).

[Lynch & Dahl 1991]
Lynch, G. R. & Dahl, O. I.
Approximations to multiple Coulomb scattering.
Nuclear Instruments and Methods in Physics Research Section B: Beam Interactions with Materials and Atoms **58,** 6 –10. ISSN: 0168-583X
(1991).

[MAGIX group 2020]
MAGIX group.
MAGIX gas jet target schematic drawing
visited 10.12.2020.
2020.
`https://magix.uni-mainz.de/target.php`.

[Matejcek *et al.* 2019]
Matejcek, C., Aulenbacher, K. & Friederich, S.
Low Energy Beam Transport System for MESA.
J. Phys. Conf. Ser. **1350** (eds Boland, M. *et al.*) 012027
(2019).

[Merkel 2018]
Merkel, H.
MAGIX group meeting
2018.

[Molière 1948]
Molière, G.
Theorie der Streuung schneller geladener Teilchen II Mehrfach-und Vielfachstreuung.
Zeitschrift für Naturforschung A **3,** 78 –97
(1948).

[Motz *et al.* 1964]
Motz, J. W., Olsen, H. & Koch, H. W.
Electron Scattering without Atomic or Nuclear Excitation.
Rev. Mod. Phys. **36,** 881–928
(1964).

[Nevay *et al.* 2020]
Nevay, L. *et al.*
BDSIM: An accelerator tracking code with particle–matter interactions.
Computer Physics Communications **252,** 107200. ISSN: 0010-4655
(2020).

[Robert & Casella 2005]
Robert, C. P. & Casella, G.
Monte Carlo Statistical Methods (Springer Texts in Statistics)

ISBN: 0387212396
(Springer-Verlag, Berlin, Heidelberg, 2005).

[Schlimme 2020]
Schlimme, S.
Few Body Physics – Local Projects
Presentation.
2020.
`https://indico.him.uni-mainz.de/event/69/contributions/357/attachments/234/256/Schlimme_BS_2020-10-29_SFB_Workshop_FewBody.pdf`.

[Schmidt 2014]
(ed Schmidt, R.)
Proceedings of the Joint International Accelerator School: Beam Loss and Accelerator Protection
(CERN, Geneva, 2016, Newport Beach, United States, 2014).

[Simon 2018]
Simon, D.
MAD-X MESA lattice model
Private communication.
2018.

[Simon 2020]
Simon, D.
Schematic MESA drawing
Private communication.
2020.

[Simon 2014]
Simon, D.
Strahlführungsentwurf für MESA
Diploma thesis (Johannes Gutenberg-University Mainz, 2014).

[Simon & Stengler 2018]
Simon, D. & Stengler, T.
Schematic MESA drawing
2018.

[Spiegel *et al.* 2009]
Spiegel, M. R., Lipschutz, S. & Liu, J.
Mathematical Handbook of Formulas and Tables 3rd Edition
(McGraw-Hill, 2009).

[Stengler 2020]
Stengler, T. U.
Entwicklung eines supraleitenden Beschleunigermoduls für den rezirkulierenden Betrieb am Mainz Energy-Recovering Superconducting Accelerator (MESA)
PhD thesis (Johannes Gutenberg-University Mainz, 2020).

[Tange 2018]
Tange, O.
GNU Parallel 2018
ISBN: 9781387509881.
`https://doi.org/10.5281/zenodo.1146014`
(Ole Tange, Mar. 2018).

[Tennant 2018]
Tennant, C. *et al.*
LERF - New Life for the Jefferson Lab FEL
in *59th ICFA Advanced Beam Dynamics Workshop on Energy Recovery Linacs*
(2018),
TUIACC001.

[Tigner 1965]
Tigner, M.
A possible apparatus for electron clashing-beam experiments.
Il Nuovo Cimento (1955-1965) **37,** 1228–1231
(1965).

[Wille & McFall 2000]
Wille, K. & McFall, J.
The Physics of Particle Accelerators: An Introduction
ISBN: 9780198505495
(Oxford University Press, 2000).